

**Experimental design and vortex analyses in
turbulent wake flows**

by

Bengt E. G. Fallenius

October 2011
Technical Reports from
Royal Institute of Technology
KTH Mechanics
SE-100 44 Stockholm, Sweden

Akademisk avhandling som med tillstånd av Kungliga Tekniska Högskolan i Stockholm framlägges till offentlig granskning för avläggande av teknologie doktorsexamen fredagen den 11 november 2011 kl. 10.30 i sal D3, Lindstedtsvägen 5, Kungliga Tekniska Högskolan, Stockholm.

©Bengt E. G. Fallenius 2011

Universitetsservice US-AB, Stockholm 2011

Bengt E. G. Fallenius 2011, **Experimental design and vortex analyses in turbulent wake flows**

Linné Flow Centre, KTH Mechanics, SE-100 44 Stockholm, Sweden

Abstract

A new experimental setup for studies on wake flow instability and its control that successfully has been designed and manufactured, is introduced and described. The main body is a dual-sided flat plate with an elliptic leading edge and a blunt trailing edge. Permeable surfaces enable boundary layer suction and/or blowing that introduce the unique feature of adjusting the inlet condition of the wake created behind the plate. This, in combination with a trailing edge that is easily modified, makes it an ideal experiment for studies of different control methods for the wake flow instability as well as extensive parameter studies. Experimental validation of the setup has been performed by means of measurements of the wake symmetry and boundary layer velocity profiles at the trailing edge. Some preliminary results on the Strouhal number versus different inlet conditions are reported.

Additionally, an *in-house* vortex detection (VD) program has been developed in order to detect, analyse and compare small-scale vortical structures in instantaneous velocity fields from flow measurements. This will be a powerful tool for comparison of wake characteristics for varying inlet conditions and control methods in the new experimental setup. Measurements from three completely separate experimental setups with different geometries and flow cases, have been analysed by the VD-program.

- (i) In order to obtain improved ventilation we have studied the effect of pulsating inflow into a closed volume compared to having the inflow at a constant flow rate. We show that the number of small-scale eddies is significantly increased and that the stagnation zones are reduced in size, which enhances the mixing.
- (ii) Instantaneous velocity fields in the wake behind a porous cylinder subjected to suction or blowing through the entire cylinder surface have also been analysed using the VD-program. The results show that the major change for different levels of blowing or suction is the location of vortices while the most common vortex size and strength are essentially unchanged.
- (iii) Another study on how the geometry of a V-shaped mixer in a pipe flow affects the mixing have also been examined, where no general differences were found between different thicknesses, why a thickness that is favourable from an acoustic point of view can be chosen.

We also propose a new method, using global mode analysis on experimental data, showing that randomly ordered snapshots of the velocity field behind the porous cylinder can be re-ordered and phase-averaged.

Descriptors: Bluff bodies, wake flow, experimental design, vortex detection, flow control, asymptotic suction boundary layer.

Preface

This doctoral thesis in engineering mechanics treats the design of a new experimental setup, from which enhanced knowledge about how the hydrodynamic stability of the flow in the wake of a bluff body can be controlled. The thesis is divided into two parts, where the first part starts with a brief overview of bluff bodies and wake flows. This is followed by a description of the different measurements techniques and experimental setups that have been utilised. A Matlab[®] program that has been developed for vortex analyses of the particle image velocimetry measurements is then also described. The first part ends with introduction of the new experimental setup and a summary. The second part consists of five papers.

October 2011, Stockholm

Bengt Fallenius

Contents

| | |
|--|-----|
| Abstract | iii |
| Preface | v |
| Part I. Overview and summary | |
| Chapter 1. Introduction | 1 |
| Chapter 2. Bluff bodies and wake flow | 3 |
| 2.1. Bluff bodies | 3 |
| 2.2. Wake flow | 5 |
| Chapter 3. Measurement techniques and experimental facilities | 8 |
| 3.1. Pitot tube measurements | 8 |
| 3.2. Hot-wire anemometry | 9 |
| 3.3. Particle Image Velocimetry | 10 |
| 3.4. The Boundary Layer wind tunnel | 11 |
| 3.5. Pipe flow mixing experiment | 11 |
| 3.6. Room ventilation model | 11 |
| Chapter 4. Vortex detection | 13 |
| 4.1. Definitions of a vortex | 13 |
| 4.2. Velocity field filtering | 16 |
| Chapter 5. New experimental setup | 21 |
| Chapter 6. Summary | 24 |
| Chapter 7. Papers and authors contributions | 25 |
| Acknowledgements | 27 |
| References | 29 |

Part II. Papers

| | | |
|-----------------|---|------------|
| Paper 1. | A new test-section for wind tunnel studies on wake instability and its control | 35 |
| Paper 2. | Experimental study on the effect of pulsating inflow to a closed volume | 69 |
| Paper 3. | Vortex analysis in the wake of a porous cylinder subject to continuous suction or blowing | 97 |
| Paper 4. | Stability analysis of experimental flow fields behind a porous cylinder for the investigation of the large-scale wake vortices | 143 |
| Paper 5. | On the vortex generation behind a passive V-shaped mixer in a pipe flow | 181 |

Part I

Overview and summary

CHAPTER 1

Introduction

The flow around and in the near downstream region of bluff bodies is a research area that has caught the interest of many people for a long period of time. The main reason is the challenge to understand the physics of the flow. Another reason for the large interest is the large number of technical applications, where different flow phenomena occur. An example is the low pressure region behind vehicles travelling at high speeds that gives a drag force on the vehicle and hence, has a direct impact on fuel efficiency and road stability. Another is vibrations and fatigue in structures caused by periodic vortex shedding.

Learning how to control these phenomena, and the vortex shedding in particular, can lead to improved energy efficiency and reduction of noise and vibrations in high aspect ratio structures. In industrial processes such as papermaking, control of the wake instability would enable the manufacturing of multiple layer paper, which by use of rough unbleached fibres in the middle of the paper sheet would maintain or improve the quality while the cost and the load on the environment are reduced.

In times when computer capacity increases exponentially and the cost decreases, more complex events may be simulated and one might question the need for expensive experiments. Though, as the complexity of the simulations increases, it is even more important to be able to validate the computer codes and find the real value of different physical parameters.

However, for high Reynolds number flows today's computers are still not fast enough to perform direct numerical simulations of the governing equations. Thus, turbulence modelling is required, which always has to be validated against accurate experimental data. Furthermore, at low Reynolds numbers, where interesting flow stability problems occur, there is today the possibility to numerically perform global mode stability analyses, which is performed on entire velocity fields and gives rise to large eigenvalue problems to be solved. There is thus a search for new experimental setups, which can produce data to test and validate numerical stability codes and physical boundary conditions.

This thesis treats the design of a new experimental setup that aims at studies and the development of different methods to control the hydrodynamic instability of the wake behind bluff bodies. The new setup enables parameter

studies that have not been performed experimentally before and gives the possibility to observe flow phenomena where the natural case have been set aside in order to investigate how the downstream flow of a bluff body is affected by the wake initial condition. Also, the setup is designed to study how different control methods, active and passive, are affected if the inflow of the wake is changed.

In order to quantify the changes in the flow, a vortex detection program has been developed. Statistics of the structures are collected for analyse and comparison. Additionally, a numerical study of experimental data from a turbulent cylinder wake has been performed where random ordered snapshots have been reordered to enable phase averaging.

CHAPTER 2

Bluff bodies and wake flow

In this chapter an overview of what can be called a bluff body is given and how a uniform stream is affected by its presence.

A two-dimensional body is a body with an arbitrary cross-sectional area, which is extended to infinity in the direction perpendicular to this area. The mean flow around a body can be considered two-dimensional¹ if the aspect ratio, defined as the extension width over the equivalent diameter of the cross-section, is large enough. This means that the end-effects do not influence the flow at the centre of the body. However, in a mean velocity perspective the flow will always be two-dimensional provided that the aspect ratio is large enough (see e.g. Norberg 1994). In the following we are assuming two-dimensional flow.

2.1. Bluff bodies

The drag force on objects placed in a flow can be divided into two parts, namely skin friction drag $F_{D,f}$, which is due to the viscous forces at the wall and the pressure drag $F_{D,p}$, also denoted form drag, which is due to the pressure distribution around the object.

In figure 2.1 a simple example is shown. A two dimensional cylinder with the perimeter $c = c(r, \theta)$, is subjected to a uniform velocity field (U_0), which causes tangential wall-shear stress $\tau_w = \tau_w(r, \theta)$ and a pressure distribution $p = p(r, \theta)$ around the body. The corresponding skin-friction drag per unit width ($F'_{D,f}$) is given by the integrated wall-shear stress projected in the direction parallel to the oncoming uniform velocity field as

$$F'_{D,f} = \int_{c(r,\theta)} \tau_w(r, \theta) \sin \theta \, ds , \quad (2.1)$$

where $ds = r d\theta$ is the path along the perimeter c . The pressure difference in the streamwise direction is obtained through direct integration around the body after projecting $p ds$ in the direction parallel to the oncoming uniform velocity field. The result is the form drag per unit width ($F'_{D,p}$), which is obtained as

¹Note, for high enough Reynolds numbers (see section 2.1) physical flow phenomena will introduce 3D effects and consequently the two-dimensionality will be altered.

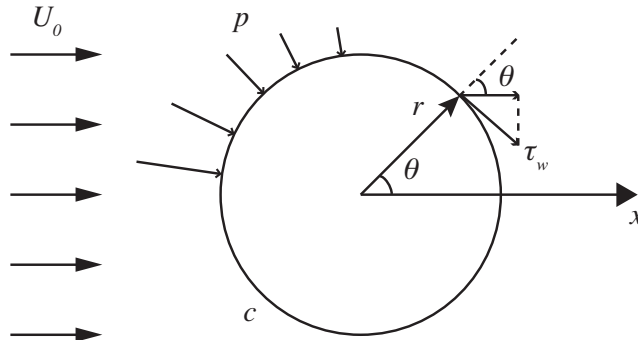


FIGURE 2.1. Drag forces acting on the cylinder. The drag on a cylinder may be divided into a pressure/form (p) and skin-friction (τ_w) contribution.

$$F'_{D,p} = \int_{c(r,\theta)} p(r,\theta) \cos \theta \, ds . \quad (2.2)$$

The sum of the two drag contributions gives the total drag force of the body as,

$$F_{D,tot} = (F'_{D,f} + F'_{D,p}) \cdot L_w , \quad (2.3)$$

where L_w is the extension width of the two-dimensional body. Generally speaking there are two types of bodies with very different flow characteristics. The first type are aerodynamically smooth bodies, which are found in many engineering applications where a low drag and/or high lift is desired, such as airplane wings and similar bodies that end with a continuously decreasing thickness in the streamwise direction. The second type is the opposite of an aerodynamically shaped body, i.e. bluff bodies, which typically has a blunt trailing edge and separated flow somewhere along the surface of the body. This makes the pressure recovery around the body incomplete and hence gives a contribution to the pressure drag. To illustrate how different the total drag is between these two types of bodies an example is given below.

Example

Consider two objects placed in a free stream with the velocity U_∞ , kinematic viscosity ν and density ρ . One of the bodies is a cylinder with the diameter d and the other is a NACA 0018 airfoil².

The Reynolds number (Re) is a flow parameter, which is defined as a characteristic velocity times a characteristic length of the flow over the kinematic viscosity. This parameter can be seen as the ratio between flow destabilising

²The number 0018 states that the maximum thickness of the airfoil is 18% of the chord.

forces, i.e. inertia forces, and flow stabilising forces, i.e. viscous forces. For the flow around a cylinder the Reynolds number becomes

$$Re = \frac{U_\infty d}{\nu}, \quad (2.4)$$

where d is the diameter. If Re is set to 2000, the drag coefficient $C_D = F'_D/(q_\infty d)$ is about unity. Here, $q_\infty = 0.5\rho U_\infty^2$ is the dynamic pressure and F'_D denotes drag force per unit width. To obtain the same F'_D of the airfoil the chord length has to be about $100d$, which gives a Reynolds number based on the chord of about 2×10^5 . Hence, the thickness of the airfoil that gives the same drag force per unit width as the cylinder is $18d$. In figure 2.2 the two bodies are shown according to scale.

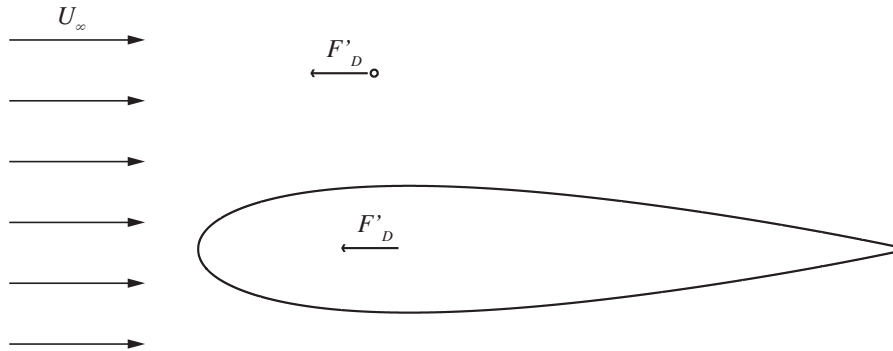


FIGURE 2.2. The drag force caused by the flow on a cylinder with diameter d is the same as for a airfoil with a maximum thickness of $18d$ and a chord of $100d$. Note, the figure is according to scale.

2.2. Wake flow

As illustrated in the previous section, the drag force on an object is not solely determined by its frontal area. For instance, the shape of its trailing edge is also important. A blunt trailing edge gives rise to a low-pressure region, also called the near wake.

The size of such a wake is governed by the Reynolds number that depends on the free stream velocity and the size of the object. Depending on the geometry of the body, there can be sudden changes of the wake flow properties at different Reynolds numbers (see section 2.1). As an example, one can look at the drag coefficient for a circular cylinder. In the range $10^2 < Re < 10^5$ it is close to unity, while at $Re \sim 10^5$ it drops suddenly down to about 0.3, whereafter it subsequently increases and levels out again at $Re \sim 10^7$ to about

0.6. For a smooth cylinder, the drop is due to formation of separation bubbles and boundary layer transition to turbulence on the cylinder surface. The drag coefficient for a square cylinder behaves differently, it is constant equal to 2 for Reynolds numbers within the range of incompressible flow, since the separation points do not move from the sharp leading edges. Although, rounding of the corners of the square cylinder makes the drag coefficient change towards that of a circular cylinder.

Another important phenomenon is the periodic vortex shedding that occurs behind objects with a blunt trailing edge. It is characterised by the alternating shedding of vortices from the two sides of the object. This phenomenon is also Reynolds number dependent and sets in at around $Re = 40 - 50$ for a circular cylinder, depending on the flow quality. The frequency of the periodic shedding can be estimated through the Strouhal number (St), a non-dimensional frequency, given as

$$St = \frac{fd}{U_\infty}, \quad (2.5)$$

where f is the frequency of the periodic shedding. The Strouhal number varies with geometry and Re . However, for Re in the range $10^2 - 10^5$ the Strouhal number is almost constant, 0.2 for the circular and square cylinder. For rectangular cylinders it depends on the aspect ratio l/d , where l is the streamwise length of the object.

The periodic vortex shedding induces alternating positive and negative side forces, which can induce vibrations of the object. This can be a source of noise and other interferences. In worst case the shedding frequency coincides with the eigenfrequency of the structure/object, which can lead to material fatigue and structural failure.

The vortex shedding phenomenon is purely two-dimensional and is called the von Kármán vortex street after Theodore von Kármán (see Kármán 1912), who first studied and described this phenomenon. Figure 2.3 shows a NASA satellite image that captures an area of $365 \times 150 \text{ km}^2$ near the island of Jan Mayen in the north Atlantic ocean. In the image one may observe a von Kármán vortex street evolving downstream of the Beerenberg volcano that raises 2200 m above the sea level. The stratified layers in the atmosphere makes the flow locally two-dimensional around the otherwise three-dimensional volcano.

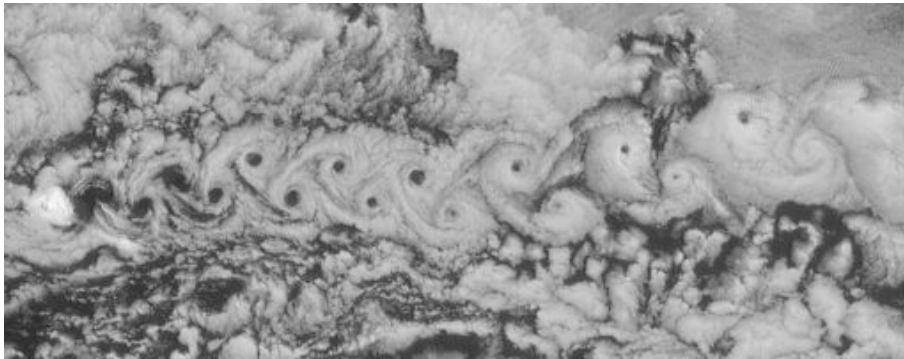


FIGURE 2.3. A more than 300 km long von Kármán vortex street near the island of Jan Mayen. (NASA)

CHAPTER 3

Measurement techniques and experimental facilities

In this chapter a brief description on the different measurements techniques and experimental setups that have been used is given. Most often it is the flow velocity distribution that is the main variable of interest and this can be measured by different means. The different methods that have been used is Pitot tube measurements, hot-wire anemometry, and Particle Image Velocitometry. Depending on the flow case and what kind of measurement that are desired, the methods have different advantages and disadvantages.

3.1. Pitot tube measurements

A classic method that is used to measure a flow velocity is with a total pressure tube, or *Pitot-tube*, which can be a simple tube with one open end facing straight to the flow. According to Bernoulli's theorem, the total, or stagnation pressure p_0 , is the sum of the static pressure p and the dynamic pressure $q = \frac{1}{2}\rho u^2$, where ρ is the fluid density and u the flow velocity so that

$$p_0 = p + \frac{1}{2}\rho u^2 \quad (3.1)$$

if the flow is incompressible and inviscid. In most windtunnel experiments, this can be assumed, and the local flow velocity is then given by the difference between the total and the static pressure. The static pressure is often taken from a pressure hole in the windtunnel wall close to the position for the velocity measurement. A Pitot-tube is then used to measure the total pressure and is positioned so that the open end faces the flow in the opposite streamwise direction. This makes the method intrusive, but the influence can be reduced by keeping the dimension of the probes down.

The walls of the Pitot-tube should be as thin as possible, and the inner diameter as small as possible. Further, if the flow is fluctuating or turbulent, the reading might not be accurate, since the response time is relatively slow. If the measurements are performed near a surface there could be wall effects that affect the result as well. All these things might need to be corrected for, why additional measurements with other techniques could be necessary, depending on the flow case. Hence, it is not necessarily straight forward to use a Pitot-tube. A more detailed description of the considerations that may have to be taken into account is given by Chue (1975).

3.2. Hot-wire anemometry

Hot-wire anemometry (HWA) is a technique that has been available since the beginning of the last century. As in Pitot-tube measurements, the technique is intrusive since it also requires that a probe is mounted inside the flow. However, HWA is generally considered to be one of the best measurement techniques in flow experiments due to its high frequency response and relatively small size. For flow velocity measurements, the Constant Temperature Anemometry (CTA) is the most commonly used method.

A simple probe single-wire probe has the look of a small fork, with two prongs to which the sensitive hot-wire is soldered or welded. The distance between prongs is in the order of 1 mm, and the diameter of the hot-wire is then around 5 μm . The prongs are normally mounted into a dual-hole ceramic tube or similar in order to keep them insulated from each other. Inserting the ceramic tube in a metal tube gives further protection and simplifies mounting in the test area.

The hot-wire is one of the legs in a Wheatstone bridge, and due to the cooling by the forced convection caused by the flow, the resistance will change. That is compensated for by an increased current in the circuit, which causes the output voltage to change accordingly. This event responds very fast to flow speed fluctuations, why sampling frequencies in tens of kHz can be used.

The voltage variation due to the change of the current needed to keep the wire at the initial temperature is monitored and can be related to the flow velocity. For this the hot-wire first needs to be calibrated, which in windtunnel experiments usually is done by first measuring near a Prandtl-tube at different velocities. The result is then fitted to an expression for the relation between the voltage and the velocity, for which commonly King's law or modified versions of the same is used. In order to avoid the need for further correction, the ambient temperature should be kept constant, which in windtunnel experiments is possible if the windtunnel is equipped with a regulated temperature system.

The size of the hot-wire makes it very vulnerable and it breaks easily if the probe is not handled with care. If the hot-wire breaks, it needs to be replaced and re-calibrated, which can be a time-consuming process. For manufacturing and repair, special equipment such as micro-manipulators, microscope and steady hands is necessary.

One has to consider how the hot-wire is placed in relation to the flow, since a single wire does not reveal anything about the direction of the flow, why back-flow can appear as a higher streamwise velocity. In order to measure all three velocity components, as well as the direction of them, one can manufacture a probe with multiple hot-wires, placed in an angle in relation to each other. This puts higher demands on the precision in the manufacturing process and the spatial resolution will be reduced. More about the details and different types of probes can be found in Bruun (2002).

3.3. Particle Image Velocimetry

Particle Image Velocimetry is most often referred to as its abbreviation, *PIV*, and is a technique that has been used for a couple of decades. Several manufacturers supply complete systems, but it is also possible to put together a system with off-the-shelf products and use available open-source software, which can be quite more economical. As the name tells, the technique is based on images of particles that are seeded into the flow, often referred to as seeding, or tracer particles. Two consecutive images of the flow reveal the direction and distance Δs of the particle motion. With a known time Δt between the images the velocity can then be estimated as $v = \Delta s / \Delta t$. A more detailed explanation can be found in Raffel *et al.* (2007), while a shorter description follows.

The principle is simple, but in order to capture rapid moments, a dual-frame camera that has a time between recordings in the order of microseconds or less is needed. For that short shutter speeds, an intense light source is needed. Typically a dual cavity laser is used for this purpose and a cylindrical lens spreads the laser beam into a sheet. The laser sheet is then placed in the plane where the measurements should be performed and the camera is then focused thereon.

In the computerised evaluation, each of the two images in all image pairs is divided into a mesh of *interrogation windows*, that has a size depending on the size of the tracer particles and the flow velocity. Correlation of each interrogation window between the two images gives the direction and the distance that the particles inside that window have moved. The result is then a vector field with vectors representing each interrogation window.

The measurements can be performed in both water and air, and if disregarding the injection of tracer particles, the method is regarded as non-intrusive. The density of the tracer particles should correspond to the one of the medium so that they are transported in the same velocity as the flow. For water solid particles such as Polyamid particles are used, while in air different types of smoke are injected, which is commonly produced by spraying fluid particles into the flow.

Using one camera perpendicular to the laser sheet gives an output of a 2D-velocity field with two components (2C). If a second camera is used the third, out-of-plane component in that plane can be extracted as well, if the cameras are placed with an angle between them. Still only giving information about the velocity distribution in the 2D-plane, this is referred to as 3C-PIV. Recently the technique has developed, and there are now possible to purchase commercial 3D-PIV systems where three or more cameras give the velocity information of a volume of the flow.

3.4. The Boundary Layer wind tunnel

The Boundary Layer (BL¹) wind tunnel is located at the department of Mechanics at KTH, and has been chosen as the experimental facility to host the new setup. The idea with the BL tunnel is to have a short time swap between different experiments by having exchangeable test sections. Below a brief description of the wind tunnel is given. For a more thorough description the interested reader is referred to Lindgren (2002).

The BL wind tunnel is a closed circuit tunnel, powered by an 15 kW axial fan. It was the first tunnel where expanding corners were utilised, making it possible to have a 9:1 contraction ratio together with an short overall wind tunnel length. The space for the testsection is 4.2 m and the cross sectional area of the contraction outlet is $0.5 \times 0.75 \text{ m}^2$. The maximum flow velocity is 48 m/s and the turbulence levels² are 0.04%, 0.06% and 0.04% in the streamwise, wall-normal and spanwise directions, respectively, at the nominal³ free stream velocity of 25 ms^{-1} . At this nominal velocity the variation in total pressure is less than $\pm 0.1\%$ and the variation in temperature is less than $\pm 0.07 \text{ }^\circ\text{C}$ over the cross sectional area.

3.5. Pipe flow mixing experiment

The experiments were performed in the MWL⁴ pipe flow facility, which is an open facility mainly used for studies on aeroacoustics. The centre line velocity in the pipe was $U_C = 50 \text{ m s}^{-1}$ in all the measurements performed.

The pipe test section is made of plexiglas with a length of 1496 mm and is located 3880 mm downstream of the pipe facility contraction. Downstream of the test section the pipe continues with an extension of 3560 mm. The inner diameter of the pipe is $D = 90 \text{ mm}$ and the wall thickness is 5 mm. At approximately 400 mm downstream of the test section entrance, the vortex generator was mounted through a slit through the pipe wall at an angle of 32° and clamped by a holder attached around the pipe. Two wedge-shaped vortex generators with varying thicknesses, t , and hence different stiffnesses, were studied. Apart from the thicknesses of $t = 3.0$ and 0.5 mm , from here on denoted the stiff and the flexible vortex generator, respectively, they were identical.

3.6. Room ventilation model

The experiments were performed in a two-dimensional (2-D) small-scale water model with the dimension $30 \times 20 \times 0.9 \text{ cm}^3$. To measure instantaneous velocity

¹BL also corresponds to the initials of the wind tunnel designer Björn Lindgren.

²The following turbulence levels correspond to the high-pass filtered intensities, with a cut-off frequency of 20 Hz.

³During the design of the BL-windtunnel, most of the planned experiments were aimed for a free stream velocity of 25 ms^{-1} .

⁴Marcus Wallenberg Laboratory

fields a PIV system was used. This system consists of a Spectra Physics 400 mJ double pulsed Nd:Yag laser operating at 15 Hz as a light source, and a double-frame CCD camera Kodak ES1.0 8-bit with 1018×1008 pixels. The size of the model makes it manageable to traverse the camera-view throughout the model and investigate statistical quantities based on the 2-D velocity vector fields but still keep high enough spatial resolution for instantaneous small-scale vortex analysis. In the lower left and the upper right corner of the model the inflow and outflow take place, respectively, through plastic tubing connected via pipe nozzles attached to the model. Hence, the inflow and outflow to the model take place through a circular cross-sectional area of a diameter $D = 9$ mm. For the PIV the water was seeded with Polyamid seeding particles with a mean particle diameter of $20 \mu\text{m}$. The seeded water is pumped from a water tank and passes through a mechanical pulse generator, which makes it possible to create a pulsating flow upstream of the model of varying frequency. In the return circuit before the tank the water passes a flowmeter in order to monitor the flow rate.

CHAPTER 4

Vortex detection

A search of the literature gives many different definitions of a vortex, see e.g. Jeong & Hussain (1995). In order to develop a vortex detection program one has to come up with some criteria that are characteristic for a vortex. A major drawback with experiments is that most available data is two-dimensional, i.e. the velocity field is only known in one plane. This seriously limits the definition of a vortex, which leads to a less restrictive definition compared to a vortex defined in a three-dimensional velocity field.

This chapter will therefore start with a brief summary of different vortex definitions and discuss their pro and cons in order to shed some light on the limitations of the present vortex detection algorithm.

4.1. Definitions of a vortex

How to define a vortex is an issue that have been discussed for several decades due to the complexity of turbulent flow fields. Numerical modelling has made the dynamics of flow fields more accessible for studies and different methods can more easily be compared. Jeong & Hussain (1995) summarise and discuss the most frequently used definitions of a vortex. Roughly speaking, the different definitions can be divided into intuitive and analytical approaches. The former is based on local properties of the flow such as local pressure minima p , the paths of the streamlines

$$\frac{dx}{u} = \frac{dy}{v} = \frac{dz}{w} , \quad (4.1)$$

and the magnitude of vorticity

$$|\omega| \equiv |\nabla \times \mathbf{u}| . \quad (4.2)$$

The latter is based on properties of the velocity gradient tensor $\nabla \mathbf{u}$.

Jeong & Hussain (1995) states two requirements for a vortex core as a preliminary check for an evaluation of the different methods. Firstly, a vortex core must have a net vorticity and hence, net circulation, and secondly, the geometry of the identified vortex should be invariant in a Galilean transformation. A short summary of the review follows.

4.1.1. *Intuitive approaches*

Pressure minima. When the centrifugal force is balanced by the pressure force, a local pressure minimum is located at the axis for the swirling motion. This is shown to be true only in a steady inviscid planar flow, why this is not a valid condition in general.

Closed or spiral pathlines or streamlines. Closed or spiral pathlines or streamlines have been proposed to be used to identify the swirling motion of a vortex. The lifetime of a vortex might however not be long enough for a particle to complete a full revolution that is required for the closed pathline, which means that vortices will occur without being detected. Furthermore, neither closed or spiral pathlines or streamlines are invariant with respect to Galilean transformation, so only vortices that are translated within a certain range of velocity will be detected.

Vorticity magnitude. Defining a vortex as a region where its vorticity magnitude is higher than some threshold has also been suggested as a method. This method turns out to be quite arbitrary since, firstly, it depends on the threshold and secondly, as soon as the background shear is within the same magnitude a distinction between the shear and the vortex may be unfeasible.

4.1.2. *Analytical approaches*

Considering the more analytical approaches, the drawbacks are fewer, although there are still cases where those approaches are unsuitable. Two older methods are presented and compared to the most accepted and used method, namely the λ_2 - *method*.

Complex eigenvalues of velocity gradient tensor, the Δ -method. This approach considers the eigenvalues, λ , of the velocity gradient tensor $\nabla \mathbf{u}$, which satisfies the characteristic equation

$$\lambda^3 - P\lambda^2 + Q\lambda - R = 0 . \quad (4.3)$$

Considering an incompressible flow ($u_{i,i} = 0$) the three invariants of $\nabla \mathbf{u}$ above become

$$P \equiv u_{i,i} = 0 , \quad (4.4)$$

$$Q \equiv \frac{1}{2}(u_{i,i}^2 - u_{i,j}u_{j,i}) = -\frac{1}{2}u_{i,j}u_{j,i} \quad (4.5)$$

and

$$R = \det(u_{i,j}) . \quad (4.6)$$

Chong *et al.* (1990) showed that complex eigenvalues imply that the local streamline pattern is closed or spiral in a reference frame moving with the

point, i.e. when the discriminant

$$\Delta = \left(\frac{1}{3}Q\right)^3 + \left(\frac{1}{2}R\right)^2 \quad (4.7)$$

is positive. Although this method is Galilean invariant, it shows when trying the method on some special cases, such as mixing layers and swirling jets, that Δ is slightly positive even outside vortex cores resulting in that the boundary of the vortices becomes noisy and the size of the vortices are overestimated.

The second invariant of the velocity gradient tensor, the Q-method. It has been suggested to define vortices as regions where $Q > 0$, with the additional condition that the pressure is lower than the ambient value. One may rewrite Q in terms of the symmetric and the antisymmetric parts of $\nabla \mathbf{u}$, i.e. the strain rate tensor and the rotational tensor, respectively. Hence, Q represents the local balance between shear strain rate and vorticity magnitude. According to (4.7) the Q -method is more restrictive than the Δ -method, however, the most appropriate method is not obvious *a priori*.

λ_2 -method. The frequently used λ_2 -method (Jeong & Hussain 1995) comes from inspection of the acceleration gradient

$$a_{i,j} = -\frac{1}{\rho}p_{,ij} + \nu u_{i,jkk} , \quad (4.8)$$

which is derived by taking the gradient of Navier-Stokes equations. Pressure minimum has been used as a starting point without being used as a requirement. The left hand side of (4.8) can be divided into a symmetric and an antisymmetric part where the antisymmetric part is the vorticity transport equation. Leaving out the unsteady irrotational straining and viscous effects in the symmetric part one gets

$$-\frac{1}{\rho}p_{,ij} = S_{ik}S_{kj} + \Omega_{ik}\Omega_{kj} = \mathbf{S}^2 + \mathbf{\Omega}^2 , \quad (4.9)$$

where $S_{ij} = (u_{i,j} + u_{j,i})/2$ and $\Omega_{ij} = (u_{i,j} - u_{j,i})/2$ are the symmetric and the antisymmetric parts of $\nabla \mathbf{u}$, and defined as the strain rate tensor and the rotational tensor, respectively. Local pressure minima existing only due to vortical motion, are then present if two of the eigenvalues of $\mathbf{S}^2 + \mathbf{\Omega}^2$ are negative. Since $\mathbf{S}^2 + \mathbf{\Omega}^2$ is symmetric its eigenvalues λ_1 , λ_2 and λ_3 are real, which requires that $\lambda_2 < 0$ within the vortex core if $\lambda_1 \geq \lambda_2 \geq \lambda_3$.

This definition is then compared, by Jeong & Hussain (1995), with the two methods above for various cases and it is found to be the most general method to identify vortices. It is referred to as the λ_2 -method and has been widely accepted and is even implemented in many numerical codes. The method, however, requires that the Hessian of the pressure is known, i.e. all three

components of the velocity gradient tensor, which are never available in experiments. For this reason the Δ - as well as the Q -method are the most widely used on two-dimensional experimental data.

4.1.3. Two-dimensional velocity fields

In order to detect vortices that are embedded in two-dimensional velocity fields, commonly acquired through PIV-measurements, Adrian *et al.* (2000) suggested that decomposition of the velocity field by low-pass filtering is an adequate way to visualise small-scale vortices. In their study, a Gaussian filter was used for the decomposition and the vortices were then detected by using the approach suggested by Chong *et al.* (1990), i.e. identifying closed or spiral streamline patterns by looking at the complex eigenvalues of the high-pass filtered two-dimensional velocity gradient tensor,

$$\nabla \mathbf{u}_{2D}'' = \begin{bmatrix} \frac{\partial u''}{\partial x} & \frac{\partial u''}{\partial y} \\ \frac{\partial v''}{\partial x} & \frac{\partial v''}{\partial y} \end{bmatrix}. \quad (4.10)$$

Regions where the imaginary eigenvalues are positive and greater than a threshold are then defined as a vortex. Agrawal & Prasad (2002) also used a Gaussian filter to perform the decomposition suggested by Adrian *et al.* (2000), while vortices were identified by looking at the neighbouring vectors of each point. If the angular orientation of the surrounding vectors experienced a monotonically angular variation from 0 to 2π the point was considered to be a vortex centre. The same decomposition will be used here, while the Δ -method according to Chong *et al.* (1990) will be used for the vortex identification.

4.2. Velocity field filtering

4.2.1. Decomposition

A turbulent flow field consists of a spectrum of different scales, from the largest geometrically allowed down to the smallest viscous scale, namely the Kolmogorov scale. To reveal the small-scale structures that are embedded in the measured turbulent flow field, the latter is decomposed into a low-pass filtered velocity field and a high-pass velocity field, corresponding to the spatially large and small scale structures, respectively. If these velocity fields are added together, one recovers the fully measured flow field, see figure 4.1. The decomposition is performed in the same manner as in e.g. Agrawal & Prasad (2002), i.e. convolving a low-pass filter on the full velocity field \mathbf{u} , and thereby get a velocity field $\bar{\mathbf{u}}$ that contains the larger scales of the full velocity field. To get the small scale velocity field \mathbf{u}'' , the large-scale field is then subtracted from

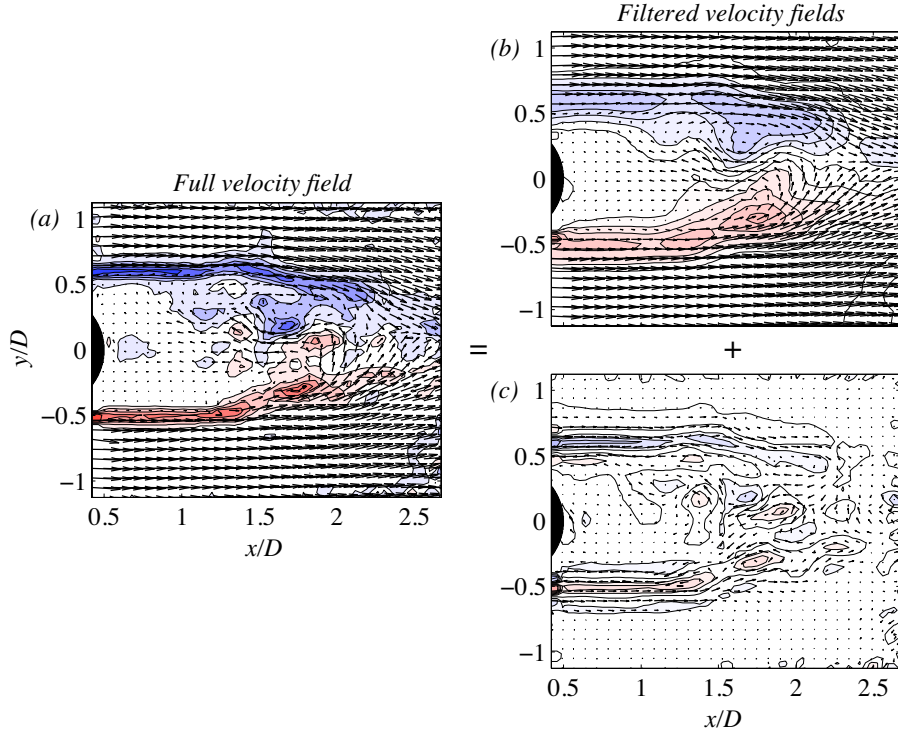


FIGURE 4.1. (a) An instantaneous velocity field behind a porous cylinder with continuous suction through the surface of 2.6% of the oncoming velocity. (b) and (c) show the low- and high-pass filtered velocity fields, respectively.

the full velocity field as

$$\mathbf{u}'' = \mathbf{u} - \bar{\mathbf{u}}. \quad (4.11)$$

4.2.2. Gaussian filter

The filter used for the decomposition is a Gaussian filter that averages the single point (m, n) with the surrounding points. This will give a smeared out velocity field which will emphasise and keep the large scale structures according to

$$\bar{\mathbf{u}}(m, n) = \frac{\sum_{j=-k}^k \sum_{i=-k}^k g(i, j) \mathbf{u}(m-i, n-j)}{\sum_{j=-k}^k \sum_{i=-k}^k g(i, j)}, \quad (4.12)$$

where (i, j) is the indices in x and y , respectively. Here, k is defined as the radius of the filter and since a discrete velocity field is considered, it has a quadratic shape, with each point (m, n) being affected by a surrounding squared region. The Gaussian kernel (g) is defined as

$$g(i, j) = \exp \left[-\frac{(i\Delta x)^2 + (j\Delta y)^2}{2\sigma^2} \right], \quad (4.13)$$

where Δx and Δy are the grid spacing and σ is the padding of the filter. The parameters k and σ can then be chosen by introducing an anisotropy measure d_{rms}^2 , which is defined as the absolute value of the normalised difference between the velocity variance components,

$$d_{rms}^2 = \left| \frac{u_{rms}^2 - v_{rms}^2}{U_\infty^2} \right|. \quad (4.14)$$

In figure 4.2(a) the maximum value of the anisotropy is shown as contour lines for varying k and σ for the velocity field downstream of a cylinder. A consistent requirement for the choice of filter would be to allow a certain amount of anisotropy in the final high-pass filtered velocity field. Typically one here chooses a $\max\{d_{rms}^2\} \leq 0.01$, which is in the order of one magnitude lower than for the unfiltered case. Figure 4.2(b) shows the shape of the Gaussian filter for $k = 5$ and $\sigma = 5$. The filter is normalised, i.e. the total weight is equal to 1, and the small difference in weight between the minima and maxima implies that this filter will smear out smaller scales, while larger scales will remain, which is the pupose with low-pass filtering.

4.2.3. Statistics

In each instantaneous PIV-image, contours where the imaginary part of the complex eigenvalues, λ_{ci} , corresponds to a threshold value is defined as a vortex. Each contour is then examined in order to determine relevant properties such as location, size, circulation and swirl strength of the vortex. This is executed in the following manner. The centre of the vortex is identified by finding the x - and y -coordinates of the maximum imaginary eigenvalue, $\lambda_{ci,max}$, within the contour. This eigenvalue is also stored as a measure of the swirl strength of the vortex (see e.g. Zhou *et al.* 1999). The size of the vortex is then determined by first calculating the area inside the threshold contour level. An equivalent radius to a corresponding circle (C) with its origin at $\lambda_{ci,max}$ is then used as a starting radius for calculating the circulation, γ , through direct integration along C 's perimeter \mathbf{l} according to

$$\gamma = \oint_C \mathbf{u}'' \cdot d\mathbf{l}. \quad (4.15)$$

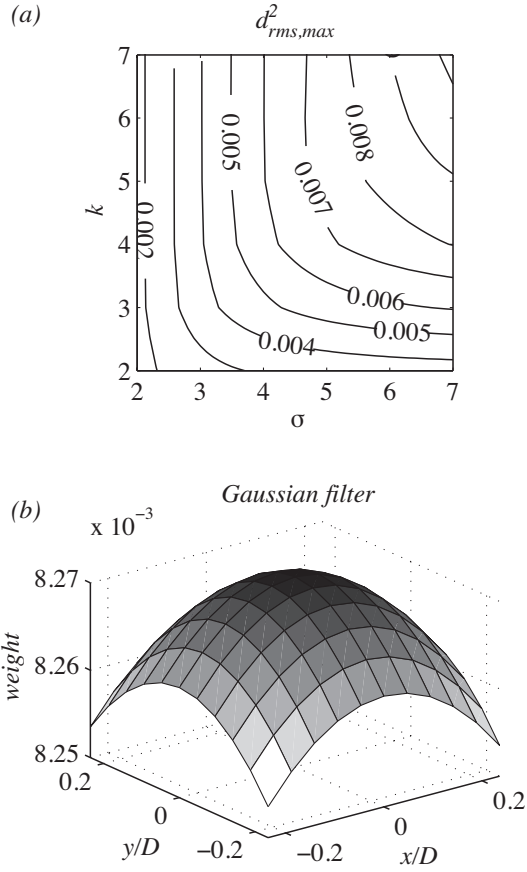


FIGURE 4.2. The maximum values of the anisotropy measure $d_{rms,max}^2$ for different values of k and σ when filtering the flow field behind a circular cylinder with the diameter $D = 50$ mm. (b) The corresponding shape of the normalised Gaussian filter for $k = 5$ and $\sigma = 5$.

This process is repeated while stepping outwards from the vortex centre until the maximum value of the circulation is reached, which then is stored. The corresponding radius is also stored as the vortex size. The two different vortex size measures are shown in figure 4.3(b). Note, that the background velocity vector field is the full velocity field in where the vortices are not necessarily shown.

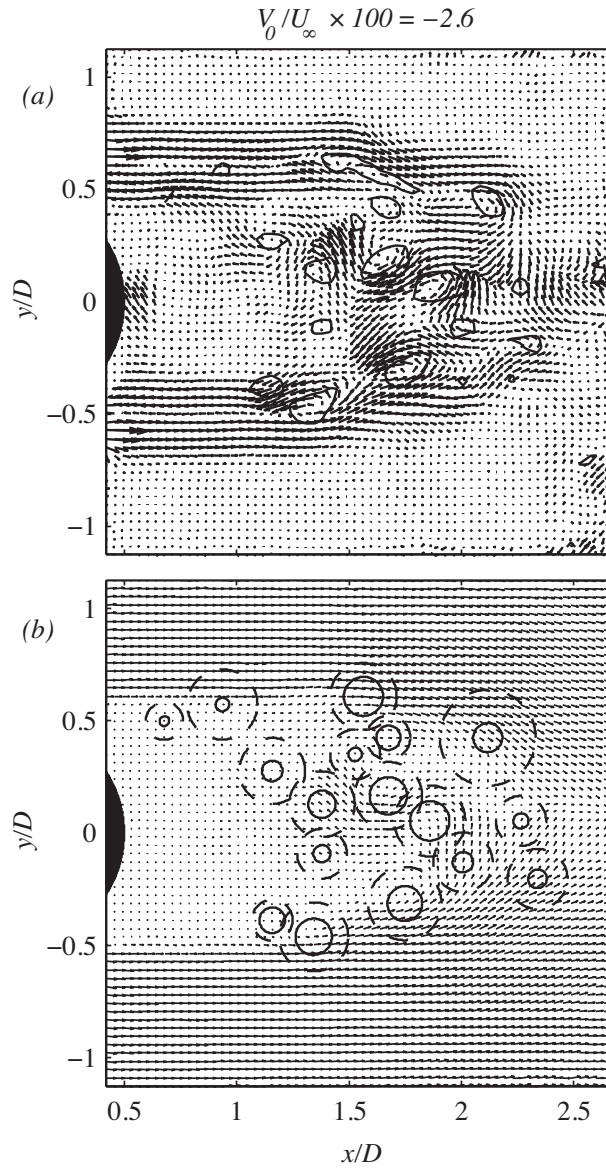


FIGURE 4.3. Instantaneous velocity field of the flow behind a circular cylinder subjected to suction. (a) shows the small scale velocity field where contour lines are regions of $\lambda_{ci} > 15$ and (b) the unfiltered velocity field where (—) corresponds to the equivalent radius of the threshold contour and (---) corresponds to the radius of the vortex, based on the definition of maximum circulation.

CHAPTER 5

New experimental setup

A new experimental setup for studies on wake flow instability and control, including a new test section, has been designed and built at the department of Mechanics, KTH. The new experimental setup introduces the unique feature to in experimental studies vary the inlet conditions of a bluff body wake by means of boundary layer modulation. This, in combination with a trailing edge that is easily modified, makes it an ideal experiment for studies of different control methods for the wake flow instability.

The new experimental setup consists of a main body, which is mounted into a new exchangeable test section, see figure 5.1. The test section is based on two steel frames and has a total length of 4 m. Plexiglas together with plywood have been used for the walls since a high level of optical access is desired for measurements with High Speed Stereoscopic Particle Image Velocimetry (HS-S-PIV). Top and bottom walls have hatches for easy access into the test section, which is important both for adjustments and cleaning. A picture of the setup with a fan and tubing connected is shown in figure 5.2

The main body, shown in figure 5.3, consists of a flat plate (1), also denoted rectangular-based forebody, with an elliptic leading edge (2) and a blunt trailing edge (3). The middle part is a sandwich construction consisting of two supporting frames (4) an aluminium sheet (5) that separates the two sides and the permeable surfaces (6), which are made of laser drilled titanium.

If continuous suction or blowing of air through the permeable surfaces is applied, the shape and thickness of the boundary layer profile along the rectangular-based forebody will be changed accordingly. This changes the characteristics of the wake flow in terms of the base pressure coefficient, Strouhal number and mean velocity profile, while the free stream velocity is kept constant. In addition, the blunt trailing edge is interchangeable, enabling various means of base flow control.

All details about the present experimental setup is thoroughly reported in Paper 1.

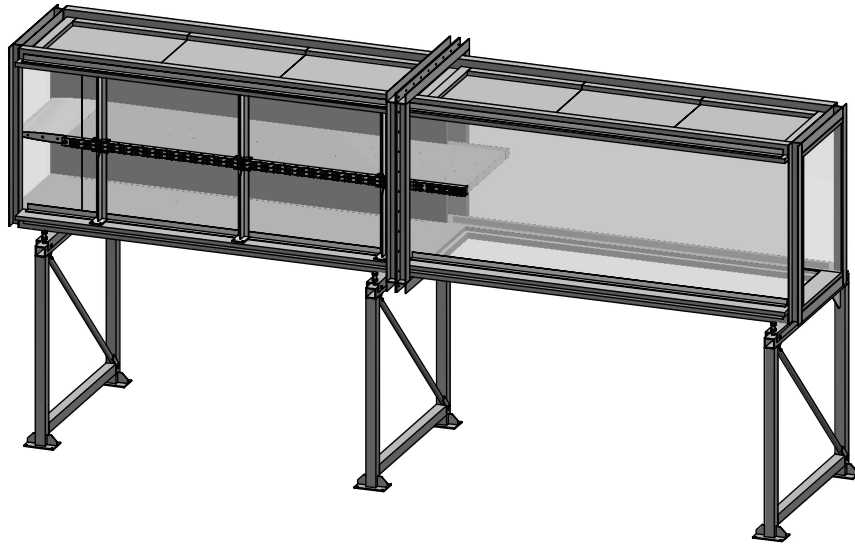


FIGURE 5.1. The main body mounted in the new test section of the wind tunnel. Tubing and measurement equipment excluded.

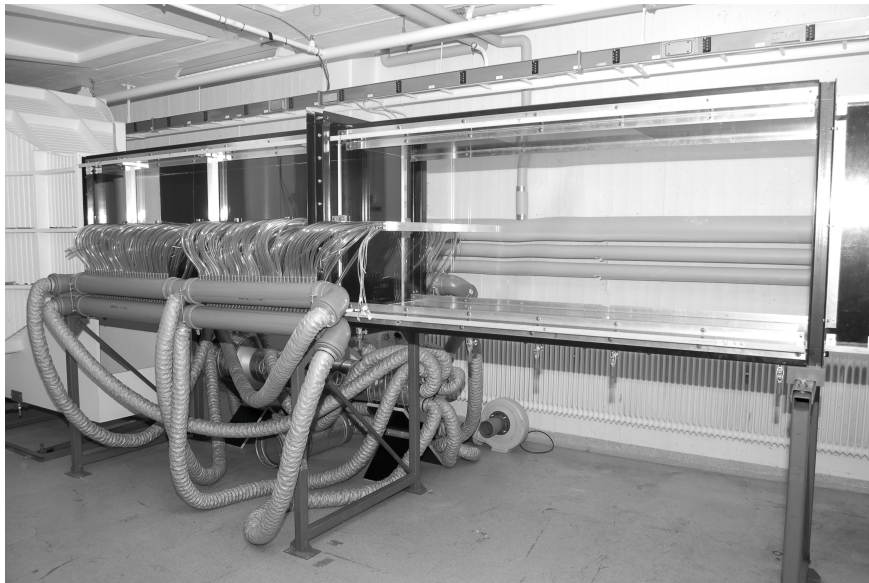


FIGURE 5.2. The main body mounted in the new test section of the wind tunnel with tubing and a fan connected for injection or withdrawal of air through the permeable surfaces.

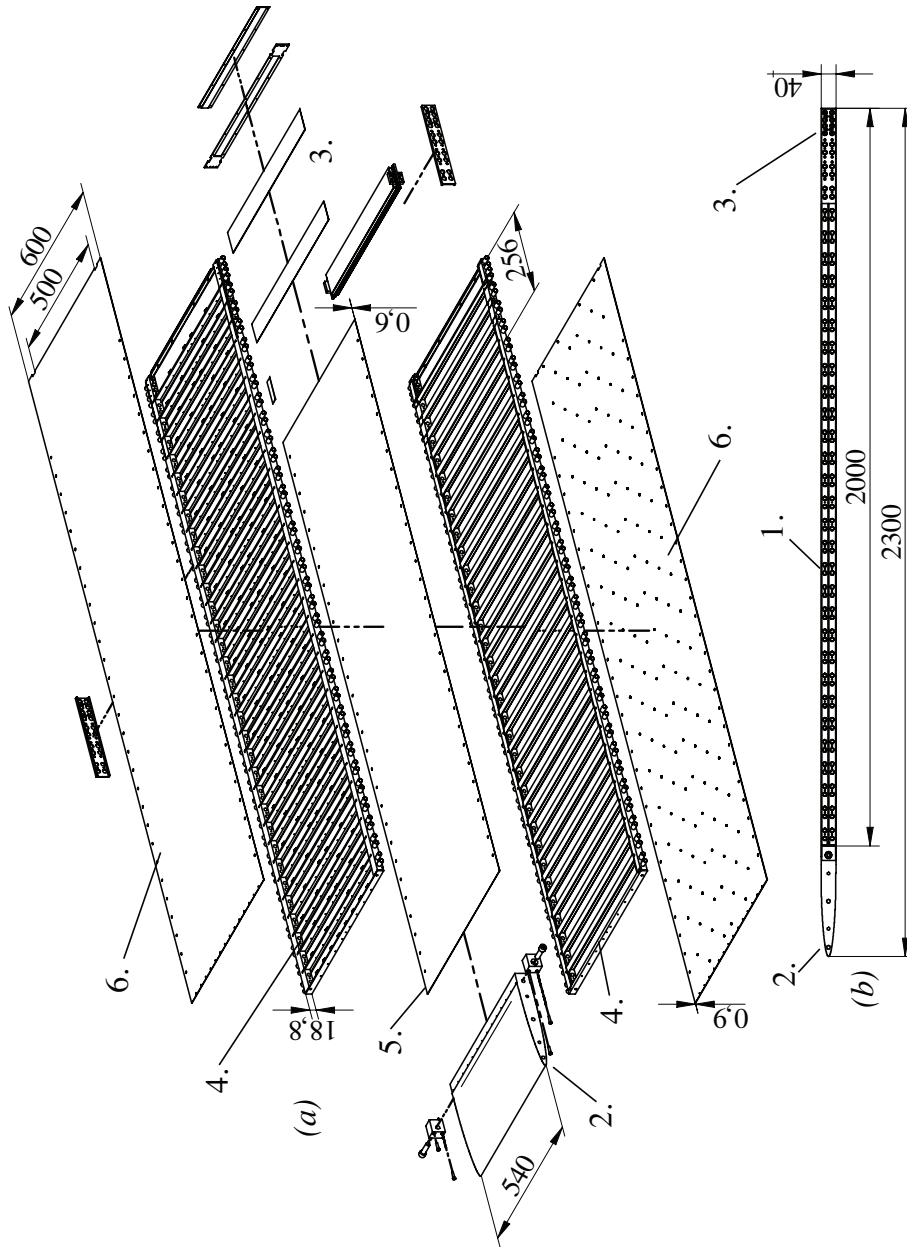


FIGURE 5.3. The rectangular-based forebody in (a) an exploded view and (b) a side view. 1. Flat plate, 2. Leading edge, 3. Trailing edge, 4. Supporting frames, 5. Separating sheet and 6. Permeable sheets.

CHAPTER 6

Summary

In this thesis a new experimental setup for studies on wake flow instabilities and control is introduced. A main body consisting of a flat plate, with an elliptic leading edge and a blunt trailing edge, was designed as a sandwich construction with an hollow interior and has been manufactured. Permeable surfaces on both sides give the unique possibility to perform boundary layer suction or blowing along the plate and thus, mastering the inlet profile of the wake. The dual layer design enables an asymmetric wake to be created, by independently adjusting the pressure difference across the surfaces on the two sides. Furthermore, the plate has separate compartments, which makes local manipulation of the boundary layer possible.

An exchangeable trailing edge of the plate adds the possibility to implement various types of active control devices, such as feed-back controlled jets or base-bleed. Passive control devices such as splitter plates and other obstacles for manipulation of the periodic separation is also easily mounted.

The new test section is designed for the use of modern measurement techniques such as high-speed stereoscopic PIV, which generates a high amount of data about the flow field. To effectively handle all the acquired data, a Matlab[®] program that automatically filters a two-dimensional velocity field and identifies small-scale vortices has been developed. The program stores information about vortex location, size, strength and circulation, which makes statistical analyses for different flow conditions a straightforward process.

Combining the new experimental setup with the developed tool for velocity field analyses, the understanding of the wake flow behaviour for different inlet conditions as well as control methods, will be enhanced. The aim is that this will contribute to the efforts in finding new means to reduce drag and oscillating structural forces on bluff bodies in different technical applications.

CHAPTER 7

Papers and authors contributions

Paper 1

A new test-section for wind tunnel studies on wake instability and its control.
B. E. G. Fallenius (BF), Renzo Trip (RT) & J. H. M. Fransson (JF).

The design of the new test-section and experimental setup has been done by BF under the supervision of JF. BF has performed the measurements and RT has been assisting. The report has been written by BF with input from JF. RT did the analysis on the Pitot tube corrections and contributed with some profile figures. Parts of this work have been presented at the 62nd Annual Meeting of the APS Division of Fluid Dynamics 2009, Minneapolis, USA, the 6th IUTAM Symposium on Bluff Body Wakes and Vortex-Induced Vibrations 2010, Capri Island, Italy, the 63rd Annual Meeting of the APS Division of Fluid Dynamics 2010, Long Beach, USA, and at Svenska mekanikdagarna 2011, Göteborg, Sweden.

Paper 2

Experimental study on the effect of pulsating inflow to a closed volume.
B. E. G. Fallenius (BF), A. Sattari (AS), J. H. M. Fransson (JF) & M. Sandberg (MS).

The measurements were performed by AS under the guidance of BF. BF analysed the results with some assistance by AS. BF created the vortex statistics and made all experimental result figures. The report was written jointly by BF and JF, with some contribution from AS and MS. MS initiated the project and manufactured the model. Parts of this work have been presented at the 12th ROOMVENT Conference 2011 in Trondheim, Norway.

Paper 3

Vortex analysis in the wake of a porous cylinder subject to suction or blowing.
B. E. G. Fallenius (BF) & J. H. M. Fransson (JF).

This work is based on experiments on a porous cylinder subjected to suction or

blowing, performed by JF. The vortex detection program was developed and finalized by BF under the guidance of JF. All the vortex statistics and figures have been made by BF. The results have been produced by BF and the article has been written jointly by the authors. Parts of this work have been presented at the European Fluid Mechanics Conference 2008, Manchester, Great Britain, at the XXII International Congress of Theoretical and Applied Mechanics 2008, Adelaide, Australia, and at Svenska mekanikdagarna 2011, Södertälje, Sweden.

Paper 4

Stability analysis of experimental flow fields behind a porous cylinder for the investigation of the large-scale wake vortices.

S. Camarri (SC), B. E. G. Fallenius (BF) & J. H. M. Fransson (JF).

The experiments were performed by JF. The results were sorted by BF and the numerical analysis was done by SC. A draft version of the paper was written by SC, which then was iterated among the authors. The original figures were made by SC, but were all re-generated by BF and JF for the final version.

Paper 5

On the vortex generation behind a passive V-shaped mixer in a pipe flow.

B. E. G. Fallenius (BF) & J. H. M. Fransson (JF).

The experiments were carried out by BF and JF in collaboration with the Marcus Wallenberg Laboratory. BF has extracted the results from the measurements and the paper has been written jointly by the authors. Parts of this work are published in AIAA Paper 2008-3057, and have been presented at the 14th AIAA/CEAS Aeroacoustics Conference 2008, Vancouver, British Columbia, Canada.

Acknowledgements

First of all I would like to express my gratitude to my supervisor Docent Jens Fransson for giving me the opportunity to perform the graduate studies and the professional guidance you have given me, as well as the optimism about my work and time. Also, I would like to thank my co-advisor Prof. Henrik Alfredsson for the nice and inspiring working environment in the Fluid Physics Laboratory.

A very big thank you to Dr. Ramis Örlü, for sharing so much of your knowledge and time, for often very simple questions. It has made things much more fun and easier.

I also would like to thank Docent Fredrik Lundell for taking time and showing so much interest to my many practical problems during the time in the lab.

And thank you so much Dr. Veronica Eliasson, for always cheering and encouraging from the very start of my studies. It has been a fantastic journey.

Thanks also to Dr. Nils Tillmark, Prof. Alessandro Talamelli and Prof. Laszlo Fuchs for encouraging advices, comments on my work and for introducing interesting references to me. Docent Luca Brandt, Docent Philipp Schlatter, Docent Gunnar Tibert and Docent Nicholas Apazidis have also given me a lot of inspiration in my research studies.

Göran Rådberg and Joakim Karlström are greatly acknowledged for the skilful manufacturing of the new setup and for patiently making last minute changes, as well as for giving constructive suggestions of improvements in the design. It has been fascinating to see how you develop the real thing from a simple sketch. Thanks also to Marcus Gällstedt and Ulf Landén for introducing me to toolmaking as well as my very first experimental setup.

Without Marcus Pastuhoff's professional skills, many things would not have been working still. I am deeply grateful for your help with all the electronics.

Special thanks to Gabriele, Thomas, Allan and Outi for the great times we had together in the lab as well as outside, from the very start. Ola, Malte and

Shahab, thank you for making the fun and relaxing atmosphere we have had in our office, which has been essential for my work. I have also very much enjoyed the fun chats with Ylva between the measurements. I am also very thankful for the probe making by Sohrab when time has been short, and to Renzo for helping me out in the end.

My gratefulness also to Olle, Sissy, Emma, Antonio, Fredrik La., Niklas, Shintaro, Alexander, Johan, Karl, Mathias, Fredrik H., Ulrika, Anna, Robert, Shiho, Monika, Charlotte and Luca F. for contributing to all the joy I have during the days in the lab. Linus, Niklas, Robert, Mattias, Tobias, Espen, Lisa, Shervin, Qiang, Lars-Uve, David, Johan, Andreas x2, Antonios, Florian, Milos and all the other colleagues and staff at OB18 have also made the days at the department of mechanics to a pleasure.

It has been interesting and fun to work together with Dr. Simone Camarri, Andreas, Mikael, Amir Prof. Mats Åbom and Prof. Mats Sandberg.

Things is so much easier when someone else takes care about them, thank you Malin, Stefan, Heide, Pär, Hans, Carolina, Karina Vivi, and Ingunn, for solving all the administrative issues. And of course, Bubba, for all the pushing to go to the gym!

Last but not least I would also thank my family and friends outside KTH for their endless support.

Tack Mor och Far, Syster och Svåger, och inte minst Marie, Calle och Erik!

The Swedish Research Council (VR) and the Göran Gustafsson Foundation is acknowledged for the financial support. I greatly appreciated the travel grants from the Bengt Ingeström Foundation and the Erik Petersohn Memory Foundation.

References

- ADRIAN, R. J., CHRISTENSEN, K. T. & LIU, Z.-C. 2000 Analysis and interpretation of instantaneous turbulent velocity fields. *Exp. Fluids* **19**, 275–290.
- AGRAWAL, A. & PRASAD, A. 2002 Properties of vortices in the self-similar turbulent jet. *Exp. Fluids* **33**, 565–577.
- BRUUN, H. H. 2002 *Hot-Wire Anemometry - Principles and Signal Analysis*. Oxford University Press.
- CHONG, M. S., PERRY, A. E. & CANTWELL, B. J. 1990 A general classification of three-dimensional flow fields. *Phys. Fluids* **2**, 765–777.
- CHUE, S., H. 1975 Pressure probes for fluid measurements. *Prog. Aero. Sci.* **16**, 147–223.
- FRANSSON, J. H. M. & ALFREDSSON, P. H. 2003 On the disturbance growth in an asymptotic suction boundary layer. *J. Fluid. Mech.* **482**, 51–90.
- GRIFFITH, A. A. & MEREDITH, B. A. 1936 The possible improvement in aircraft performance due to the use of boundary layer suction. *Tech. Rep.*. Royal Aircraft Establishment.
- JEONG, J. & HUSSAIN, F. 1995 On the identification of a vortex. *J. Fluid. Mech.* **285**, 69–94.
- KÁRMÁN, T. 1912 Über der Mechanismus des Widerstandes, den ein bewegter Körper in einer Flüssigkeit erfährt. *Göttingen Nachr., Math.-Phys. Klasse* pp. 547–556.
- LINDGREN, B. 2002 Flow facility design and experimental studies of wall-bounded turbulent shear-flows. PhD thesis, Royal Institute of Technology.
- NORBERG, C. 1994 An experimental investigation of the flow around a circular cylinder: influence of aspect ratio. *J. Fluid. Mech.* **258**, 287–316.
- RAFFEL, M., WILLERT, C. E., WERELEY, S. T. & KOMPENHANS, J. 2007 *Particle Image Velocimetry - A practical guide*, 2nd edn. Springer-Verlag.
- ZHOU, J., ADRIAN, R. J., BALACHANDAR, S. & KENDALL, T. M. 1999 Mechanisms for generating coherent packets of hairpin vortices in channel flow. *J. Fluid. Mech.* **387**, 353–396.

Part II

Papers

Paper 1

A new test-section for wind tunnel studies on wake instability and its control

By Bengt E. G. Fallenius, Renzo Trip and
Jens H. M. Fransson

Linné Flow Centre, KTH Mechanics, SE-100 44 Stockholm, Sweden

Drag reduction is an important issue in today's debate on *global warming*. The EU transport system stands, alone, for 25% of the total carbon dioxide emissions in Europe, implying that the transport industry is one of the gravest environmental thieves. One way to attack the problem is to develop alternative and *greener* propulsion and another would be to reduce the emissions by reducing the aerodynamic drag. The latter may be accomplished simply by gaining further fundamental knowledge about the aerodynamics in the wake flow behind bluff bodies, as for instance a truck.

In this report we describe a new test-section for an existing wind tunnel, which has been designed and manufactured at the Department of Mechanics, KTH. The test-section is specially built for experimental studies on the instability of wakes behind bluff bodies from a fundamental research point of view. The new experimental setup is designed in order to realise parameter variations, which most often are impossible in usually fixed experimental geometries. The present bluff body is a so called rectangular-based forebody with permeable surfaces on both sides of the forebody, which add the *unique* feature of being able to vary the boundary layer along the body and thereby the inlet flow condition of the wake. Furthermore, it will be possible to create the so called asymptotic suction boundary layer with a *unique* feature itself, namely, the fact that the Reynolds number is decoupled from the boundary layer thickness. Above features allow for systematic parameter studies, on the classical phenomenon of vortex shedding instability behind bluff bodies, in a way that has not been done previously.

The setup is very flexible for changes on the rear part of the body, which makes it suitable for testing various methods of both passive and active flow control. Here, the distinction between passive and active control refers to whether the energy in the flow is used for the control, passive, or if energy has to be added to the flow system in order to perform the control, active. Importance will be attached on the fluid dynamical response upon the control and the understanding of the fundamental fluid dynamic differences between the natural and controlled system by studying turbulence statistics, force balances as well as changes of small-scale structures in the wake.

An enhanced comprehension of the fluid mechanics around and behind bluff bodies as well as its effect when applying different control methods is essential in order to develop more safety, more energy efficient, and adapted design within many areas of practical application. Furthermore, by using both experimental and theoretical data analyses, the new experimental setup is of central importance in order to reach a fundamental knowledge of the effect of active control and its fluid dynamics. The results will shed new light on the fluid mechanics for future development of experimental as well as theoretical models.

1. Introduction

The vortex shedding instability behind bluff bodies is a self excited oscillation that will set in even if all sources of noise are removed (see Gillies 1998), and can be shown to be attributed to the local stability property of the two-dimensional mean velocity wake profile behind a bluff body. For the canonical wake flow problem behind a circular cylinder Monkewitz (1988) identified a sequence of stability transitions by using a family of wake profiles, that resulted in $Re_C < Re_A < Re_K$, where Re_C (≈ 5), Re_A (≈ 25), and Re_K (≈ 47) are critical Reynolds numbers that mark the onset of convective, absolute, and von Kármán shedding instability, respectively. This sequence was in fully agreement with the qualitative model predictions by Chomaz *et al.* (1988) the same year. The onset of the global von Kármán shedding mode occurs via a so-called supercritical Hopf bifurcation (see e.g. Provansal *et al.* 1987). For a review on the stability properties of open flows in general the interested reader is referred to Huerre & Monkewitz (1990), and for reviews on cylinder flows in particular see e.g. Williamson (1996); Buresti (1998); Norberg (2003); Zdravkovich (1997, 2003).

Having introduced the von Kármán vortex shedding phenomenon the emphasis will from here on lie on the rectangular-based forebody and the research problems of immediate interest. The Strouhal number (St) used below is the non-dimensional shedding frequency.

Rectangular-based forebody versus circular cylinder

For rectangular-based forebodies the critical Reynolds number, defined by the base height and the free stream velocity over the kinematic viscosity, for the onset of vortex shedding is $Re_K \simeq 120$. Independent research results (see e.g. Sreenivasan *et al.* 1986; Williamson 1989, for the circular cylinder geometry) have shown a linear increase in Strouhal number (St) with Reynolds number. At approximately $Re = 2000$ the Strouhal number reaches a local maximum around $St = 0.21$ (see e.g. Norberg 2003) showing a complex variation with Reynolds number. Different numerical simulations of the rectangular-based forebody have shown slightly different St for the same Re . Hannemann &

Oertel (1989) report a $St = 0.113$ at $Re = 200$, while Hammond & Redekopp (1997) report $St = 0.102$ for the same Reynolds number. These results suggest that for direct comparisons there is a need to take into account the displacement thickness (δ_1) of the boundary layer at the separation, i.e. at the trailing edge of the rectangular-based forebody, implying that a match of the Reynolds number is not enough. An interesting fundamental investigation would be the study of independent variations of the Reynolds number and the displacement thickness.

The ability to control the wake and the vortex shedding of a bluff body can for instance be used to reduce drag, increase heat transfer and mixing, and enhance combustion. Over the second half of last century there has been a number of successful attempts to control the shedding wake behind bluff bodies with the practical goal of reducing the pressure drag on the body. A control approach that has shown to be effective in reducing the average strength of the vortices and the shedding frequency is base bleed (cf. e.g. Wood 1967; Bearman 1967). For successively increasing bleeding rates the regular shedding of vortices ceases, intermittently at first, and then completely. Hannemann & Oertel (1989) performed numerical simulations on the effect of uniform blowing from the base, and reported a critical value¹ ($c_q = 0.214$) for which vortex shedding was suppressed. Uniform suction from the base was considered numerically by Hammond & Redekopp (1997) and they report a continuous decline of the wake shedding frequency with a gradual increase of suction until an abrupt suppression occurs at a sufficiently high suction rate.

Again, going back to the circular cylinder for interesting comparisons. Mathelin *et al.* (2001*a,b*) considered the case of continuous blowing through the entire cylinder surface (see Mathelin *et al.* 2001*a*, for a detailed description of the experimental setup). Among the effects observed are the wider wake and a decrease of the Strouhal number with increasing blowing. They report on an analytical relation of an equivalent Reynolds number of the canonical case, which produces the same flow characteristics in terms of vortex shedding instability as the case with blowing, versus the blowing rate. The result is that the Strouhal number decreases with blowing, which was experimentally verified by Fransson *et al.* (2004*b*), who also considered the effect of continuous suction which turns out to have the contrary effect on the Strouhal number. Note that uniform suction from the base of a rectangular-based forebody (marked in bold in the previous paragraph), interestingly, gives the opposite behaviour (cf. Hammond & Redekopp 1997). These opposite trends are of direct fundamental interest and deserves further investigation.

Furthermore, an even simpler control method is the passive approach obtained by placing a thin splitter plate aligned in the streamwise direction on

¹ $c_q = m^*/U_\infty D^*$, where m^* is the mass flow rate divided by density and for unit depth which is blown into the wake at the base of the plate, U_∞ is the free stream velocity, and D^* is the thickness of the plate.

the centreline of the near wake (see e.g. Roshko 1955, 1961, where circular cylinders were studied). For a specific length of the splitter plate the sinuous von Kármán mode is altered for a varicose mode that causes a pair of twin-vortices to be formed, one on each side of the plate. More recently, Grinstein *et al.* (1991) carried out numerical simulations on the effect of an interference plate in the wake of a plate and found that the base pressure coefficient could decrease by a factor of 3 depending on the length of the plate and its separation from the base. The important length scale ratio for the effectiveness of a splitter plate is L/D , where L and D are the streamwise extent of the splitter plate and the cross-flow dimension of the bluff body, respectively (see e.g. Nakamura 1996). This is true for short bluff bodies in the streamwise extent where boundary layer thicknesses are negligible compared to D , on the other hand for rectangular-based forebodies the displacement thickness will have to be taken into account and a fundamental study on this parameter, decoupled from the Reynolds number, would be of immediate interest.

2. Investigations for the new test-section

Some ideas on investigations to be performed in the new experimental test-section are presented below. The planned investigations may be divided into two parts consisting of a fundamental wake flow study in an idealized and recently built experimental setup followed by studies on both passive and active control methods on the wake instability. This will enhance the physical understanding of the wake instability.

First part

The new test-section will be used in fundamental studies on the wake flow instability behind a rectangular-based forebody. This setup consists of a flat plate with an elliptic leading edge and a blunt trailing edge, which is described in section 4. Permeable surfaces on both sides of the rectangular-based forebody add the *unique* feature of being able to vary the boundary layer along the body and thereby the inlet flow condition of the wake. It will even be possible to create the asymptotic suction boundary layer (ASBL), which has a unique feature itself, namely, that the boundary layer thickness (δ) is decoupled from the Reynolds number (Re), since the Reynolds number is given by the free stream velocity (U_∞) over the suction velocity (V_0), i.e. $Re = U_\infty/V_0$, and $\delta \sim \nu/V_0$ (where ν is the kinematic viscosity). The ASBL has an analytical solution to the Navier–Stokes eqs. and consequently the displacement and momentum thicknesses can be integrated exactly ($\delta_1 = \nu/V_0$ and $\delta_2 = \nu/(2V_0)$, respectively) giving a shape factor $H_{12}^{ASBL} = 2$.

Above features allow for systematic parameter studies, on the classical phenomenon of vortex shedding instability behind bluff bodies, in a way which has not been done previously. As an example the effect of below listed parameters on the primary two dimensional von Kármán shedding frequency (f_K),

or alternatively its corresponding Strouhal number (St), are relatively easy accessed,

- trailing edge Re as function of St ,
- trailing edge boundary layer displacement or momentum (δ_1 or δ_2) thickness dependence on St ,
- trailing edge $H_{12} = \delta_1/\delta_2$ as function of St .

How these parameters are related to each other and affect the f_K is so far not fully understood and would serve as a step forward in the strive after further fundamental knowledge in the area of bluff body wakes. Note that continuous suction or blowing has similar effect on the boundary layer as an external adverse or a favorable pressure gradient, respectively. This would add the additional possibility to describe the shape of the boundary layer, H_{12} , by means of a similarity solution meaning that an extra parameter m can be introduced and varied. Furthermore, it should be pointed out that the first and the second bullets above may be varied independent of each other in the limit of the ASBL, which is not possible in ordinary developing boundary layers.

Second part

As a second part of planned studies both passive and active control methods will be tested. In this context we refer to a *passive* control technique as a method where no energy is added to the system in order to perform the control. This in contrast to *active* control where energy has to be added. The passive control device will be the well-trying splitter plate. Again, the *unique* possibility to vary the initial wake condition will bring new insight in this passive control field. Length and material stiffness of the splitter plate are planned to be varied, while the vortex dynamics in the wake is studied. Base bleed and suction are meant to be the first candidates as active control methods. Both continuous and pulsated control will be applied and the effect of gap width variations will be studied. This will be a springboard towards feed-back control ideas by gaining fundamental knowledge of the fluid dynamical response with various active control parameters.

Analyses

The analyses of the data will be performed using different methodologies. One may model the base pressure of bluff bodies, by working with the balance of stress forces on the mean near wake defined by the stagnation line of the mean wake flow recirculation region. The wake aspect ratio is then given by the balance between the shear-stress force and the pressure-rise force (see e.g. Roshko 1993; Balachandar *et al.* 1997), which approach universal values as the Reynolds number becomes large enough. Hence, the shape of the wake may be anticipated. Another methodology which has been developed and applied by the applicant is a small-scale vortex detection program, which gives vortex statistics of the vortex size, strength and rotational-direction. This program is based on previous ideas by Chong *et al.* (1990); Zhou *et al.* (1999); Adrian *et al.*

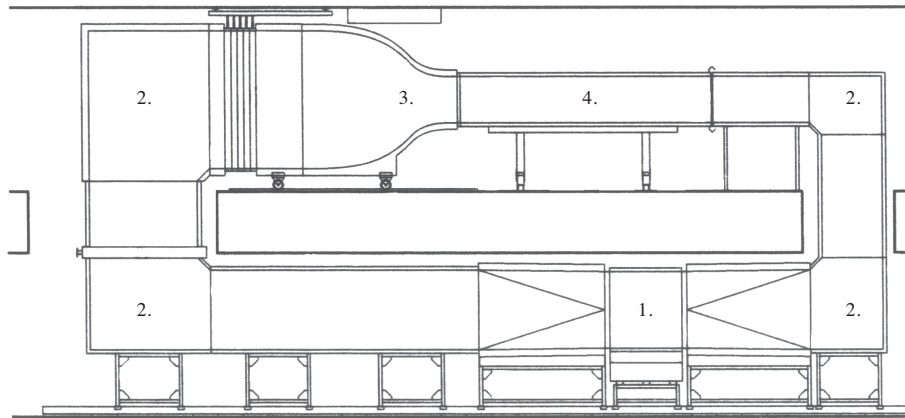


FIGURE 1. Sketch of the BL wind tunnel.

(2000); Agrawal & Prasad (2002) and has also been applied on the porous cylinder configuration with continuous suction or blowing through the entire surface of the cylinder. This latter methodology and application is published as a paper in Fallenius (2009). Furthermore, the wake flow behind the rectangular-based forebody will be studied using global mode stability analysis for direct comparisons with the experimental results. All three methodologies require the access of entire velocity fields in the wake, which will be obtained by the aid of a High Speed Stereo Particle Image Velocimetry (HS-S-PIV) system. These type of measurements will be able to capture the events of role-up of vortices and consequently detailed comparisons will be possible to make.

3. The Boundary Layer wind tunnel

The Boundary Layer (BL²) wind tunnel is located at the department of Mechanics at KTH, and has been chosen as the experimental facility to host the new setup. The idea with the BL tunnel is to have a short time swap between different experiments by having exchangeable test sections. Figure 1 shows a side view sketch of the wind tunnel and below a brief description is given. For a more thorough description the interested reader is referred to Lindgren (2002).

The BL wind tunnel is a closed circuit tunnel, powered by an 15 kW axial fan (1). It was the first tunnel where expanding corners (2) were utilised, making it possible to have a 9:1 contraction (3) ratio together with a short overall wind tunnel length. The space for the testsection (4) is 4.2 m and the cross sectional area of the contraction outlet is $0.5 \times 0.75 \text{ m}^2$. The maximum flow velocity is 48 m/s and the turbulence levels³ are 0.04%, 0.06% and 0.04%

²BL also corresponds to the initials of the wind tunnel designer Björn Lindgren.

³The following turbulence levels correspond to the high-pass filtered intensities, with a cut-off frequency of 20 Hz.

in the streamwise, wall-normal and spanwise directions, respectively, at the nominal⁴ free stream velocity of 25 ms^{-1} . At this nominal velocity the variation in total pressure is less than $\pm 0.1\%$ and the variation in temperature is less than $\pm 0.07 \text{ }^\circ\text{C}$ over the cross sectional area.

4. New experimental setup

A new experimental setup for studies on wake flow instability and its control, which has been designed and manufactured, is here introduced and described.

The new experimental setup consists of a main body, which is mounted into a new exchangeable test section, see figure 2, designed to fit into the BL wind tunnel (cf. section 3). The main body can be divided into three parts, which are described individually below, i.e. the leading edge, the rectangular forebody and the trailing edge. The latter is basically part of the rectangular-based forebody, but different configurations of this trailing edge can have high impact of the setup as a whole, why it is treated separately. The test section is designed with two criteria in mind: (i) different measurement techniques should be possible to use, (ii) the main body should have an easy access for adjustments and cleaning during experiments.

⁴During the design of the BL-windtunnel, most of the planned experiments were aimed for a free stream velocity of 25 ms^{-1} .

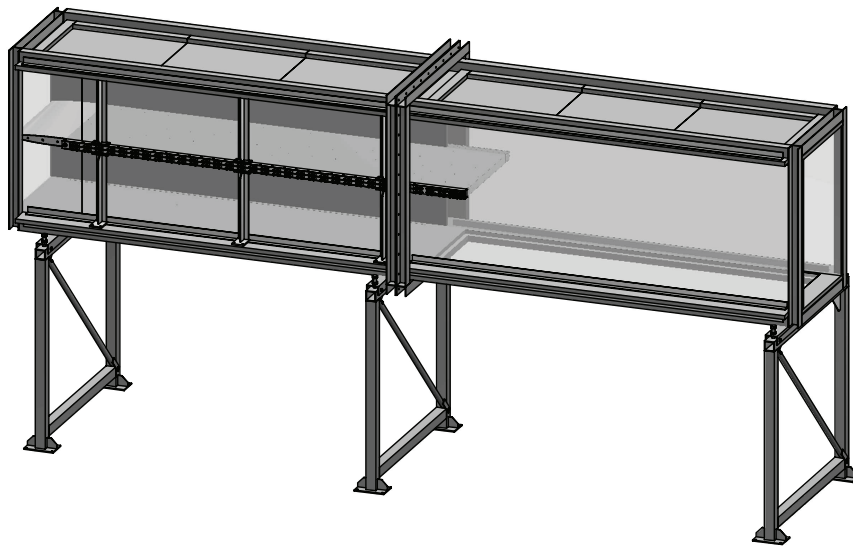


FIGURE 2. The main body mounted in the new test section of the wind tunnel. Tubing and measurement equipment excluded.

4.1. Test section

The test section is made of steel frames with walls made of plywood and plexiglass. An exploded view of the test section is shown in figure 3, where the flow direction is from left to right.

The base components are the two steel frames (1), with wooden panels as top and bottom walls (2). The panels have openings for hatches of wood (3) and plexiglass (4), where the latter is mainly used as inlet for the laser sheet during High Speed Stereoscopic Particle Image Velocimetry (HSS-PIV) measurements. There are also additional wooden hatches (5) with slits for traversing during Pitot tube or hot-wire measurements. The side walls (6) are mainly made of plexiglass for high optical access and wood (7). A frame of aluminium (8) with rubber insert makes sure that the joint to the wind tunnel contraction is sealed firmly. The inside cross-sectional area of the test section is (W×H) $500 \times 750 \text{ mm}^2$, and the length is 4 m.

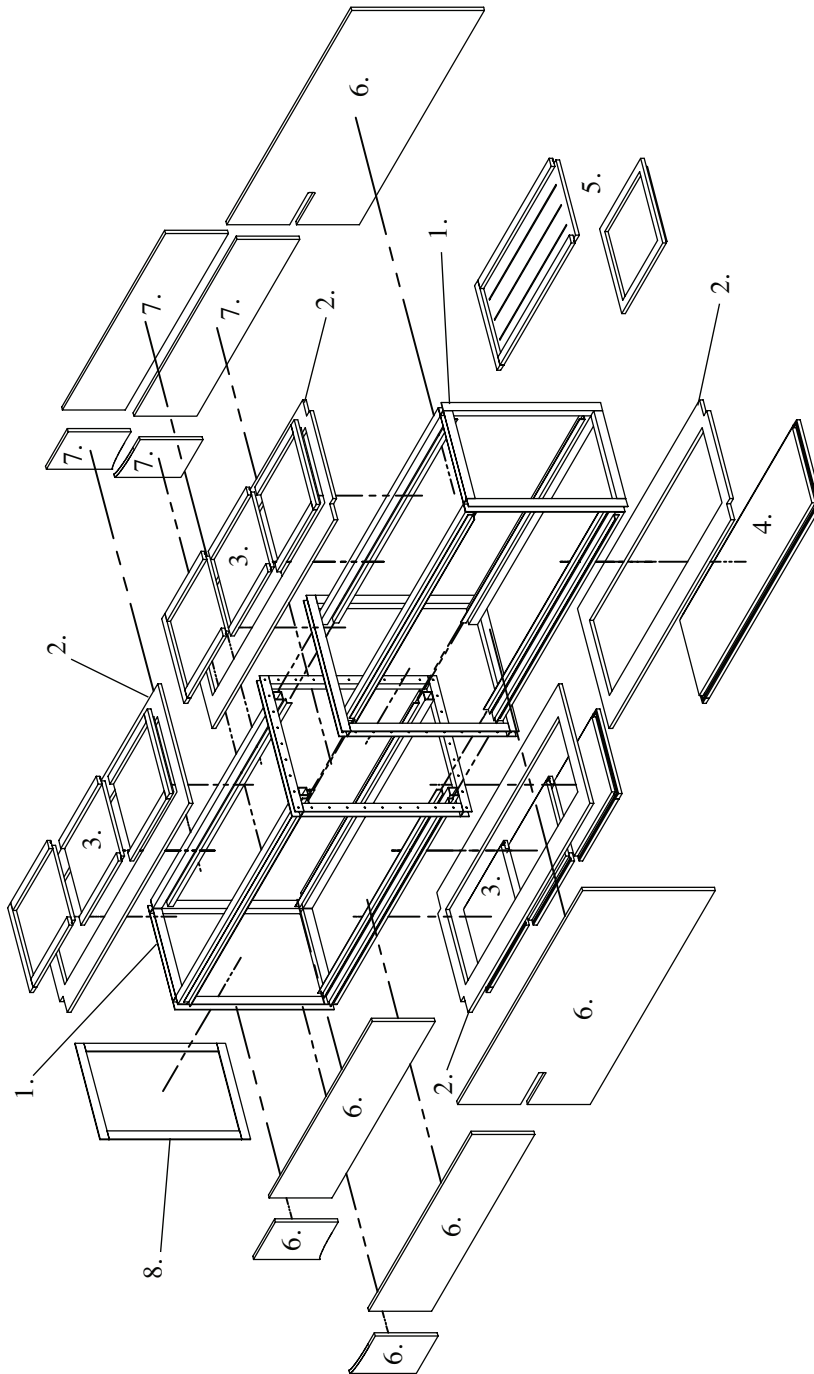


FIGURE 3. Exploded view of the test section. 1. Steel frames, 2. Wooden panels, 3. Wooden hatches, 4. Plexiglass hatch, 5. Additional hatches with slits, 6. Plexiglass walls, 7. Wooden walls and hatches, 8. Aluminium frame.

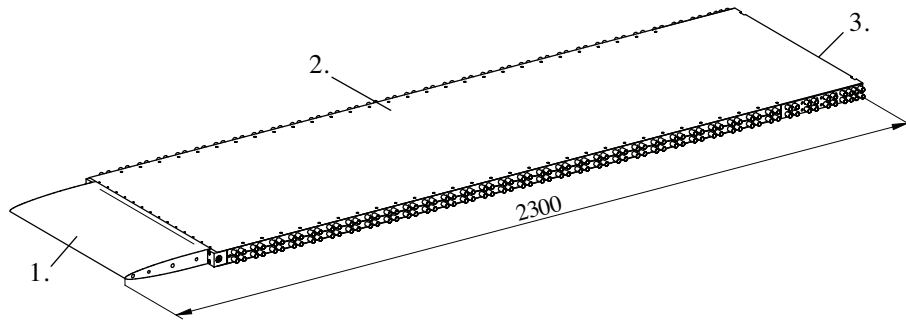


FIGURE 4. The rectangular-based forebody, consisting of 1. the leading edge, 2. the flat plate and 3. the trailing edge.

4.2. Rectangular forebody

The rectangular-based forebody can be divided into three parts as seen in figure 4; a leading edge (1), a flat plate (2) and a trailing edge (3). The latter is a part of the flat plate but can be extended with additional pieces. A closer look to the details of these parts follows, starting with a description of the principle of the new setup.

4.2a. *Principle of setup.* The main body in the new experimental setup is symmetric, i.e. a dual-sided plate with permeable surfaces. Changing the pressure difference across the permeable surfaces will affect the boundary layer growth along the plate and consequently the inlet condition of the wake.

In figure 5 a schematic of the main body shows the principle and its feasibility. Note, the dimensions are not according to scale due to the high aspect ratio of the body. The co-ordinates are defined as, x in the streamwise direction, y normal to the body and z in the spanwise direction. The corresponding velocity components are U , V and W , respectively. A free stream flows past the body with the streamwise velocity U_∞ . In the schematic the upper side of the body is subjected to suction through the permeable surface, with the uniform suction velocity V_0 . By varying the direction and velocity of the flow through the permeable surfaces, different boundary layer profiles can be obtained. Moderate levels of suction gives an asymptotic suction boundary layer (I), while a high suction velocity can result in an inviscid slip-condition (II). Blowing can also be applied through the full length or only partly (III). Depending on the chosen flow through the surfaces the initial condition of the wake and consequently the shape of the wake profile (IV) may be varied.

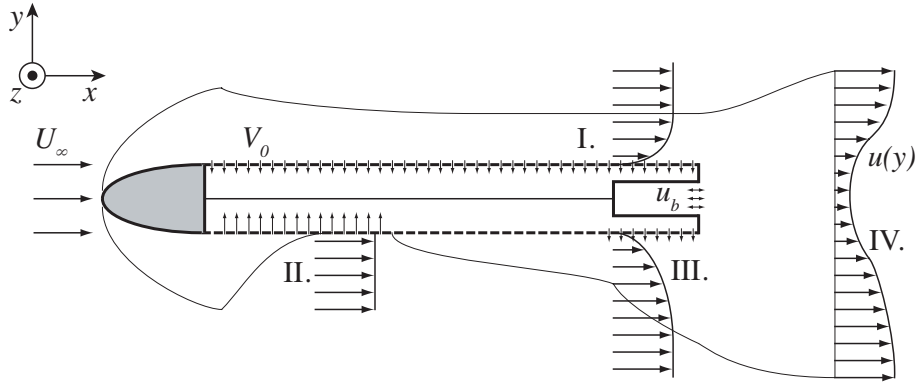


FIGURE 5. Schematic of the the bluff body in the new setup.
Note, not according to scale.

4.2b. *Leading edge.* The leading edge is symmetric in the xz -plane and its profile is described by a modified super ellipse (MSE),

$$\left[\frac{a-x}{a} \right]^{m(x)} + \left[\frac{y}{b} \right]^n = 1, \quad 0 < x < a,$$

where $m(x) = 2 + (x/a)^2$ and $n = 2$, see Saric *et al.* (2002). The aspect ratio, given by the quotient between the semi-major axis a and the semi-minor axis b , is 12.5. The advantage with a modified super ellipse versus an ordinary super ellipse is the continuous derivative of the curvature at the junction between the leading edge and the following flat plate. Figure 6 shows a comparison of the MSE and an ordinary ellipse $(x/a)^2 + (y/b)^2 = 1$, where it can be seen that there is no major difference between the profiles.

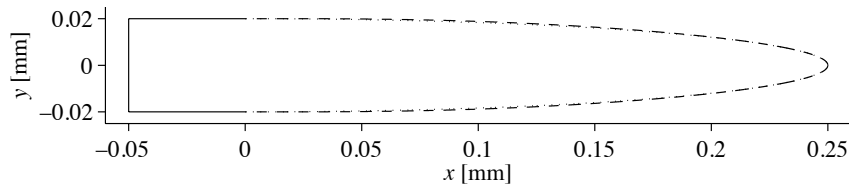


FIGURE 6. Comparison of the MSE (---) and an ordinary super ellipse (···).

The leading edge was milled out from a solid block of aluminium. In order to avoid tensions and deformations of the material in the milling process, the aluminium alloy of type Plancast[®] Plus 5083 was used as raw material. A sketch of the leading edge is shown in figure 7. Threaded holes on the sides were made for the manufacturing process but were also used to attach the

leading edge in the setup. The semi major axis is 250 mm, but in order to have a smooth overlap to the following flat plate, additionally 50 mm where added. Here 30 mm was milled as a step where the perforated sheets could be attached firmly with screws.

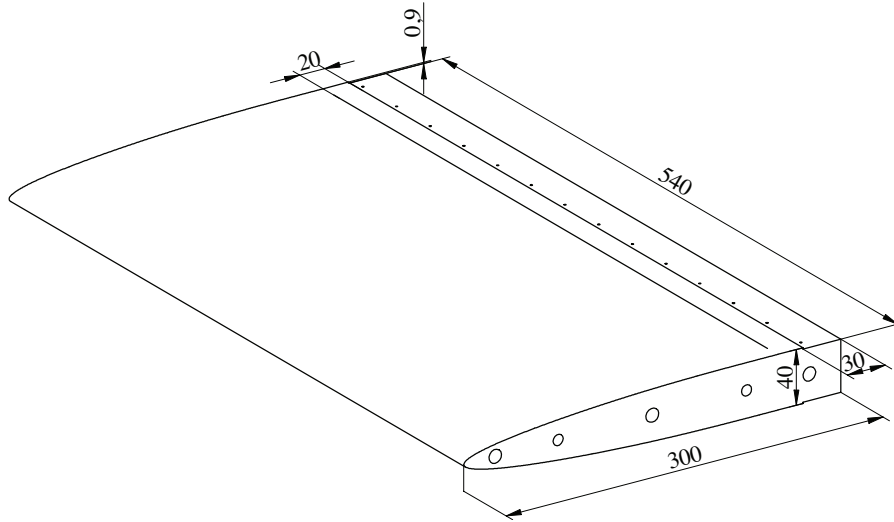


FIGURE 7. Sketch of the leading edge with dimensions in [mm].

4.2c. *Flat plate.* The flat plate is a sandwich construction with identical top and bottom sections. Figure 8 shows an exploded view and a side view of the flat plate, with the trailing edge excluded. The total length of the setup is 2.3 m and the base thickness (H) is 40 mm.

The main components are the permeable sheets (1), which are made of titanium with perforations made through laser drilling. The total length of the permeable sheets is 2030 mm, with a permeable length of 2000 mm. The additional 30 mm is added in order to have an overlap with the leading edge. A more thorough description of the properties for the permeable sheets is given below in section 4.3. The permeable sheets are attached to two frames with arrays of T-profiles (2). An aluminum sheet (3) separates the two sides.

Since the sheets are intended for flow experiments, roughnesses such as screw-heads through the surfaces are undesired. Furthermore, since the material is rather expensive, permanent damage due to large amounts of glue or similar is also undesired. In order for the sheets to not be deformed when suction or blowing is applied, the sheets are fastened in such a way so that they can withstand pressure loads in both the negative and positive normal directions. Consequently, the solution to attach the permeable sheets to the

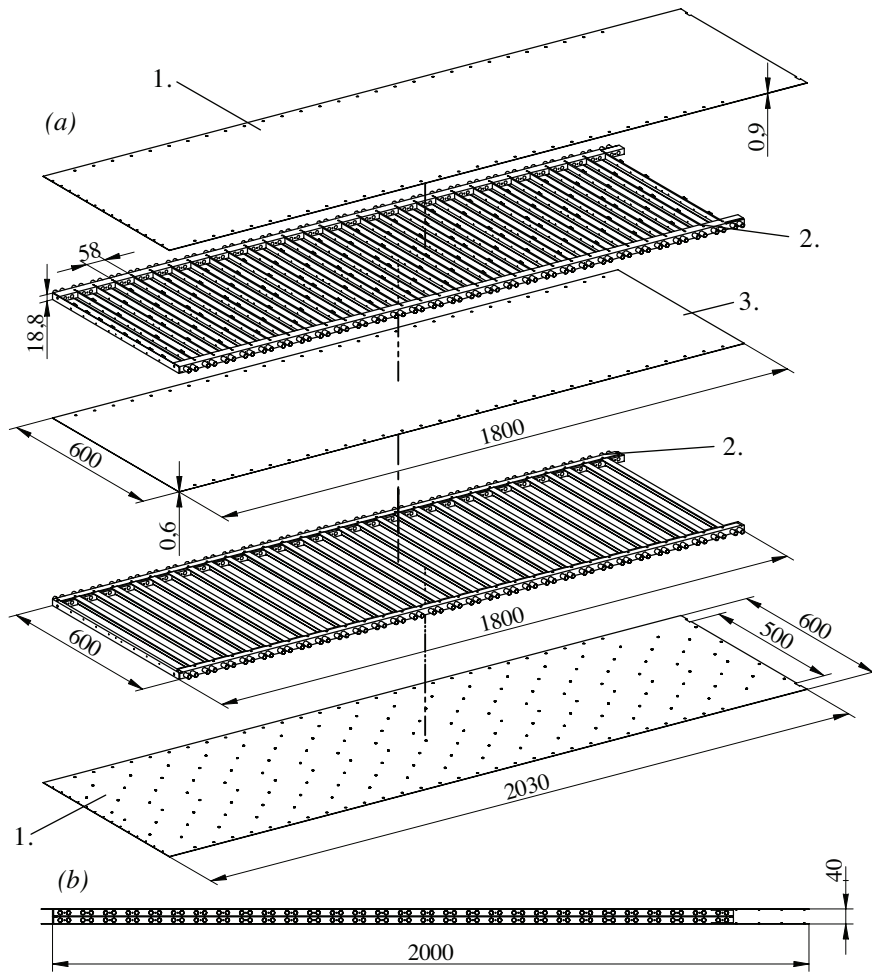


FIGURE 8. Sketch of the flat plate as exploded view (a) and a side view (b) with all dimensions in [mm]. 1. Permeable sheets, 2. Supporting frames, 3. Separating sheet.

supporting frames is to point-wise glue M2-nuts to the sheets. This also makes it possible to detach the sheets for cleaning and inspection if needed. The only destructive modification to the sheets is the drilling of a row of countersink holes along the upstream edge, which are used to fasten the sheets the leading edge with M2 screws. The screws are then covered by a thin strip of tape.

Figure 9(a) shows one supporting frame, which sides are made of two solid aluminum bars that have milled slits for twenty-nine T-profiles, of which one is shown in 9(b). Each T-profile has nine threaded M3 holes where custom

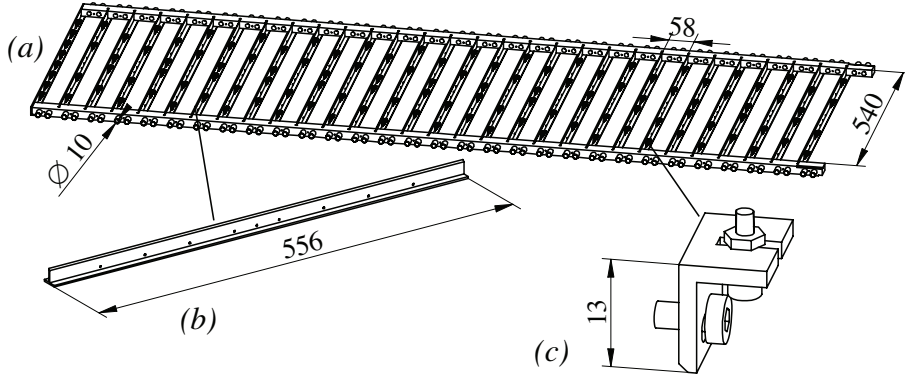


FIGURE 9. Sketch of (a) the supporting frame, (b) a T-profile and (c) an attachment element. Dimensions are in [mm].

made attachment elements (see figure 9(c)) are fastened with a screw. The attachment elements then have a M2 screw that are paired with one of the nuts that are glued to the permeable sheet. Two additional nuts on the attachment element makes sure that it is fastened with the correct length. The design of the attachment element makes its adjustable in two directions, which reduces the need for precision when the nuts are glued to the sheets.

The space between the T-profiles creates twenty-nine separate compartments. On each side two 10 mm holes are drilled through the side bars where pipes and tubing are connected for withdrawal and/or injection of air. The total area of the outlets is about twice the perforated area in each compartment, which is desired in order to have the maximum pressure drop across the sheets. More details about the permeable material will be given in section 4.3.

The streamwise distance between the T-profiles extending in the spanwise direction has carefully been chosen. There must be enough space for tubing and at the same time the titanium sheets have to withstand the imposed pressure difference across them. A study in the commercially available multiphysics and finite element solver program Comsol[®] was performed in order to ensure that neither bulging nor curving of the sheet will occur when blowing and/or suction are applied. To compensate for the porosity of the material, the elasticity module was reduced based on the diameter of the holes. This gives an elasticity module of 102 GPa instead of 106 GPa, which was supplied by the manufacturer.

An average pressure drop of 535 Pa at the flow velocity around 5 cm s^{-1} was also given by the manufacturer. This was used as a load in the displacement calculations using Comsol[®] with the argument that the contemplated velocity mostly will be less than 3 cm s^{-1} . Figure 10 shows that the maximum displacement is less than $50 \mu\text{m}$ for the blowing as well as the suction

case. This is considered to be an acceptable displacement considering both the flatness of the material and the boundary layer thickness. The suction case in

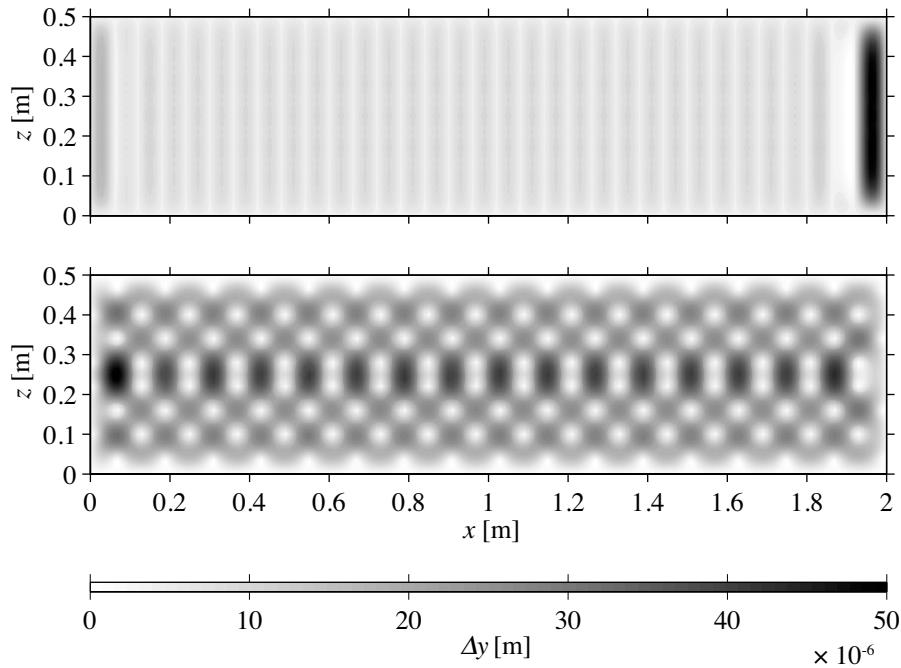


FIGURE 10. A finite element computation of the displacement in the y -direction due to suction (*upper*), with negative displacement and blowing (*lower*) with positive displacement.

figure 10 shows, regularly, regions extending in the spanwise direction where there is no displacement (white regions). These regions correspond to the location of the spanwise pointing T-profiles. In contrary, the blowing case shows, locally, regions of no displacement (i.e. white regions), which correspond to the point-wise glued elements holding the sheet in place (see section above).

Figure 8(b) shows that the length of the supporting frames is shorter than the permeable sheets. This in order to have the ability to change the shape or interior of the trailing edge, which is further described in section 4.2d.

4.2d. *Trailing edge.* As described above the trailing edge of the setup is interchangeable, which makes it possible to change the configuration and/or add additional devices for wake flow control, either passive, active or both. Figure 11 shows the basic configuration of the trailing edge, which has an internal chamber for base bleed or base suction. The opening in the base is here covered

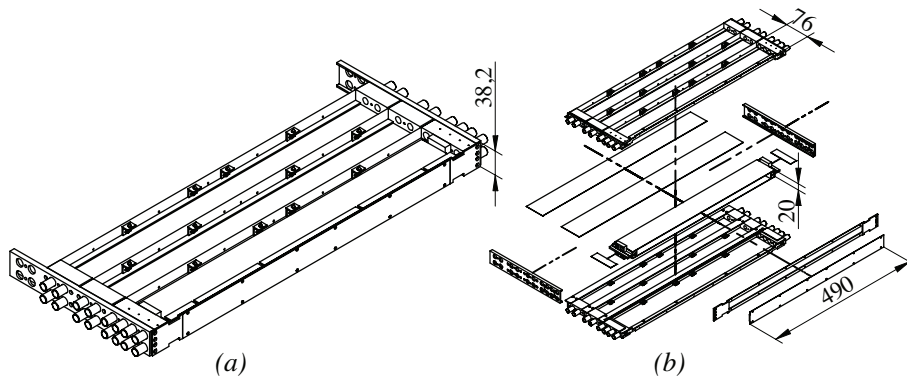


FIGURE 11. A trailing edge configuration (a) and an exploded view (b) of the same.

by a plate that can be equipped with pressure holes for base pressure measurements. The plate is easily replaced with alternative plates, e.g. with a slot for base bleed or suction or with the possibility to mount of a horizontal splitter plate.

4.3. Permeable sheet properties

Studies on the asymptotic suction boundary layer as well as the flow past a circular porous cylinder have been carried out at the department of Mechanics, KTH, see Fransson & Alfredsson (2003); Yoshioka *et al.* (2004) and Fransson *et al.* (2004b), respectively. In those experiments, a sintered plastic material with a maze-like structure were used. However, experiences from the setups have shown that such a material is not suitable for extensive particle image velocimetry measurements, since the smoke that is used as seeding clogs the pores. Furthermore, such material has problems with ageing, which results in undesirable cracks and changes of the material properties and must typically be replaced regularly.

For the new setup, a material without the above drawbacks was preferable, which resulted in the choice of *laser drilled titanium sheets*. This material has several advantages, it is stiff, it can stand strong detergent used for cleaning, it is resistant to corrosion and it has a smooth surface after the perforation process. The discrete holes of the perforation makes the inspection of the cleanness easy simply by placing a light source behind the sheet. Similar materials such as aluminium and stainless steel were also considered, however, the former is difficult to perforate and the latter has problem with debris in the perforation process, which results in a rugged surface.

4.3a. *Perforations.* The diameter of the laser drilled holes is $60\ \mu\text{m}$ with a distance between the holes of $0.75\ \text{mm}$, which gives a total number of about 1.78 M holes per sheet and an open area of 0.5%. The rows are aligned with axis in the streamwise direction and shifted in the spanwise direction. The thickness of the sheets is $0.9\ \text{mm}$ and because of the focusing of the laser beam the hole diameter on the side where the laser enters is larger (about $0.11\ \text{mm}$), see figure 12.

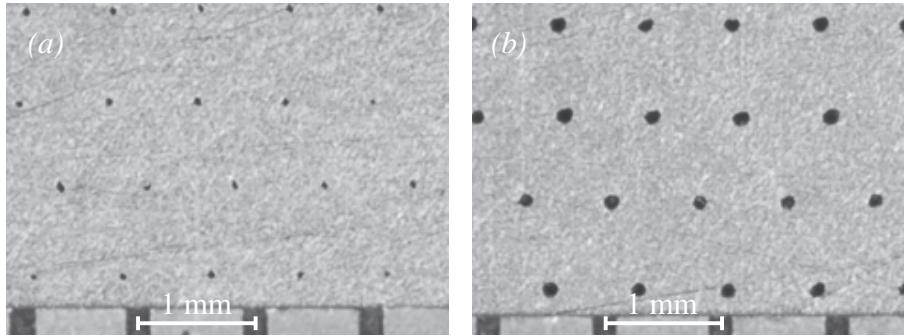


FIGURE 12. Images of the laser drilled titanium sheet. (a) the smaller hole diameter on the outlet side of the laser beam. (b) the larger hole diameter on the inlet side. At the bottom of the images a reference ruler is shown.

4.3b. *Permeability.* Boundary layer control and drag reduction by suction through permeable sheets have been studied over several decades, mainly with applications within the aeronautical field. This extensive research has led to many investigations about permeable materials, which are suitable for boundary layer control.

There are two main types of permeable materials, granular and fibrous materials with a labyrinth-like structure and materials perforated straight through. A major difference between these two types of materials is the relation between the flow velocity and the pressure drop over the material. The flow velocity through a labyrinth-like material increases linearly with the pressure difference, following Darcy's law, which reads

$$V = \frac{\kappa \Delta p}{\mu t}, \quad (1)$$

where V is the flow velocity through the material of thickness t . Δp is the pressure difference across the material and μ and κ is the dynamic viscosity and permeability, respectively.

However, for perforated materials the relation between V and Δp is different. The velocity, through such material, may be approximated by the flow

through individual pipes. A theoretical analysis was carried out in Goldstein (1938), yielding narrow pipes, which may be applied on perforated materials. Provided that $t/(r \cdot Re_{2r}) \ll 1$, where r and Re_{2r} correspond to the radius of the holes and the Reynolds number based on the hole diameter and the mean velocity through a single hole, respectively, the relation reads

$$V = \left(\frac{2\Delta p}{\rho\{\beta + 32t/(r \cdot Re_{2r})\}} \right)^\alpha. \quad (2)$$

Here, $\alpha = 1/2$ and $\beta = 2.41$. This theoretical relation has been verified experimentally by Poll, Danks & Humphreys (1992).

The titanium sheets used in the present study are denoted 2TA1 and have a thickness of $t = 0.9$ mm. The hole diameter is $2r = 60 \mu\text{m}$ in average and the distance from centre to centre is 0.75 mm which gives a distance to diameter ratio of 12.5. The row to row distance was also chosen to be 0.75 mm and each row in the streamwise direction is shifted. Figure 12 shows pictures of the holes on both sides of the sheets. Due to the focus of the laser beam during drilling, the holes have a taper angle of approximately 3 degrees. This makes the hole larger on the drilling side compared to the back, which has the desired diameter of $60 \mu\text{m}$.

Measurements to determine the permeability of the material were also performed. Figure 13 shows the setup. A sample of the titanium sheet was clamped between two pipes with an inner diameter of 5 cm (a). One end was connected to a vacuum cleaner (b) and the other end to a flowmeter (c). The flow velocity was varied by changing the voltage (d) supplied to the vacuum cleaner. By measuring the pressure drop over the sample (e) for different flow velocities the permeability could be determined. A barometer (f) and a thermometer (g) were used to calculate the air density. The result of the permeability measurement is shown in figure 14(a) where (\circ) and (\square) represent suction and blowing, respectively. For the present perforated sheet with a typical cross flow velocity of 3 cm s^{-1} we get $t/(r \cdot Re_{2r}) > 1$ and, hence, relation (2) does not hold. However, the constant β and the exponent α in relation (2) may be determined through curve fitting to the data in a least square sense. We obtain $\beta = 42.0$ and 38.9 and $\alpha = 6/7$ and $9/11$ for the suction and the blowing case, respectively, which are shown with solid and dashed lines in figure 14(a). The difference is attributed to the different inlet conditions (see figure 12). During the laser drilling process, the pressure drop over the sheet for a chosen flow velocity of 5 cm s^{-1} was monitored in order to secure the quality of the perforation. The drilling was conducted in the spanwise direction and the pressure drop was measured at the end of each row and in figure 14($b - c$) the pressure drop along the sheets is shown.

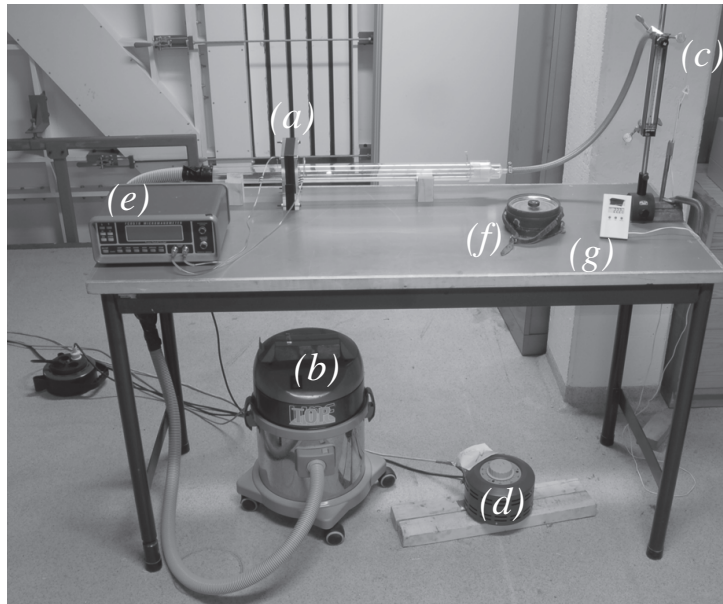


FIGURE 13. Setup of permeability measurements. (a) sample mount, (b) vacuum cleaner, (c) flowmeter, (d) transformer, (e) difference pressure gauge, (f) barometer and (g) thermometer.

5. Experimental validation of the setup

In the present section we show some validation of the experimental setup. For this experimental validation we have used hot-wire anemometry as well as Pitot tube measurements, which are firstly described very briefly. Secondly, we describe the theoretical asymptotic suction profile, then we show how the inlet condition of the wake is successfully varied and that we can reach the asymptotic suction region over the flat plate. Secondly, we show some wake profiles for validating the symmetry of the setup.

5.1. Measurement techniques

Hot-wire anemometry

Hot-wire anemometry is generally considered to be one of the the best measurement techniques in flow experiments due to its high frequency response and small size, which gives relatively high spatial resolution as well (see e.g. Bruun 2002, for a full reference on the hot-wire anemometry). However, the sensitive wire breaks easy, which requires probe change and re-calibration. It also does not reveal the direction of the flow if not a more complicated, multi-wire probe is used. The probe that has been used for the present measurements has been made in-house at the Fluid Physics Laboratory. It is a single wire probe with

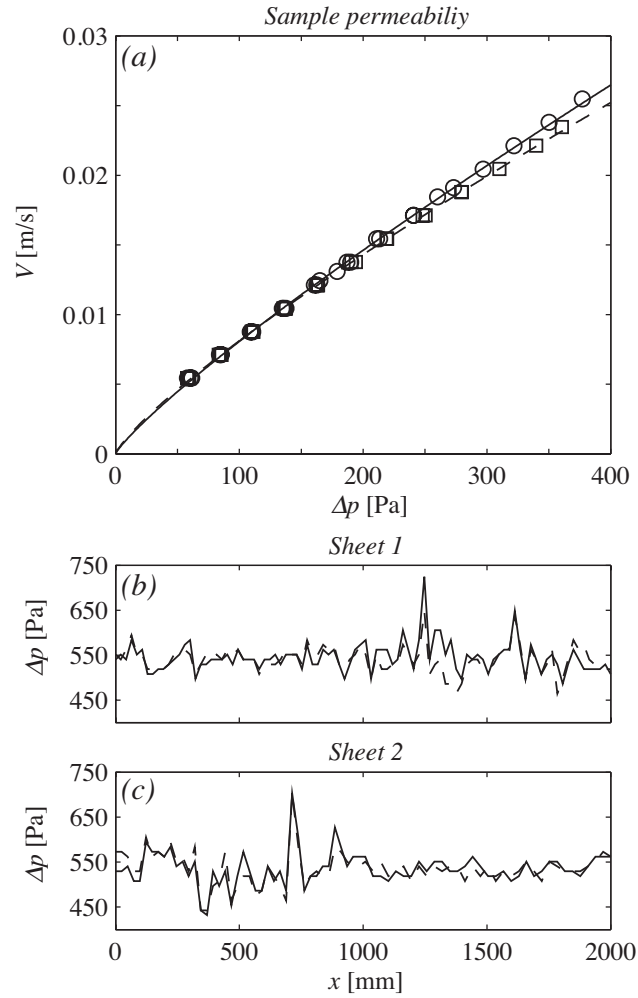


FIGURE 14. (a) permeability measurement on the sample. (\circ) suction and (\square) blowing configuration, with least square fits with the relation (2) in (—) and (---), respectively. (b – c) pressure drop along the sheets in the streamwise direction at a cross flow velocity of 5 cm s^{-1} . (—) and (---) represents the left and right side of the sheets, respectively.

a length of 0.5 mm and a nominal diameter of $2.5 \mu\text{m}$. The anemometer is run in constant temperature mode with an overheat of 80%.

Pitot tube

The Pitot tube is considered to be a simple and accurate device to measure the

time-averaged velocity profile in a fluid flow (Ranga Raju *et al.* 1997). However, to obtain accurate results for the time-averaged velocity profile in the wake of a bluff body requires a-posteriori corrections. The measured velocity has to be corrected for the influence of the Pitot tube itself on the flow due to its presence. Furthermore, the velocity is overestimated due to the turbulent nature of the flow in a wake of moderate to high values of the Reynolds number. Below a brief summary of necessary corrections which have to be considered in Pitot-tube measurements.

- The viscous or low Reynolds number correction is required for probe Reynolds numbers Re_D of $30 < Re_D < 100$, with Re_D given by:

$$Re_D = \frac{UD_p}{\nu} \quad (3)$$

where U is the local velocity, D_p the Pitot tube outer diameter and ν the kinematic viscosity. For the present case the Reynolds number $278 \leq Re_D \leq 1391$ which leads to the conclusion that viscous effects can be neglected.

- The shear correction should be considered if a velocity gradient is present, which is the case for a wake flow. The total pressure measured with the Pitot tube in place is larger than without the probe due to asymmetric deflection of the streamlines. The shear correction is commonly applied by a shift Δy of the measurement position of the pitot tube towards the higher velocity. Δy is given by McKeon *et al.* (2003):

$$\Delta y = \epsilon D_p, \quad (4)$$

with:

$$\epsilon = 0.15 \tanh(4\sqrt{\alpha}) \quad (5)$$

$$\alpha = \frac{D_p}{2U} \frac{dU}{dy} \quad (6)$$

For the present case $\epsilon < 0.1$ in combination with the outer dimension of the Pitot tube ($D_p = 1.4$ mm) makes this correction negligible.

- The turbulent nature of a wake flow results in an increase in the dynamic pressure measured with a Pitot tube because the velocity fluctuation u' does not cancel out:

$$\Delta P = \frac{1}{2} \rho \left(U^2 + \overline{u'^2} \right) \quad (7)$$

where ΔP is the dynamic pressure and ρ the density. The velocity fluctuation can not be measured with a Pitot tube and the correction is therefore based on a hot-wire measurement. Since the hot-wire measurement is not conducted at the same vertical position y the hot-wire data is interpolated. Figure 15 shows the velocity profile across the wake before and after the turbulence correction is applied.

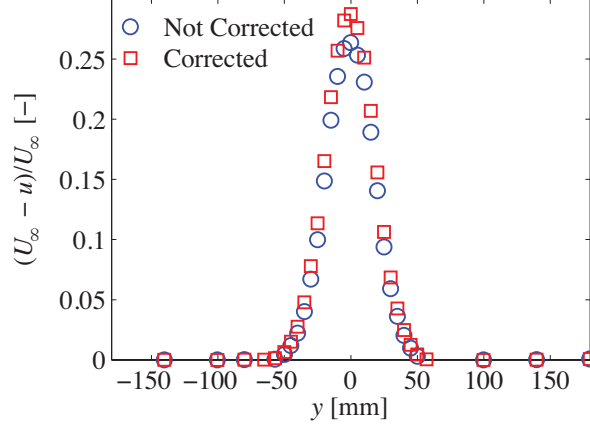


FIGURE 15. Pitot tube measurements of the wake velocity profile without (\circ) and with (\square) turbulence correction.

5.2. Adjustability of the inlet condition of the wake

Modulation of the boundary layer profile at the trailing edge of the rectangular-based forebody, i.e. the inlet condition of the wake, is managed by withdrawal and/or injection of air through the permeable surfaces by applying suction and/or blowing, respectively. Suction reduces the boundary layer thickness and at sufficiently high levels it will completely disappear. A special case of boundary layer suction is the so called asymptotic suction boundary layer (ASBL). The analytical expression for the ASBL profile was first derived by Griffith & Meredith (1936), but was not fully experimentally verified until 2003 by Fransson & Alfredsson. The expression for the streamwise velocity component in the ASBL reads

$$U(y) = U_\infty \left(1 - e^{yV_0/\nu} \right), \quad (8)$$

where U_∞ is the free stream velocity, $V_0 = \text{const.}$ is the suction velocity, y is the wall-normal direction and ν is the kinematic viscosity. Note, here V_0 is defined as being negative, implying that $U \rightarrow U_\infty$ as $y \rightarrow \infty$. The analytical expression (8) enables direct integrations of the integrands corresponding to the displacement (δ_1) and the momentum loss thickness (δ_2), which result in

$$\delta_1 = \int_0^\infty \left(1 - \frac{U(y)}{U_\infty} \right) dy = -\frac{\nu}{V_0} \quad (9)$$

and

$$\delta_2 = \int_0^\infty \frac{U(y)}{U_\infty} \left(1 - \frac{U(y)}{U_\infty}\right) dy = -\frac{1}{2} \frac{\nu}{V_0}, \quad (10)$$

respectively. This means that the shape factor $H = \delta_1/\delta_2$ is equal to 2. The boundary layer thickness δ_{99} , defined as the wall distance where U reaches 99% of U_∞ , becomes

$$\delta_{99} = \frac{\nu}{V_0} \log(0.01) = \delta_1 \log(100). \quad (11)$$

In the asymptotic suction region the Reynolds number based on the displacement thickness becomes

$$Re = \frac{U_\infty \delta_1}{\nu} = -\frac{U_\infty}{V_0}. \quad (12)$$

This provides the ASBL with a unique feature, namely, that one may vary the Reynolds number and the boundary layer thickness independent of each other.

Examples of boundary layer velocity profiles near the trailing edge of the rectangular-based forebody are presented in figure 16. In figure 16(a) the free stream velocity is constant as the suction level is increased. It is clear how the boundary layer thickness is reduced, as the suction level is increased. When the suction reaches a level corresponding to a Δp across the sheets of around 125 Pa, the boundary layer has reached the asymptotic region. Figure 16(b) shows the same profiles as in (a) but scaled by the boundary layer displacement thickness in the wall-normal direction and the free-stream velocity, along with the analytical solution of the ASBL. Velocity profiles that have a lower suction level than 125 Pa do not collapse perfectly. Neither do the profiles with a suction corresponding to $\Delta p > 500$ Pa. The boundary layer velocity profiles in figure 16(c) are measured $1H$ upstream of the trailing edge at a constant suction level of 150 Pa as the free stream velocity is varied in the range 3–16 m s⁻¹. The dotted lines represent the boundary layer thickness for the different free stream velocities. They are randomly distributed with a low deviation from the mean value (dashed), indicating that the boundary layer thickness can be regarded as constant for all measured velocities. The same profiles are shown in 16(d), but scaled as in (b), which makes all profiles collapse on the same analytical solution of the ASBL.

5.3. Wake symmetry

To validate that the the flow along and behind the rectangular-based forebody is symmetric, measurements of the wake velocity profiles have been performed at different levels of suction at a constant free stream velocity as well as increasing free stream velocity with a constant level of suction.

- In figure 17 the free stream velocity is kept constant at 3 m/s while the suction level through the permeable surfaces is increased.

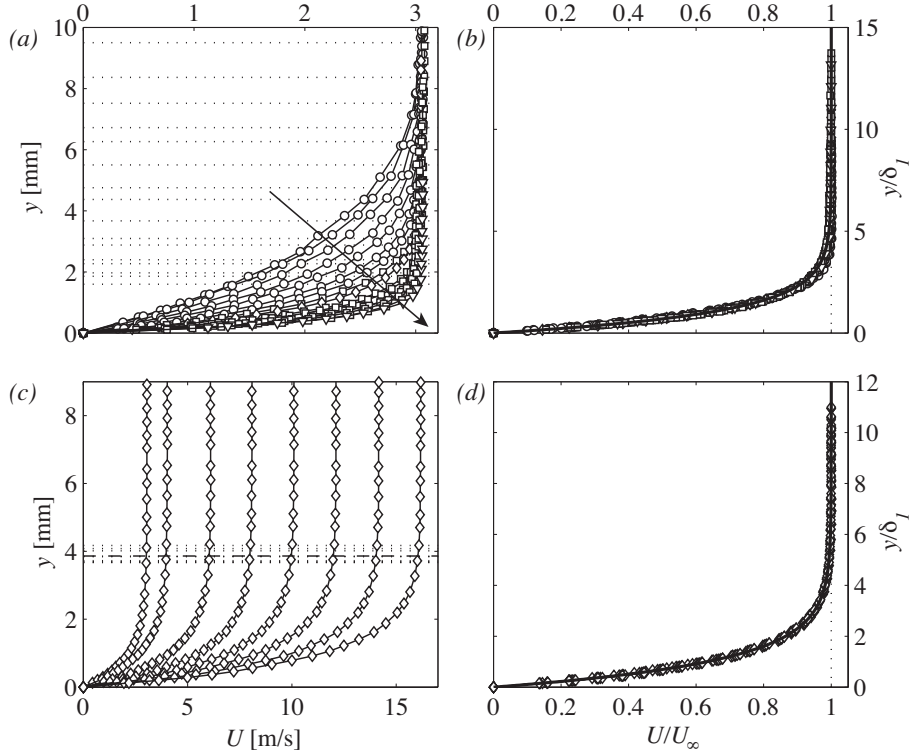


FIGURE 16. Boundary layer profiles measured $-1H$ from the trailing edge. In (a) the free stream velocity is constant while the suction level increases. (b) is the same but normalised. The arrow shows in which direction the suction level increases. In (c) the suction pressure is constant while the free stream velocity is increased, (d) is the same but normalised. (\circ) indicates 0–100 Pa suction pressure, (\diamond) 150 Pa, (\square) 125–450 Pa and (∇) is 500 Pa. (\cdots) and ($---$) is the boundary layer thickness and the mean boundary layer thickness, respectively. ($-$) in (b) and (d) is the analytical solution of the ASBL.

- Figure 18 shows wake velocity profiles at a constant suction level of 150 Pa for different downstream locations when the free stream velocity is varied.
- In figure 19 both the suction level and the free stream velocity is constant at 150 Pa and 3 m s^{-1} , respectively, as the downstream position is changed. The wake velocity deficit decreases monotonically as the distance increases.

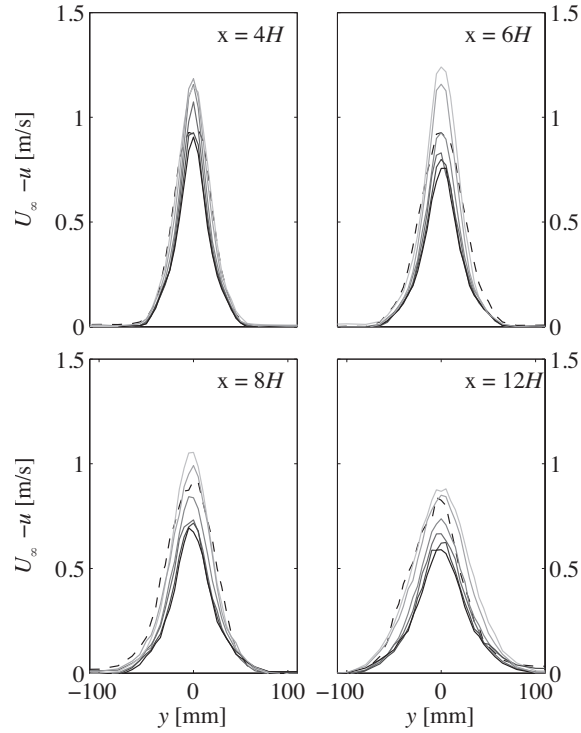


FIGURE 17. Wake velocity profiles measured at different downstream locations for different levels of suction at a constant free stream velocity of 3 m/s.

The result is that the wake is symmetric when varying the suction and the free stream velocity independent of each other. This is a first check point of the setup and we can conclude that the setup has been successfully manufactured.

6. Preliminary results

Some preliminary results regarding the Strouhal number and the base pressure in the wake behind the rectangular-based forebody is presented below. Figure 20 shows the Strouhal plotted against the Reynolds number based on the displacement thickness and the displacement thickness itself, respectively. The Reynolds number depends on both the free stream velocity and the suction velocity and interestingly one finds a branch near $Re = 300$, where constant suction level and constant free stream velocity have different trends. Looking at the relation between the St and the displacement thickness, an increased

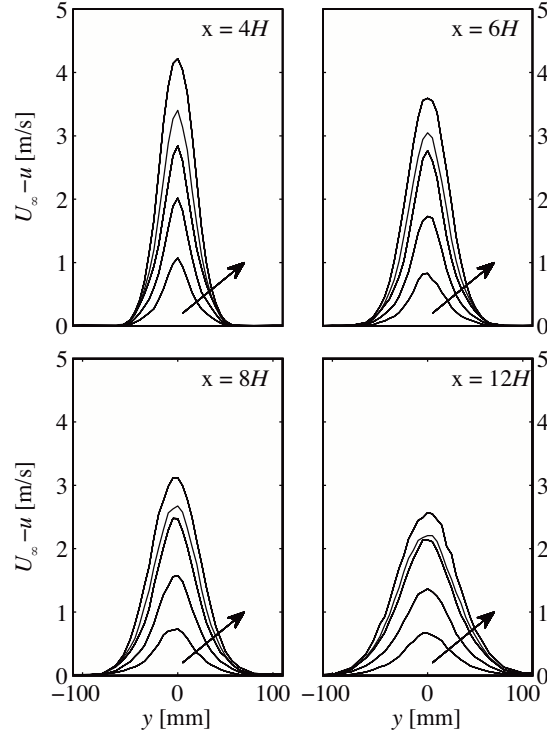


FIGURE 18. Wake velocity profiles at different downstream locations for the free stream velocities 3, 6, 9, 12 and 15 m/s. The arrow point in the direction of increasing free stream velocity.

suction level has an almost linear increasing trend on the Strouhal number. On the other hand while keeping the thickness constant while increasing the velocity have a decreasing effect.

In figure 21 we show the effect on the base pressure as a function of Re_{δ_1} and δ_1 . In comparing figures 20 and 21, we can conclude that the base pressure decreases as the suction level is increased (resulting in a lower Re_{δ_1} and δ_1). On the other hand while varying the Re_{δ_1} by means of changing the free stream velocity the base pressure increases, but much slower, as Re_{δ_1} increases.

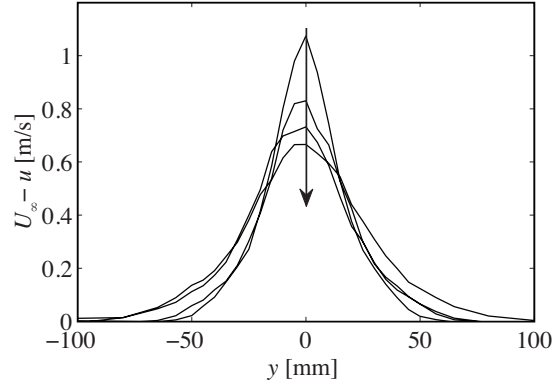


FIGURE 19. The wake velocity profile at different downstream locations $[4, 6, 8, 12]H$ at a free stream velocity of 3 m/s. The arrow points in the direction of increasing downstream distance.

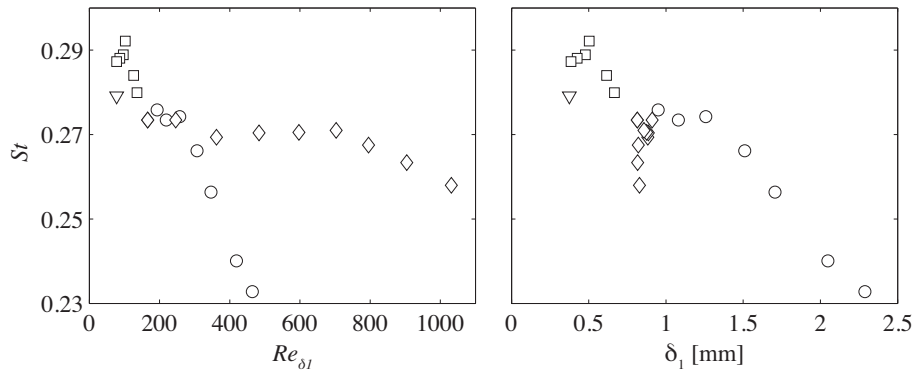


FIGURE 20. The Strouhal number of the vortex shedding in the wake at different suction levels and free stream velocities. To the left the variation with Re_{δ_1} and to the right the variation with δ_1 are shown, respectively. (\circ) indicates 10–100 Pa suction pressure, (\diamond) 150 Pa, (\square) 125–450 Pa and (∇) is 500 Pa.

7. Summary

The new experimental setup that is presented introduces the unique feature to in experimental studies vary the inlet conditions of a bluff body wake. This, in combination with a trailing edge that is easily modified, makes it an ideal

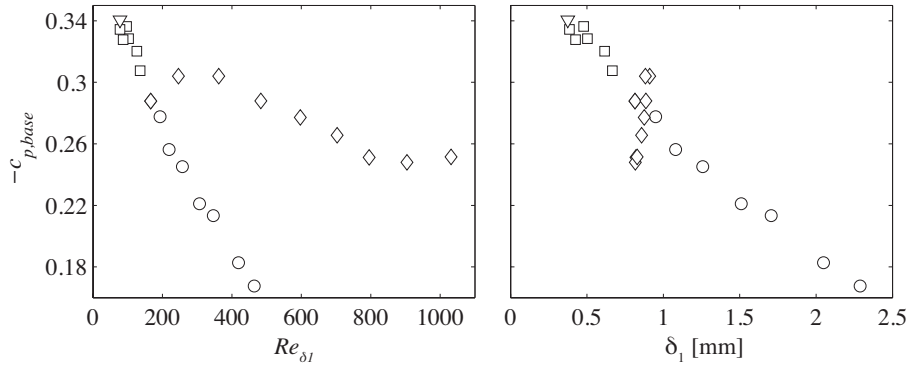


FIGURE 21. The base pressure at different suction levels and free stream velocities. To the left the variation with Re_{δ_1} and to the right the variation with δ_1 is shown, respectively. Symbols same as in figure 20

experiment for studies of different control methods for the wake flow instability. It has been shown that by varying the suction level through the permeable surfaces, the shape and thickness of the boundary layer profile along the rectangular-based forebody, is modulated. This changes the characteristics of the wake flow in terms of the base pressure coefficient, Strouhal number and mean velocity profile, while the free stream velocity is kept constant.

References

- ADRIAN, R. J., CHRISTENSEN, K. T. & LIU, Z.-C. 2000 Analysis and interpretation of instantaneous turbulent velocity fields. *Exp. Fluids* **19**, 275–290.
- AGRAWAL, A. & PRASAD, A. 2002 Properties of vortices in the self-similar turbulent jet. *Exp. Fluids* **33**, 565–577.
- BALACHANDAR, S., MITTAL, R. & NAJJAR, F. M. 1997 Properties of the mean recirculation region in the wakes of two-dimensional bluff bodies. *J. Fluid Mech.* **351**, 167–199.
- BEARMAN, P. W. 1967 On vortex street wakes. *J. Fluid Mech.* **28**, 625–641.
- BRUUN, H. H. 2002 *Hot-Wire Anemometry - Principles and Signal Analysis*. Oxford University Press.
- BURESTI, G. 1998 Vortex shedding from bluff bodies. *Wind Effects on Buildings and Structures*, pp. 61–95, Riera & Davenport (eds.), Balkema, Rotterdam.
- CHOMAZ, J. M., HUERRE, P. & REDEKOPP, L. G. 1988 Bifurcations to local and global modes in spatially developing flows. *Phys. Rev. Lett.* **60**, 25–28.
- CHONG, M. S., PERRY, A. E. & CANTWELL, B. J. 1990 A general classification of three-dimensional flow fields. *Phys. Fluids* **2**, 765–777.
- FALLENIOUS, B. E. G. 2009 A new experimental setup for studies on wake flow instability and its control. TRITA-MEK Tech. Rep. 2009:05. Licentiate Thesis, KTH, Stockholm.
- FRANSSON, J. H. M. & ALFREDSSON, P. H. 2003 On the disturbance growth in an asymptotic suction boundary layer. *J. Fluid. Mech.* **482**, 51–90.
- FRANSSON, J. H. M., KONIECZNY, P. & ALFREDSSON, P. H. 2004b Flow around a porous cylinder subject to continuous suction or blowing. *J. Fluids Struct.* **19**, 1031–1048.
- GILLIES, E. A. 1998 Low-dimensional control of the circular cylinder wake. *J. Fluid Mech.* **371**, 157–178.
- GOLDSTEIN, S. 1938 *Modern developments in fluid dynamics*, vol. 1. Clarendon Press Oxford.
- GRIFFITH, A. A. & MEREDITH, B. A. 1936 The possible improvement in aircraft performance due to the use of boundary layer suction. *Tech. Rep.*. Royal Aircraft Establishment.

- GRINSTEIN, F. F., BORIS, J. P. & GRIFFIN, O. M. 1991 Passive pressure-drag control in a plane wake. *AIAA J.* **29**, 1436–1442.
- HAMMOND, D. A. & REDEKOPP, L. G. 1997 Global dynamics of symmetric and asymmetric wakes. *J. Fluid Mech.* **331**, 231–260.
- HANNEMANN, K. & OERTEL, H. 1989 Numerical simulation of the absolutely and convectively unstable wake. *J. Fluid Mech.* **199**, 55–88.
- HUERRE, P. & MONKEWITZ, P. A. 1990 Local and global instabilities in spatially developing flows. *Annu. Rev. Fluid Mech.* **22**, 473–537.
- LINDGREN, B. 2002 Flow facility design and experimental studies of wall-bounded turbulent shear-flows. PhD thesis, Royal Institute of Technology.
- MATHELIN, L., BATAILLE, F. & LALLEMAND, A. 2001a Near wake of a circular cylinder submitted to blowing - I Boundary layers evolution. *Int. J. Heat Mass Transf.* **44**, 3701–3708.
- MATHELIN, L., BATAILLE, F. & LALLEMAND, A. 2001b Near wake of a circular cylinder submitted to blowing - II Impact on the dynamics. *Int. J. Heat Mass Transf.* **44**, 3709–3719.
- MCKEON, B., LI, J., JIANG, W., MORRISON, J. & SMITS, A. 2003 Pitot probe corrections in fully developed turbulent pipe flow. *Meas. Sci. Technol.* **14**, 1449.
- MONKEWITZ, P. A. 1988 The absolute and convective nature of instability in two-dimensional wakes at low Reynolds numbers. *Phys. Fluids* **31**, 999–1006.
- NAKAMURA, Y. 1996 Vortex shedding from bluff bodies with splitter plates. *J. Fluids Struct.* **10**, 147–158.
- NORBERG, C. 2003 Fluctuating lift on a circular cylinder: review and new measurements. *J. Fluids Struct.* **17**, 57–96.
- POLL, D. I. A., DANKS, M. & HUMPHREYS, B. E. 1992 The aerodynamic performance of laser drilled sheets. *First European Forum on Laminar Flow Technology* pp. 274–277.
- PROVANSAL, M., MATHIS, C. & BOYER, L. 1987 Benard-von Karman instability: transient and forced regimes. *J. Fluid Mech.* **182**, 1–22.
- RANGA RAJU, K., POREY, P. & ASAWA, G. 1997 Displacement effect in pitot tube measurements in shear flows. *J. Wind Eng. Ind. Aerodyn.* **66** (2), 95–105.
- ROSHKO, A. 1955 On the wake and drag of bluff bodies. *J. Aeronaut. Sci.* **22**, 124–132.
- ROSHKO, A. 1961 Experiments on the flow past a circular cylinder at very high Reynolds number. *J. Fluid Mech.* **10**, 345–356.
- ROSHKO, A. 1993 Free shear layers, base pressure and bluff-body drag. In *Proc. Symp. on Developments of Fluid Dyn. and Aerospace Eng.*, Bangalore, India, Dec. 9–10, 1993.
- SARIC, W. S., REED, H. L. & KERSCHEN, E. J. 2002 Boundary-layer receptivity to freestream disturbances. *Annu. Rev. Fluid Mech.* **34**, 291–319.
- SREENIVASAN, K. R., STRYKOWSKI, P. J. & OLINGER, D. J. 1986 Hopf bifurcation, landau equation, and vortex shedding behind circular cylinders. In *Proc. Forum on Unsteady Flow Separation* (ed. K. H. Ghia). ASME FED, vol. 52.
- WILLIAMSON, C. H. K. 1989 Oblique and parallel modes of vortex shedding in the wake of a circular cylinder at low Reynolds numbers. *J. Fluid Mech.* **206**, 579–627.

- WILLIAMSON, C. H. K. 1996 Vortex dynamics in the cylinder wake. *Annu. Rev. Fluid Mech.* **28**, 477–539.
- WOOD, C. J. 1967 Visualization of an incompressible wake with base bleed. *J. Fluid Mech.* **29**, 259–272.
- YOSHIOKA, S., FRANSSON, J. H. M. & ALFREDSSON, P. H. 2004 Free stream turbulence induced disturbances in boundary layers with wall suction. *Phys. Fluids* **16**, 3530–3539.
- ZDRAVKOVICH, M. M. 1997 *Flow around circular cylinders, Vol 1: Fundamentals*. Oxford University Press.
- ZDRAVKOVICH, M. M. 2003 *Flow around circular cylinders, Vol 2: Applications*. Oxford University Press.
- ZHOU, J. ADRIAN, R. J., BALACHANDAR, S. & KENDALL, T. M. 1999 Mechanisms for generating coherent packets of hairpin vortices in channel flow. *J. Fluid Mech.* **387**, 353–396.

Paper 2

Experimental study on the effect of pulsating inflow to a closed volume

By Bengt E. G. Fallenius¹, Amir Sattari²,
Jens H. M. Fransson¹ and Mats Sandberg²

¹ Linné Flow Centre, KTH Mechanics, SE-100 44 Stockholm, Sweden

² Dept. of Tech. and Built Env., University of Gävle, SE-80176 Gävle, Sweden

Optimal control of inlet jet flows is of broad interest for enhanced mixing in ventilated rooms. The general approach in mechanical ventilation is forced convection by means of a constant flow rate supply. However, this type of ventilation may cause several problems such as draught and appearance of stagnation zones, which reduces the ventilation efficiency. A potential way to improve the ventilation quality is to apply a pulsating inflow, which has been hypothesized to reduce the stagnation zones due to enhanced mixing. The present study aims at testing this hypothesis, experimentally, in a small-scale two-dimensional water model using Particle Image Velocimetry with an *in-house* vortex detection program. We are able to show that for an increase in pulsation frequency or alternatively in the flow rate the stagnation zones are reduced in size and the distribution of vortices becomes more homogeneous over the considered domain. The number of vortices (all scales) increases by a factor of four and the swirl-strength by about 50% simply by turning on the inflow pulsation. Furthermore, the vortices are well balanced in terms of their rotational direction, which is validated by the symmetric Probability Density Functions of vortex circulation (Γ) around $\Gamma = 0$. There are two dominating vortex length scales in the flow, namely 0.6 and 0.8 inlet diameters and the spectrum of vortex diameters become broader by turning on the inflow pulsation. We conclude that the positive effect for enhanced mixing by increasing the flow rate can equally be accomplished by applying a pulsating inflow.

1. Introduction

The most common type of air distribution method for ventilation is mixing ventilation created by a continuous supply of air with constant flow rate into the room. Mixing ventilation is often used when there is a high heat load in the room or a large generation of contaminants. A constant ventilation flow rate gives rise to a jet across the room, which by air entrainment by the jet sets up a

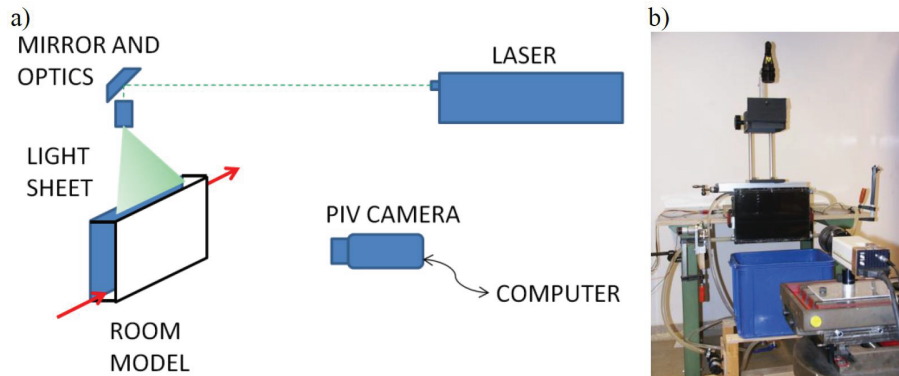


FIGURE 1. *a)* Schematic of the experimental PIV setup. *b)* Photo of the experimental model setup: reflector mirrors and camera (laser is not seen in this picture).

secondary motion of air. When using the ventilation air for cooling or heating a buoyant jet is created. In case of supply of isothermal air or cooled air there is always a risk for draught if one is directly exposed to the jet. Furthermore, when using ventilation air for heating there is a risk for setting up stagnation zones, which gives rise to unacceptable low air exchange efficiencies.

The above list of drawbacks calls for the need of developing new air distribution systems. In this paper we explore a new system based on varying the supply flow rate rapidly. Our hypothesis is: (i) that the air is better distributed over the whole room giving rise to a higher air exchange efficiency, and (ii) that the ventilation air is better spread out over the whole room lowering the velocity and thereby reducing the risk of draught. There is a support for above hypothesis (i) in the tests reported by Sandberg & Elvsén (2004). These authors showed, by means of flow visualization, that a varying flow rate generated secondary vortices, which were shed into the stagnant areas within the room. However, the observation has never been quantified.

The focus of this paper is to report on results from a fundamental study of a system with rapidly varying supply flow rate using Particle Image Velocimetry (PIV) along with a specially developed software for quantifying the occurrence of vortices and get information about the probability distributions of vortex size, vortex strength as well as vortex location. Since the presence of vortices is a prerequisite for good mixing this type of vortex analysis is motivated for quantifying the performance of the actual ventilation system.

The paper has the following outline. Section 2 describes the experimental setup, measurement technique and the parameter variation study. This is followed by a brief summary of the vortex detection program that has been used

for the collection of the vortex statistics. The results are shown in section 3 and the summary and conclusions are found in section 4.

2. Experimental model and flow cases

2.1. Experimental setup

The experiments were performed in a two-dimensional (2-D) small-scale water model with the dimension $30 \times 20 \times 0.9$ cm³. To measure instantaneous velocity fields a PIV system was used. This system consists of a Spectra Physics 400 mJ double pulsed Nd:Yag laser operating at 15 Hz as a light source, and a double-frame CCD camera Kodak ES1.0 8-bit with 1018×1008 pixels. The size of the model makes it manageable to traverse the camera-view throughout the model and investigate statistical quantities based on the 2-D velocity vector fields but still keep high enough spatial resolution for instantaneous small-scale vortex analysis. In the lower left and the upper right corner of the model the inflow and outflow take place, respectively, through plastic tubing connected via pipe nozzles attached to the model. Hence, the inflow and outflow to the model take place through a circular cross-sectional area of a diameter $D = 9$ mm. For the PIV the water was seeded with Polyamid seeding particles with a mean particle diameter of $20 \mu\text{m}$. The seeded water is pumped from a water tank and passes through a mechanical pulse generator, which makes it possible to create a pulsating flow upstream of the model of varying frequency. In the return circuit before the tank the water passes a flowmeter in order to monitor the flow rate. Figure 1 *a)* and *b)* show a schematic and a photograph of the experimental setup, respectively.

2.2. Parameter variations

In this experimental investigation a pressure driven 2-D steady flow is considered as the base flow. The inflow to the room model is a so-called wall-jet with a supply flow rate Q and corresponding supply bulk velocity U_b . The nominal time constant (τ) is a function of Q for a given volume (V) of the room model. In this investigation we considered two different flow rates $Q_1 = 0.16$ and $Q_2 = 0.24$ lit/min, located on either side of the threshold flow rate (Q_{tr}) corresponding to the onset of natural roll-up of vortices in the outer shear layer of the wall-jet. This Q_{tr} -value was qualitatively determined, from flow visualisations using an ordinary CCD video camera, to $Q_{tr} = 0.2$ lit/min and the considered flow rates Q_1 and Q_2 were set to $\pm 20\%$ of this value. The nominal time constants for these flow rates are $t = V/Q = 225$ and 150 sec and the inlet jet Reynolds numbers based on the inlet diameter are 376 and 564 , respectively.

The characteristics of the flow field in the room model will change depending on the flow rate and pulsation frequency. Here we have studied four different pulsation frequencies $F = (F0, F1, F2, F3) = (0, 0.3, 0.4, 0.5)$ Hz, which also were chosen from flow visualization observations.

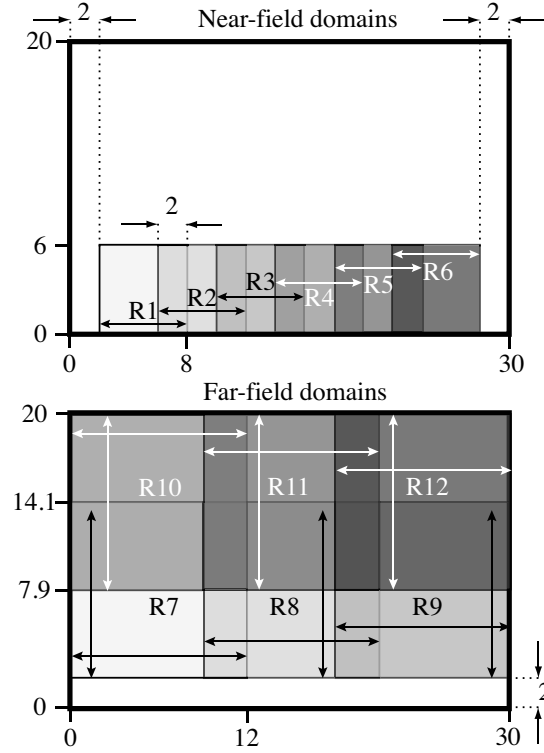


FIGURE 2. Schematic of the near-field and far-field PIV domains.

2.3. PIV Domain decomposition and measurements

The area of the model ($30 \times 20 \text{ cm}^2$) is too large to be collected in one PIV image, using the current camera, if a descent spatial resolution is desired. Therefore, the area of the model was decomposed into 12 smaller domains. The captured data is then exported to Matlab for post-processing and analyses using domestic programs. The regions of the 12 domains are grouped into near-field and far-field domains with respect to the inflow wall-jet, with some overlap with neighbouring domains. This is illustrated in figure 2 and in table 2.2 the limits of the domains are specified.

In each one of the domains measurements have been carried out at the two base flow rates Q_1 and Q_2 with the pulsation frequency as the variable parameter, read $F = (F_0, F_1, F_2, F_3)$. This results in eight subsets of PIV measurements in each domain. In the near-field domains, R1–6, about 1 000 PIV image pairs were collected with two seconds time delay between the recordings. In the far-field domains, R7–12, with lower velocities, about 500 image

| Region | R1 | R2 | R3 | R4 | R5 | R6 |
|-----------|--------|--------|--------|--------|--------|--------|
| x limit | 2–8 | 6–12 | 10–16 | 14–20 | 18–24 | 22–28 |
| y limit | 0–6 | 0–6 | 0–6 | 0–6 | 0–6 | 0–6 |
| Region | R7 | R8 | R9 | R10 | R11 | R12 |
| x limit | 0–12 | 9–21 | 18–30 | 0–12 | 9–21 | 18–30 |
| y limit | 2–14.1 | 2–14.1 | 2–14.1 | 7.9–20 | 7.9–20 | 7.9–20 |

TABLE 1. Extents of measurement domains (see figure 2). Figures are given in [cm].

pairs were collected with three seconds time delay. In total this amounts to about 72 000 PIV image pairs considering all domains and parameter variations of the room model.

2.4. Method of vortex identification

To access statistical properties of vortices from instantaneous PIV images we will use an *in-house* developed vortex detection program described in Fallenius (2009). In order to detect vortices that are embedded in 2-D velocity fields, commonly acquired through PIV-measurements, Adrian *et al.* (2000) suggested that decomposition of the velocity field by low-pass filtering is an adequate way to visualise small-scale vortices. In their study, a Gaussian filter was used for the decomposition and the vortices were then detected by using the approach suggested by Chong *et al.* (1990), i.e. identifying closed or spiral streamline patterns by looking at the complex eigenvalues of the high-pass filtered (hpf) 2-D velocity gradient tensor,

$$\nabla \mathbf{u}_{2D}^{\text{hpf}} = \begin{bmatrix} \frac{\partial u}{\partial x} & \frac{\partial u}{\partial y} \\ \frac{\partial v}{\partial x} & \frac{\partial v}{\partial y} \end{bmatrix}. \quad (1)$$

Regions where the imaginary eigenvalues, λ_{ci} , are positive and greater than a threshold value are then defined as a vortex. In the present investigation we have consistently used $\lambda_i = 0.025$ as the threshold value. Agrawal & Prasad (2002) also used a Gaussian filter to perform the decomposition suggested by Adrian *et al.* (2000), while vortices were identified by looking at the neighbouring vectors of each point. If the angular orientation of the surrounding vectors experienced a monotonically angular variation from 0 to 2π the point was considered to be a vortex centre. The same decomposition will be used here, while the Δ -method according to Chong *et al.* (1990) will be used for the vortex identification.

Each contour region is then examined in order to determine relevant properties such as location, size, circulation and swirl strength of the vortex. This is executed in the following manner. The centre of the vortex is identified by finding the x - and y -coordinates of the maximum imaginary eigenvalue, $\lambda_{ci,max}$, within the contour. This eigenvalue is also stored as a measure of the swirl strength of the vortex (see e.g. Zhou *et al.* 1999). The size of the vortex is then determined by first calculating the area inside the threshold contour level. An equivalent radius to a corresponding circle (C) with its origin at $\lambda_{ci,max}$ is then used as a starting radius for calculating the circulation, γ , through direct integration along C 's perimeter \mathbf{l} according to

$$\gamma = \oint_C \mathbf{u}_{2D}^{\text{hpf}} \cdot d\mathbf{l} . \quad (2)$$

This process is repeated while stepping outwards from the vortex centre until the maximum value of the circulation is reached, which then is stored. The corresponding radius is also stored as the vortex size.

3. Results

3.1. Base flow

Mean velocity profiles of the wall-jet at the bottom surface are shown in figure 3 *a*) and *b*) as unscaled and scaled data, respectively. The solid line in *b*) corresponds to the self-similar solution of the Glauert 2-D wall-jet problem (see e.g. Kundu & Cohen 2008). The scaled wall-normal coordinate η corresponds to $y/\delta(x)$, where $\delta(x)$ is the boundary layer length scale defined as

$$\delta(x) = \sqrt{x\nu/\overline{U}(x)} .$$

Here $\overline{U}(x)$ is taken as the mean velocity of the wall-jet as

$$\overline{U}(x) = \frac{1}{\delta^*(x)} \int_0^{\delta^*(x)} U(x,y) dy ,$$

and ν is the kinematic viscosity. δ^* is a truncated wall-normal distance outside the wall-jet where the velocity is close to zero. The experimental wall-jet scales as expected and one may conclude that it also agrees well with the self-similarity solution of the Glauert wall-jet problem provided that a virtual origin of $x_0 = -0.04$ m is introduced. The virtual origin takes into account the undeveloped region close to the inlet, where furthermore the boundary layer equation is not valid. The virtual origin was chosen for good agreement with the theoretical profile by Glauert but was then applied consistently to all profiles independent of the x -location. Note that the fundamental difference between the experimental setup and the assumption in the Glauert problem is that the experimental wall-jet is highly confined between the two vertical walls of a spacing of 1 cm, whereas the Glauert wall-jet is assumed to be two-dimensional.

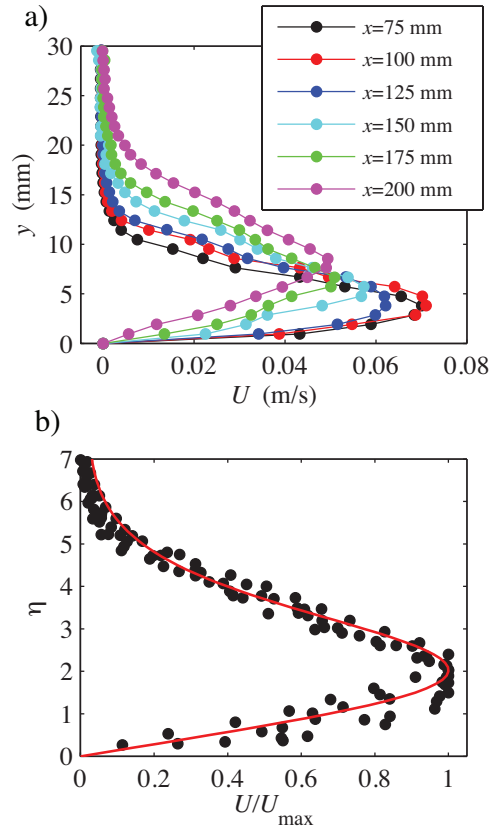


FIGURE 3. Downstream evolution of wall-normal streamwise velocity profiles of the incoming wall-jet. $Q = Q_1$. *a*) Dimensional profiles. *b*) Dimensionless profiles. Solid line in *b*) corresponds to the theoretical Glauert wall-jet.

In figure 4 the entire flow field (domains R1–12) of the base flow cases Q_1 and Q_2 , i.e. without inflow pulsation, are shown in *a*) and *b*), respectively. The background contour plot shows the magnitude of the velocity vector, $|U|$, and the white arrows correspond to the 2-D velocity vector plot. In comparing these two cases one may note that the larger the inflow rate is the thicker is the wall-jet, which gives rise to a wider vertical jet towards the outflow location of the model. This in turn causes a larger region to be affected by the pressure driven inflow, which enhances the mixing. One may note that there is a main stream from the inlet to the outlet of the model, so the challenge is to make

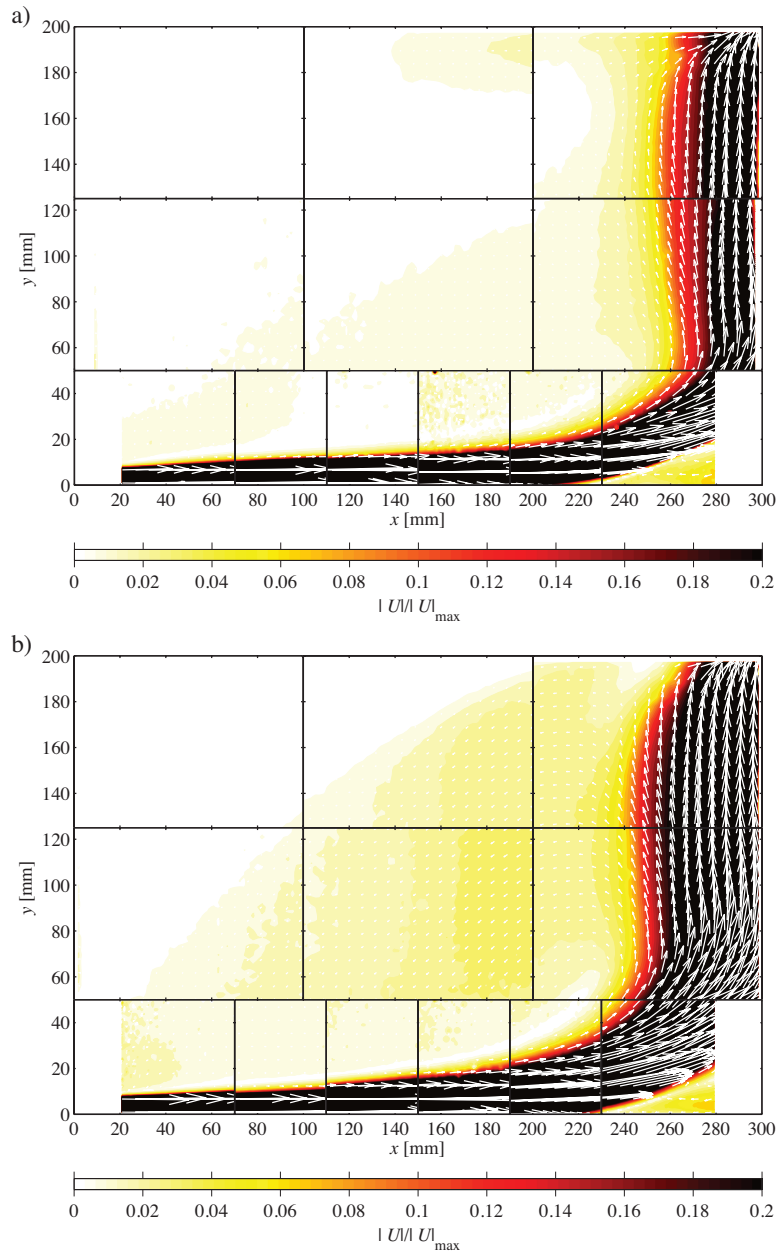


FIGURE 4. Base flow cases without inlet pulsation $F = F_0$. a) and b) show the velocity vector fields with the velocity vector magnitude in the background for Q_1 and Q_2 , respectively. The data is normalized using the maximum value in the Q_2 case.

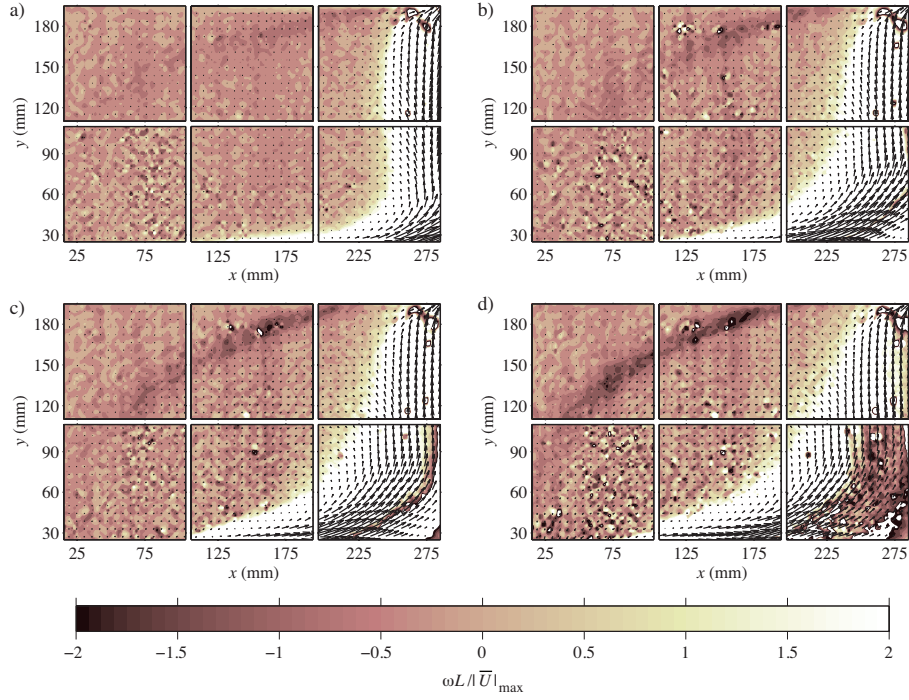


FIGURE 5. Mean vorticity field (R7–12) as the background contour plot overlaid by the vector velocity field. *a*) – *d*) show the Q_1 case for successively increasing inlet pulsation frequency $F_0 - F_3$, respectively.

the calm region more active in the sense that the considered fluid is exchanged to a larger degree.

3.2. Effect of pulsating inflow

In order to illustrate the effect of applying a pulsating inflow we focus here on the far-field domains (R7–12), which are relatively calm except for the vertical main stream along the outflow side originating from the strong inlet wall-jet. In figure 5 the mean vorticity field is shown as a contour plot in the background with the overlaid velocity vector field. The mean vorticity field tells us something about the mean velocity gradients, so regions of high vorticity are desired for good ventilation. Furthermore, instantaneous vorticity fields (not shown here) can be seen as a quantity to identify regions of eddies, which is necessary for good mixing. However, using the vorticity field as a mean to identify vortex structures has several drawbacks and can be seen as quite arbitrary. This method fails as soon as the background shear is within the same order of

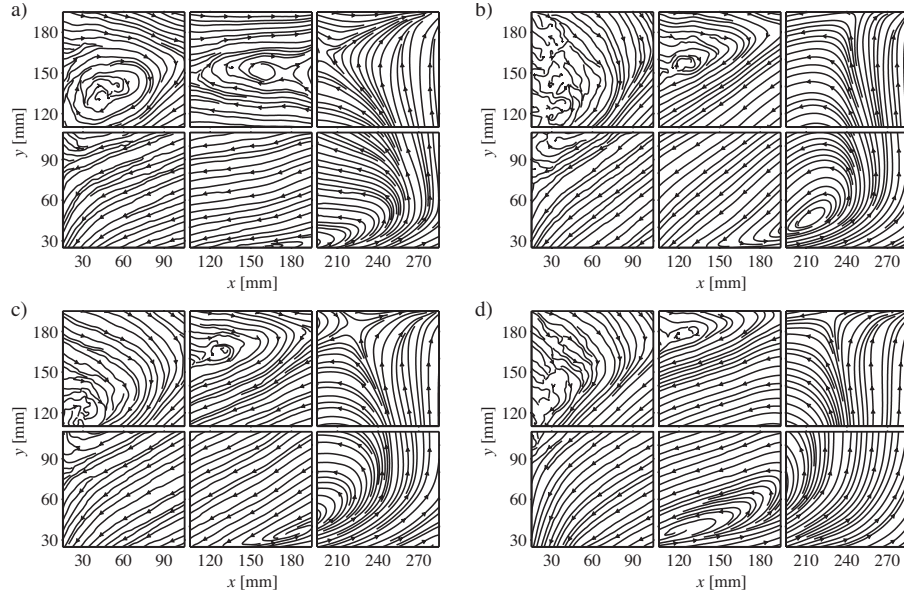


FIGURE 6. Streamlines in the far-field domains (R7–12) for Q_1 and for increasing pulsation frequency F_0 , F_1 , and F_3 in $a)$, $c)$ and $d)$, respectively. $b)$ Shows the Q_2 F_0 case as a second reference.

magnitude as the vortex itself. Thus, in identifying vortices the method outlined in section 2.4 is used and the results will be shown in the next subsection. In figure 5 $a)$ – $d)$ the Q_1 case is shown for successively increased pulsation frequency F_0 , F_1 , F_2 , and F_3 , respectively. The spanwise vorticity (ω) is normalized with the maximum value of the velocity vector magnitude and the length scale L , corresponding to the diagonal length of the model. From this set of figures it is clear that for an increase in pulsation frequency of the inflow condition a mean vorticity streak is established with increasing intensity in the domains R10–11. Furthermore, even though the averaged volume flow rate is the same it is seen that the mean velocity field seems to be accelerated and the portion of re-circulated fluid in the domains R7, 8, 10, and 11 is successively increased.

A streamline plot of a flow field has the distinct feature of elucidating regions of stagnant flow and hence are shown for the Q_1 case for successively increasing pulsation frequency F_0 , F_1 and F_3 in figure 6 $a)$, $c)$ and $d)$, respectively. In $b)$ the Q_2 case of the non-pulsating inflow condition is shown as a second reference. In $a)$ three stagnation points may be observed in the domains R8, 10 and 11, which are reduced in size and moved away to the sides of the model for increasing pulsation frequency (best illustrated in R11).

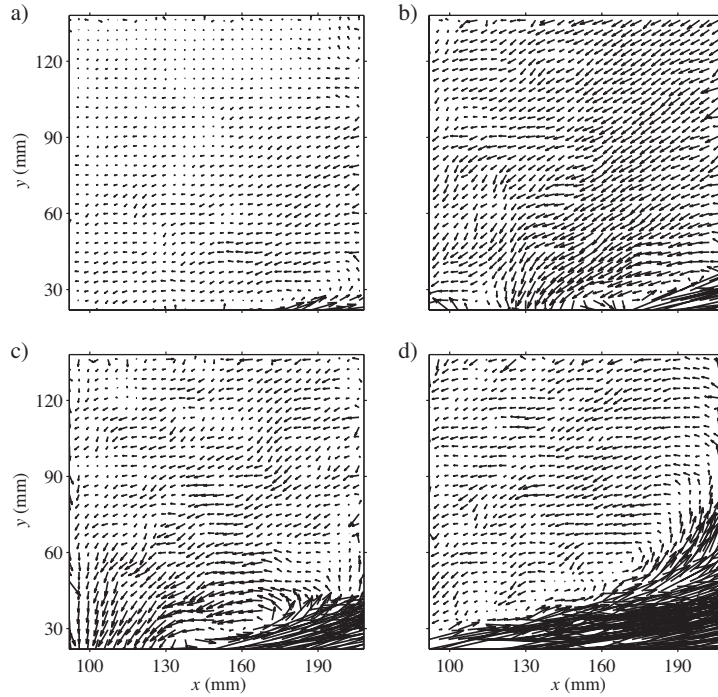


FIGURE 7. The small-scale structures in the domain R8 for Q_1 and for increasing pulsation frequency $F = F0, F1,$ and $F3$ in *a), c)* and *d)*, respectively. *b)* Shows the $Q_2 F0$ case.

The stagnation point in R10 is almost resolved for the highest frequency $F3$ as compared to $F0$. It should be pointed out that there is at least one more stagnation point in the near-field domains (not shown) since the flow going in the negative y -direction in R7–8 has to turn around and follow the wall-jet in positive x -direction. In figure 6*b*), for increasing flow rate, one may observe that the stagnation point in R10 is somewhat resolved as compared to *a)*, the stagnation point in R11 is reduced but not as much as in *d)*, i.e. for the highest considered pulsation frequency $F = F3$. Here we may conclude that by applying a pulsation frequency to a constant flow rate one may improve the re-circulation considerably as compared to what may be accomplished by applying more raw power, in terms of increasing the flow rate with 50% as done in figure 6*b*).

Another observation is that the main stream, from the vertical jet, is spread out more in the negative x -direction for increasing pulsation frequency as compared to an increase in flow rate (compare figure 5*c)–d)* with figure 5*b*). Recall section 2.2 how Q_1 and Q_2 were chosen. The wider vertical jet (observed from

| F | Q_1 | | Q_2 | |
|------|-----------|----------|-----------|----------|
| | no. of IP | vortices | no. of IP | vortices |
| $F0$ | 511 | 2978 | 511 | 12464 |
| $F1$ | 511 | 12021 | 511 | 20946 |
| $F2$ | 511 | 15409 | 511 | 21759 |
| $F3$ | 511 | 16229 | 511 | 24341 |

TABLE 2. The number of PIV-image pairs (IP) taken during the experiments and the number of detected vortices for each F .

figure 4a) – b)) is the effect of break-down to turbulence in the outer shear-layer due to an increase in wall jet Reynolds number. The transition onset in the free shear-layer is triggered at subcritical Reynolds number when flow pulsation is turned on (see figure 5c) and d).

3.3. Vortex statistics

In order to evaluate the presence of small-scale structures the small-scale velocity field is extracted by convolving a Gaussian low-pass filter on the full velocity field. The filter averages each point with the surrounding points resulting in a large-scale velocity field. The large-scale velocity field is then subtracted from the full velocity field, which consequently gives the small-scale velocity field as briefly described in section 2.4. The result of this filtering is shown in figure 7 for the domain R8 with a) – d) corresponding to the same parameters as in figure 6. Interesting to note is that the eddy motion appears to increase with increasing pulsation frequency (cf. figure 7c) – d)) as compared to an increase in flow rate (cf. figure 7b)) when originally compared to the low volume flow rate without any inlet pulsation (cf. figure 7a)).

In the following, vortex statistics will be presented in order to quantify the effect of inlet pulsation. The analysis is restricted to domain R11, which is one of the the least active domains (for $Q = Q_1$) looking at the vorticity field in figure 5 a) and is therefore the most interesting to trace changes in. In table 2 the number of captured PIV image pairs as well as the number of detected vortices in R11 are shown for each parameter combination of Q and F . An interesting observation is that the number of detected vortices increases by a factor of four when pulsation is turned on, and the number keeps increasing for a successive increase in pulsation frequency.

3.3a. *Distribution of vortices.* An overview picture of the presence of vortices is shown in figure 8. Left and right columns of this figure correspond to $Q = Q_1$

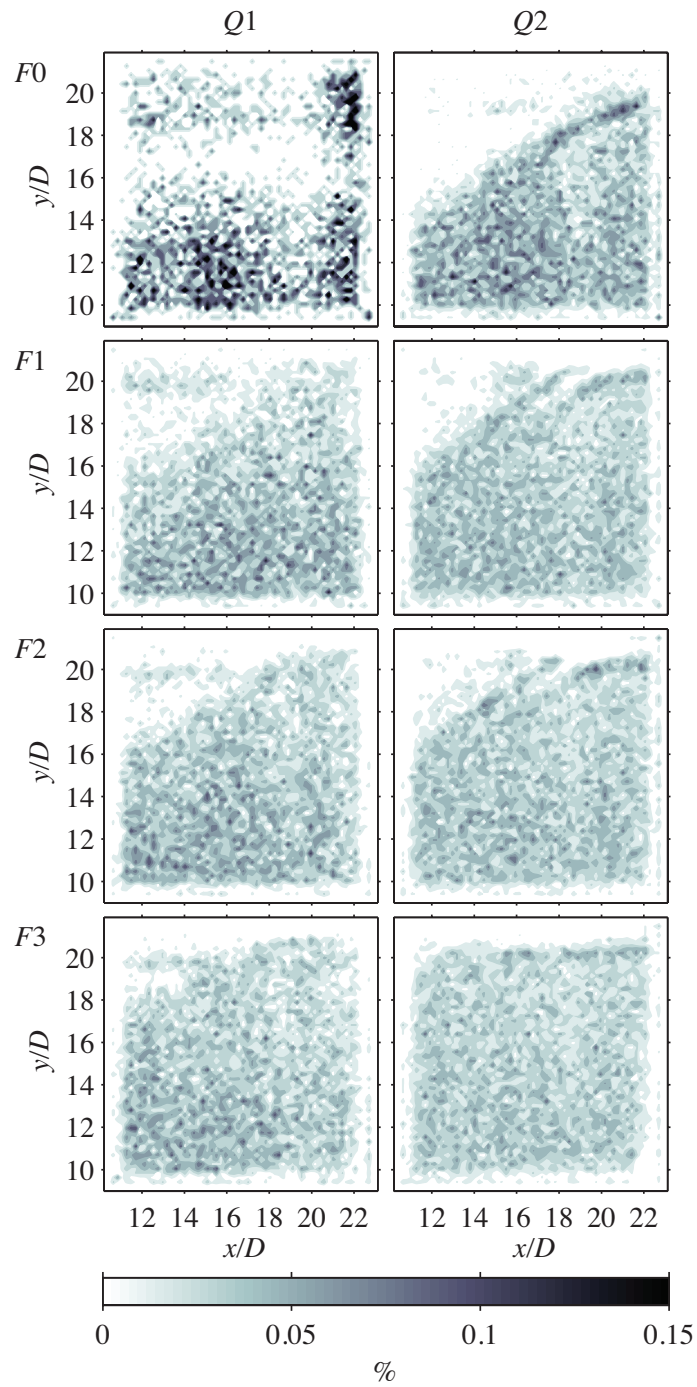


FIGURE 8. Distribution of vortices in each grid point expressed in percentage of the total number of vortices detected. Number of contour steps is 10.

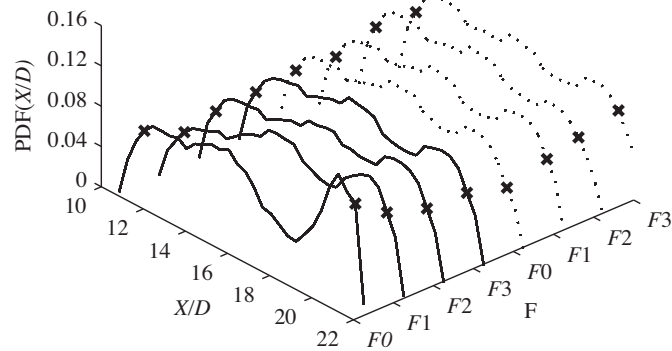


FIGURE 9. PDF of the distribution of vortices in the x -direction in the domain R11. (—) and (\cdots) shows the Q_1 and Q_2 flow rate, respectively. The number of bins is 29 and 90% of the vortices are located between the (\times)-marks.

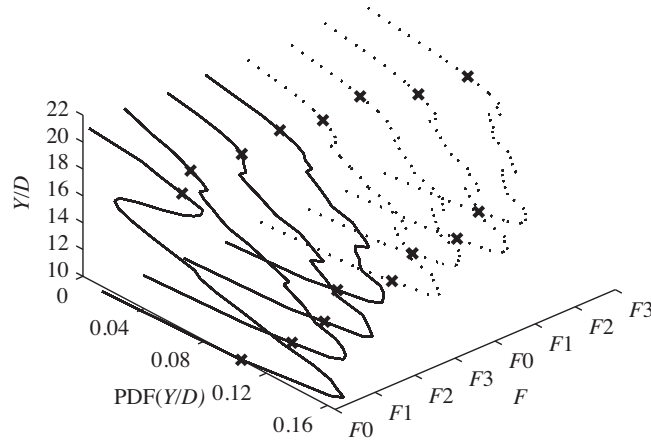


FIGURE 10. PDF of the distribution of vortices in the y -direction in the domain R11. (—) and (\cdots) shows the Q_1 and Q_2 flow rate, respectively. The number of bins is 29 and 90% of the vortices are located between the (\times)-marks.

and Q_2 , respectively, and the rows to successively increasing pulsation frequency. Without pulsation ($F = F_0$) there are inactive regions for both Q_1 and Q_2 , and for Q_2 in particular the upper left corner of the flow field is completely passive. Following the evolution of vortex distribution for increasing pulsation frequency it is seen that the passive regions are reduced in size and that a more homogeneous distribution of vortices is obtained.

In figures 9 and 10 the Probability Density Functions (PDFs) of the vortex distributions are shown for the horizontal (X/D) and the vertical (Y/D) directions, respectively. The low activity zones, for $F = F_0$, are reflected in the dip of the number of vortices with minima around $X/D = 18$ and $Y/D = 17$, respectively. This dip is reduced in average over the considered direction for increasing pulsation frequency or alternatively for an increase in the flow rate. The (\times)-symbols in figures 9 and 10 indicate the locations enclosing 90% of the total number of detected vortices for each case. The fact that the number of vortices goes to zero at the ends of the domain is inherent in the vortex detection program and should be seen as a boundary domain problem and not as a true result.

In summary, the presence of small scale vortices is the first prerequisite of good mixing and is here shown to be fulfilled with a more homogeneous distribution of the vortices in the domain for an increase in pulsation frequency or alternatively in the flow rate.

3.3b. *Vortex size.* The diameter, d , of the vortices and their rotational directions, clock-wise (CW) or counter-clock-wise (CCW), are of importance for the mixing. Having the whole spectrum of vortices, from tiny to large, and a balanced number of CW versus CCW rotations, would be advantageous. In figure 11 the positions of the most frequently appearing vortex diameter, namely $\pm 0.5\%$ of the diameter PDF peak value, are plotted. One may conclude from the figure that the diameter PDF peak becomes broader with increasing pulsation frequency, since the number of vortices in the figures from F_0 to F_3 clearly increases. Another observation is that a more homogeneous distribution of the most common vortex diameter is obtained and that the rotational direction seems to be well balanced (cf. the caption of figure 11 and the significance of the different symbols).

The broader vortex diameter PDF peak is clearly seen by looking at the PDFs directly, as in figure 12. This figure also shows that the most frequently appearing vortex size is about 0.6 inlet diameters (D) and that there are two peaks in the PDF, with the second corresponding to $0.8D$. The (\times)-symbols indicate the limits for the 5% smallest and 5% largest vortices, which correspond to about $0.5D$ and $1D$, respectively.

In figures 13 and 14 the positions of the vortices with sizes less than $0.5D$ and greater than $1D$ are plotted, respectively. The small scale vortices show the same trend as the overall picture (see figure 11), i.e. a more homogeneous distribution in the domain with a balanced number of CW and CCW vortex rotations. The large scale vortices, on the other hand, show a line-up of CW and CCW vortices as alternating streaky regions in the diagonal direction (lower-left to upper-right). This alinement of vortices is best observed for the high flow rate case $Q = Q_2$, but can also be noted for the $Q = Q_1$ for $F \geq F_2$.

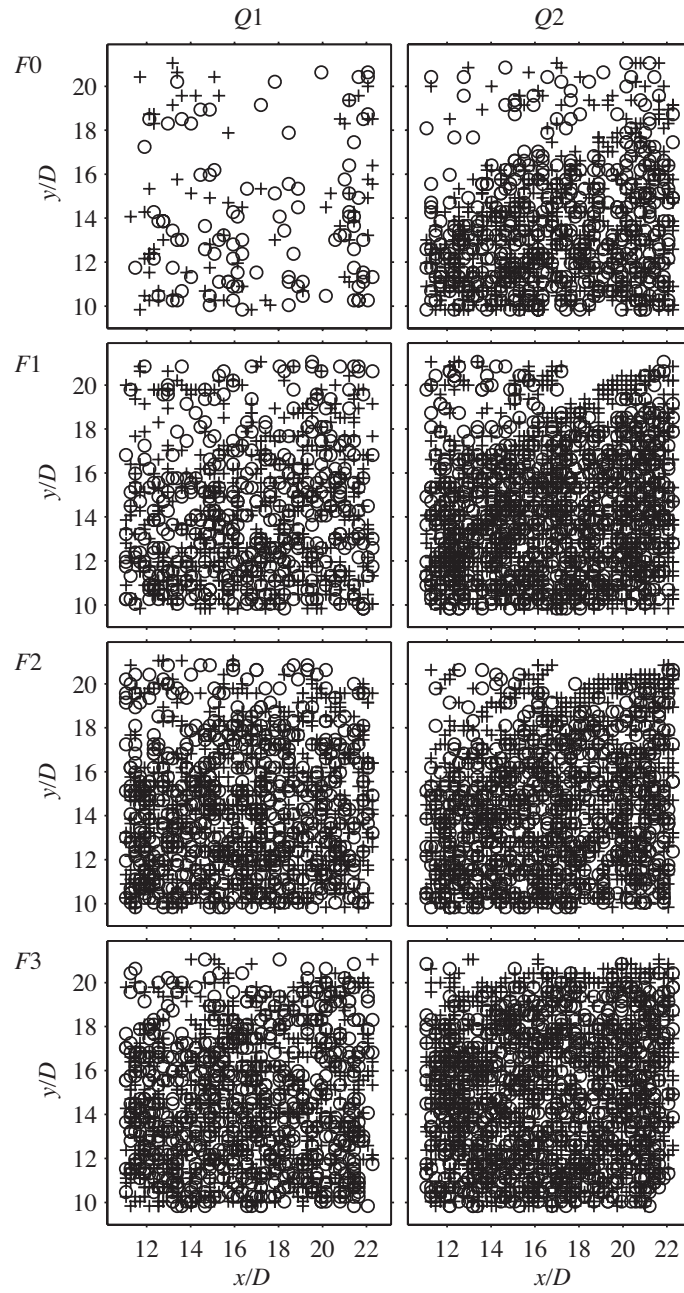


FIGURE 11. Vortices with a size corresponding to $\pm 0.5\%$ of the PDF peak value. (o)- and (+)- symbols have CCW and CW rotational direction, respectively.

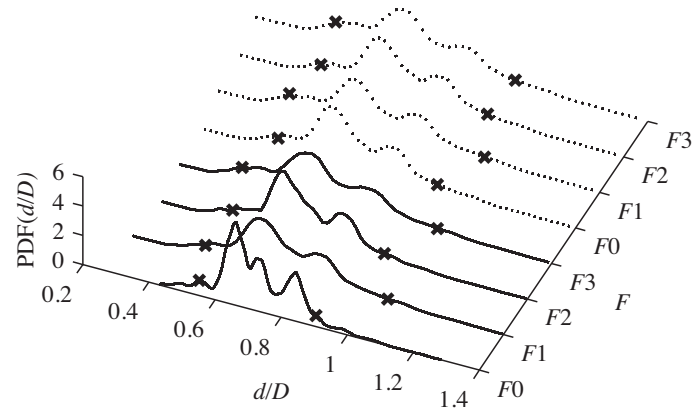


FIGURE 12. PDF distribution of vortex size. (—) and (\cdots) shows the Q_1 and Q_2 flow rate, respectively. (\times) marks the limits for the 5% smallest and the 5% largest vortices. The number of bins is 99 and for a better view the plots are truncated at $d/D = 1.4$.

In summary, a second prerequisite of good mixing is that a broad span of the diameter spectrum is present and that the rotational direction of the vortices are well balanced of CW versus CCW rotations. These two vortex statistics are improved for an increase in pulsation frequency or alternatively in the flow rate.

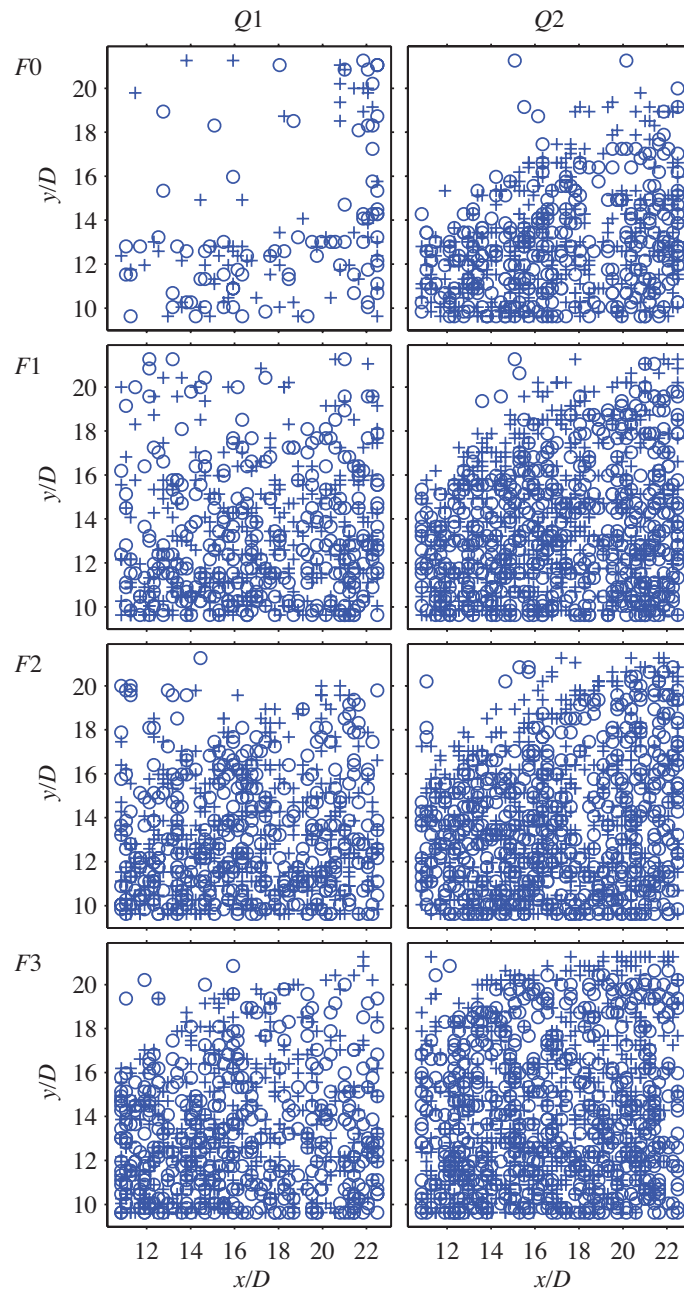


FIGURE 13. Vortices with a size corresponding to 5% smallest vortices. (o)- and (+)- symbols have CCW and CW rotational direction, respectively.

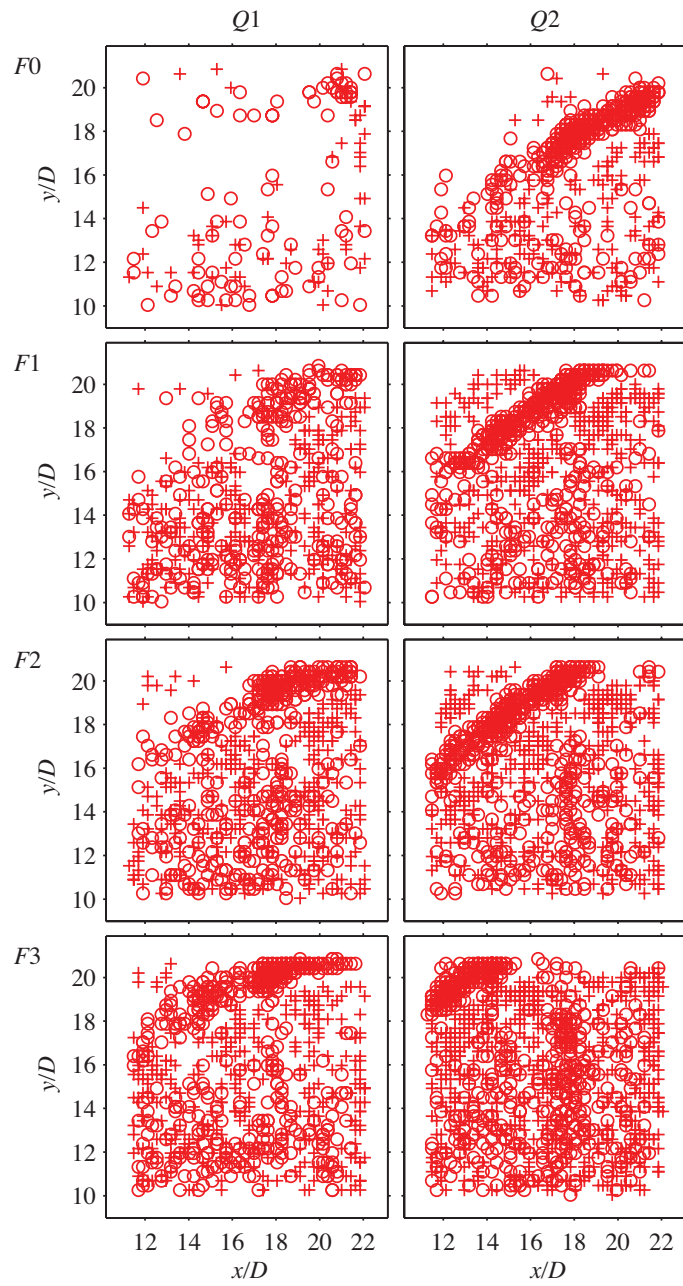


FIGURE 14. Vortices with a size corresponding to 5% largest vortices. (\circ)- and ($+$)- symbols have CCW and CW rotational direction, respectively.

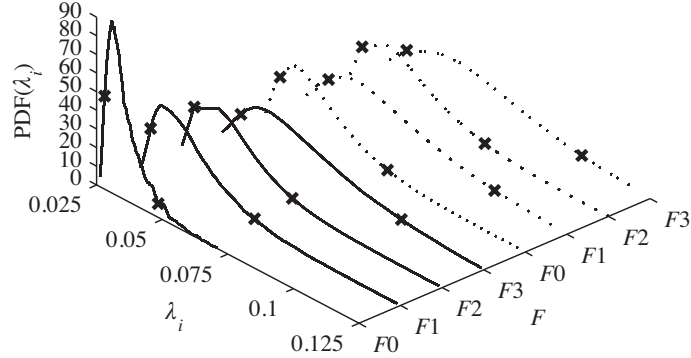


FIGURE 15. PDF distribution of vortex swirl-strength. The number of bins is 99 and for better view the plots are truncated at $\lambda_i = 0.125$. (\times) marks the limits for the 5% weakest and the 5% strongest vortices.

3.3c. *Vortex swirl-strength.* The swirl-strength of the vortices is directly defined by the imaginary part of the eigenvalue, λ_i (see section 2.4). In figure 15 the PDFs are shown for all cases. An interesting result is that as soon as the pulsation frequency is turned on the number of strong vortices increases drastically. The very narrow PDF peak for the $(Q_1, F0)$ -case is reduced in height for the favorable effect of re-distributing a number of vortices into the more intensified range of vortices. Obviously, the stronger the vortices are the better becomes the mixing. For a further increase in pulsation frequency there is no further improvement. One may also conclude that increasing the flow rate will have the same effect on the vortex swirl-strength. Again the (\times)-symbols indicate the onset for the 5% weakest and the 5% strongest vortices. Simply by looking at the movement of this onset for the 5% strongest vortices one may estimate the increase in swirl-strength to around 50% (from around 0.05 to 0.075 in figure 15) when the pulsation frequency is turned on or alternatively the flow rate is increased.

The vortices corresponding to $\pm 0.5\%$ of the PDF peak value are shown in figure 16, where one may conclude (i) again that the CW and CCW vortex rotations are more or less equally represented, (ii) that the distribution of the strongest vortices are fairly homogeneous, specially for $Q = Q_1$, and (iii) that the number of strong vortices increases drastically when turning on the pulsation frequency.

In summary, from this result it is clear that the vortices contributing to an improved mixing originates from the shear-layer instability and role-up of vortices, since this process of vortex role-up sets in at a subcritical Reynolds number, i.e. for $Q = Q_1$, with pulsation or alternatively at a overcritical Reynolds number, as for the $Q = Q_2$ case (see figure 15).

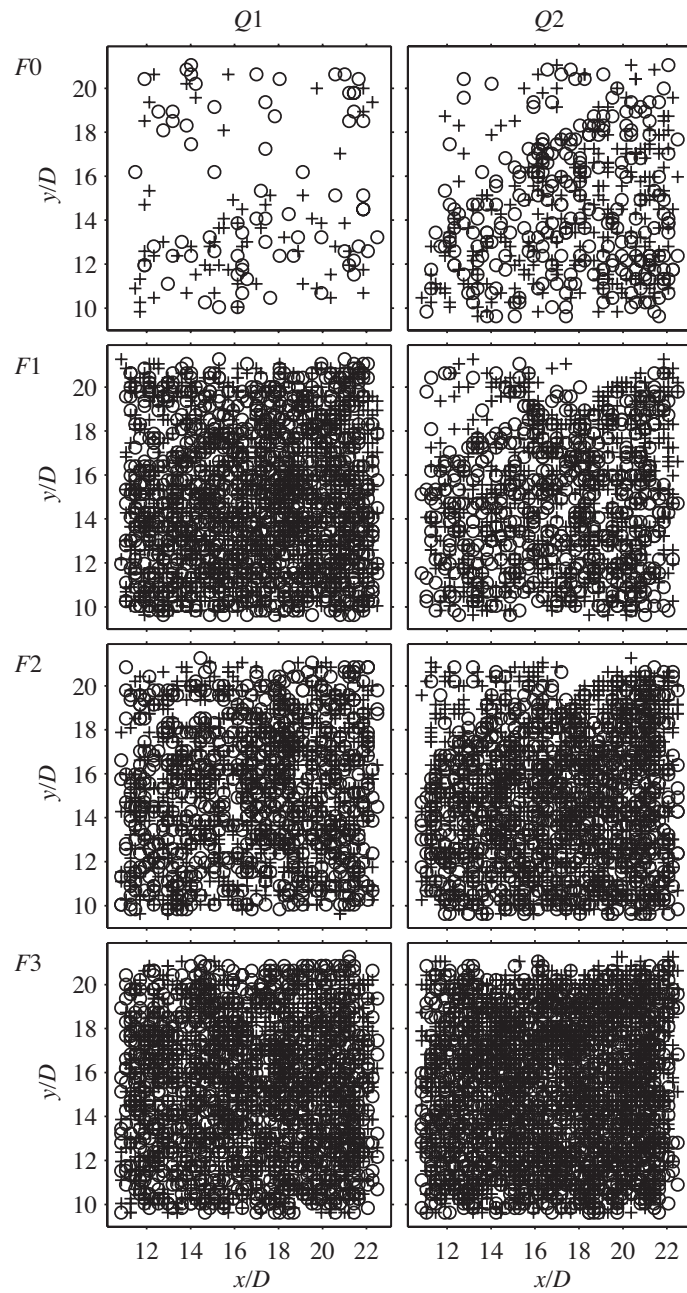


FIGURE 16. Vortices with a swirl-strength corresponding to $\pm 0.5\%$ of the PDF peak value. (\circ)- and ($+$)- symbols have CCW and CW rotational direction, respectively.

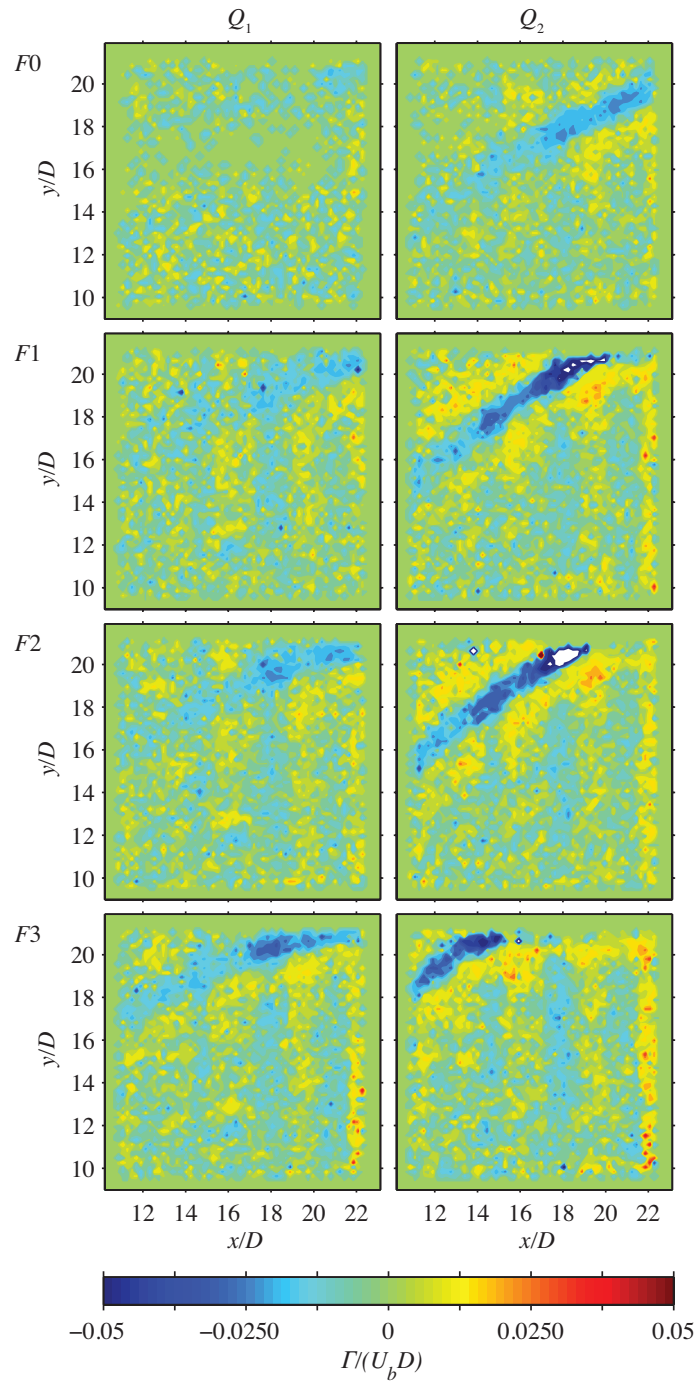


FIGURE 18. Distribution of the mean vortex circulation. The number of contour steps is 10 and to increase the resolution the limits are set to $\Gamma/(U_b D) = \pm 0.05$.

4. Summary and conclusions

The general approach in mechanical ventilation is to use a constant flow rate forced convection system providing the ventilation air. This type of ventilation may cause several problems such as draught and appearance of stagnation zones, which subsequently give rise to a low ventilation efficiency. An alternative to increase the ventilation quality is to introduce flow variations. The aim with the present study is to quantify the effect of pulsating inflow to a closed volume using the PIV technique. The experiments were performed in a small-scale water model.

We have shown that the wall-jet developing over the lower surface, as a result from the inlet jet to the closed volume, obeys the expected scaling from theory. The wall-normal distance scales with $\{x\nu/\bar{U}(x)\}^{1/2}$ and the experimental wall-jet profiles agree well with the Glauert wall-jet similarity solution.

For increasing pulsation frequency, while keeping the flow rate constant, there is a mean vorticity streak in the re-circulation region, which gradually increases in size and intensifies as the pulsation frequency is progressively increased. This is a favourable effect since the vorticity is directly related to mean velocity gradients and often rotational effects, which in turn implies an improved mixing. The streamline plots in the far-field indicate also an improved flow map considering the stagnation points. For increasing pulsation frequency the stagnation zones are reduced in size and their locations move in a favourable direction from a mixing point of view.

Regarding the small-scale vortex analysis we may conclude the following.

- The presence of small scale vortices is the first prerequisite of good mixing and is here shown to be fulfilled with a more homogeneous distribution of the vortices in the considered domain for an increase in pulsation frequency or alternatively in the flow rate (see figure 8).
- In comparison with the natural case without any pulsation frequency the number of vortices (all scales) increases by a factor of four as soon as the lowest pulsation frequency is turned on. Note that the number of vortices keeps increasing for a successive increase in pulsation frequency. At the highest pulsation frequency (*F3*) the number has increased by another 35% compared to the lowest (*F1*) (see table 2).
- A second prerequisite of good mixing is that a broad span of the diameter spectrum is present and that the rotational direction of the vortices are well balanced of CW versus CCW rotations. These two vortex statistics are shown to improve for an increase in pulsation frequency or alternatively in the flow rate. Figure 12 shows that vortices are present with diameters in the range $0.4 < d/D < 1$. The PDFs of the vortex circulation confirm that the CW and CCW vortex rotations are well balanced, since the PDFs are close to symmetric around $\Gamma = 0$ (see figure 17).

- A more homogeneous distribution of the most common vortex diameter is also obtained with an increase in pulsation frequency or alternatively in the flow rate. The broader vortex diameter PDF peak is clearly seen by looking at the PDFs directly, as in figure 12. One may also observe that there are two dominating vortex sizes, since there are two peaks in the PDFs. The most frequently appearing vortex size is about $0.6D$ and the second one is around $0.8D$.
- Regarding the vortex swirl-strength we can estimate an increase of about 50% when the pulsation frequency is turned on or alternatively the flow rate is increased.

In summary, from these results we conclude that the vortices contributing to an improved mixing originates from the shear-layer instability and role-up of vortices, since this process of vortex role-up sets in at a subcritical Reynolds number, i.e. for $Q = Q_1$, with pulsation or alternatively at a overcritical Reynolds number, as for the $Q = Q_2$ case. With a pulsating inflow the role-up of vortices in the shear layer strengthens. Furthermore, the results tell us that the positive effect for enhanced mixing by increasing the flow rate can equally be accomplished by applying a pulsating inflow.

Acknowledgements

BEGF and JHMF would like to acknowledge the financial support from the Göran Gustafsson Foundation and the Swedish Research Council (VR). Within the framework of the research AS did the measurements at the Department of Mechanics, KTH. We would like to thank Tekn. L. Shahab Shahinfar, Dr. Hans Wigö, Mr. Göran Rådberg and Mr. Joakim Karlström for their help with the experimental setup.

References

- ADRIAN, R. J., CHRISTENSEN, K. T. & LIU, Z.-C. 2000 Analysis and interpretation of instantaneous turbulent velocity fields. *Exp. Fluids* **19**, 275–290.
- AGRAWAL, A. & PRASAD, A. 2002 Properties of vortices in the self-similar turbulent jet. *Exp. Fluids* **33**, 565–577.
- CHONG, M. S., PERRY, A. E. & CANTWELL, B. J. 1990 A general classification of three-dimensional flow fields. *Phys. Fluids* **2**, 765–777.
- FALLENIOUS, B. E. G. 2009 A new experimental setup for studies on wake flow instability and its control. TRITA-MEK Tech. Rep. 2009:05. Licentiate Thesis, KTH, Stockholm.
- KUNDU, P. K. & COHEN, I. M. 2008 *Fluid Mechanics*, 4th edn. Academic Press, Elsevier.
- SANDBERG, M. & ELVSÉN, P. 2004 Rapid time varying ventilation flow rates as a mean of increasing the ventilation efficiency. *ROOMVENT, 9th International Conference on Air Distribution in Rooms, Sept. 5–8, Coimbra, Portugal*.
- ZHOU, J. ADRIAN, R. J., BALACHANDAR, S. & KENDALL, T. M. 1999 Mechanisms for generating coherent packets of hairpin vortices in channel flow. *J. Fluid. Mech.* **387**, 353–396.

Paper 3

3

Vortex analysis in the wake of a porous cylinder subject to continuous suction or blowing

By Bengt E. G. Fallenius and Jens H. M. Fransson

Linné Flow Centre, KTH Mechanics, SE-100 44 Stockholm, Sweden

Wake flow effects behind a porous cylinder subject to varying levels of continuous suction or blowing have been investigated using particle image velocimetry (PIV). Due to large mean flow changes in the wake, but with opposite trends when suction and blowing are applied, the location of interesting events, such as the mean confluence point of the twin-vortices and the position of maximum back-flow, move and consequently two different PIV-frames were investigated for the suction and the blowing cases. This limits the analysis to relative comparisons with the natural case, i.e. without suction or blowing applied. For moderate levels of suction and blowing (less or equal to 6.5% of the free stream velocity), suction can completely suppress the boundary layer growth and the flow becomes *potential-like* around the cylinder. Blowing gives the opposite effect with an increase of the wake size, which has been quantified by means of vortex formation length measures. The Reynolds number is around 3.5×10^3 implying that the wake flow is turbulent with a wide range of vortex sizes and intensities. It is shown that streamwise streaky regions with induced secondary vortices from the primary von Kármán vortices are present. In general, the secondary vortices are smaller, weaker and of opposite rotational direction compared to the primary ones. The streamwise streaky regions are reduced in their streamwise extent and move towards the shoulders of the cylinder, when suction is increased. Blowing has the opposite effect but experiences an interesting change in trend for high enough blowing levels, i.e. the smaller vortices become the strongest ones. This is suggested to be a result of the energy transfer from the primary to the secondary vortices.

1. Introduction

The phenomenon of periodic vortex shedding behind bluff bodies is of direct relevance to many practical and industrial applications, such as in telecom masts, aircraft and missile aerodynamics, civil and wind engineering, marine structures, and underwater acoustics. It is well known that this periodic vortex shedding can lead to devastating structural vibrations that finally lead to material fatigue and structural failure.

The vortex shedding instability, in the wake behind bluff bodies, is a self excited oscillation that will set in even if all sources of noise are removed (see Gillies 1998), and can be shown to be attributed to the local stability property of the two-dimensional mean velocity wake profile behind a bluff body. Monkewitz (1988) identified a sequence of stability transitions by using a family of wake profiles, that resulted in $Re_C < Re_A < Re_K$, where Re_C (≈ 5), Re_A (≈ 25), and Re_K (≈ 47) are critical Reynolds numbers that mark the onset of convective, absolute, and von Kármán shedding instability, respectively. This sequence was in fully agreement with the qualitative model predictions by Chomaz *et al.* (1988) the same year. The onset of the global von Kármán shedding mode occurs via a so-called supercritical Hopf bifurcation (see e.g. Provansal *et al.* 1987). For a review on the stability properties of open flows in general the interested reader is referred to Huerre & Monkewitz (1990), and for reviews on cylinder flows in particular see e.g. Williamson (1996); Buresti (1998); Norberg (2003); Zdravkovich (1997, 2003).

The wake flow behind circular cylinders have been studied thoroughly the last century and lately also different methods to control its instability. Both passive and active control methods have successfully been applied. Here, the distinction between passive and active control methods is made based on whether the energy in the flow system is used for the control or if energy has to be added to the system in order to obtain the control. Examples of passive and active control methods are for instance, splitter plates or obstacle placements in the very near wake, and base-bleed or cylinder vibrations, respectively. Below a brief review of different control methods, that have been applied on circular cylinders, is given.

A simple passive control method is to place a thin splitter plate aligned in the streamwise direction on the centreline of the near wake (see Roshko 1955, 1961). For a specific length of the splitter plate the sinuous von Kármán mode is altered for a varicose mode that causes a pair of twin-vortices to be formed, one on each side of the plate. More recently, Grinstein *et al.* (1991) carried out numerical simulations on the effect of an interference plate in the wake of a plate and found that the base pressure coefficient could decrease by a factor of 3 depending on the length of the plate and its separation from the base.

Experiments on circular cylinders with forced rotary oscillations have shown to give a drag reduction of up to 80% at $Re = 15 \times 10^3$ for certain ranges of frequency and amplitude of the sinusoidal rotary oscillation (see Tokumaru & Dimotakis 1991). Shiels & Leonard (2001) performed numerical simulations of this control approach where the above experimental findings were verified and showed indications that this kind of control could be even more efficient at higher Re .

A rotating circular cylinder with a constant angular frequency can also suppress the vortex shedding, but due to an increased shearing mechanism

for even higher rotation speeds a second mode appears and the drag starts increasing again. At high enough rotation speeds the second mode will also be suppressed by the rotation (see e.g. El Akoury, Braza, Perrin, Harran & Hoarau 2008). Moreover, El Akoury *et al.* were able to show that a constant angular frequency is able to attenuate the secondary instability related to the spanwise undulation and therefore increase the critical Reynolds number for shear layer transition of the wake.

Control approaches using feedback control have also been attempted. Rousopoulos (1993) carried out experiments in a wind tunnel with acoustic waves from a loudspeaker as actuation as well as by vibrating the cylinder. In a numerical study by Park *et al.* (1994) blowing and suction through slots on the rear part of the cylinder were utilized as actuation. However, this investigation were performed at relatively low Reynolds numbers (< 300) and so far it does not exist any results on higher Re -flows.

Glezer & Amitay (2002) used synthetic jets, which provide a localized addition of momentum normal to the surface, on selected positions over the cylinder in order to delay separation in both laminar and turbulent boundary layers. They argued that this delay was caused by increased mixing within the boundary layer. In addition, the interaction between the jet and the cross flow has a profound effect both on the separated shear layer and on the wake; the magnitude of the Reynolds stresses is reduced indicating that the delay in separation is not merely the result of a transition to turbulence in the boundary layer.

Experiments with suction or blowing through the entire surface of the cylinder in order to control the vortex shedding have been considered by e.g. Pankhurst & Thwaites (1950); Hurley & Thwaites (1951); Mathelin *et al.* (2001*a,b*); Fransson *et al.* (2004). Pankhurst & Thwaites (1950) made combined experiments with continuous suction through the surface and a flap in form of a short splitter plate at different angles. They showed through surface pressure and wake velocity measurements that with the flap directed in the streamwise direction and for sufficient suction¹ ($C_q\sqrt{R} \gtrsim 10$) the separation is entirely prevented and a remarkable close approximation to the potential flow solution is achieved. Furthermore, Hurley & Thwaites (1951) performed boundary layer measurements on the same porous cylinder and found in general good agreement with laminar boundary layer theory. However, no time resolved measurements to determine the vortex shedding frequency were reported.

The von Kármán frequency is Reynolds number dependent, whilst the dimensionless frequency known as the Strouhal number is constant (≈ 0.2) in the range $10^2 \lesssim Re \lesssim 10^5$. Mathelin *et al.* (2001*a,b*) considered the case of continuous blowing through the entire cylinder surface (see Mathelin *et al.* 2001*a*,

¹Here C_q is a suction coefficient defined as the suction velocity per unit area divided by the free stream velocity.

for a detailed description of the experimental setup). Among the effects observed are a wider wake and a decrease of the Strouhal number with increasing blowing. They report an analytical relation of an equivalent Reynolds number of the canonical case, which produces the same flow characteristics in terms of vortex shedding instability as the case with blowing versus the blowing rate. The result is that the Strouhal number decreases with blowing, which was experimentally verified by Fransson *et al.* (2004), who also considered the effect of continuous suction, which turns out to have the contrary effect on the Strouhal number. In Fransson *et al.* (2004) the changes in the flow due to blowing or suction were analyzed in terms of mean and fluctuating velocity profiles in the wake through hot-wire anemometry, pressure distributions on the cylinder, and drag and vortex shedding measurements. Furthermore, smoke visualizations of the flow field in the near wake of the cylinder for different blowing or suction rates were reported. Image averaging enabled the retrieval of quantitative information, such as the vortex formation length, which showed that the vortex formation length is decreased by 75% and increased by 150% for 5% of suction and blowing of the free stream velocity, respectively.

In this study the effect of continuous suction or blowing through the entire surface of a porous cylinder has been investigated with the emphasis on vortex statistics in the wake of the cylinder, which complements above cited works on porous cylinders. Vortex analysis, apart from the Kármán vortices, can only be performed with an instantaneous flow field measurement technique and here a two-dimensional Particle Image Velocimetry (PIV) system has been used. As stated above it has previously been shown that suction and blowing of continuous type have a large impact on the mean velocity field and consequently the drag force, but has not given any information about the effect on the individual vortices and small scale structures. The Reynolds number is around 3.5×10^3 , which is in the subcritical regime (cf. Roshko 1961), implying laminar boundary layers around the cylinder with a purely laminar separation and a turbulent wake with a wide range of both vortex sizes and strengths.

The present paper has the following outline, in section 2 the experimental setup and measurement technique is reported, which is followed by a summary of the applied vortex detection program in section 3. In section 4 the results are presented and the paper ends with a summary and conclusion section (5).

2. Experimental setup and measurement technique

2.1. Wind tunnel

The experiments were performed in the BL wind tunnel² at KTH Mechanics, Stockholm. The cross sectional area of the test section is $0.5 \times 0.75 \text{ m}^2$, and it is 4.2 m long with a maximum speed of 48 m s^{-1} . The flow quality in this tunnel is considered good with a turbulence intensity (of all three components) of less

²Boundary Layer or Björn Lindgren named after its designer.

than 0.04% of the free stream velocity. The tunnel has a heat exchanger after the fan, prior to the first corner. At 25 m s^{-1} the temperature variation over the cross section area is less than $\pm 0.07 \text{ }^\circ\text{C}$ and the variation over a time period of 4 hours is less than $\pm 0.03 \text{ }^\circ\text{C}$. At this speed the total pressure variation is less than $\pm 0.1\%$. The tunnel was successfully designed with expanding corners (larger outlet than inlet cross section area) in order to reduce the total wind tunnel circuit length with only a negligible increase of the total pressure loss. The interested reader is referred to Lindgren (2002) for further details.

2.2. Cylinder

The same porous cylinder as was used by Fransson *et al.* (2004) for flow visualisation was used in the present investigation. The cylinder consists of a cross profile made of brass as an inner skeleton. A sintered plastic material shaped to a cylinder is then slid over the brass profile and sealed, creating four isolated chambers through where different amount of blowing or suction may be applied. The end parts were made of brass pieces and act as plugs on each side of the cylinder. These were equipped with four inlets for tube connections that were confluent before connected to a flow meter (rotameter type). Tubing was also used to lead air to or from a low or high pressure vessel, respectively, depending on whether suction or blowing was desired. The pressure source was either a regular vacuum cleaner, for suction, or a compressor, for blowing.

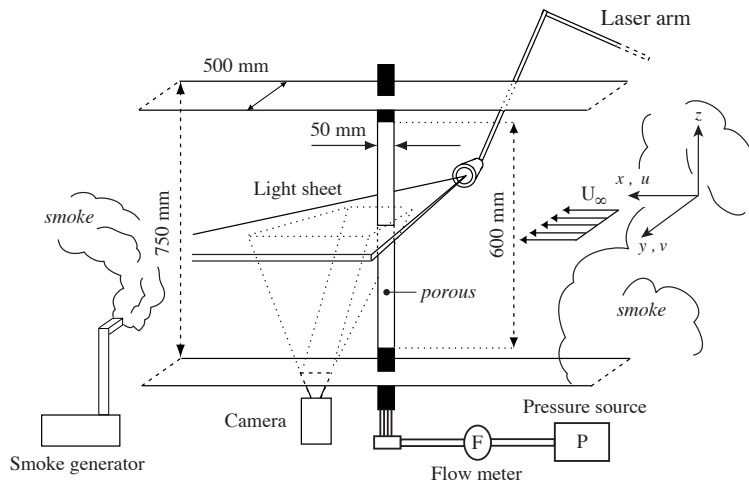


FIGURE 1. Schematic of the experimental setup. Flow is from right to left.

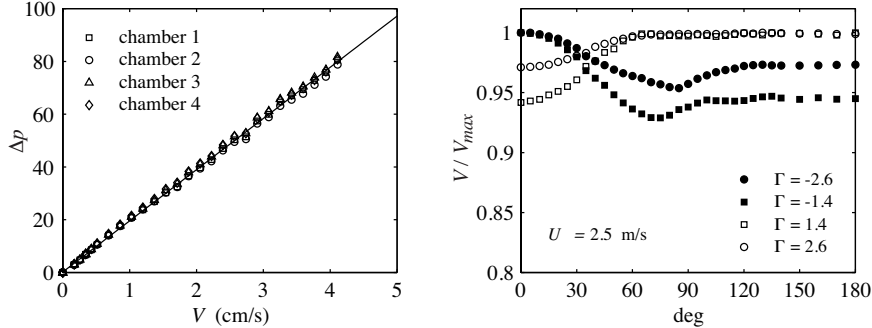


FIGURE 2. (a) Permeability determination of the porous material (repeated for all chambers). Solid line is the best fit to all data. (b) Suction/blowing distribution due to the static pressure variation around the circumference of the cylinder.

In figure 1 a schematic of the experimental setup is shown with relevant measures. The cylinder was mounted vertically in the test section and has a diameter of $D = 50$ mm and a porous length of 600 mm. The porous material is a sintered plastic material with an average pore size of $16 \mu\text{m}$, and the thickness (t) is 2.5 mm. Previous surface roughness measurements on a similar but flat porous plate (see Fransson & Alfredsson 2003) showed a deviation of $\pm 1 \mu\text{m}$ from the mean surface, which for the present case can be considered to be hydraulically smooth. The cylinder is made from a flat plate which is bent to form a circular cylinder. This means that there is a joint in the axial direction along the full length of the cylinder, and this gives rise to a small asymmetry with a 0.5 mm larger diameter in average when measured over the joint. The joint is therefore positioned at 180° , i.e. behind the cylinder in the streamwise direction, in order to avoid any flow asymmetry.

The rate of suction or blowing is quantified by the parameter $\Gamma = V_0/U_\infty \times 100$, where V_0 is the velocity through the cylinder surface and U_∞ is the free stream velocity. Throughout this investigation the free-stream velocity was set to $U_\infty = 1 \text{ m s}^{-1}$. Negative and positive values of Γ are associated with suction and blowing, respectively. To determine the permeability of the material the pressure difference (Δp) over the cylinder wall and the flow rate $Q = V \times S$, where V and S are the velocity through the porous material and the surface area, respectively, were measured, when suction was applied. Through Darcy's law the permeability (κ) is then determined to be $\kappa = \mu t V / \Delta p = 2.31 \times 10^{-7} \text{ m}^2$, by means of a least square line fit to the data (μ is the dynamic viscosity), see figure 2(a). Once the cylinder is mounted inside the testsection a non-uniform suction/blowing rate is expected in the circumferential direction of the cylinder surface since the static pressure on the cylinder surface varies when

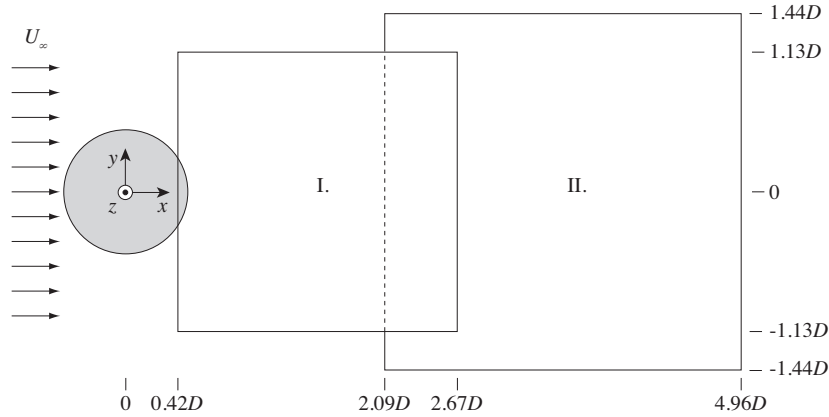


FIGURE 3. The position of the image frames and their coordinates in the PIV measurements for the suction case (I) and the blowing case (II).

exposed to an oncoming flow and the fact that the tubing from the different chambers are conflued before connected to the pressure source. However, the influence can be shown to be rather small. For the suction case the largest suction velocity occurs along the front stagnation line and then it decreases towards the rear. In the separated region the suction velocity is fairly constant and for a suction rate of 1.4% of the free stream velocity the suction velocity is reduced by about 6% smaller in this region as compared to the front. For larger suction rates the difference becomes smaller. In contrast, for the blowing case the smallest injection velocity is along the frontal stagnation line and then increases and becomes constant beyond 65° . In this case the maximum variation is less than 7% and the variation decreases with increasing blowing rate, see figure 2(b).

2.3. Measurement technique

For the velocity measurements a Particle Image Velocimetry (PIV) system was used in order to allow entire flow fields to be captured instantaneously. The PIV-system used consists of a Spectra Physics 400 mJ double pulsed Nd:Yag laser operating at 15 Hz as a light source, and the camera is a double-frame Kodak ES1.0 8-bit CCD camera with 1018×1008 pixels. Furthermore, a laser arm was connected to the laser, which facilitates traversing of the laser sheet. The air was seeded with smoke particles generated by heating a glycol based liquid with a disco smoke generator, JEM ZR20 Mk II. The smoke inlet to the tunnel was in the open cross section between the end of the test section and the diffuser. Before the measurements the smoke was recirculated in the tunnel until the air became homogeneously seeded. See figure 1 for an illustration.

Since the location of the events of interest in the wake changes depending on the rate of suction or blowing applied through the cylinder surface the frame location of the PIV-images had different positions and sizes depending on the sign and level of Γ . Figure 3 shows the two frames where frame I starts by overlapping the cylinder at $x = 0.42D$ and stretches up to $x = 2.67D$ with $y = \pm 1.13D$. Frame II starts at $x = 2.09D$ and ends at $x = 4.96D$ with $y = \pm 1.44D$. The latter is slightly larger due to the wake growth, and the two regions were chosen so that they would capture the position of maximum backflow in their respective cases.

In the post-processing of the measured data conventional validation criteria were applied. Displacements of the particles larger than 25% of the interrogation area length was not allowed, in order to avoid low-velocity bias due to loss-of-pairs. This criterion is set before the measurements by choosing the appropriate time between the two consecutive captured images. Furthermore, spurious measurement errors were eliminated by applying a Peak-Value-Ratio (PVR) of 1.2, implying that the ratio of the highest to the second highest peak in the cross-correlation is not allowed to be smaller than 1.2. The images were divided into 32×32 interrogation areas with a 50% overlap, which after the post-processing results in a vector field with 62×62 velocity vectors with a grid spacing of 1.85 mm.

3. Vortex detection methodology

A vortex detection algorithm was developed in order to examine the effect on small-scale structures in the wake behind the porous cylinder when subjected to different levels of suction or blowing. Several different methods for detecting vortices are available and a review and comparison of the most common ones is found in Jeong & Hussain (1995). In this study they reported on the λ_2 -method, which is shown to be the most appropriate method to detect vortices in a velocity field. The λ_2 -method has been widely accepted since its introduction and has been implemented, as a post-processing option, into many numerical codes. However, for the λ_2 -method to be used properly, the Hessian of the pressure, i.e. all three components of the velocity gradient tensor, has to be known. This implies that the velocity vector has to be known in the entire flow volume, which experimentally is unfeasible.

From two-dimensional velocity fields, as in PIV-measurements, Adrian *et al.* (2000) showed that by applying a high-pass filter on the full velocity field the small-scale velocity structures are revealed. Vortices were then detected through a two-dimensional version of the Δ -method proposed by Chong *et al.* (1990). This method is based on the search for complex eigenvalues of the velocity gradient tensor, which implies that the streamlines have closed circular paths around the vortex core and is here used as the definition for a vortex. The same methodology will be used in the following.

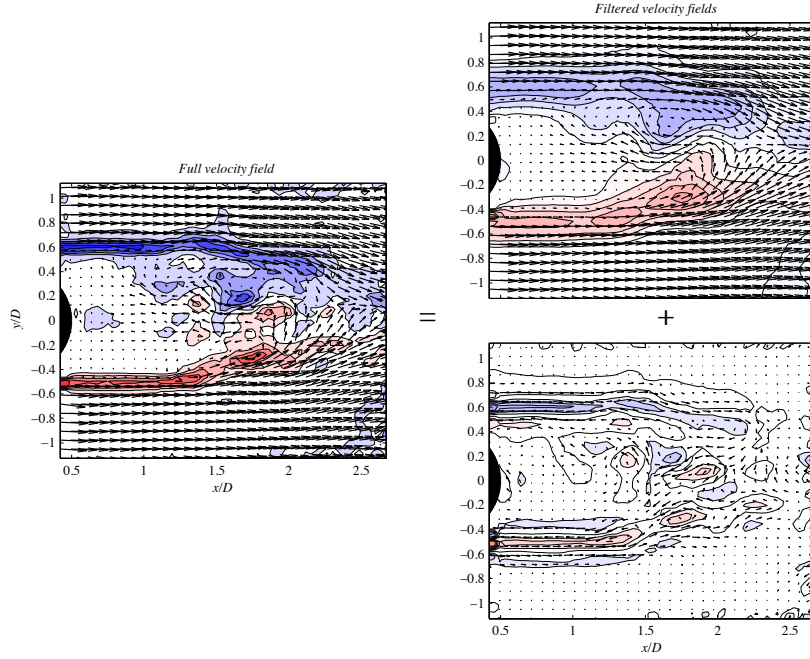


FIGURE 4. (a) An instantaneous velocity field (\mathbf{u}) behind a porous cylinder with continuous suction through the surface of 2.6% of the oncoming velocity. (b) and (c) show the low-pass ($\bar{\mathbf{u}}$) and high-pass (\mathbf{u}'') filtered velocity fields, respectively.

3.1. Decomposition of the velocity field

The high-pass filtering of the full velocity field, \mathbf{u} , is performed by convolving a low-pass filter on \mathbf{u} . This low-pass filtered velocity field, $\bar{\mathbf{u}}$, is then subtracted from the full velocity field, which consequently gives the high-pass filtered velocity field \mathbf{u}'' . The decomposition may be written as,

$$\mathbf{u}'' = \mathbf{u} - \bar{\mathbf{u}}, \quad (1)$$

which is illustrated in figure 4. Here, an instantaneous velocity field behind the porous cylinder subject to a suction velocity of 2.6% of the freestream velocity has been decomposed. In figure 4(a) the full velocity field is shown and in (b) and (c) the large scale and small-scale velocity fields are depicted, respectively.

In accordance with Agrawal & Prasad (2002), a Gaussian filter that averages the single (m, n) -point with the surrounding points is used for the decomposition, so that

$$\bar{\mathbf{u}}(m, n) = \frac{\sum_{j=-k}^k \sum_{i=-k}^k g(i, j) \mathbf{u}(m-i, n-j)}{\sum_{j=-k}^k \sum_{i=-k}^k g(i, j)}, \quad (2)$$

where (i, j) is the step in x and y , respectively, and k is the *radius*. The Gaussian kernel (g) is defined as

$$g(i, j) = \exp \left[-\frac{(i\Delta x)^2 + (j\Delta y)^2}{2\sigma^2} \right], \quad (3)$$

where Δx and Δy are the grid spacing and σ is the padding of the filter. The parameters k and σ were chosen by introducing an anisotropy measure d_{rms}^2 of the \mathbf{u}'' -field, which is defined as the absolute value of the normalised difference between the velocity variance components,

$$d_{rms}^2 = \left| \frac{u_{rms}^2 - v_{rms}^2}{U_\infty^2} \right|. \quad (4)$$

The maximum value of d_{rms}^2 is compared for varying combinations of k and σ , and $\max\{d_{rms}^2\} \leq 0.01$ was decided to be a suitable criterion after field inspections. In this way the filter parameters can be chosen in a consistent manner and with a qualitative measure of the filter strength. For the present flow field analyses both k and σ were chosen to be equal to 5. Figure 5(a) shows the contours of $d_{rms,max}^2$ for the natural case ($\Gamma = 0$) for different filter

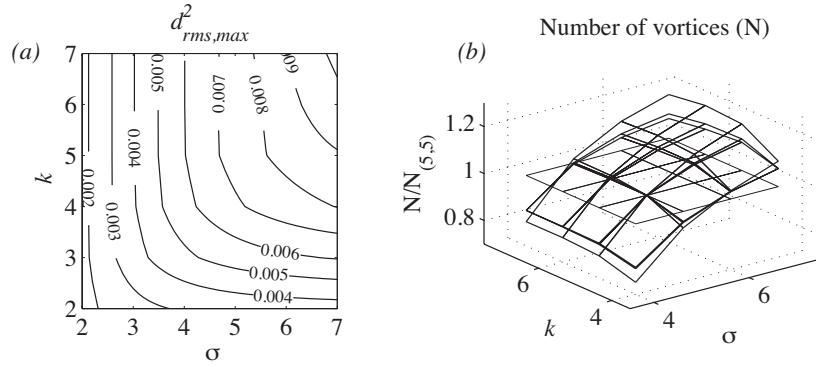


FIGURE 5. (a) The maximum value of the anisotropy measure d_{rms}^2 for different values of k and σ for the natural case $\Gamma = 0$ and (b) the number of vortices for scaled by the number of vortices for the chosen parameters $k = \sigma = 5$ for the cases $\Gamma = [0, -2.6, -5]$.

parameters along with the a surface plot of how the number of vortices varies with different filter settings for the cases $F = [0, -2.6, -5]$ in figure 5(b).

3.2. Detection of vortices

As previously stated, the vortex definition and detection method by Chong *et al.* (1990) is here used to detect the small-scale vortices. It amounts to identify regions where the eigenvalues of the two-dimensional high-pass filtered velocity gradient tensor,

$$\nabla \mathbf{u}''_{2D} = \begin{bmatrix} \frac{\partial u''}{\partial x} & \frac{\partial u''}{\partial y} \\ \frac{\partial v''}{\partial x} & \frac{\partial v''}{\partial y} \end{bmatrix}, \quad (5)$$

are complex. The eigenvalues of $\nabla \mathbf{u}''_{2D}$ are either real or complex conjugate and consequently vortices can easily be identified by plotting contours of the regions where the imaginary part λ_{ci} of the eigenvalues are positive. A threshold level is required to have a distinct and reasonable boundary between the vortices. The value of the chosen threshold level was found by studying the output of the vortex identification at different levels. Plotting contours of $\lambda_{ci} = 15$ turned out to be a good choice to distinguish vortices with reasonable boundaries in these particular wake flow measurements.

An additional criterion for the vortex detection is proposed in Chakraborty *et al.* (2005), where also the *inverse spiralling compactness* is considered. This is defined as the ratio between the real and imaginary part of the eigenvalue $\lambda_{cr}/\lambda_{ci}$, which measures the local compactness of the particle trajectory. A ratio equal to zero corresponds to a circular path in the plane of the vortex. A positive value means that the particle orbit will spiral outwards in the plane of the vortex, implying that the structure cannot be considered coherent in the plane if the ratio becomes too large. If the ratio is negative the particle spirals inwards and fulfills the vortex plane compactness. On the other hand for too large negative ratios the vortex would violate the compactness along the vortex axis. In order to exclude vortices with a particle path that rapidly spirals out- or inwards in the vortex plane or along the vortex axis, we introduce the criterion

$$\left| \frac{\lambda_{cr}}{\lambda_{ci}} \right| \leq 0.1, \quad (6)$$

on all identified vortex structures as suggested by Chakraborty *et al.* (2005).

3.3. Vortex statistics

For each instantaneous velocity field image the vortices are first identified and then their position, size, strength and circulation are determined. These vortex parameters are stored for statistical analyses before the next instantaneous velocity field is being processed.

The position within each identified region, where the highest λ_{ci} is found determines the centre of the vortex expressed in the discrete coordinates x and y . The highest eigenvalues in each region is also, per definition, the swirl strength of the vortex, (see e.g. Zhou *et al.* 1999). Furthermore, the area of the contour region containing the imaginary eigenvalues is calculated, and a circle C around the vortex centre with an equivalent radius to this area is used as a starting point for calculating the circulation γ . This is done through direct integration along C 's perimeter \mathbf{l} according to

$$\gamma = \oint_C \mathbf{u}'' \cdot d\mathbf{l} . \quad (7)$$

The calculation of the circulation is repeated for a continuous stepwise increase in the radius until the value of the circulation has saturated. This radius is defined as the vortex radius and its corresponding diameter will be denoted d_γ from here on. A further increase of the radius in the calculation of γ would eventually give a $d\gamma/dr$ with opposite sign simply indicating that one has entered a neighboring vortex.

4. Experimental results

In the following the results of the vortex analysis in the wake of a porous cylinder are shown. Vortex parameters such as vortex position, size, strength and circulation are reported for different levels of suction and blowing through the cylinder surface. The number of PIV-image pairs along with the number of identified vortices for suction and blowing cases in the two frames are presented in table 1. A relatively high number of samples have been collected for different levels of suction and blowing, which makes the statistical comparison reliable. The number of vortices within parenthesis is the number of vortices detected without the criterion (eq. 6) for inverse spiralling compactness, described in section 3.2. Figure 6 shows the distribution of the ratio $\lambda_{cr}/\lambda_{ci}$ for the detected vortices in all cases.

As described in section 2.3, the frame of interest depends on the level and sign of Γ , a direct comparison between the effect of suction and blowing is not possible except for $\Gamma = 0, \pm 0.7, \pm 1.9$ and ± 2.6 . For other values of Γ the study is limited to relative changes from the reference case at $\Gamma = 0$ in the two different frames.

An example of an instantaneous velocity field for the natural case ($\Gamma = 0$) along with a case where suction is applied through the cylinder surface ($\Gamma = -5$) is shown in the upper left part of figure 7, frame I. The lower part in this figure the positions where $U < 0$, which indicates the presence of back-flow, are marked with (+)-symbols for the two cases. Figure 7, frame II, shows similar instantaneous velocity fields, but for the blowing case. The instantaneous back-flow figures are representative for their respective cases. In the suction case

| near wake | | | far wake | | |
|-----------|-----------|-----------------|----------|-----------|-----------------|
| Γ | no. of IP | no. of vortices | Γ | no. of IP | no. of vortices |
| 2.6 | 1086 | 5175 (13955) | | | |
| 1.9 | 1054 | 7981 (18961) | | | |
| 0.7 | 1086 | 8259 (22285) | | | |
| 0 | 1054 | 5121 (13122) | 0 | 1022 | 3877 (11587) |
| -0.7 | 1054 | 7407 (19943) | 0.7 | 1086 | 4555 (13323) |
| -1.4 | 1054 | 6881 (17996) | 1.4 | 1054 | 4065 (12005) |
| -1.9 | 1054 | 6234 (16494) | 1.9 | 1054 | 4477 (12942) |
| -2.6 | 1054 | 7200 (19273) | 2.6 | 1024 | 4548 (13384) |
| -3.2 | 1054 | 5873 (15030) | 3.2 | 1055 | 4882 (14996) |
| -3.9 | 1054 | 6944 (19109) | 3.9 | 1054 | 5210 (15706) |
| -5.0 | 1118 | 6881 (19503) | 5.0 | 1054 | 6158 (21189) |
| -6.5 | 401 | 1131 (3574) | 6.5 | 1054 | 5314 (17069) |

TABLE 1. The number of PIV-image pairs (IP) taken during the experiments and the number of detected vortices in each frame for different Γ . The numbers within parenthesis show the number of vortices detected for each case without the swirling compactness criterion (eq. 6) implemented.

one can see that the backflow-region moves closer to the cylinder while in the blowing case it moves away from the cylinder.

From these instantaneous images one can calculate the back-flow coefficient, χ , which is defined as the amount of time there is back-flow in a particular position in the flow field. A χ -value of 1 means that there is always back-flow in this position and 0 means the opposite. Figure 8, frame I and frame II, shows the mean velocity field, the back-flow coefficient and the standard deviation velocity field. One can here see how the region of back-flow decreases and increases for the suction and the blowing case, respectively. Furthermore, the white dot shows the location where the back-flow coefficient has its maximum.

In a mean perspective moderate levels of suction or blowing have a large impact on the wake. With suction the wake decreases in size and for Γ about -6 the flow around the cylinder becomes *potential-like* and hence the drag is significantly reduced compared to the natural case ($\Gamma = 0$). With blowing the *twin-vortices* in the wake, appearing in the mean velocity field, grow in size, which causes a large region of back-flow and consequently the drag increases. This was quantified by Fransson *et al.* (2004), where the drag coefficient was plotted versus Γ .

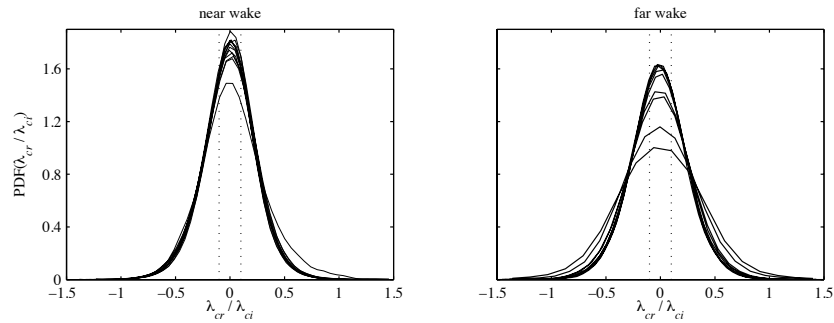


FIGURE 6. Probability density functions of the ratio between the real- and imaginary part of the complex eigenvalue of the velocity gradient tensor. (\cdots) indicate the chosen interval. The figures have been truncated at $\lambda_{cr}/\lambda_{ci} = \pm 1.5$, excluding 0.01% and 0.5 % of the data for the near and far wake, respectively.

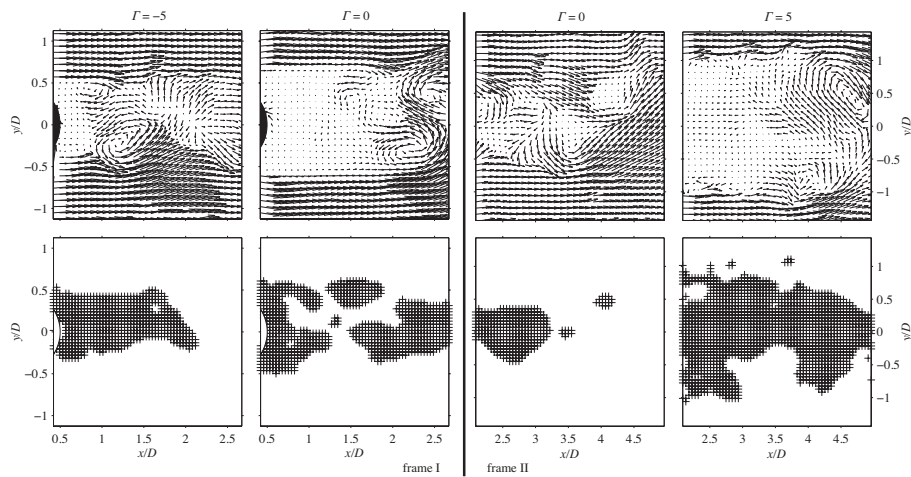


FIGURE 7. Instantaneous vector velocity fields (top row) and their corresponding back-flow coefficient maps (bottom row) for the natural case and when suction ($\Gamma = -5$) and blowing ($\Gamma = 5$) are applied.

The size of the wake may be quantified in various ways, such as the position of maximum χ (cf. the white bullets in figure 8 middle row), by the stagnation point in the wake, which corresponds to the confluence point of the two stationary *twin-vortices* (cf. the open square symbols in figure 8 top row),

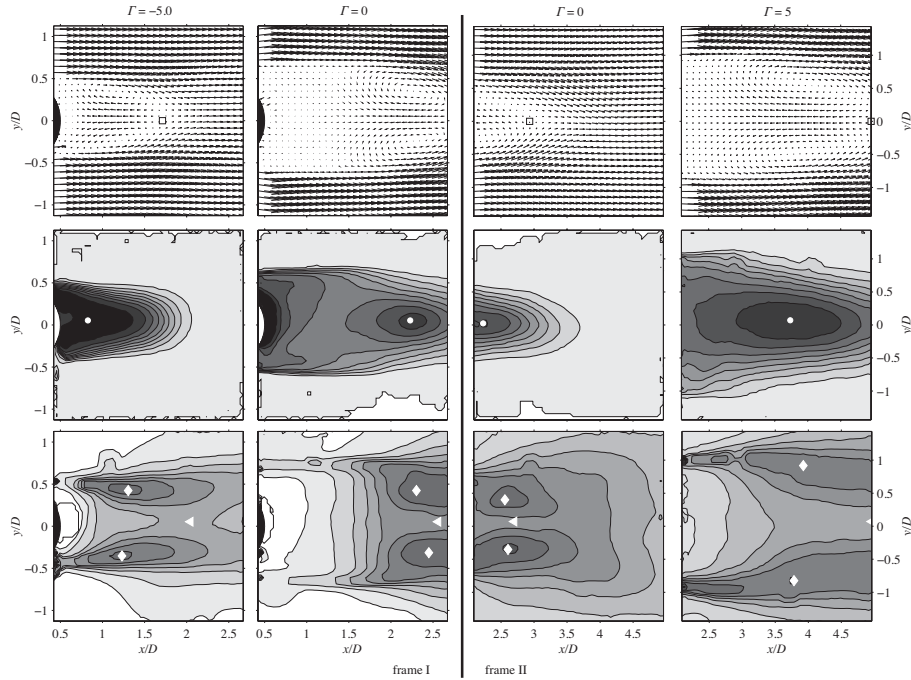


FIGURE 8. Mean vector velocity fields (top row), the back-flow coefficient maps (middle row) and the standard deviation velocity fields (u_{rms}/U_∞) (bottom row) for the natural case ($\Gamma = 0$) and when suction ($\Gamma = -5$) and blowing ($\Gamma = 5$) are applied. The filled contours correspond to an increment of 0.1 and 0.05 from 0 (white) to 1 (black), for the middle and bottom rows, respectively.

or by the maximum value of u_{rms} along the centreline, or, in the recirculation regions (cf. the white (\triangleleft)- and (\diamond)-symbols, respectively).

In figure 9 above measures of the vortex formation length are plotted versus Γ . From this figure it is clear that suction reduces the extent of the near-wake, and the maximum back-flow and the stagnation point measures decrease with 63% and 36%, respectively, from $\Gamma = 0$ to $\Gamma = -5$. In contrast, blowing increases the near-wake extension with 67% and 69%, respectively, from $\Gamma = 5$ to $\Gamma = 0$. Looking at the maximum u_{rms} along the centreline and in the recirculation regions, this gives corresponding values of 21% and 56% for the centreline and 49% and 24% for the recirculation regions, respectively. Here, we conclude that the different measures show the same trend and there is essentially only a vertical shift of the curves which makes the difference. Worth

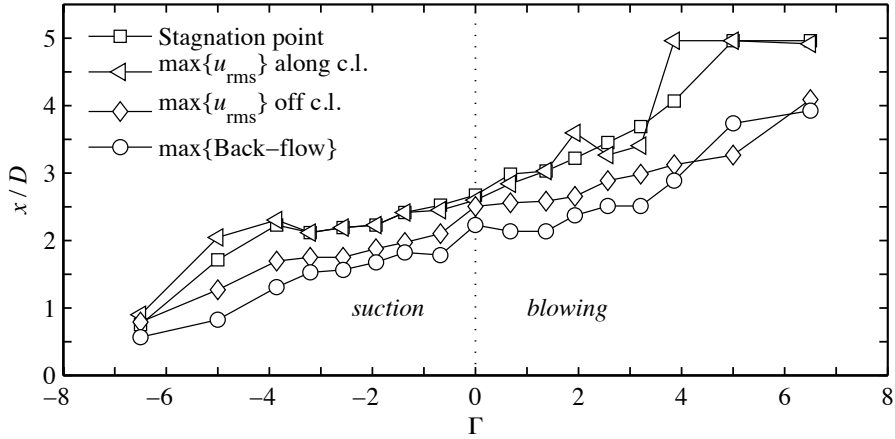


FIGURE 9. Four different measures of the near-wake extension as a function of the suction and blowing parameter. See text for the different measures.

pointing out is that the measure of stagnation point and maximum u_{rms} along the centreline falls almost on top of each other.

Having concluded that moderate levels of suction or blowing have a large impact on the mean velocity field around the cylinder, it is interesting to see how the vortices in the wake are affected. Starting with frame I, and followed by frame II, the statistics for the vortices will be presented.

4.1. Near wake: frame I

Location of vortices. In figure 10(a) the Probability Density Functions (PDFs) of the streamwise position of the detected vortices are plotted. The number of bins are 30, and the PDFs are normalised such that the area under the individual curves equals unity. Furthermore, to improve visibility the plotted curves have been smoothed by averaging each point with the neighbouring four points. Here one may observe that the position of maximum probability moves from about $x/D = 2.2$ downstream of the cylinder for $\Gamma = 0$ to about $x/D = 1.2$ for $\Gamma = -5$. It turns out that this position moves along with the position of maximum backflow (x_{BF}) in the wake. This is illustrated in figure 10(b), where x_{BF} from each suction rate has been subtracted from the streamwise position. The location of the maximum value of the PDFs are now close to zero, i.e. independent of the suction rate. At high levels of suction ($\Gamma \leq -5$), the wake almost disappears, and the result might differ from lower levels. In figure 10(a) low levels of blowing shows the opposite trend where the maximum value moves slightly downstream. For $\Gamma = 0$ the results for the

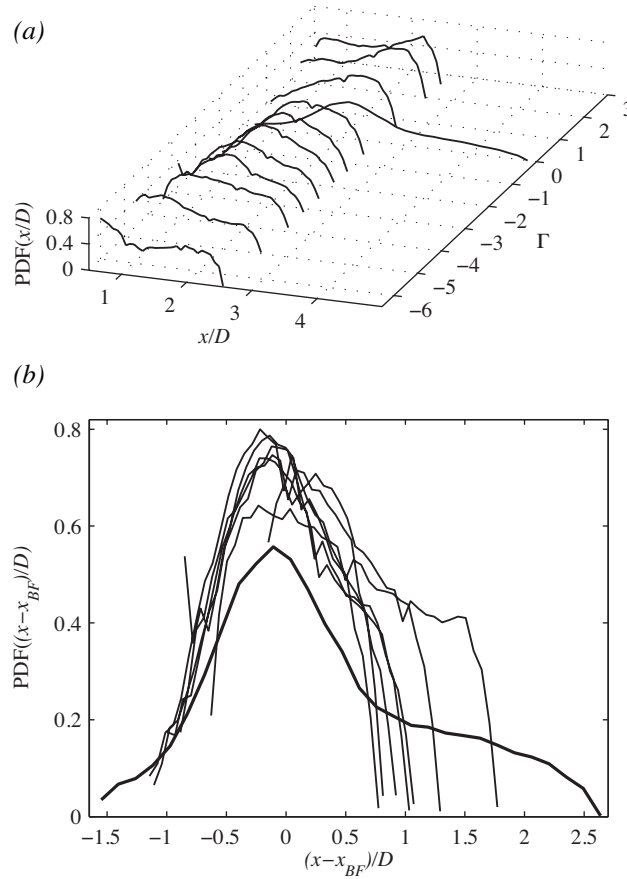


FIGURE 10. (a) PDFs of the streamwise position of vortices. (b) Same as in (a), but with the position of maximum backflow, x_{BF} , subtracted.

two frames, both the suction case (frame I) and the blowing case (frame II), have been combined, which shows that no other peaks are present. It should be noted that vortices close to the streamwise boundaries of the frame may be partly outside the frame and thereby disregarded by the vortex detection program. This causes the PDFs of the streamwise position of the vortices to end rather abruptly, especially for high levels of suction, which should be interpreted as a limitation of the detection program rather than the absence of vortices. Furthermore, to avoid spurious velocity vectors near the cylinder, the program detects vortices only for $x/D > 0.6$.

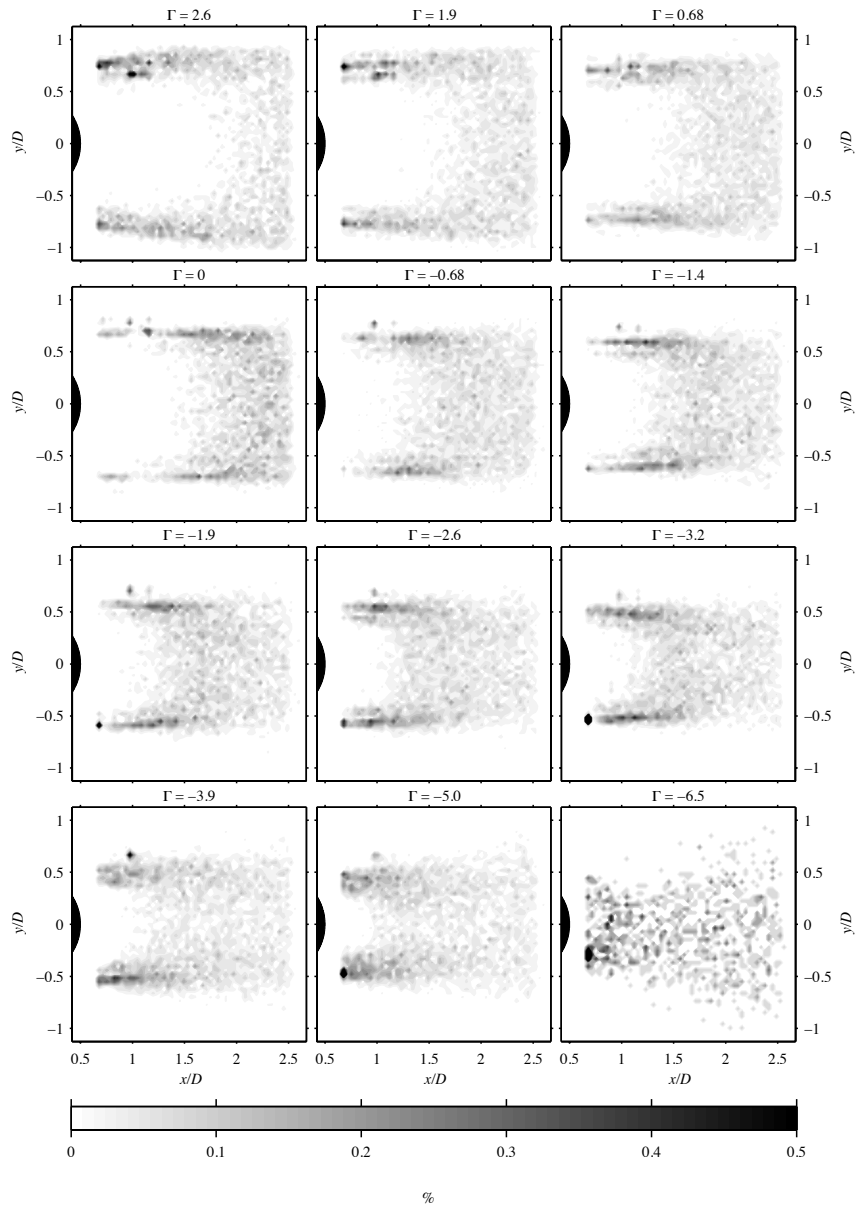


FIGURE 11. Percentage of the total number of vortices in each point where vortices are detected. The number of contour steps is 20.

While figure 10 indicates the probability for vortices to occur in a certain streamwise position, figure 11 shows the number of vortices in percentage of the total number of vortices in each point where vortices are detected. One can notice that most vortices pass along two streaky regions aligned with the streamwise tangents of the cylinder ($y/D = \pm 0.5$). The streaky regions seem to be divided into an inner and an outer streak with a larger amount of vortices in the outer one. Furthermore, when the cylinder is subjected to blowing, the streaks are inclined outwards and the vortices in the wake, which initially is quite uniformly distributed in the wake, are pushed downstream, while as suction is increasing, the vortices move from the centre of the wake towards two streaky regions, which then for higher levels of suction ($\Gamma < -5$) vanishes.

Vortex size. Figure 12 shows the PDFs of the vortex diameters d_γ , defined as the saturation value of the circulation when stepping out from the vortex core (cf. section 3.3). The number of bins used for each PDF is 50 and the plotted curves are normalised and smoothed as previously described. As seen in the figure, suction have little effect on the most common vortex diameter, which

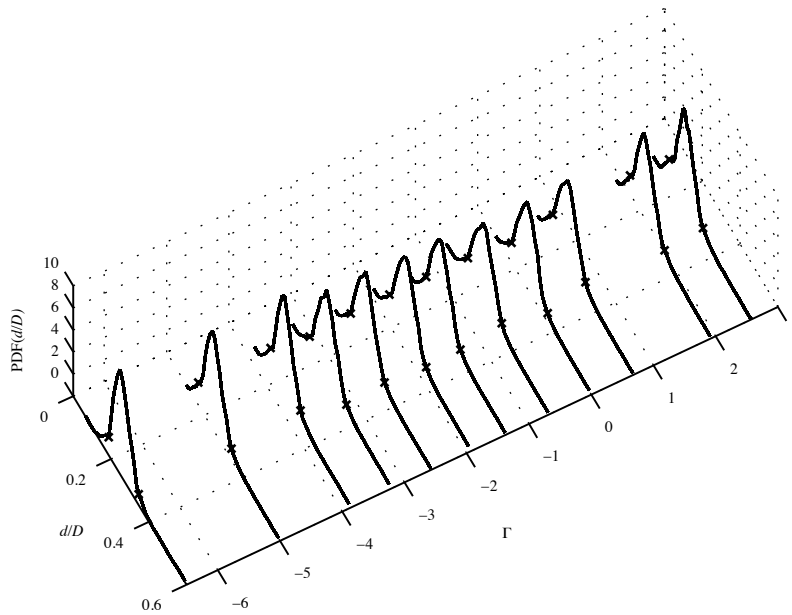


FIGURE 12. PDFs of the diameter of the vortices. (\times)-symbols mark the limits of the 5% smallest and 5% largest vortices. To improve visibility, the plots are truncated at $d_\gamma/D = 0.6$, disregarding at most 0.5% of the data.

in average over all suction cases is $0.25D$. The peaks in the blowing cases are shifted slightly to the left but on the other hand the frame is smaller relatively to the effective cylinder diameter why larger vortices might pass outside the frame. The (\times)-symbols for each Γ mark the limits of the 5% smallest and 5% largest vortices.

Figure 13 shows, in the left and right columns, the location of the 5% smallest and 5% largest vortices, respectively, together with their corresponding cut-off values which is given to the right of the figure. The mid-column shows the location of the vortices, which have a diameter falling within $\pm 0.5\%$ of the peak value from the PDFs in figure 12. The amount of vortices within this range is about 7-8% of all the detected vortices. Here, the rotational direction of the vortices are also shown, which is given by the sign of the circulation. Vortices with positive circulation are marked with (+)-symbols, which by definition means a counter-clockwise (CCW) rotational direction, while vortices with negative circulation are marked with (\circ)-symbols and hence, have a clockwise (CW) rotational direction. The mid-column shows that vortices with the most common diameter are quite uniformly distributed in the wake and that both CCW and CW rotational vortices are encountered. Looking at the smaller (left column) and the larger (right column) vortices, one can see how they organise themselves into streamwise streaky regions, especially for the smaller vortices as suction, or blowing, increases. A closer look reveals that the smaller vortices have the opposite rotational direction compared to the larger vortices, which may imply that they correspond to secondary vortices induced by the larger primary ones.

In figure 14 the mean value of the vortex diameters that have been detected in each point is shown as a filled contour plot. It shows that the streaky regions of smaller and larger vortices discussed in relation with figure 13 do not coincide since they are revealed in this mean perspective contour plot. However, for $\Gamma \leq -5$ the streaky regions have essentially disappeared. Furthermore, one may note that the presence of vortices (any size) moves upstream and closer to the cylinder as suction is increased, while the blowing cases show the opposite.

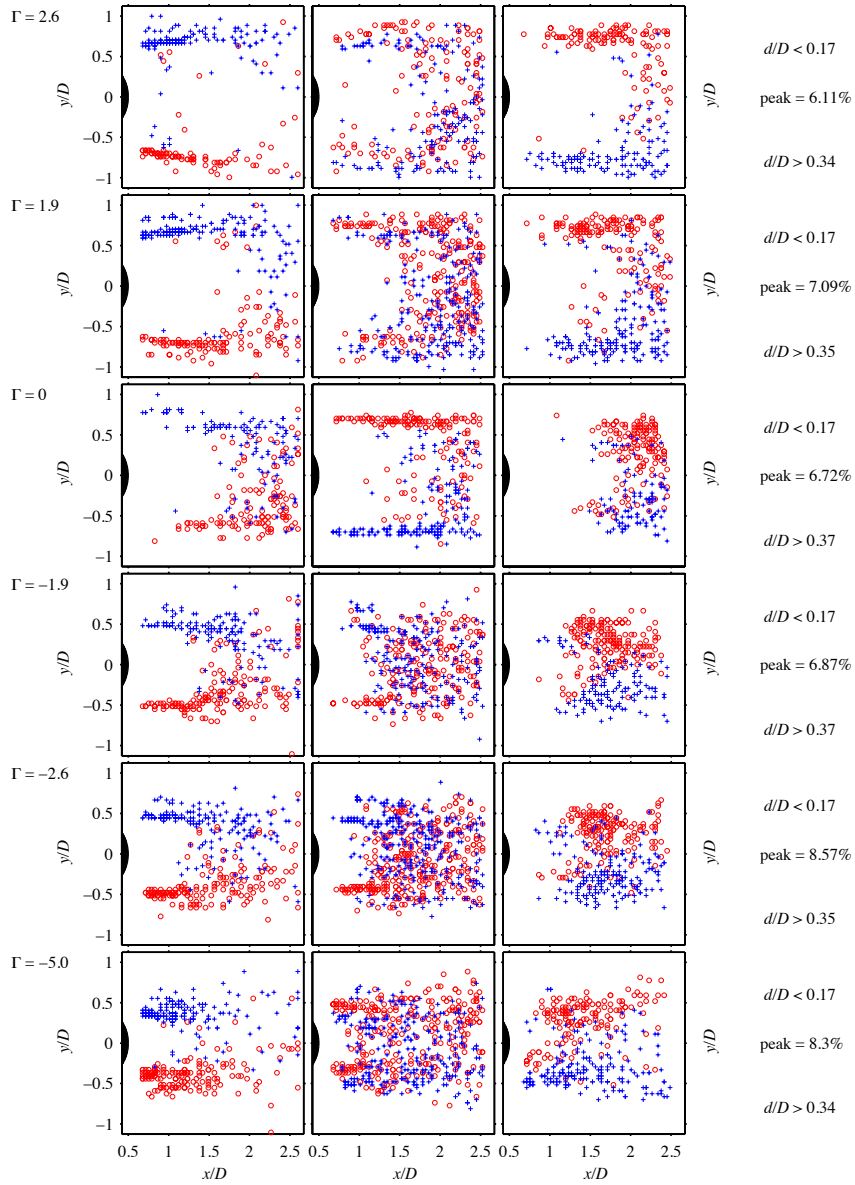


FIGURE 13. The position of the vortices corresponding to the smallest, most common and largest vortex sizes. Left column: shows the 5% smallest vortices. Mid-column: shows the vortices within $\pm 0.5\%$ of the peak value in the PDFs. Right column: shows the 5% largest vortices. The 5% cut-off limits and the amount of vortices in percent of the total number of vortices that are within $\pm 0.5\%$ of the peak value is given to the right of the figure. (+) and (o)-symbols correspond to CCW and CW rotational directions, respectively.

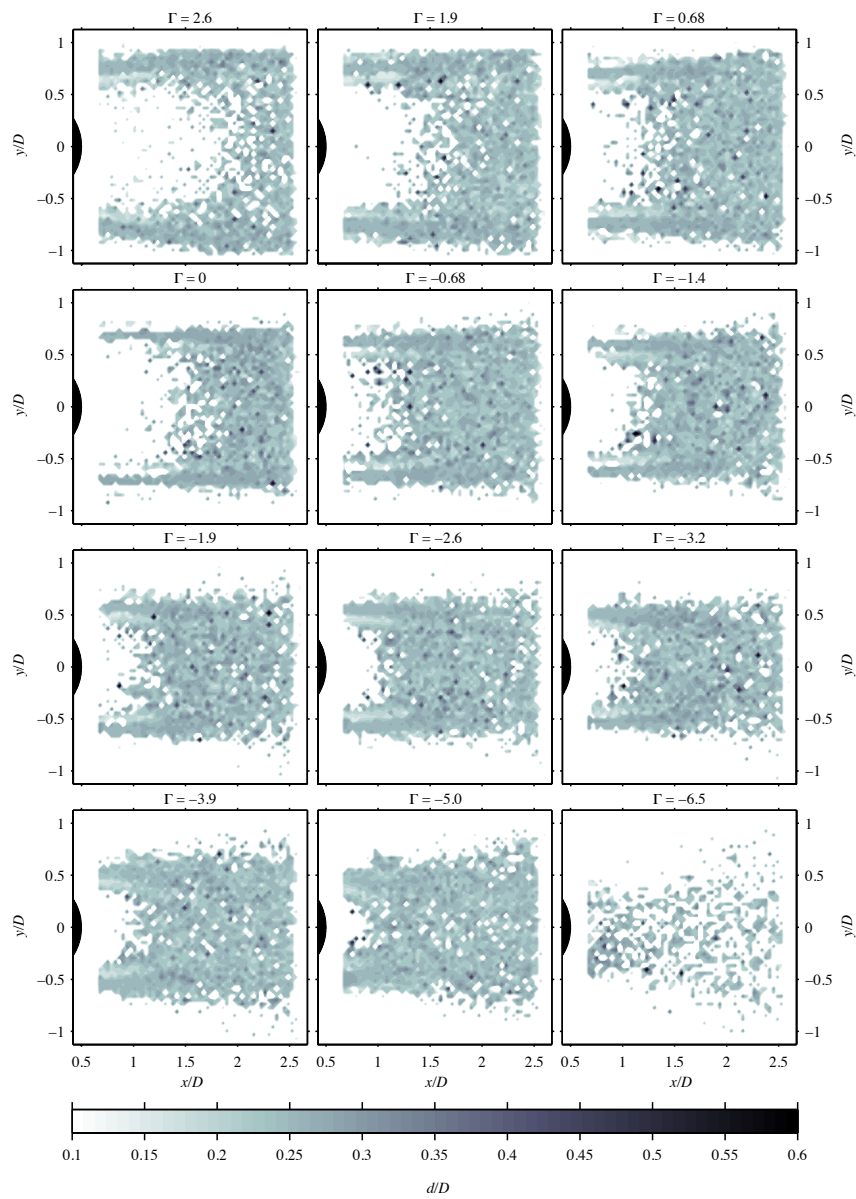


FIGURE 14. Mean vortex diameter in each point. The number of contour steps is 20.

Vortex strength. The PDFs of the vortex strength, λ_{ci} , are shown in figure 15 for the different levels of Γ . The most common vortex strength seems to be more or less unchanged for the different levels of suction. The mean vortex strength is about $\lambda_{ci} = 22 \pm 2$ and the limits for the 5% weakest and 5% strongest vortices are marked with (\times)-symbols. The number of bins are 50, and the curves are normalised and smoothed in the same manner as in previous plots.

Vortices with the most common strength have a similar distribution in the xy -plane as the most common vortex diameter. This can be concluded by comparing the mid-columns of figures 13 and 16. The left and the right columns in figure 16 show the 5% weakest and 5% strongest vortices, respectively. Since the peak value is close to the limit of the 5% weakest vortices (cf. figure 15) the distribution of the left and mid-columns look quite similar. On the other hand, looking at the stronger vortices (right column) one finds that, as the blowing level increases, the vortices move away from the wake centre and align themselves in streaky streamwise regions that moves away from the cylinder, while the suction case, the stronger vortices forms more compact regions around the shoulders of the cylinder ($y/D = \pm 0.5$). Furthermore, one may conclude that the rotational direction of the stronger vortices is solely determined by on which side of the centre line they are located, which intuitively can be related to the shedded vortices from the cylinder. The corresponding cut-off limits of

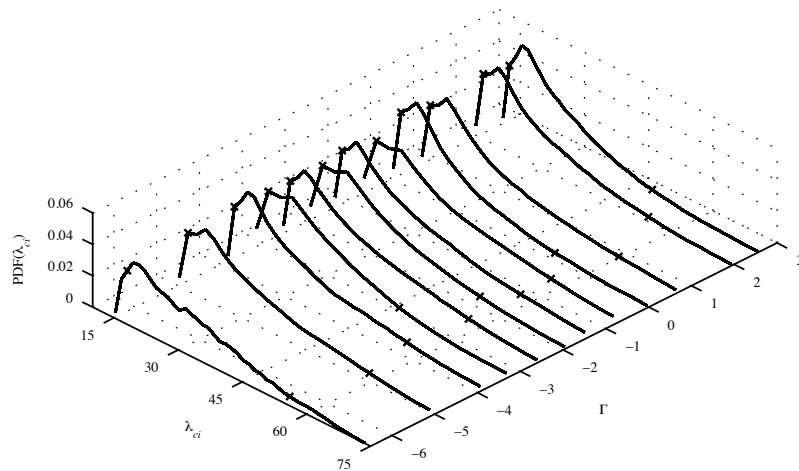


FIGURE 15. PDFs of the vortex strength for different levels of suction. The limit of the 5% weakest and 5% strongest vortices are marked with (\times)-symbols. To improve visibility the results have been truncated at $\lambda_{ci} = 75$, disregarding at most 1.1% of the data.

the 5% weakest and strongest vortices are shown to the right in figure 16. One may conclude that the vortices are intensified with increasing suction since both the limits increases with suction, which may be interpreted as a shift of the PDFs in the direction of stronger vortices. For the blowing case one should be more careful with such a conclusion since the streaks moves out of the frame, although the trend seems to be similar if one looks at low levels of blowing.

The mean value of of the vortex strengths in each point where vortices have been detected is shown as a filled contour plot in figure 17. Here, the same behaviour as in figure 16 is found, i.e. as the magnitude of Γ increases, stronger vortices form along the streamwise tangents of the cylinder, while weaker vortices are dominant in the centre of the wake. Furthermore, one may note that the presence of vortices (any size) moves downstream away from the cylinder as blowing is increased, while when suction is increased they move upstream and closer to the cylinder.

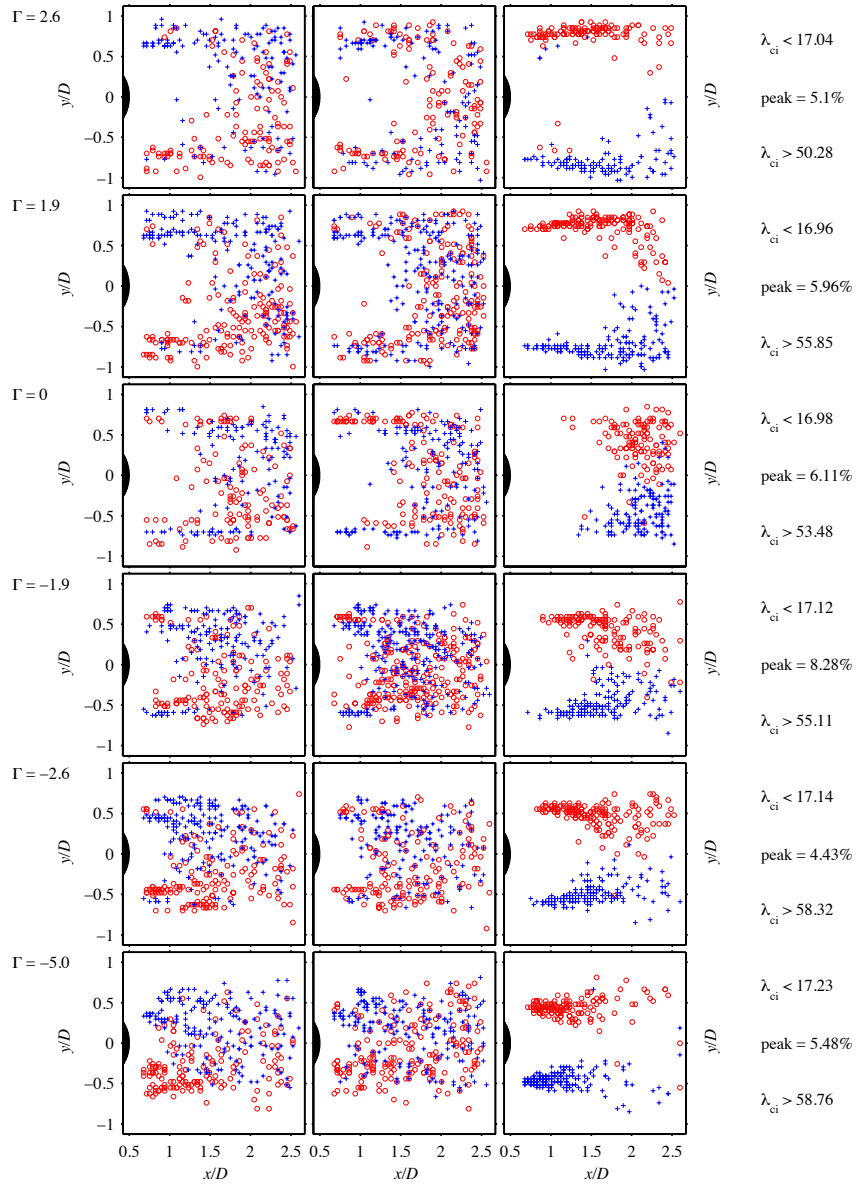


FIGURE 16. The position and limit of the 5% weakest vortices (left column), the position and percentage of the total number of vortices within $\pm 0.5\%$ of the peak value (mid-column) and the position and limit of the 5% strongest vortices (right column). (+)- and (o)-symbols have CCW and CW rotational direction, respectively.

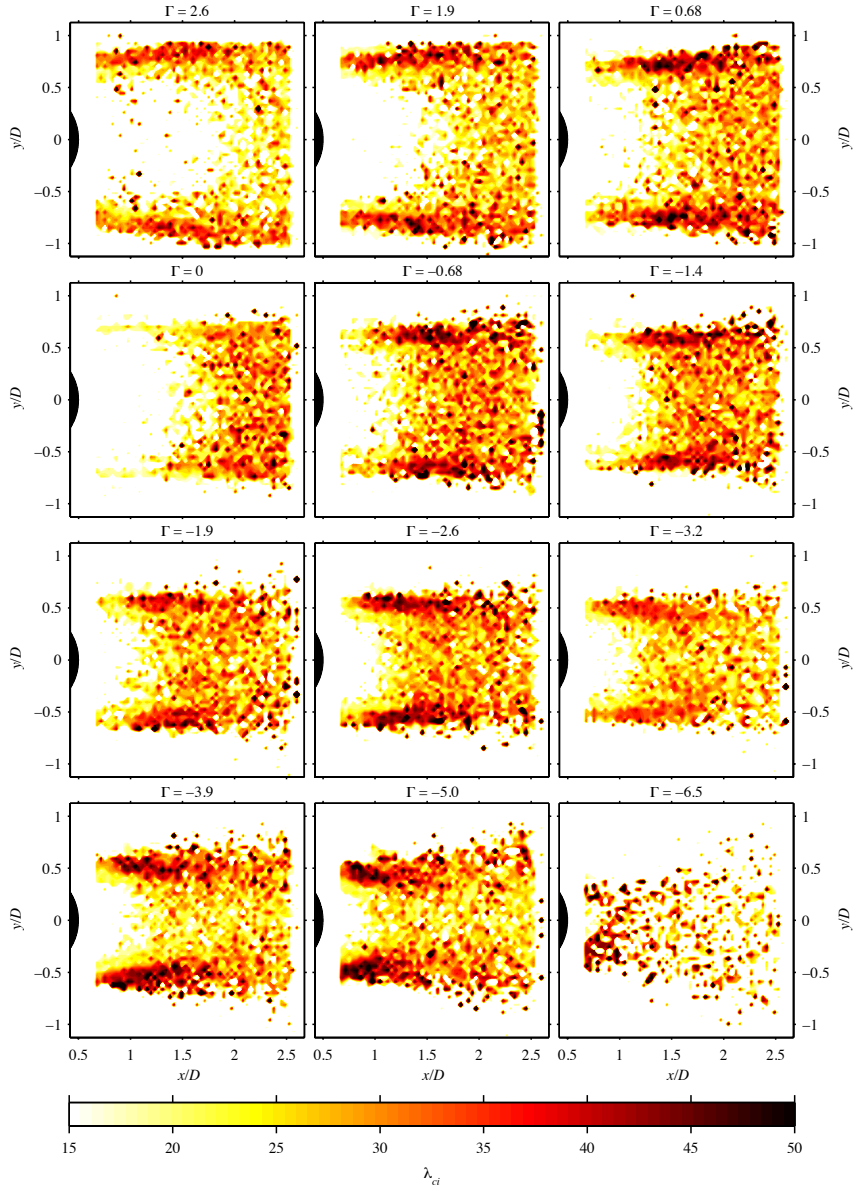


FIGURE 17. Mean vortex strength in each point where vortices are detected. The lower limit is determined by the threshold ($=15$) in the detection code and the upper limit has been truncated at $\lambda_{ci} = 50$ to enhance visibility. The number of contour steps is 20.

Vortex circulation. In figure 18 the PDFs of the vortex circulation, γ , are shown. For a large number of detected vortices and provided that the geometry is symmetric but also that blowing or suction, when applied, is applied uniformly, the circulation should have a symmetric distribution around zero. Both on the positive and the negative half of γ one may observe two peaks in the distribution. The highest peak is at $\gamma = \pm 0.04U_\infty D$ with a maximum deviation of $\gamma = \pm 0.01U_\infty D$. The second peak, appearing at higher absolute values of γ relative to the maximum peak, is more pronounced on the negative half of the PDF. It is persistent in the blowing cases and for suction levels of up to $-I < 5$, whereafter it disappears. As for the other vortex parameters the limits for the 5% lowest and 5% highest values of circulation are marked with (×)-symbols in figure 18.

In figure 19 the vortices corresponding to the 5% lowest (left column) and 5% highest (right column) values of the circulation together with the vortices within $\pm 0.5\%$ of the maximum peak value (mid-column). A natural choice of vortex strength measure would be the circulation of a vortex. By comparing figures 16 and 19 one may conclude that the two measures give similar results. While the circulation γ is a measure with some physical relevance the λ_{ci} measure is not. On the other hand, λ_{ci} is the key parameter in the chosen

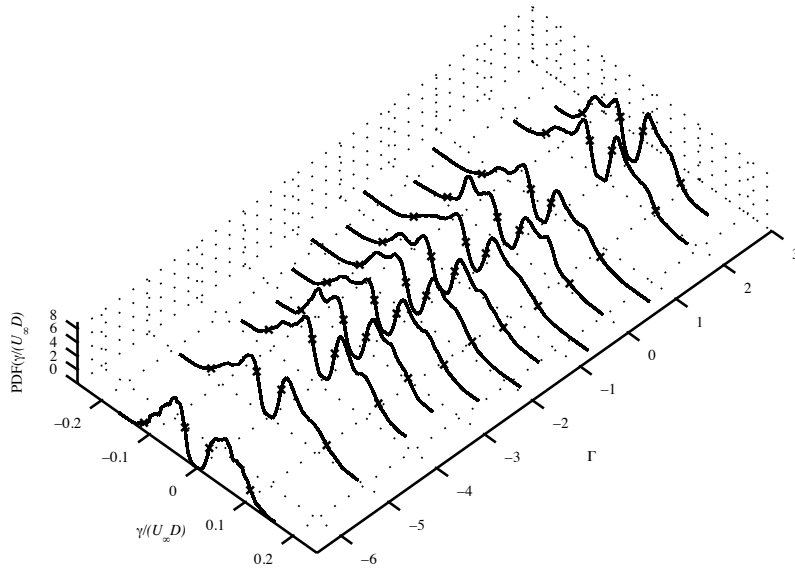


FIGURE 18. PDFs of the vortex circulation for different levels of suction. (×)-symbols mark the limits of the 5% smallest and 5% largest circulation based on the absolute value. To enhance visibility every second line is bold.

vortex detection method (cf. section 3.2) and is at hand as soon as a vortex has been identified in the velocity field, while the circulation has to be calculated in a *smart* and consistent way for each identified vortex and, hence, is not as easily accessed. In this context one should also mention that there is a clear advantage of the circulation measure over the λ_{ci} measure, which is the information of the rotational direction of the vortex. A careful inspection between figures 16 and 19 reveals some differences between the two measures, but are most likely attributed to the cut-off limits for the two different measures which will not extract exactly the same vortices. Vortices within $\pm 0.5\%$ of the maximum peak value in γ (mid-column) are more or less evenly distributed in the wake and the number of vortices in the very near wake of the cylinder increases as the suction level is increased. Otherwise, the concluding remarks are similar to what was concluded in the *vortex strength* paragraph and, hence, are not repeated here.

In a mean perspective, as shown in figure 20, the conclusion about the role up of secondary vortices due to the primary shedded vortices from the cylinder is strengthened. Streamwise streaky regions of negative (red) and positive (blue) circulation are encountered on both sides of the cylinder. The streamwise extent of these regions are inclined away from the cylinder as blowing is increased while they are shortened and move towards the shoulders of the cylinder ($y/D = \pm 0.5$) as suction is increased. The primary vortex regions correspond to the red one on the upper half and the blue one on the lower half in the figures. A careful inspection reveals streaky regions on both sides of the primary vortices with opposite sign, which supports the previously mentioned induction of secondary vortices.

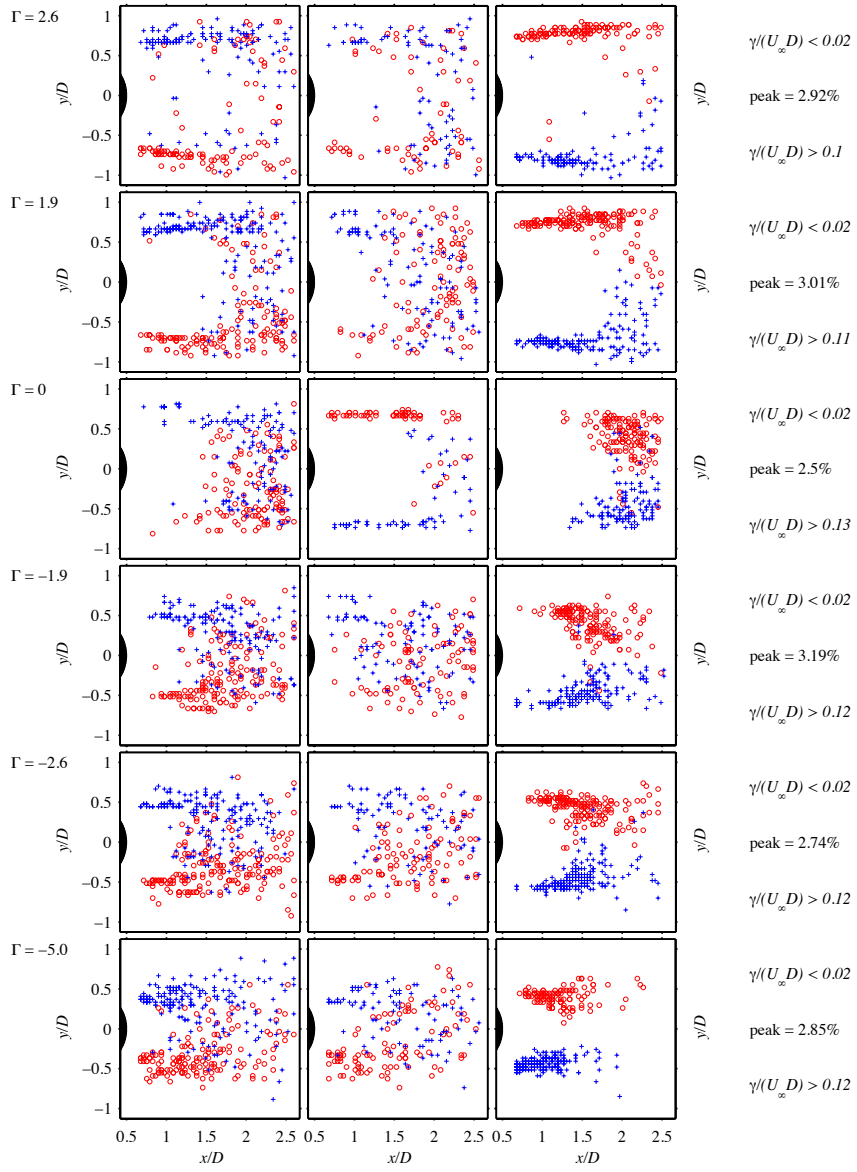


FIGURE 19. The position and limit of vortices corresponding to the 5% smallest absolute circulation value (left column), the vortex location and the percentage of the total number of vortices within $\pm 0.5\%$ of the absolute peak value (mid-column) and the position and limit of the vortices corresponding to the 5% largest absolute value (right column). (+)- and (o)-symbols correspond to positive and negative circulation, i.e. CCW and CW rotational direction, respectively.

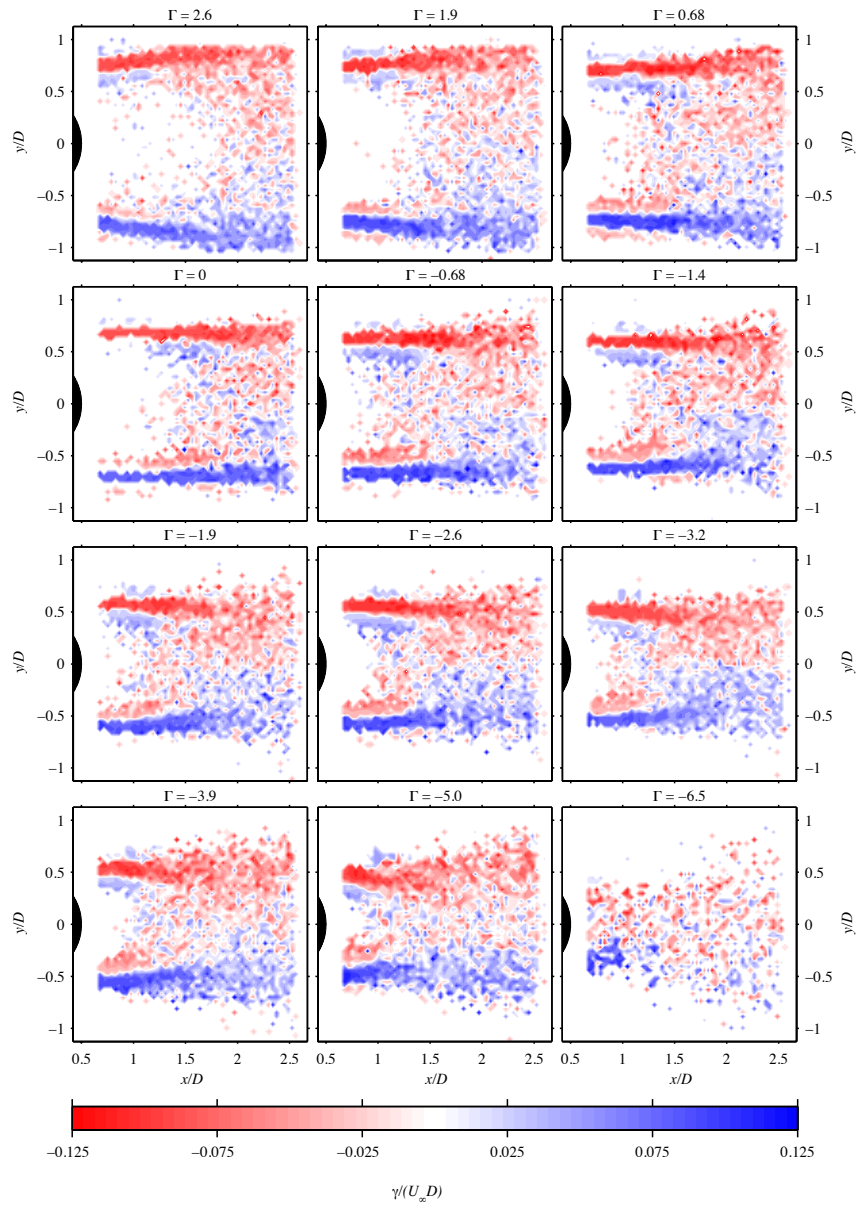


FIGURE 20. Mean vortex circulation in each point where vortices are detected. Negative circulation is clockwise rotation and positive counterclockwise. The number of contour steps is 20.

4.2. Far wake: frame II

Location of vortices. Figure 21 shows the PDFs of the location of the vortices for increasing blowing, i.e. vortices identified in frame II. The number of bins are 30 and the curves have been smoothed by averaging every point with the neighbouring four. For $\Gamma = 0$ the distribution is combined with frame I and we recall the observation of one single peak in the PDF around $x/D = 2.3$, which is located in the overlap region between frame I and II. For blowing, in the interval $0 < \Gamma < 5$, it is shown that there is no major difference in the streamwise position of identified vortices nor the peak value in the PDFs, but there are two general remarks on the observed distributions that have to be mentioned. Firstly, the distributions start quite abrupt at around $x/D = 1.8$ and, secondly, for $\Gamma > 5$ there is a significant increase of identified vortices at the inlet boundary of frame II. A simple explanation would be to blame the vortex detection program and to classify the remarks as being unphysical, however, in the process of analyzing the vortex parameters explanations will be attempted and we will consequently come back to above remarks in the end of this section.

In figure 22 the percentage of the total number of vortices in each point where vortices have been detected is shown. This confirms the unchanged distribution at lower levels of blowing, while at higher levels (here from $\Gamma = 5$) a high concentration is found along the inlet boundary of the frame, which is followed by a region with less vortices in the central region of the wake.

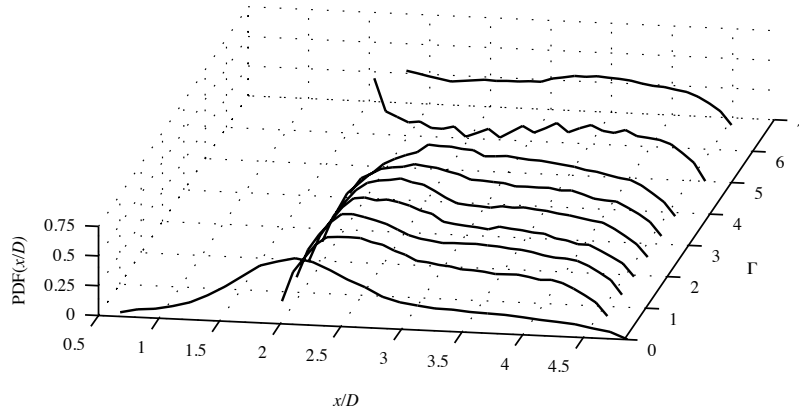


FIGURE 21. PDFs of the streamwise position of vortices for different levels of blowing.

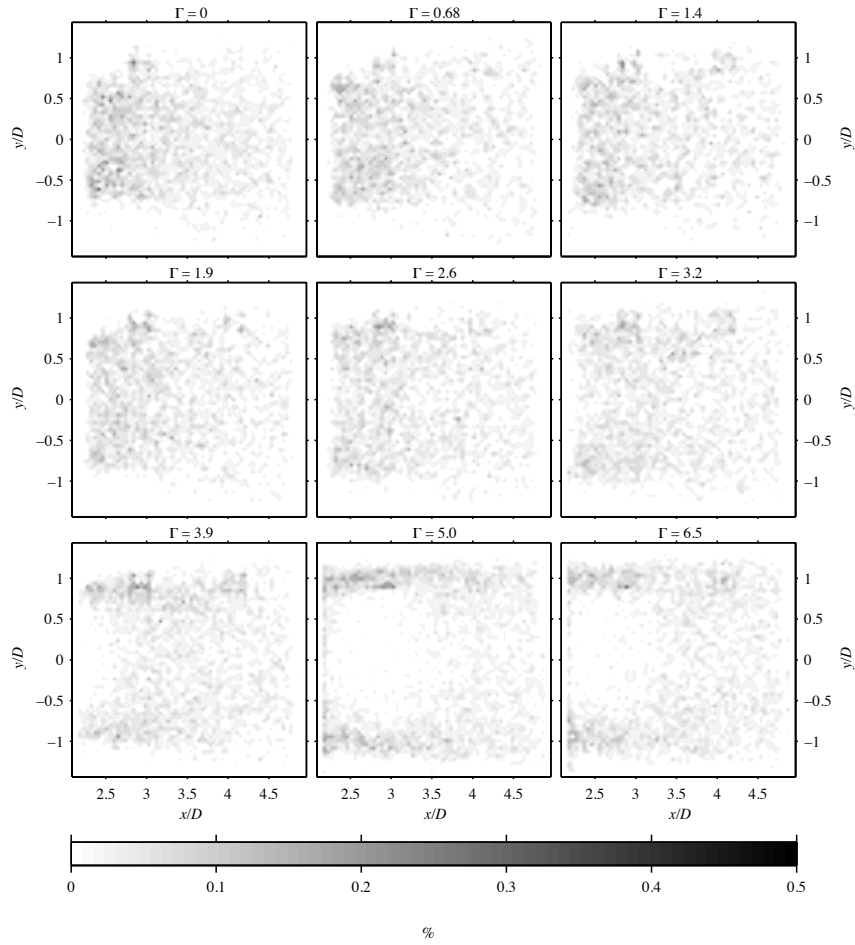


FIGURE 22. Percentage of the total number of vortices in each point where vortices are detected. The number of contour steps is 20.

Vortex size. The PDFs of the vortex diameters are shown in figure 23 for different levels of blowing. These distributions are plotted in the same manner as in the suction case and with the limits of the 5% smallest and 5% largest vortices marked by (×)–symbols in the figure. One may conclude that the peak values are fairly unchanged when blowing is increased. The averaged peak value is $0.29D$, which should be compared with the averaged peak value in the suction case (figure 12) of $0.25D$. While in the suction case there is a small trend of decreasing diameters for the peak value, there is a small trend of increasing

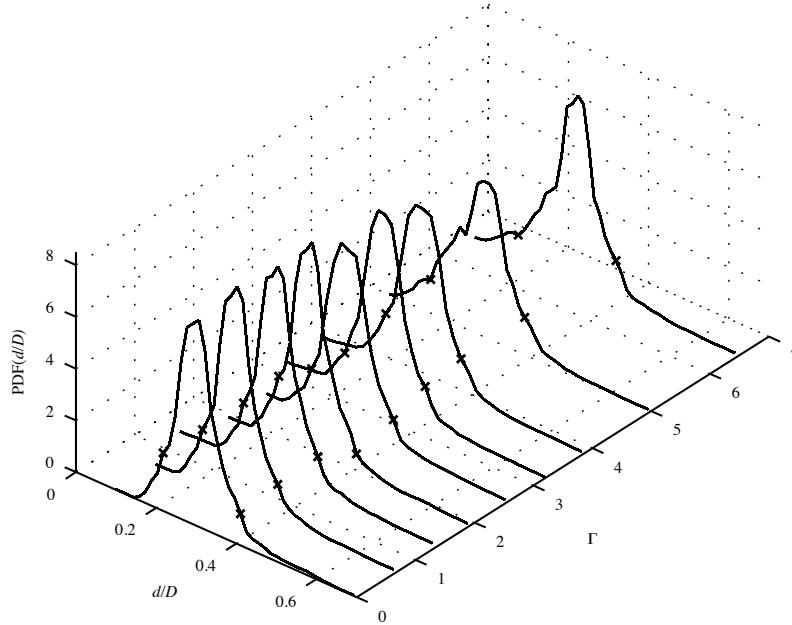


FIGURE 23. PDFs of the vortex diameters for different levels of blowing. (\times)-symbols mark the limits of the 5% smallest and 5% largest vortices. To improve visibility, the plots are truncated at $d_\gamma/D = 0.7$, disregarding at most 0.2% of the data.

diameters in the blowing case. These trends may be explained by the actual cylinder diameter seen by the flow. A physically larger cylinder would naturally generate larger vortices in the flow field compared to a smaller cylinder, and the effect of blowing and suction causes an increase and a decrease of a fictitious cylinder diameter seen by the incoming flow. However, a comparison between the PDFs from frame I (figure 12) and frame II (figure 23) for the natural case, i.e. $\Gamma = 0$, reveals that the distribution centered around its peak is moved towards larger diameters. This mismatch may, on the other hand, be explained by the locations of frame I and II. The largest vortices are connected to the von Kármán vortices and a central position in the flow field is the confluence point of these large eddies, which in the suction case (frame I) is just captured while in the blowing case (frame II) it is located about one third from the inlet boundary of the frame (see left column in figure 8).

Figure 24 shows the location of the 5% smallest (left column) and 5% largest (right column) vortices with their corresponding cut-off values given to the right in the figure. In the mid-column the location of the vortices with

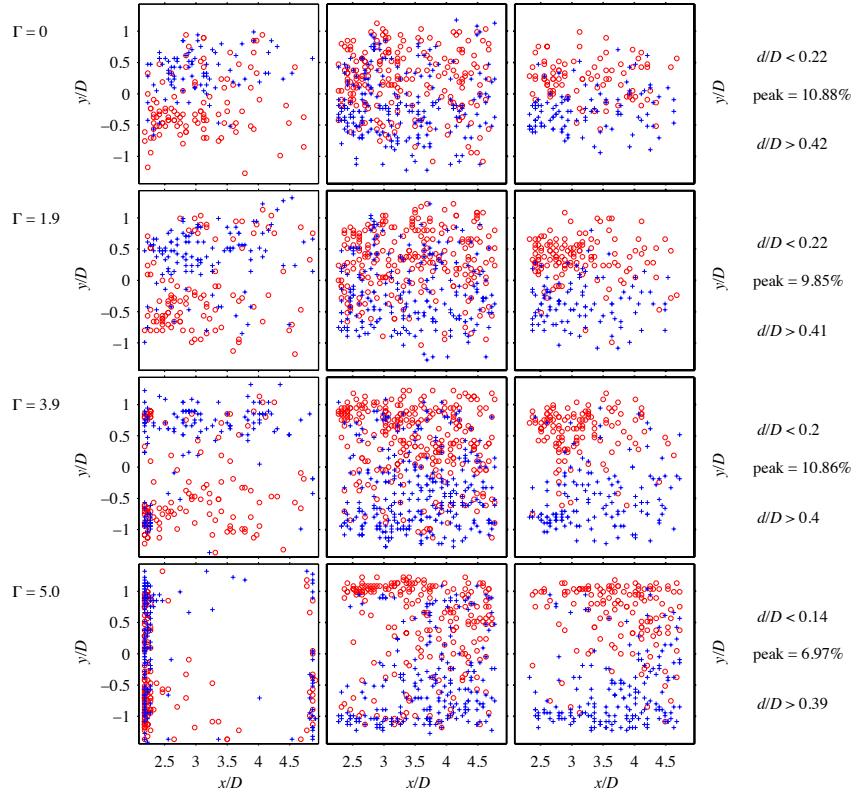


FIGURE 24. The positions and limit of the 5% smallest vortices (left column), the position and percentage of the total number of vortices within $\pm 0.5\%$ of the peak value (mid-column) and the position and limit of the 5% largest vortices (right column) for different levels of blowing. (+)- and (o)-symbols have CCW and CW rotational direction, respectively.

diameters falling within $\pm 0.5\%$ of the peak value diameter are shown. Here, CCW and CW rotational direction are marked by (+)- and (o)- symbols, respectively. Vortices with the most common diameter (mid-column) is quite evenly distributed in frame II. However, for the largest vortices (right column), just as in the suction case in frame I, the vortex diameters with CW and CCW rotational directions are found on the upper and lower frame halves, respectively. For the highest blowing rate a clear increase of the wake size is observed with the largest vortices moving away from the wake centre, which is the result of an extension of the wake. For the smallest vortices (left column), the rotational direction is opposite compared to the largest, and have been induced by the

primary von Kármán vortices as previously discussed for the suction case. The mean diameter in each point in the xy -plane does not reveal anything new and the figure is, hence, not reproduced here.

Vortex strength. PDFs of the vortex strength are shown in figure 25 for the different blowing rates. In average the peaks of the vortex strength is $\lambda_{ci} = 18.8 \pm 1$. The (\times)—symbols mark the limits for the 5% weakest and 5% strongest vortices. In overall, one may conclude that there is no large effect for increasing blowing on the vortex strength distributions.

In figure 26 the 5% weakest and 5% strongest vortices are plotted in the left and in the right columns, respectively. The mid-column shows the vortices falling within ± 0.5 of the PDF peak values in figure 25. In general one may say that the strongest vortices are connected to the largest vortices, this was the case for suction and up to blowing rates of $\Gamma = 3.9$. However, for $\Gamma \geq 5.0$ it turns out to be the smallest vortices, which are strongest (compare the last rows of figures 24 and 26). This view is supported when the vortex strength is plotted in a mean perspective, see figure 27, keeping in mind the collection of the smallest vortices along the inlet boundary of the frame when blowing is increased. Here the $\Gamma = 6.5$ case is also shown in order to strengthen the viewpoints that small and strong vortices are gathered around the inlet of frame II.

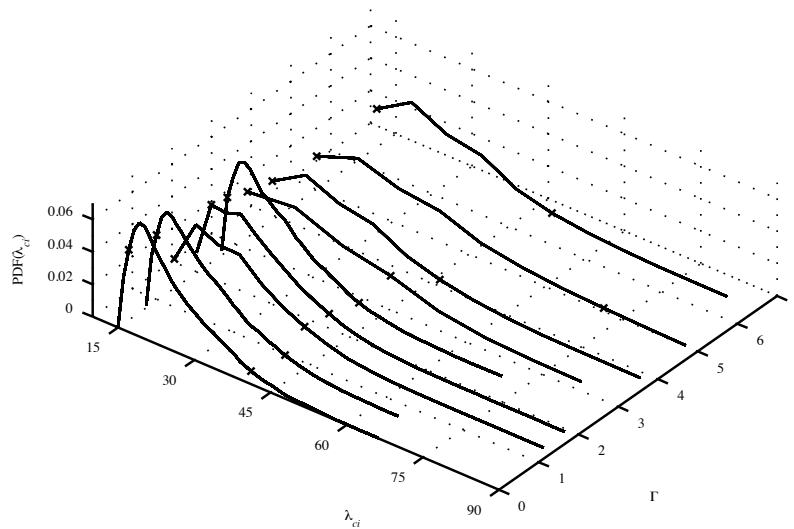


FIGURE 25. PDFs for the vortex strength. To improve visibility the results have been truncated at $\lambda_{ci} = 90$ disregarding at most 3.5% of the data.

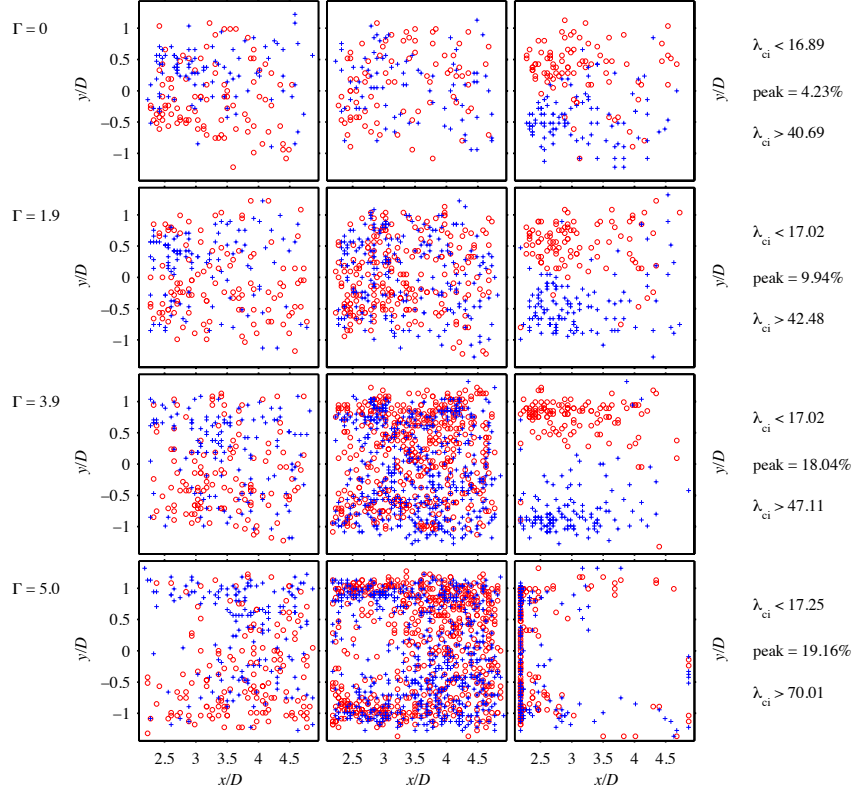


FIGURE 26. The position and limit of the 5% weakest vortices (left column), the position and percentage of the total number of vortices within $\pm 0.5\%$ of the peak value (mid-column) and the position and limit for the 5% strongest vortices (right column) at different levels of blowing. (+)- and (o)-symbols have CCW and CW rotational direction, respectively.

Vortex circulation. For completeness the vortex circulation with increasing blowing is also shown. The results are, however, similar to the *Vortex strength* results. In figure 28 the PDFs for the vortex circulation are shown for increasing blowing. Again, the (x)-symbols mark the limits of the 5% lowest and 5% highest absolute values of the circulation. The PDFs are symmetric and essentially unchanged when blowing is increased with an averaged peak value of the PDFs of $\gamma = 0.06U_\infty D$ with a maximum deviation of about $0.005U_\infty D$. The positions of the vortices, classified after their corresponding absolute circulation value, are shown in figure 29, which look quite similar to figure 26.

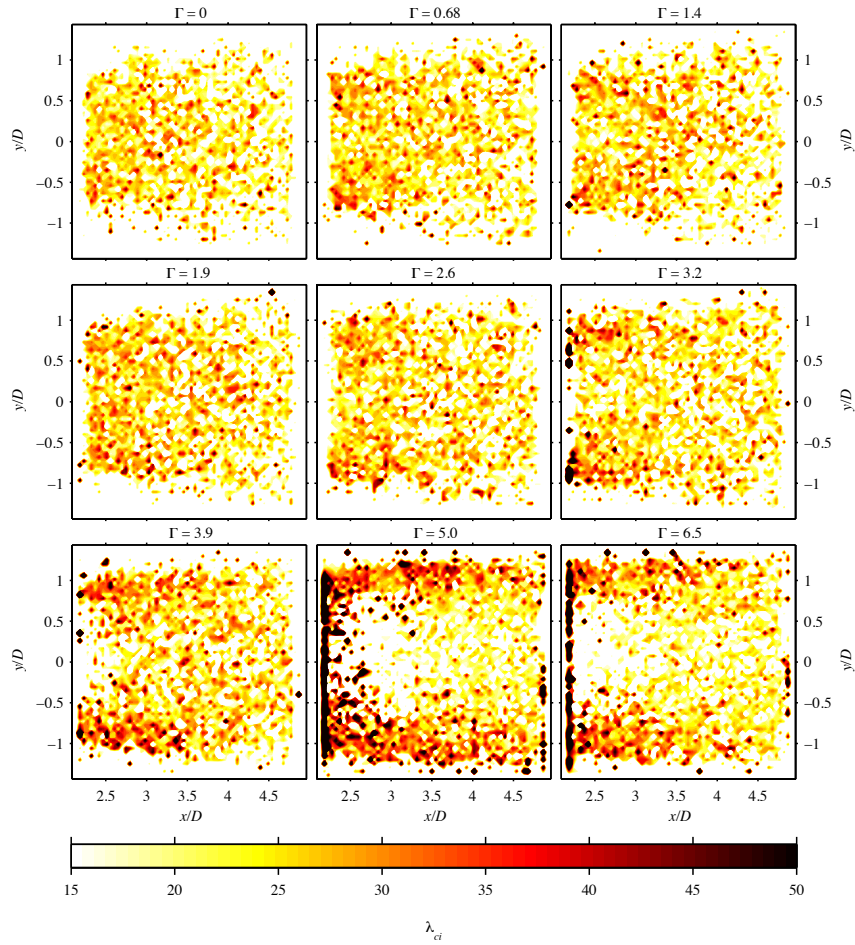


FIGURE 27. The mean vortex strength in each point where vortices are detected. The lower limit is set by threshold in the detection code and the upper limit has been truncated at 50 to enhance visibility. The number of contour steps are 20.

The mean of the circulation in each point shows that the sign of the circulation and, hence, the rotational direction in a mean perspective, is governed by the location of the vortices relative the wake centre line, see figure 30. As the level of blowing increases, the mean circulation of the vortices at the upper and lower boundaries of the frame also increases. The high number of detected vortices at the inlet boundary of the frame, seen in figure 29, is not found

when looking at the mean value circulation, indicating that the mean of those vortices is close to zero.

Now, coming back to the remarks, which were stated in the first paragraph under *Location of vortices* in this section. The first remark may be explained by the sudden appearance of frame II and the way that the vortex detection program can handle this. Small vortices may be detected close to a boundary but not large vortices, since they will partly be located outside the frame and hence will be cut-out as a detected vortex. Therefore the number of detected vortices will be biased and the PDFs will show an abrupt increase from the inlet boundary due to the sudden, physical, possibility to detect large vortices. This also explains the second remark, and it is clear from figure 24 that it is the collection of small vortices at the boundary inlet to the frame which causes the significant increase in the total number of vortices along this boundary. One may further conclude that these small vortices are stronger than the largest vortices in the flow field and that they rotate in both directions.

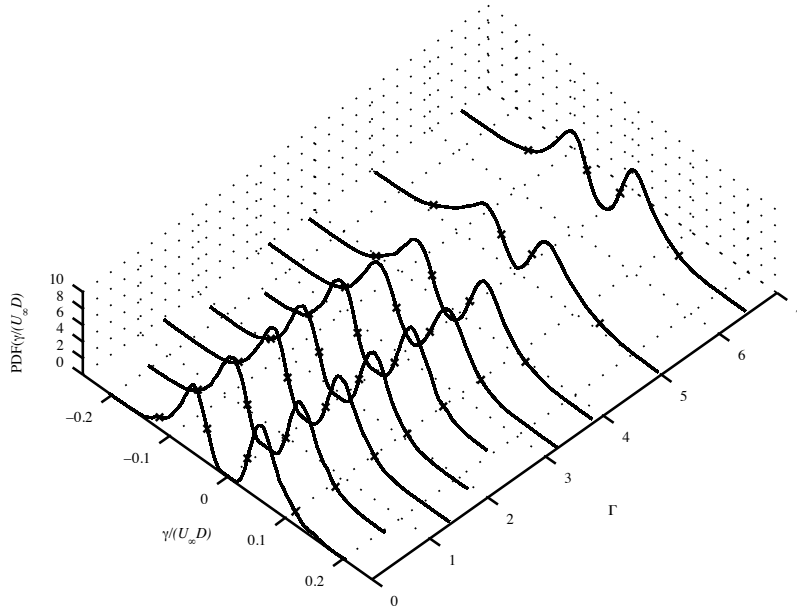


FIGURE 28. PDFs for the circulation for different levels of blowing. To improve visibility the line styles have been alternated and the results have been truncated at $\Gamma/(U_\infty D) = \pm 0.25$, disregarding at most 0.5% of the data.

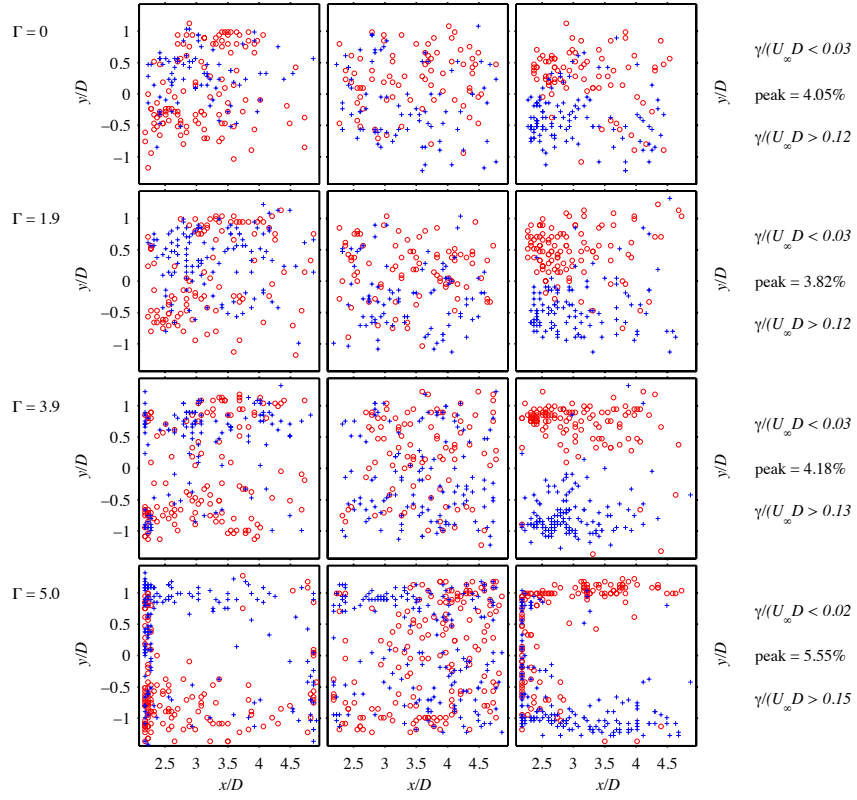


FIGURE 29. The position and limit of the vortices that have a circulation corresponding within 5% of the lowest absolute value (left column), the vortex location and the percentage of the total number of vortices that have a circulation of $\pm 0.5\%$ of the absolute peak value (middle column) and the position and limit of the vortices that have a circulation corresponding within 5% of the highest absolute value (right column). (+) and (o) have positive and negative circulation, i.e. CCW and CW rotational direction, respectively.

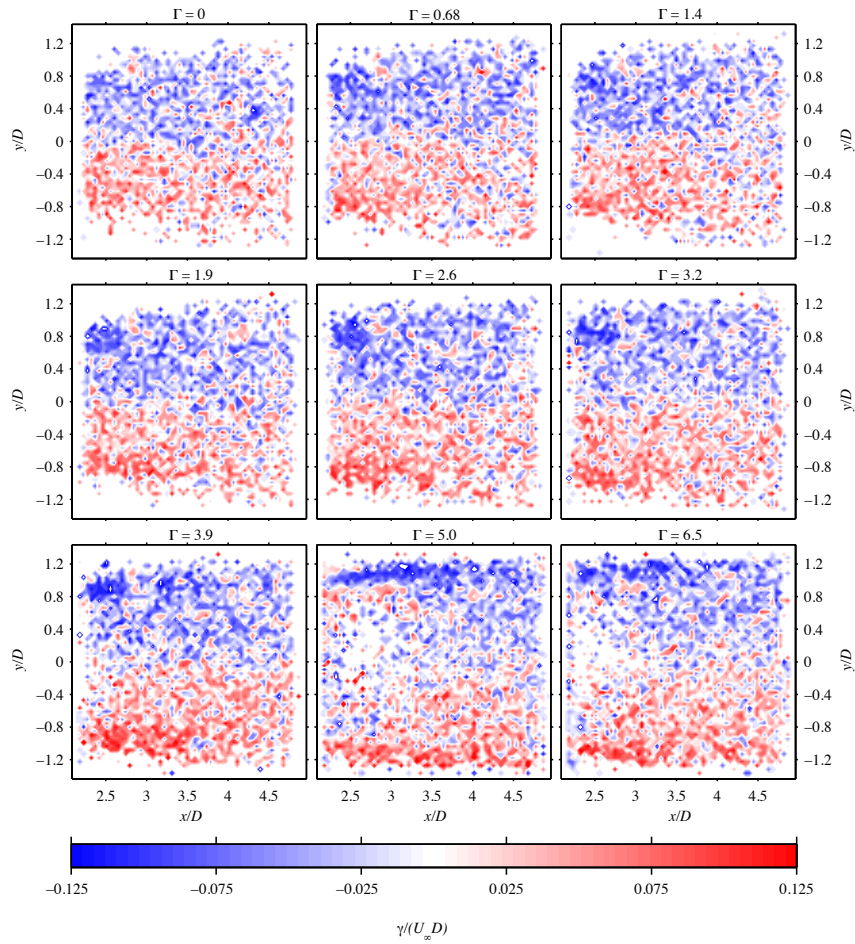


FIGURE 30. Mean vortex circulation in each point where vortices are detected. Negative circulation is equal to CW rotation and positive to CCW rotation. The number of countour steps are 20.

5. Summary and conclusions

In this paper we report on the effect of continuous suction or blowing through the entire surface of a porous cylinder with the emphasis on vortex statistics. The Reynolds number is around 3.5×10^3 , which implies that the boundary layers around the cylinder are laminar with a purely laminar separation and a turbulent wake. This implies that there is a wide range of both vortex sizes and strengths. Previously, it has been shown that continuous suction or blowing have a large impact on the vortex shedding frequency, mean velocity field and consequently the drag force. However, there is no information about the small-scale structures and how they are affected by suction or blowing. For this purpose a vortex detection program has been developed, which identifies vortices in two-dimensional instantaneous PIV images, with the purpose of analyzing small-scale structures in the wake behind bluff bodies. Vortex parameters such as strength, size and rotational direction, but also the locations of the vortex centres are outputs from the program. With a large number of PIV images vortex statistics may be created.

The results are presented by means of PDFs of the vortex parameters. For increasing suction the size of the wake decreases and the location of the maximum back-flow turns out to be a relevant position for the distribution of vortex location. For $\Gamma > -4$ the PDFs essentially collapse on each other when the location of maximum back-flow is subtracted from the streamwise axis.

By looking at the 5% largest/smallest and strongest/weakest vortices, and vortices within $\pm 0.5\%$ of the most common value of a particular vortex parameter, additional information is achieved and further conclusions may be drawn. Successively increasing suction creates streamwise streaky regions where small and large scale vortices, relative to the most common vortex size, are collected. These streamwise streaky regions move towards the shoulders of the cylinder ($y/D = \pm 0.5$) and are reduced in the streamwise direction with increasing suction. A close look reveal that the regions do not overlap and that the larger vortices are found on the outer side of the smaller vortices relative the wake centre line. The large vortices have rotational direction in accordance with the von Kármán vortices while the small vortices have the opposite rotational direction. This suggests that the larger vortices originate from the shedding of vortices from the cylinder, and may be seen as primary vortices, while the smaller vortices are secondary vortices which are induced by the primary ones.

From the vortex analysis one may also conclude that the vortices are slightly intensified with increasing suction and that the largest vortices are the strongest ones while the smallest ones are also the weakest ones. Generally speaking, the effect of continuous suction on the vortex parameters is quite weak. What changes most is the location of the vortices in the xy -plane behind the cylinder.

With increasing blowing one may conclude that the peak value in the PDFs of vortex size is fairly unchanged. The averaged peak value in the blowing case is $0.29D$, which should be compared with the averaged peak value of $0.25D$ for the suction case. This means that the most common vortex diameter is between 25–30% of the cylinder diameter depending on the sign and level of Γ . Increasing suction shows a small trend of decreasing peak values of the vortex size while increasing blowing shows a small trend of increasing peak values.

An interesting result in the blowing case is that for high enough blowing rates ($\Gamma > 5$) there is a change in trend of the vortices. Suddenly, it is the smallest vortices that are the strongest ones and they are located at the near wake stagnation point, which rises due to the secondary flow from the cylinder with positive U and the wake back-flow with negative U . The reason for this change of trend can only be speculated upon. An hypothesis is that the change of trend is an artifact of the energy transfer from the primary to the secondary vortices and that they are forced towards the wake centre line when approaching the streamwise extent of the confluence point. These small vortices are pushed away from the cylinder by the surface blowing and pulled towards the cylinder by the wake back-flow, which will lead to a line up of vortices across the wake. Due to the vertical stagnation line the vortices will continuously be fed with new energy in both the positive and the negative rotational directions, which is the reason why the vortices are mixed between positive and negative circulation.

Acknowledgements

The Swedish Research Council (VR) is greatly acknowledged for the financial support. We would also like to acknowledge The Göran Gustafsson foundation for supporting the project in the initial stage.

References

- ADRIAN, R. J., CHRISTENSEN, K. T. & LIU, Z.-C. 2000 Analysis and interpretation of instantaneous turbulent velocity fields. *Exp. Fluids* **19**, 275–290.
- AGRAWAL, A. & PRASAD, A. 2002 Properties of vortices in the self-similar turbulent jet. *Exp. Fluids* **33**, 565–577.
- BURESTI, G. 1998 Vortex shedding from bluff bodies. *Wind Effects on Buildings and Structures*, pp. 61–95, Riera & Davenport (eds.), Balkema, Rotterdam.
- CHAKRABORTY, P., BALACHANDAR, S. & ADRIAN, R. J. 2005 On the relationships between local vortex identification schemes. *J. Fluid. Mech.* **535**, 189–214.
- CHOMAZ, J. M., HUERRE, P. & REDEKOPP, L. G. 1988 Bifurcations to local and global modes in spatially developing flows. *Phys. Rev. Lett.* **60**, 25–28.
- CHONG, M. S., PERRY, A. E. & CANTWELL, B. J. 1990 A general classification of three-dimensional flow fields. *Phys. Fluids* **2**, 765–777.
- EL AKOURY, R., BRAZA, M., PERRIN, G., HARRAN, G. & HOARAU, Y. 2008 The three-dimensional transition in the flow around a rotating cylinder. *J. Fluid. Mech.* **607**, 1–11.
- FRANSSON, J. H. M. & ALFREDSSON, P. H. 2003 On the disturbance growth in an asymptotic suction boundary layer. *J. Fluid. Mech.* **482**, 51–90.
- FRANSSON, J. H. M., KONIECZNY, P. & ALFREDSSON, P. H. 2004 Flow around a porous cylinder subject to continuous suction or blowing. *J. Fluids Struct.* **19**, 1031–1048.
- GILLIES, E. A. 1998 Low-dimensional control of the circular cylinder wake. *J. Fluid Mech.* **371**, 157–178.
- GLEZER, A. & AMITAY, M. 2002 Synthetic jets. *Annu. Rev. Fluid Mech.* **34**, 503–529.
- GRINSTEIN, F. F., BORIS, J. P. & GRIFFIN, O. M. 1991 Passive pressure-drag control in a plane wake. *AIAA J.* **29**, 1436–1442.
- HUERRE, P. & MONKEWITZ, P. A. 1990 Local and global instabilities in spatially developing flows. *Annu. Rev. Fluid Mech.* **22**, 473–537.
- HURLEY, D. G. & THWAITES, M. A. 1951 An experimental investigation of the boundary layer on a porous circular cylinder. *Brit. Aero. Res. Council, Rep. and Memo.* 2829.
- JEONG, J. & HUSSAIN, F. 1995 On the identification of a vortex. *J. Fluid. Mech.* **285**, 69–94.

- LINDGREN, B. 2002 Flow facility design and experimental studies of wall-bounded turbulent shear-flows. PhD thesis, Royal Institute of Technology.
- MATHELIN, L., BATAILLE, F. & LALLEMAND, A. 2001*a* Near wake of a circular cylinder submitted to blowing - I Boundary layers evolution. *Int. J. Heat Mass Transf.* **44**, 3701–3708.
- MATHELIN, L., BATAILLE, F. & LALLEMAND, A. 2001*b* Near wake of a circular cylinder submitted to blowing - II Impact on the dynamics. *Int. J. Heat Mass Transf.* **44**, 3709–3719.
- MONKEWITZ, P. A. 1988 The absolute and convective nature of instability in two-dimensional wakes at low Reynolds numbers. *Phys. Fluids* **31**, 999–1006.
- NORBERG, C. 2003 Fluctuating lift on a circular cylinder: review and new measurements. *J. Fluids Struct.* **17**, 57–96.
- PANKHURST, R. C. & THWAITES, M. A. 1950 Experiments on the flow past a porous circular cylinder fitted with a Thwaites flat. *Brit. Aero. Res. Council*, Rep. and Memo. 2787.
- PARK, D. S., LADD, D. M. & HENDRICKS, E. W. 1994 Feedback control of von Karman vortex shedding behind a circular cylinder at low Reynolds numbers. *Phys. Fluids* **6**, 2390–2405.
- PROVANSAL, M., MATHIS, C. & BOYER, L. 1987 Benard-von Karman instability: transient and forced regimes. *J. Fluid Mech.* **182**, 1–22.
- ROSHKO, A. 1955 On the wake and drag of bluff bodies. *J. Aeronaut. Sci.* **22**, 124–132.
- ROSHKO, A. 1961 Experiments on the flow past a circular cylinder at very high Reynolds number. *J. Fluid Mech.* **10**, 345–356.
- ROUSSOPOULOS, K. 1993 Feedback control of vortex shedding at low Reynolds number. *J. Fluid Mech.* **248**, 267–296.
- SHIELS, D. & LEONARD, A. 2001 Investigation of a drag reduction on a circular cylinder in rotary oscillation. *J. Fluid Mech.* **431**, 297–322.
- TOKUMARU, P. T. & DIMOTAKIS, P. E. 1991 Rotary oscillation control of a cylinder wake. *J. Fluid Mech.* **224**, 77–90.
- WILLIAMSON, C. H. K. 1996 Vortex dynamics in the cylinder wake. *Annu. Rev. Fluid Mech.* **28**, 477–539.
- ZDRAVKOVICH, M. M. 1997 *Flow around circular cylinders, Vol 1: Fundamentals*. Oxford University Press.
- ZDRAVKOVICH, M. M. 2003 *Flow around circular cylinders, Vol 2: Applications*. Oxford University Press.
- ZHOU, J. ADRIAN, R. J., BALACHANDAR, S. & KENDALL, T. M. 1999 Mechanisms for generating coherent packets of hairpin vortices in channel flow. *J. Fluid Mech.* **387**, 353–396.

Paper 4

4

Stability analysis of experimental flow fields behind a porous cylinder for the investigation of the large-scale wake vortices

By **Simone Camarri**¹, **Bengt E. G. Fallenius**² and **Jens H. M. Fransson**²

¹ Dipartimento di Ingegneria Aerospaziale, Università di Pisa, Italy

² Linné Flow Centre, KTH Mechanics, SE-100 44 Stockholm, Sweden

It is known in the literature that the linear stability analysis of the time-averaged flow field past a circular cylinder, after the primary wake instability, predicts a global mode which is marginally stable with a frequency in time that well approximates the one of the saturated vortex shedding. This behavior has recently been shown to hold up to Reynolds number $Re = 600$ by direct numerical simulations. In the present work we verify that the global stability analysis provides reasonable estimation also when applied to experimental velocity fields measured in the wake past a porous circular cylinder at $Re \simeq 3.5 \times 10^3$. Different intensities of continuous suction and blowing through the entire surface of the cylinder are considered. The global direct and adjoint stability modes, derived from the experimental data, are used to realign the random instantaneous snapshots of the velocity field in phase. The proposed method is remarkable, realigning the snapshots in phase with respect to the vortex shedding, allowing phase-averaged velocity fields to be extracted from the experimental database. The phase averaged flow fields are analyzed in order to study the effect of the transpiration on the kinematical characteristics of the large-scale wake vortices.

1. Introduction

It is known in the literature (see e.g. Barkley 2006) that the linear stability analysis of the time-averaged flow field past a circular cylinder, after the primary wake instability, predicts a global mode which is marginally stable with a frequency in time that well approximates the one of the saturated vortex shedding. On the other hand, if the analysis is carried out on the steady unstable flow field, an unstable global mode is obtained with (i) an amplification factor which increases with Reynolds number (Re), and (ii) a frequency which diverges with respect to the experimental one as Re increases. An interpretation of above

behavior was reported already in 2003 by Noack *et al.*, based on a reduced-order model of the flow, which suggests that the amplitude of the oscillating wake saturates precisely when the mean flow becomes marginally stable. The same behavior has been explained in detail in Sipp & Lebedev (2007), where a multiple scale analysis is carried out for the Navier-Stokes equations for Re in the neighborhood of the critical one for the onset of the unsteady von Kármán eddy street, i.e. $Re_{cr} \simeq 46$. The paper shows that above behavior cannot be generalized to any flow, as an example it is shown that in the driven cavity flow the analysis on the time-averaged flow field does not yield the right frequency of the saturated global mode, but conditions for this to happen are given. The analysis carried out in Sipp & Lebedev (2007) is linearized around Re_{cr} , and it cannot be extended for $Re \gg Re_{cr}$, which is a common condition at least for a bluff body. In Barkley (2006) the behavior described above is shown to hold up to $Re = 180$, and all the work is carried out numerically through direct numerical simulation (DNS). More recently, Leontini *et al.* (2010) has shown by DNS that the same behavior holds up to $Re = 600$.

As a first objective, in the present paper we try to extend the analysis described in Leontini *et al.* (2010) to higher values of the Reynolds number, verifying whether or not a linearized stability analysis on the mean flow field still provides reasonable results for a bluff body flow. Here, we consider the flow around a circular cylinder with transpiration from the walls at a Reynolds number, based on the free-stream velocity and on the cylinder diameter, equal to 3.5×10^3 . For this flow, we have performed experiments in the very-near wake of the cylinder for different rates of continuous suction and blowing through the cylinder surface. Entire flow fields have been captured using particle image velocimetry (PIV) and the Strouhal frequency was measured using hot-wire anemometry, the latter being published in Fransson *et al.* (2004). The Strouhal numbers estimated through the global stability analysis of the mean flow fields are here compared with the experimental ones. Moreover, the global direct and adjoint modes found by the stability analysis of the time-averaged flow fields are used for several purposes. First of all, they are used to locate the core of the instability following the work in Giannetti & Luchini (2007). This information is useful for comparison with the equivalent maps found for the primary wake instability and to verify a-posteriori the adequacy of the PIV measurement window for the linearized stability analysis. Moreover, the global direct and adjoint modes are used to realign the available instantaneous PIV flow snapshots with respect to the phase of the vortex shedding. In fact, for each transpiration velocity, a database consisting of about 1000 instantaneous snapshots is available, and the snapshots have been taken at a low frequency with respect to the vortex shedding one (ratio of about 1 over 2) without phase triggering. As a result, only statistical quantities can be directly extracted from the database. In this work we propose and test a procedure, based on the global direct and adjoint modes found in the stability analysis of the mean

flow field, to realign the available snapshots with respect to the phase of the vortex shedding. As a consequence, it is possible to derive phase-averaged flow fields from the available database, which allows a detailed analysis of the characteristics of wake vortices, such as their trajectory, formation length, velocity and shape. This analysis is carried out here for different values of the transpiration velocity through the cylinder surface in order to show the effects of transpiration on the large-scale wake vortical structures.

2. Experimental setup and collected database

2.1. Experimental setup

The experiments were performed in the Boundary Layer (BL) wind tunnel at KTH Mechanics, Stockholm. The cross sectional area of the test section is $0.5 \times 0.75 \text{ m}^2$, and it is 4.2 m long with a maximum speed of 48 m s^{-1} . The flow quality in this tunnel is considered good with a turbulence intensity (of all three components) of less than 0.04% of the free stream velocity. For more details about the tunnel the interested reader is referred to Lindgren (2002).

The same porous cylinder as was used by Fransson *et al.* (2004) for flow visualisation was used in the present investigation. The cylinder consists of a cross profile made of brass as an inner skeleton. A sintered plastic material shaped to a cylinder is then slid over the brass profile and sealed, creating four isolated chambers through where different amount of blowing or suction may be applied. The end parts were made of brass pieces and act as plugs on each side of the cylinder. These were equipped with four inlets for tube connections that were confluent before connected to a flow meter (rotameter type). Tubing was also used to lead air to or from a low or high pressure vessel, respectively, depending on whether suction or blowing was desired. The pressure source was either a regular vacuum cleaner, for suction, or a compressor, for blowing.

In figure 1 a schematic of the experimental setup is shown with relevant measures. The cylinder was mounted vertically in the test section and has a diameter of $D = 50 \text{ mm}$ and a porous length of 600 mm. The porous material is a sintered plastic material with an average pore size of $16 \mu\text{m}$, and the thickness (t) is 2.5 mm. Previous surface roughness measurements on a similar but flat porous plate (see Fransson & Alfredsson 2003) showed a deviation of $\pm 1 \mu\text{m}$ from the mean surface, which for the present case can be considered to be hydraulically smooth. The cylinder is made from a flat plate which is bent to form a circular cylinder. This means that there is a joint in the axial direction along the full length of the cylinder, and this gives rise to a small asymmetry with a 0.5 mm larger diameter in average when measured over the joint. The joint is therefore positioned at 180° , i.e. behind the cylinder in the streamwise direction, in order to avoid any flow asymmetry.

For the velocity measurements a PIV-system was used in order to allow entire flow fields to be captured instantaneously. The PIV-system used consists

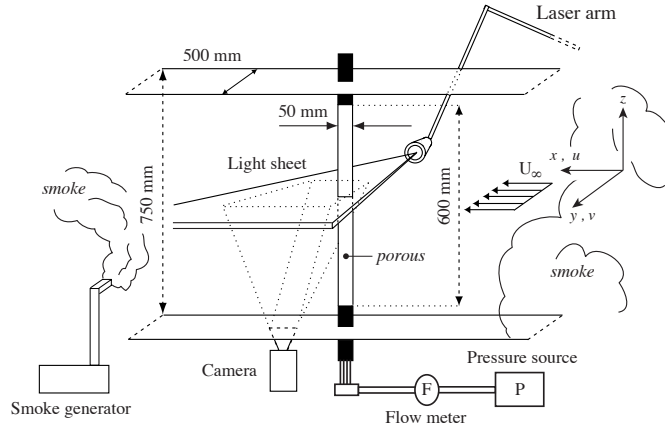


FIGURE 1. Schematic of the experimental setup. Flow is from right to left.

of a Spectra Physics 400 mJ double pulsed Nd:Yag laser operating at 15 Hz as a light source, and the camera is a double-frame Kodak ES1.0 8-bit CCD camera with 1018×1008 pixels. Furthermore, a laser arm was connected to the laser, which facilitates traversing of the laser sheet. The air was seeded with smoke particles generated by heating a glycol based liquid with a disco smoke generator, JEM ZR20 Mk II. The smoke inlet to the tunnel was in the open cross section between the end of the test section and the diffuser. Before the measurements the smoke was recirculated in the tunnel until the air became homogeneously seeded. See figure 1 for an illustration.

2.2. PIV database

In the present work we will consider a cartesian frame of reference with the z -axis coinciding with the symmetry axis of the cylinder centre and the x -axis aligned with the free stream velocity (cf. figure 1). All quantities are normalized using the free stream velocity (U_∞), which was kept constant at 1 m s^{-1} , and the diameter of the cylinder (D). The transpiration parameter Γ , measuring the flow across the cylinder surface, is defined as $\Gamma = V_t/U_\infty \times 100$ giving positive or negative values depending on the direction of the transpiration velocity (V_t).

Once the cylinder is mounted inside the test section a non-uniform suction/blowing rate is expected in the circumferential direction of the cylinder surface since the static pressure on the cylinder surface varies when exposed to an oncoming flow and the fact that the tubing from the different chambers are

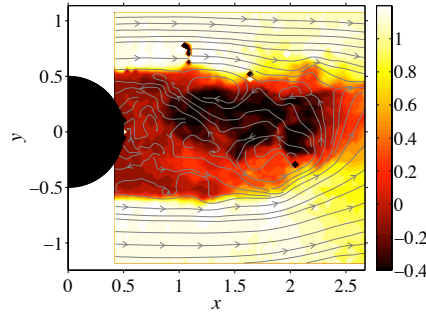


FIGURE 2. EXP: Instantaneous velocity fields for the case $\Gamma = -2.57$: streamlines and x -component of the velocity vector (colorscale map).

confluent before connected to the pressure source. However, the influence can be shown to be rather small. For the suction case the largest suction velocity occurs along the front stagnation line and then it decreases towards the rear. In the separated region the suction velocity is fairly constant and for a suction rate of 1.4% of the free stream velocity the suction velocity is reduced by about 6% smaller in this region as compared to the front. For larger suction rates the difference becomes smaller. In contrast, for the blowing case the smallest injection velocity is along the frontal stagnation line and then increases and becomes constant beyond 65° . In this case the maximum variation is less than 7% and the variation decreases with increasing blowing rate.

The PIV measurements are taken over several shedding cycles, giving the two velocity components in the x - and y -directions, in a window which comprises the mean recirculation bubble behind the cylinder. In particular, for the cases with suction from the cylinder, one measurement window is available, which approximately comprises the box $[0.4, 2.7] \times [-1.1, 1.1]$, in the x - and y -directions, respectively. For the blowing cases (case $\Gamma=0$ included), a second measurement window was also taken since the recirculating bubble elongates in the x direction as Γ is increased. The second window comprises the box $[1.8, 4.7] \times [-1.4, 1.4]$, in the x - and y -directions, respectively. In both windows, the velocity field is estimated over a uniform grid of 62×62 points. Consequently, the spatial resolution is equal to $\Delta_x \simeq \Delta_y \simeq 3.6 \cdot 10^{-2}$ in the first window, and equal to $\Delta_x \simeq \Delta_y \simeq 4.8 \cdot 10^{-2}$ in the second.

In order to give examples of the available experimental dataset, an instantaneous velocity field for the suction case of $\Gamma = -2.57$ is shown in figure 2, and the corresponding time-averaged velocity field along with the time-averaged field of the blowing case of $\Gamma = +2.57$ are reported in figure 3(a) and (b), respectively. In figure 3(b) the two overlapping measuring windows can clearly

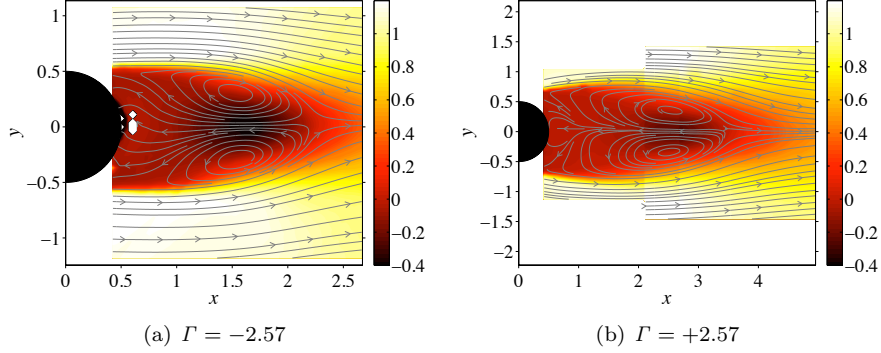


FIGURE 3. EXP: Time-averaged velocity field for the cases $\Gamma = -2.57$ and $\Gamma = +2.57$: streamlines and x -component of the velocity vector (colorscale map).

be seen. Moreover, the white region in figure 3(a), just behind the cylinder, indicates a region where the available velocity measurements are not trustable.

3. Stability problem formulation

In this section we concisely describe the mathematical problem related to the stability and sensitivity analysis for a porous cylinder. In the last subsection we finally discuss the case in which the stability analysis is applied to a mean flow field instead of a steady solution of the Navier-Stokes (NS) equations.

3.1. Linear stability analysis

The problem at issue is governed by the incompressible NS equations:

$$\frac{\partial \mathbf{u}}{\partial t} + \mathbf{u} \cdot \nabla \mathbf{u} = -\nabla p + \frac{1}{Re} \Delta \mathbf{u}, \quad (1a)$$

$$\nabla \cdot \mathbf{u} = 0, \quad (1b)$$

where (\mathbf{u}, p) is the non-dimensional flow field (velocity and pressure) and Re is the flow Reynolds number based on the reference velocity U_∞ and length D . We consider here the open flow around a porous cylinder. In this case, we suppose to have the following boundary conditions: (i) at the inflow the free-stream velocity is imposed, (ii) at the outflow we impose null stresses, i.e. $p\mathbf{n} - Re^{-1}(\mathbf{n} \cdot \nabla \mathbf{u})$, (iii) on the lateral boundaries we assume symmetry conditions and (iv) transpiration conditions are suppose to hold on the solid walls, i.e. $\mathbf{u} \cdot \mathbf{n} = V_t$. Recall, V_t is the transpiration velocity, which is set to a constant value over the cylinder surface in the numerical simulations.

We indicate with $Q_s = (\mathbf{U}_s, P_s)$ the steady solution to Eqs. (1). In order to study the linear stability of this steady solution we derive the linearized evolution equations for a small perturbation (\mathbf{u}', p') imposed on Q_s in agreement with Eqs. (1). As a further step, the linearized perturbation (\mathbf{u}', p') is sought in the form of normal modes:

$$\mathbf{u}'(x, y, t) = \hat{\mathbf{u}}(x, y) \exp(\sigma t) , \quad (2a)$$

$$p'(x, y, t) = \hat{p}(x, y) \exp(\sigma t) , \quad (2b)$$

The evolution equations for $(\hat{\mathbf{u}}, \hat{p})$ become:

$$\sigma \hat{\mathbf{u}} + \mathbf{U}_s \cdot \nabla \hat{\mathbf{u}} + \hat{\mathbf{u}} \cdot \nabla \mathbf{U}_s - \frac{1}{Re} \Delta \hat{\mathbf{u}} + \nabla \hat{p} = 0 , \quad (3a)$$

$$\nabla \cdot \hat{\mathbf{u}} = 0 , \quad (3b)$$

with homogeneous velocity boundary conditions at the inflow and on the cylinder surface, and the same boundary conditions as for Eqs. (1) on the remaining boundaries. The Eqs. (3), together with the boundary conditions, is an eigenvalue problem. Any solution $(\hat{\mathbf{u}}, \hat{p})$, associated to the eigenvalue $\sigma = \lambda + i\omega$, is a global mode with time growth rate equal to λ ($\lambda > 0$ indicates an unstable mode) and angular frequency ω . Note, that the associated frequency is given by $f = \omega/(2\pi)$, and is given directly in non-dimensional form as a Strouhal number based on the same reference quantities U_∞ and D used to normalize the NS equations.

3.2. Sensitivity to a structural perturbation of the linearized NS equations

Let us consider a global mode $\sigma, (\hat{\mathbf{u}}, \hat{p})$, and let us suppose that a perturbation of the following form is applied to the Eqs. (3):

$$\sigma'' \hat{\mathbf{u}}'' + \mathbf{U}_s \cdot \nabla \hat{\mathbf{u}}'' + \hat{\mathbf{u}}'' \cdot \nabla \mathbf{U}_s - \frac{1}{Re} \Delta \hat{\mathbf{u}}'' + \nabla \hat{p}'' = \delta H(\hat{\mathbf{u}}'', \hat{p}'') , \quad (4a)$$

$$\nabla \cdot \hat{\mathbf{u}}'' = 0 , \quad (4b)$$

where δH is a generic linear operator of the flow field. Since σ'' is a perturbation of the eigenvalue σ caused by the perturbation δH , it is convenient to relate the two as $\sigma = \sigma'' + \delta\sigma$. Carrying out a linearized analysis, we can directly derive the perturbation of the eigenvalue $\delta\sigma$ (see e.g. Giannetti & Luchini 2007; Marquet *et al.* 2008):

$$\delta\sigma = \langle \hat{\mathbf{u}}^+, \delta H(\hat{\mathbf{u}}, \hat{p}) \rangle , \quad (5)$$

where $\langle \cdot, \cdot \rangle$ is the scalar product defined as:

$$\langle \mathbf{a}, \mathbf{b} \rangle = \int_{\Omega} \mathbf{a}^* \cdot \mathbf{b} \, d\Omega , \quad (6)$$

where Ω is the flow domain and $()^*$ stands for complex conjugate. The vector field $\hat{\mathbf{u}}^+$ is the velocity field of the mode adjoint to $\sigma, (\hat{\mathbf{u}}, \hat{p})$, solution of the following eigenvalue problem:

$$\sigma^* \hat{\mathbf{u}}^+ - \mathbf{U}_s \cdot \nabla \hat{\mathbf{u}}^+ + \nabla \mathbf{U}_s \cdot \hat{\mathbf{u}}^+ - \frac{1}{Re} \Delta \hat{\mathbf{u}}^+ + \nabla \hat{p}^+ = 0, \quad (7a)$$

$$\nabla \cdot \hat{\mathbf{u}}^+ = 0, \quad (7b)$$

where $()^{(T)}$ stands for the transpose and $\sigma^*, (\hat{\mathbf{u}}^+, \hat{p}^+)$ is the adjoint mode of $\sigma, (\hat{\mathbf{u}}, \hat{p})$. As concerns the boundary conditions, $\hat{\mathbf{u}}^+ = 0$ at the inlet and on the solid walls, symmetry boundary conditions hold on the lateral walls and the following conditions hold at the outflow: $\hat{p}^+ \mathbf{n} - Re^{-1} (\mathbf{n} \cdot \nabla \hat{\mathbf{u}}^+) = (\mathbf{U}_s \cdot \mathbf{n}) \hat{\mathbf{u}}^+$. Moreover, the velocity field $\hat{\mathbf{u}}^+$ is normalized such that:

$$\langle \hat{\mathbf{u}}^+, \hat{\mathbf{u}} \rangle = 1. \quad (8)$$

As discussed in Giannetti & Luchini (2007), the wavemaker of the global instability can be identified from the analysis of the sensitivity to a particular form of the perturbation $\delta \mathbf{H}$, which is a local velocity-force feedback through a constant feedback matrix \mathbf{C}_0 :

$$\delta \mathbf{H}(\mathbf{u}, p) = \mathbf{C}_0 \delta(x - x_0, y - y_0) \mathbf{u}. \quad (9)$$

Substituting this particular form of perturbation in (5) we obtain

$$\delta \sigma = \mathbf{C}_0 : \left(\int_{\Omega} \hat{\mathbf{u}}^{+*} \hat{\mathbf{u}} \right). \quad (10)$$

The term within brackets is a sensitivity tensor, the symbol $:$ indicating matrix scalar product, and we can estimate an upper bound for $\delta \sigma$ of the following type:

$$|\delta \sigma| \leq \|\mathbf{C}_0\| \Lambda(x, y), \quad (11)$$

where

$$\Lambda(x, y) = \|\hat{\mathbf{u}}^+(x, y)\| \|\hat{\mathbf{u}}(x, y)\|. \quad (12)$$

The sensitivity analysis described in this section can also be carried out at the discrete level, starting from the numerically discretized eigenvalue problem (3). Independently of the numerical method used to discretize the differential operators, the result can be recast in the form:

$$\sigma \mathbf{B} \mathbf{w} = \mathbf{A} \mathbf{w}, \quad (13)$$

where \mathbf{w} is a vector collecting all the discrete unknowns of the problem, i.e. velocity components and pressure on each degree of freedom of the discrete problem, \mathbf{B} is a matrix which has zeros on the rows corresponding to the boundary conditions and, on the remaining parts, it is equal to a mass matrix for Galerkin methods or a diagonal identity matrix for a finite-difference method. The matrix \mathbf{A} contains the discretization of the differential operators and includes the boundary conditions. At the discrete level, the perturbation

operator δH acts as a perturbation of the discrete operators $\delta \mathbf{A}$. Thus, the perturbed problem becomes:

$$\sigma \mathbf{B} \mathbf{w} = (\delta \mathbf{A} + \mathbf{A}) \mathbf{w} . \quad (14)$$

Carrying out a linearized analysis, the perturbation of the eigenvalue $\delta \sigma = \sigma'' - \sigma$ can be obtained as

$$\delta \sigma = \frac{\langle \xi, \delta \mathbf{A} \mathbf{w} \rangle}{\langle \xi, \mathbf{B} \mathbf{w} \rangle} , \quad (15)$$

where ξ is the adjoint eigenvector associated with σ , corresponding to the solution of the problem:

$$\mathbf{A}^* \xi = \sigma^* \mathbf{B}^* \xi . \quad (16)$$

The Eq. (15) is equivalent to Eq. (5) at a discrete level, but with the advantage that the boundary conditions for the discrete adjoint problem are automatically taken into account and it is not necessary to derive them explicitly. Thus, for the sensitivity analysis in the present work we will be using this latter method, i.e. the discrete adjoint method.

3.3. Linear stability analysis on the mean flow field

The analysis described above remains formally identical irrespective of whether we consider a time-averaged flow field \mathbf{U}_m or a steady solution of the NS equations \mathbf{U}_s . However, we have to point out that the field \mathbf{U}_m is not generally a solution to the NS equations, but it is to the following set of equations:

$$\mathbf{U}_m \cdot \nabla \mathbf{U}_m = -\nabla P_m + \frac{1}{Re} \Delta \mathbf{U}_m - \nabla \cdot (\overline{\mathbf{u}'' \mathbf{u}''}) , \quad (17a)$$

$$\nabla \cdot \mathbf{U}_m = 0 , \quad (17b)$$

where \mathbf{U}_m is the time-averaged flow field, $\mathbf{u}'' = \mathbf{u} - \mathbf{U}_m$ is the fluctuating velocity field and $-\overline{(\mathbf{u}'' \mathbf{u}'')}$ is the Reynolds-stress tensor.

However, the analysis documented in Sipp & Lebedev (2007) gives a precise meaning to the stability analysis carried out on the mean flow field, as stated also in the introduction, at least for values of Re close to Re_{cr} .

3.4. Numerical method for the stability analysis

The stability analysis has been carried out discretizing all the differential operators by standard centered second-order finite difference schemes. The equations are discretized in conservative form and a staggered grid is employed to eliminate spurious pressure modes. The resulting generalized eigenvalue problem, which has the form given in Eq. (13), has been solved with an inverse iteration method (see Giannetti & Luchini 2007) and/or with the Krylov-Schur subspace method implemented using the SLEPC library (Hernández *et al.* 2009). The corresponding adjoint eigenvalue problem has been derived directly at a

discrete level (as discussed above), so that the boundary conditions are automatically taken into account and the bi-orthogonality property is preserved up to machine accuracy.

4. Results

4.1. Preliminary stability analyses for case $\Gamma = -2.57$

A first set of stability analyses have been carried out in order to test the sensitivity of the results with respect to the different numerical aspects of the analysis, with a particular attention to the problem boundary conditions. Indeed, the mean flow field is available only in a small measuring window which contains just the recirculating bubble. From previous works in the literature (see Giannetti & Luchini 2007) we know that the wavemaker of the primary wake instability is located in two symmetric lobes centered on the streamlines bounding the recirculating bubble. This behavior is supposed to hold also for the mean flow field, and an indication in this direction is given by the results of the local stability analysis of mean wake flows that are available in the literature. Consequently, we expect that the results of a global stability analysis of the mean flow (in terms of predicted frequency of the global mode) is insensitive to the boundary conditions applied to the perturbation velocity field, provided that the recirculation bubble is well included in the computational domain for the analysis. However, the available measurement windows do not always respect this constraint for all the considered values of Γ , and thus the suitability of the available measurements needs to be evaluated a-posteriori as described in the following.

The case with $\Gamma = -2.57$ has been selected as a reference case, because in this case the recirculation bubble is well included into the available measurement window. Moreover, a suction case has been selected in order to avoid complications deriving from the overlapping of the two available measurement windows. The linear stability analysis has been carried out on the time-averaged flow field described in section 2.2 and reported in figure 3(a), and the flow has been considered starting from $x_{in} \simeq 0.57 D$, i.e. the body is not included in the global analysis. Uniform cartesian grids with different spatial resolutions are build for the stability analysis, and the flow field of figure 3(a) is (i) interpolated on the grids and (ii) symmetrized around line $y = 0$ (taking the average between the original field and the reflected one with respect to $y = 0$). Cubic splines are used for interpolation, and it has been verified that the type of interpolation (linear or cubic) does not affect the results. The coarser resolution is the same as the one of the original PIV fields, with almost coinciding nodes (for one velocity component only since a staggered grid is used), in order to minimize the role of interpolation at least for one case. Three grid resolutions have been used here: 58×62 , 120×120 and 400×60 . An

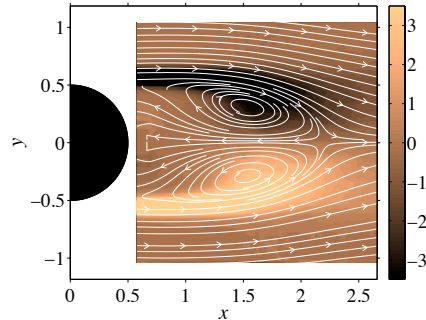


FIGURE 4. EXP: Time-averaged flow field interpolated and made symmetrical on a uniform staggered cartesian grid of resolution 120×120 for the porous cylinder ($\Gamma = -2.57$): streamlines and vorticity (colorscale map; the colors in the legend has been saturated in order to see the vortical structures in the wake, the maximum vorticity value on the shear layers being approximately equal to ± 13).

example of time-averaged flow field used for the stability analysis is reported in figure 4.

Concerning the boundary conditions for the linearized equations, two different sets have been used, (BC1, BC2), differing for the outlet conditions. For both it is assumed that the velocity disturbance vanishes on the inflow and lateral surfaces. On the outflow boundary, for BC1 it is imposed that (i) the continuity equation is valid also on the boundary, (ii) $\frac{\partial v}{\partial x} = 0$ and (iii) $p = 0$. For BC2 the unphysical condition that the velocity disturbance vanishes on the outflow boundary is imposed. We wish to point out that it is impossible here to impose realistic boundary conditions on the domain boundary. However, as already discussed, the eigenvalue associated to the unstable mode is not sensitive to the boundary conditions, provided that the computational domain contains the core of the instability. In any case, for the problem at issue, the size of the computational domain is dictated here by the available experimental flow measurements. However, as it is shown in table 1, the eigenvalue associated to the vortex shedding instability is slightly sensitive to the outflow boundary conditions and to the boundary conditions on the lateral faces of the computational box (this second aspect is not shown in the present results). Indeed, for a resolution equal to 120×120 , the variation of the predicted Strouhal number St , switching from BC1 to BC2, is approximately 7%. This variation is acceptable considering that BC2 contains a definitely strong and unphysical condition at the outflow boundary, since it is imposed that the disturbance velocity vanishes. The tests in table 1 confirms a low sensitivity of the estimated unstable eigenvalue with respect to the conditions imposed at the outflow. This

| Resolution | BCs | Stabilized | Divergence-Free | Strouhal N. | Ampl. Fact. |
|-------------|-----|------------|-----------------|----------------|-------------|
| 58×62 | BC1 | N | N | 0.285 | 0.200 |
| 120×120 | BC1 | N | N | 0.286 | 0.213 |
| 400×60 | BC1 | N | N | 0.287 | 0.188 |
| 58×62 | BC1 | N | Y | 0.276 | 0.215 |
| 120×120 | BC1 | Y | N | 0.285 | 0.212 |
| 120×120 | BC2 | Y | N | 0.306 | 0.220 |
| Experiments | | | | $\simeq 0.283$ | |

TABLE 1. Results obtained from several stability analysis of the cylinder mean flow; the experimental value has been extracted approximately from Eq. (2) reported in Fransson *et al.* (2004).

statement will further substantiated by the combined analysis of the direct and adjoint unstable modes reported in the following.

Since the flow Reynolds number is large ($Re = 3.5 \times 10^3$), thin boundary layers can form near the domain boundaries. In particular, this problem is important near the outflow boundary for the direct problem, especially for the boundary conditions BC2, and for the inlet boundary for the adjoint problem. We recall that the adjoint equations are derived building the adjoint of the discretized direct problem, and thus the associated boundary conditions are automatically found such that (i) the eigenvalue of the adjoint problem is equal to the conjugate of the direct one up to machine accuracy and (ii) bi-orthogonality property is preserved between direct and adjoint modes up to machine accuracy. It is well known that thin boundary layers, typical of convection-dominated problems, can cause numerical spurious oscillations for coarse resolutions, and there are several ways to avoid this problem, usually by addition of artificial diffusion on the boundary layers. In the present problem the regions where oscillations can be generated are close to the boundaries of the computational domain, which do not sensibly influence the estimated unstable eigenvalue. Thus, artificial diffusion has been added in a thin layer adjacent to the inflow and outflow boundaries to damp the oscillations in the flow field. As we will see, this will not affect the found eigenvalues, but spurious oscillations are eliminated in the eigenmodes. This is important when the stability direct/adjoint modes are used in the reordering procedure of the snapshots reported later (see section 4.3), since in this case discrete scalar product needs to be carried out between the modes and the flow snapshots. To give an example, in figure 5 we report on the same figure the modulus of the vertical component of the adjoint unstable mode obtained at $Re = 3.5 \times 10^3$, with BC1 (a) without and (b) with additional dissipation near the domain boundaries.

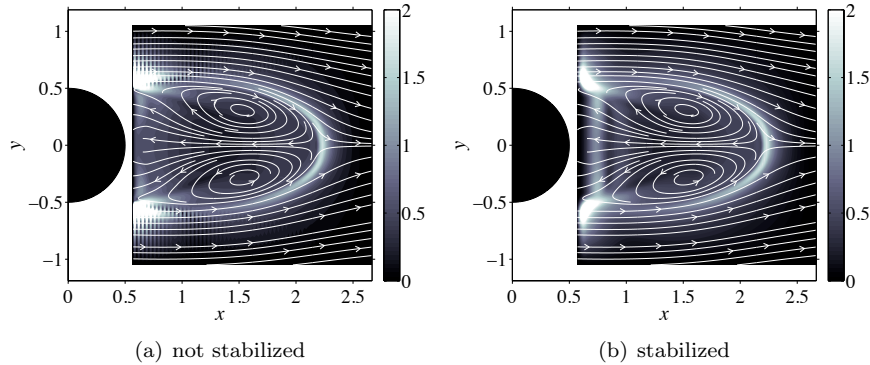


FIGURE 5. Modulus of the vertical velocity of the adjoint mode obtained at $Re = 3.5 \times 10^3$ behind the porous cylinder with a spatial resolution 120×120 (a) without and (b) with artificial dissipation near the domain boundaries; the streamlines of the time-averaged flow field are also reported in the figure.

Artificial dissipation is obtained in practice by decreasing the flow Reynolds number to a value equal to 20 with an exponential function which acts on a layer of width equal to $0.2D$ at the inflow boundary and to $0.1D$ on the other boundaries. These values have been chosen heuristically on the basis of a few numerical experiments. The results reported in table 1 confirms that the estimated eigenvalues are almost insensitive to the stabilization, as expected.

Lastly, the time-averaged flow field is a divergence-free field. However, if the divergence is evaluated numerically by a discrete scheme it will not be exactly null, the error being due to both (i) measurements and (ii) numerical error in the discretization of the differential operators. However, from a numerical viewpoint, it might be important to have a field that is exactly divergence free at the discrete level, compatibly with the numerical scheme used for the linear stability analysis. In order to verify the sensitivity of the results to this aspect, a test has been carried out in which the mean flow, coming from the experiments and interpolated on the computational grid for the stability analysis, has been projected on a divergence-free subspace, so as to obtain a corrected flow field which is exactly divergence free at the discrete level. The stability analysis is then carried out on the corrected mean flow. The results, reported in table 1, show an influence on the computed Strouhal number and amplification factor which is however rather small, the variation on the Strouhal number being of the order of 3%. The projection of the mean flow has been carried out in a similar way to that used in projection methods to advance incompressible NS equations in time, i.e. a scalar field $\psi(x, y)$ has been searched such that the

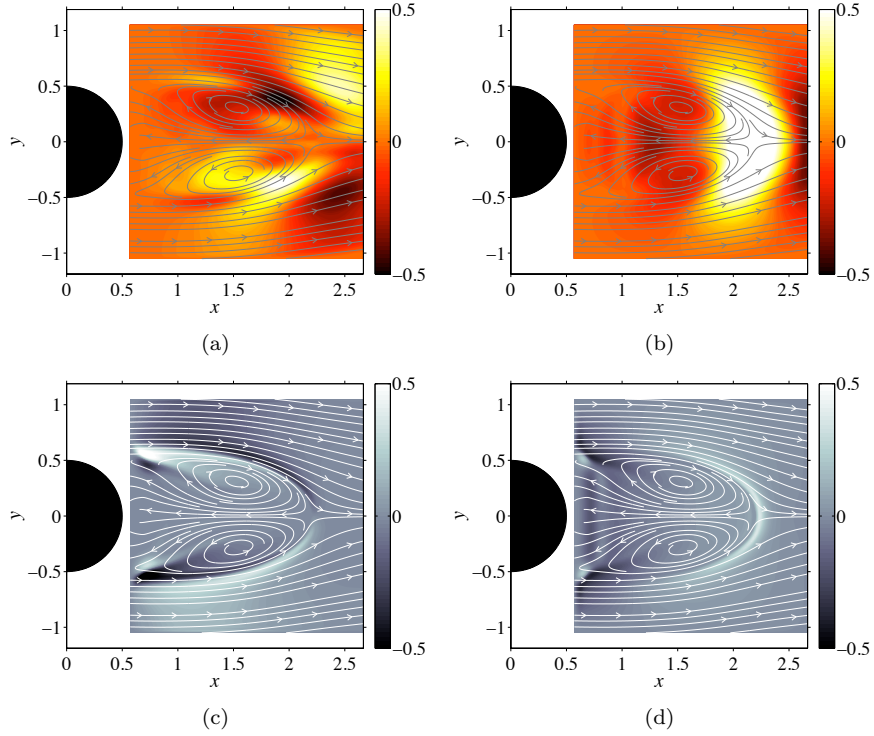


FIGURE 6. NUM from EXP: Unstable mode obtained at $Re = 3.5 \times 10^3$ behind the porous cylinder with a spatial resolution 120×120 at one particular phase: (a) horizontal and (b) vertical velocity of the direct mode and of its adjoint one (c, d respectively); the streamlines of the time-averaged flow field are also reported in the figure. The maps are obtained by normalizing the modes so that the maximum value of the velocity modulus in the field is equal to unity.

corrected mean flow $\mathbf{U}_m^c = \mathbf{U}_m - \nabla\psi$ is divergence-free, with proper boundary conditions on ψ such that the divergence-free property is preserved also on the boundaries.

The direct and adjoint unstable modes, artificially stabilized on the boundary, obtained with a resolution 120×120 at $Re = 3.5 \times 10^3$ are reported in figure 6.

In agreement with the theory in section 3.2, we can now quantify the sensitivity of the unstable mode to a localized velocity-force feedback in the linearized operator, in order to identify the core of the instability, i.e. the

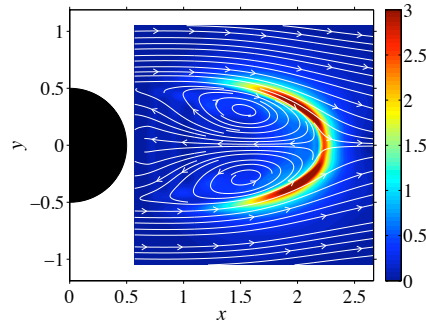


FIGURE 7. NUM from EXP: Sensitivity to a local velocity-force feedback $\Lambda(x, y)$ (see Eq. 12) obtained with a grid resolution 120×120 for the porous cylinder ($\Gamma = -2.57$); the streamlines of the time-averaged flow field are also reported in the figure.

region of the baseflow on which the instability depends. In particular, we report the map Λ of Eq. (12) in figure 7.

This map closely resembles the equivalent map obtained from the stability analysis of the primary instability of the cylinder at $Re \simeq 46$, see for instance figure 17 reported in Giannetti & Luchini (2007) or, equivalently, figure 6 reported in Marquet *et al.* (2008). However, the map is definitely more localized on the shear layers delimiting the average recirculation bubble, towards the closure of the bubble itself.

As a final comment on the obtained results, it is important to underline that the Strouhal number estimated by the linear stability analysis accurately predicts the experimentally measured one, especially when the more realistic boundary conditions BC1 are used, as shown in table 1. The experimental value of the Strouhal number, $St \simeq 0.283$, can be extracted from Eq. (2) reported in Fransson *et al.* (2004). It should be noted that the experiments performed in Fransson *et al.* were done in the Re -range, $8\,500 \leq Re \leq 21\,700$, but as expected no Re -dependence was shown and we are therefore also confident in our assumption that Eq. (2) in Fransson *et al.* also holds for $Re = 3.5 \times 10^3$. In table 1 the amplification factor obtained by this analysis is also shown (although physically meaningless), but was expected to be lower. In fact, at least up to $Re \simeq 180$, the stability analysis on the mean flow, obtained numerically through well resolved DNS simulations, leads to a global mode that is marginally stable, i.e. with an amplification factor near 0 (see Barkley 2006). This is also in agreement with the interpretation given in Noack *et al.* (2003) which suggests that the amplitude of the oscillating wake saturates precisely when the mean flow is marginally stable. However, the considered value of the Reynolds number here is definitely larger ($Re = 3.5 \times 10^3$), the wake is

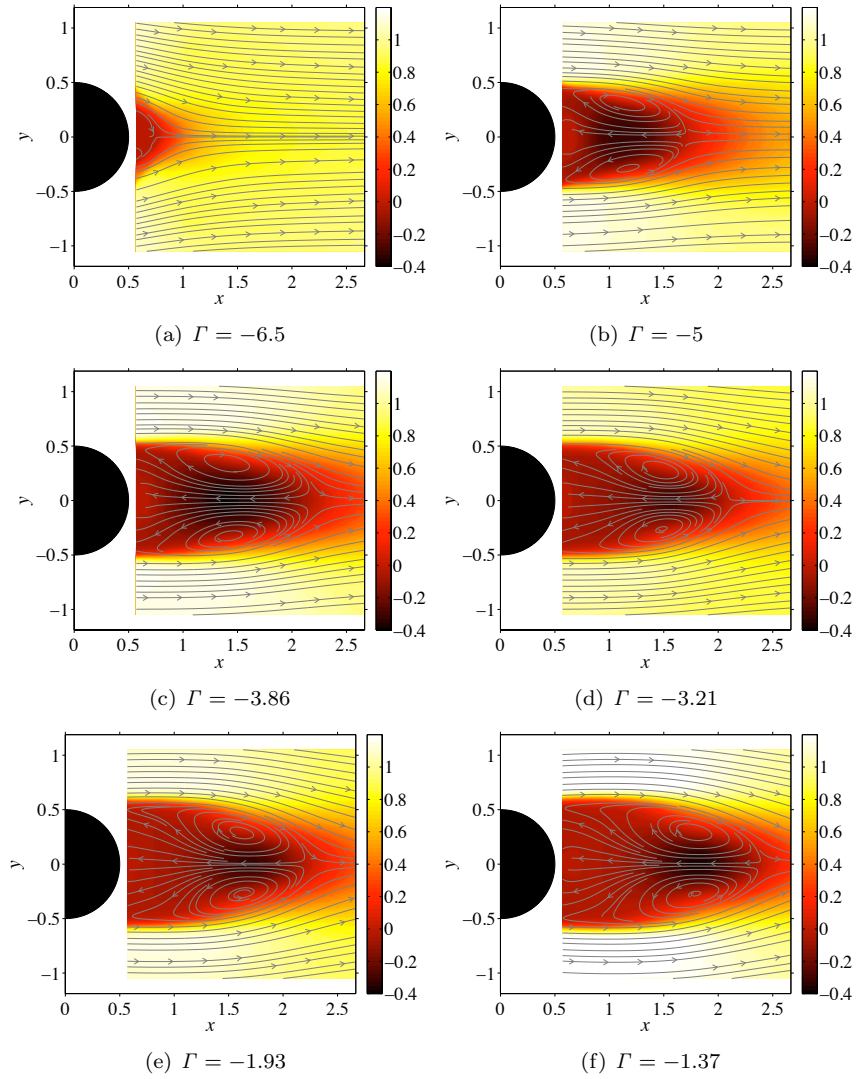


FIGURE 8. EXP: Time-averaged velocity fields interpolated and made symmetrical on a uniform cartesian grid of resolution 120×120 for different values of negative Γ : streamlines and horizontal velocity. Near field PIV window.

turbulent and, as far as the authors know, there are not other examples in the literature of a global stability analysis of experimental mean flow at this Reynolds number for a circular cylinder. Thus, we miss a criterion to judge

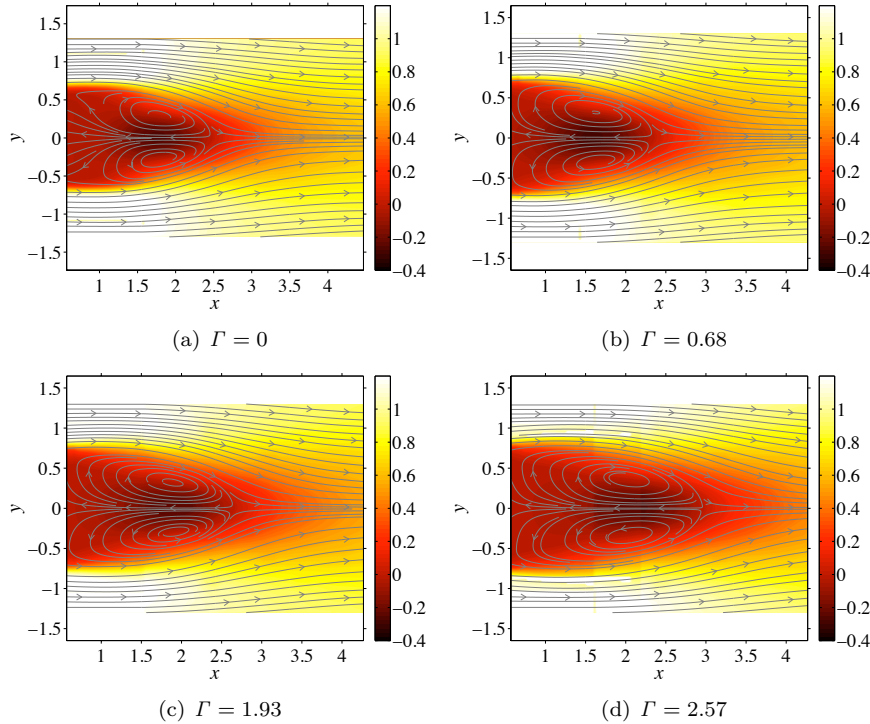


FIGURE 9. EXP: Time-averaged velocity fields interpolated and made symmetrical on a uniform cartesian grid of resolution 120×120 for different values of positive Γ : streamlines and horizontal velocity. Combined near- and far-field PIV windows. Near-field extrapolated in order to obtain a global field on a rectangular domain.

whether the obtained amplification factor is too large or not. Furthermore, we have to keep in mind that the stability analysis is carried out on experimental data, which are affected by some noise (even if averaged in time), the spatial resolution of the mean flow is fixed by the PIV measurements and might be poor in the shear layers delimiting the recirculating bubble (region of high sensitivity of the estimated eigenvalue) and, finally, the measurement window is just sufficient to obtain meaningful results, as it just includes the region of high sensitivity for the global mode.

4.2. Results of the linear stability analysis

In this subsection we concisely present the results obtained by applying the analysis described above to the mean flow fields measured for different values

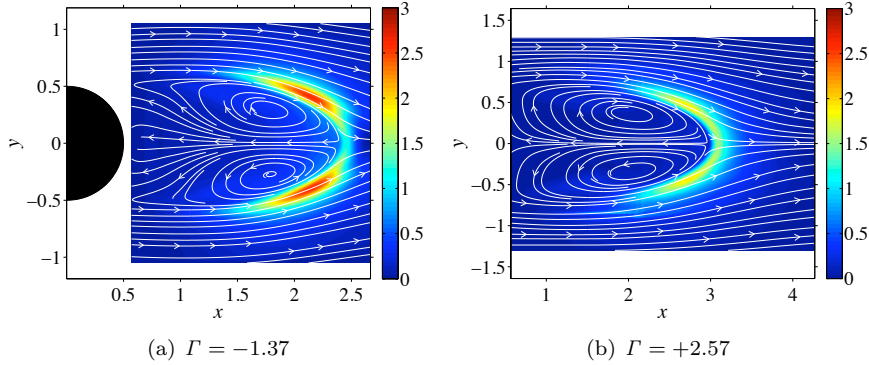


FIGURE 10. NUM from EXP: Sensitivity to a local velocity-force feedback $\Lambda(x, y)$ for cases $\Gamma = -1.37$ (a) and $\Gamma = +2.57$ (b) (see Eq. 12) obtained with a grid resolution 120×120 for the porous cylinder; the streamlines of the time-averaged flow field are also reported in the figure.

of the transpiration parameter Γ . On the basis of the results described in the previous section, all the tests documented here have been carried out on 120×120 grids, with a stabilization near the domain boundaries to avoid spurious oscillations of the eigenmodes and without projection of the mean flow fields on divergence-free subspace. Some of the experimental mean flow fields among the available ones are reported in figure 8 for the suction cases and in figure 9 for the blowing case. In the cases of blowing (positive Γ values), the two available measurement windows have an overlapping region. Alignment between the two windows has been adjusted for each case by maximizing the correlation coefficient between the two velocity fields in the overlapping region. Moreover, only for computational purposes, the flow field of the smaller window has been extrapolated in the "free-stream" in order to obtain a global field on a rectangular domain (compare, for instance, figure 9 and figure 3b). This extrapolation does not affect the results as long as the extrapolated region is far enough from the boundaries of the recirculating bubble. This aspect has been verified a-posteriori visualizing the core of the instability. However, already from the analysis of figure 9 it is clear that the recirculating bubble width increases as Γ is increased, and the results for $\Gamma = 2.57$ are expected to be affected by the extrapolation described above. This is confirmed by the sensitivity to a local velocity-force feedback $\Lambda(x, y)$ plotted in figure 10(b). On the other hand, in the suction cases, the length of the recirculating bubble increases as Γ is decreased. Again, the obtained results can be affected by the truncation of the measurement window if the closure of the recirculating bubble approaches the outflow boundary of the window. By inspecting figure 8 it can

| Γ | Reso- lution | BCs | Stabi- lized | Strouhal Numb. | Ampl. Fact. | Exp. value | Devia- tion |
|----------|-----------------|-----|-----------------|-------------------|----------------|---------------|----------------|
| -6 | 120×120 | BC1 | Y | – | stable | – | – |
| -5 | 120×120 | BC1 | Y | 0.290 | 0.186 | – | – |
| -3.86 | 120×120 | BC1 | Y | 0.266 | 0.203 | – | – |
| -3.21 | 120×120 | BC1 | Y | 0.255 | 0.174 | – | – |
| -2.57 | 120×120 | BC1 | Y | 0.285 | 0.212 | 0.283 | 0.7% |
| -1.93 | 120×120 | BC1 | Y | 0.267 | 0.14 | 0.241 | 9.7% |
| -1.37* | 120×120 | BC1 | Y | 0.308 | 0.124 | 0.216 | 30.0% |
| 0 | 120×120 | BC1 | Y | 0.232 | 0.106 | 0.2 | 13.8% |
| +0.68 | 120×120 | BC1 | Y | 0.218 | 0.039 | 0.190 | 12.8% |
| +1.93 | 120×120 | BC1 | Y | 0.193 | 0.024 | 0.188 | 2.6% |
| +2.57* | 120×120 | BC1 | Y | 0.1919 | -0.04 | 0.176 | 8.3% |

TABLE 2. Results obtained from the stability analysis of the cylinder mean flow at different values of Γ ; the symbol * for Γ indicates that the domain dimensions are not enough to have reliable results, as discussed in the text.

be noticed that this happens in cases characterized by $\Gamma \geq -1.37$. This is again confirmed a-posteriori by the analysis of the Λ map, reported in figure 10(a).

The Strouhal numbers versus Γ obtained in the tests are reported in table 2. The table shows that a reasonable agreement is obtained with respect to the experimental data. Moreover, the trend of the Strouhal number versus the parameter Γ is in complete agreement with the experiments. As expected, accuracy is lost for those cases ($\Gamma \geq -1.37$ on one measurement window and $\Gamma \geq 2.57$ for two measurement windows) in which the core of the instability approaches the boundary of the available experimental data. Surprisingly, the stability results confirm an inversion in the behavior of the Strouhal number vs Γ for cases $\Gamma = -3.21$ and $\Gamma = -3.86$. Indeed, the Strouhal number always increases as Γ is decreased, except for the two aforementioned cases. The same trend has been observed in the experiments, and it is related to an anomalous behavior of the recirculating bubble that can be observed in the mean flow fields in figure 8. In particular, the length and the width of the recirculation bubble decrease as Γ is increased, but this trend is inverted for cases $\Gamma = -3.21$ and $\Gamma = -3.86$. This aspect is not fully understood at present and it needs to be further investigated. We are confident that the results obtained from the stability analysis described here might provide useful information in this respect. Still in agreement with the experiments, at $\Gamma = -6$ the vortex shedding seems to be completely stabilized. Also the predicted

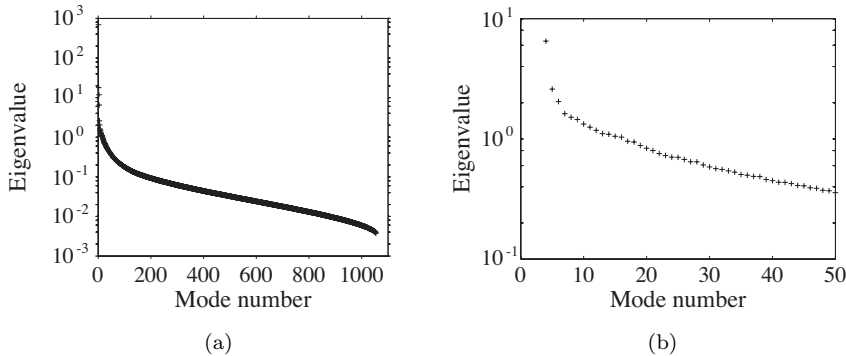


FIGURE 11. NUM from EXP: POD spectrum obtained at $Re = 3.5 \times 10^3$ behind the porous cylinder: (a) whole spectrum (1054 modes) and (b) detailed view of the first 50 modes.

amplification factors are reported in table 2, even if this value is not meaningful in the stability analysis of mean flows, as already discussed.

4.3. Reordering of the available snapshots according to the phase of the vortex shedding

The available experimental snapshots have been taken over several vortex shedding cycles and even in different experimental runs. Thus, their order with respect to the phase of the vortex shedding cycle can be considered uniformly randomized. However, for the analysis of the large-scale wake vortical structures, it is important to approximately align them with respect to the phase of the shedding process, so that information on the flow topology might be retrieved by properly averaging in phase the snapshots. One possibility to obtain this result is to use the Proper-Orthogonal-Decomposition (POD) technique to extract the dominant modes describing the vortex-shedding process, and later to project the snapshots on those modes so as to estimate a value for the phase angle of each snapshot, similarly to the approach described in Oberleithner *et al.* (2011). However, this method does not work here (maybe ad-hoc improvements might be possible), because the measuring window is small and located in the vortex-formation region. Thus, the significant turbulent velocity fluctuations makes it difficult to extract clear energetically dominant modes in the POD analysis. An alternative strategy is to use the modes obtained by the stability analysis instead of the POD modes to obtain the same result. Moreover, even if not necessary, we have available the mode adjoint to the vortex-shedding mode, which can be used to project the snapshots on the unstable mode itself. This method and its results are described in the following.

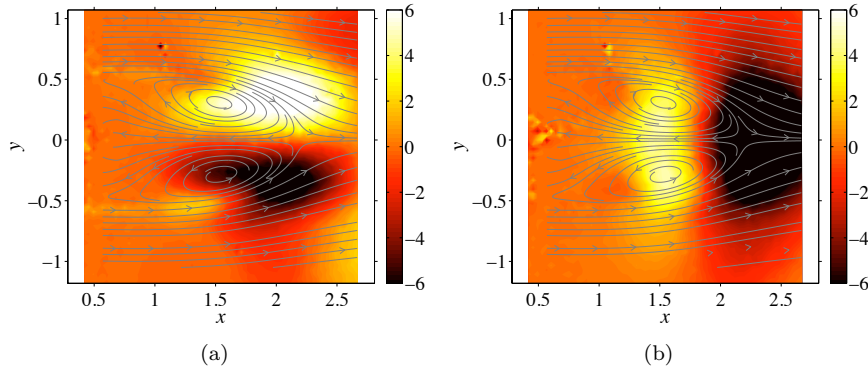


FIGURE 12. NUM from EXP: POD mode no. 2 obtained at $Re = 3.5 \times 10^3$ behind the porous cylinder: (a) horizontal and (b) vertical velocities.

The results obtained by the POD analysis are also described in the following, for the sake of completeness.

4.3a. *POD analysis: results.* The POD analysis has been carried out following the method of the snapshots of Sirovich (1987). As a prototype example, we consider the case with $\Gamma = -2.57$. The number of snapshots used for the POD analysis is $N_s = 1054$. The time-averaged flow field is not subtracted from the snapshots in the POD analysis, so that the first POD mode is the averaged flow field. Tests have been carried out also subtracting the averaged flow field but no significant differences have been noticed with respect to the results reported here.

From the spectrum of the POD eigenvalues, reported in figure 11, it is clear that the method is not able to isolate a dominant couple of modes that is typical when a vortex shedding flow is analyzed (see e.g. the spectra reported in Noack *et al.* 2003). Indeed, in this case, the dominant POD modes are typically organized in couples of equally energetic modes, associated to the vortical structures of the wake, which travel in the downstream direction. For this reason, the two modes of each couple are displaced in phase by a phase angle of $\pi/4$, as it happens between the real and the imaginary parts of the unstable mode resulting from the linear stability analysis of the wake. In this case there is not a structure of this kind in the found POD spectrum probably because (i) the turbulent fluctuations are strong, the measurement window is (ii) small and (iii) located near the vortex formation region, where the vortical structures are not energetically as strong as in the well-developed wake that can be observed just downstream of the mean recirculation bubble. Probably, in this case the information concerning the shedding mode are contained in more

than two modes, and this fact makes it tricky, or even impossible, to retrieve phase information from snapshots projection on the modes.

However, the dominant modes are clearly related to the vortex shedding process, as can be evinced for instance by comparing mode 2, reported in figure 12 and the unstable mode obtained by the stability analysis reported in figure 6.

4.3b. *Snapshots reordering using linear stability analysis: procedure description.*

It is well known that the unstable modes obtained by the linear stability analysis of the primary wake instability are a couple of complex conjugate modes. Each mode has its real and imaginary parts shifted in phase by an angle of $\pi/4$, so that when they are linearly combined together using a coefficient of the form $\exp(iCt)$, they describe flow structures moving in time t in the downstream direction. In particular, a picture of the vortex shedding process described by the unstable linear mode can be obtained as follows. If we indicate with $(\hat{\mathbf{u}}, \hat{p})$ the unstable mode associated with the eigenvalue $\sigma = \lambda + i\omega$ (obtained by the stability analysis on the time-averaged flow field \mathbf{U}_m), there will be also another complex-conjugate mode, associated with $\sigma^* = \lambda - i\omega$, of the form $(\hat{\mathbf{u}}^*, \hat{p}^*)$, due to the symmetry of the problem. A picture of the shedding process is then described by the following field:

$$\mathbf{u}_{vs}(x, y, t) = \mathbf{U}_m + \frac{A}{2}(\exp(i\omega t) \hat{\mathbf{u}}(x, y) + \exp(-i\omega t) \hat{\mathbf{u}}^*(x, y)) , \quad (18)$$

where the real coefficient A stands for the amplitude of the oscillating mode; A cannot be obtained by the linear stability analysis but can be estimated *a-posteriori* by an ad-hoc post-processing of the snapshots. In Eq. (18) the product $\Phi_T = \omega t$ is a phase angle at time t of the vortex-shedding process. Thinking of a normal mode decomposition of the velocity field $\mathbf{u}(x, y, t)$, and using the bi-orthogonality between the modes and their adjoint modes, i.e. $\langle \hat{\mathbf{u}}_j^+, \hat{\mathbf{u}}_k \rangle = \delta_{jk}$, we have:

$$\frac{A}{2} \exp(i\Phi_T) = \langle \hat{\mathbf{u}}^+, \mathbf{u}(x, y, t) - \mathbf{U}_m \rangle . \quad (19)$$

Consequently, ordering the snapshots with respect to the phase Φ_T , estimated according to Eq. (19), is equivalent to realign them with respect to the phase of the vortex shedding. The corresponding procedure can be summarized as follows:

1. a global stability analysis is carried out on the time averaged flow field, computing the unstable (marginally stable) mode $\hat{\mathbf{u}}$ corresponding to the vortex shedding mode in the wake and its adjoint mode $\hat{\mathbf{u}}^+$;
2. for each instantaneous velocity snapshot \mathbf{u}_k we estimate a phase angle $\Phi_T(k)$ according to Eq. (19);
3. we reorder the snapshots according to the values of Φ_T ;

An equivalent procedure can be obtained also in cases in which the adjoint mode $\hat{\mathbf{u}}^+$ is not available. In this case it is possible to build a field \mathbf{r} orthogonal to $\hat{\mathbf{u}}^*$ as follows:

$$\mathbf{r} = \hat{\mathbf{u}} - \frac{\langle \hat{\mathbf{u}}^*, \hat{\mathbf{u}} \rangle}{\langle \hat{\mathbf{u}}^*, \hat{\mathbf{u}}^* \rangle} \hat{\mathbf{u}}^* . \quad (20)$$

Consequently, according to Eq. (18), it is possible to obtain a phase angle Φ_T as:

$$\Phi_T = \text{Phase}(\langle \mathbf{r}, \mathbf{u}(x, y, t) - \mathbf{U}_m \rangle) . \quad (21)$$

Once reordered, the snapshots can be averaged in phase in order to smooth the visualization and to eliminate the uncorrelated velocity fluctuations that are due to the fact that (i) the flow is turbulent and (ii) the turbulent fluctuations are not correlated at all, since neighboring snapshots can have been taken at very different times in the experiment (or even in different experimental runs). The POD analysis can be used as a filter in order to reduce the noise in the velocity fluctuations in a pre-processing phase, before the alignment described above. However, our tests have shown that this preprocessing step is not necessary at all, the results being almost unaffected by it. For this reason we will not use a POD-based filter for the snapshots.

4.3c. *Numerical example.* As an example of the overall procedure, we have carried out the following numerical experiment. A two-dimensional bluff-body flow with a well developed vortex shedding instability has been simulated in time until a periodic-in-time flow was obtained. Then, several snapshots have been saved in time on a vortex shedding period. A POD analysis has been carried out on those snapshots, which allowed the identification of a couple of equally-energetic dominant modes associated to the vortex shedding. The order of the snapshots has been then randomized, and the angle Φ_T for each snapshot in the new random order has been estimated by projection on the two POD modes, which are real and mimic the real and imaginary parts of the complex mode found by the linear stability analysis. Once aligned for decreasing values of Φ_T , the snapshots returned perfectly aligned in time. The same result has been obtained using the stability modes instead of the POD ones. This small experiment shows that, as a proof of concept, the procedure described above works perfectly for a simple case with only one unstable global mode and well resolved flow fields over a large computational domain.

4.3d. *Application to the experimental snapshots.* We describe here the results of the reordering procedure when applied to the case $\Gamma = -2.57$. Results obtained for different values of Γ are analogous to those described here. The stability modes obtained in the analysis described in table 2 are used here. The modes, obtained on a grid 120×120 , have been resampled (bilinear interpolation) on the grid used in the PIV images, and all the points outside the window on which the numerical modes have been obtained were set to zero, in order to

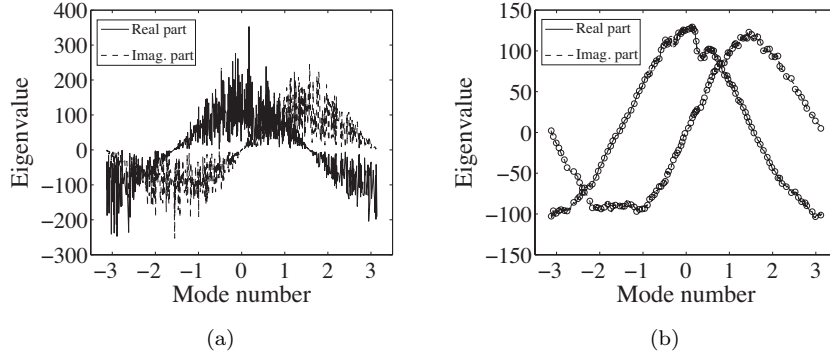


FIGURE 13. (a) Discrete scalar product between the adjoint unstable mode, obtained by a linear stability analysis of the time-averaged flow field at $\Gamma = 0$ with a resolution 120×120 and the available snapshots, once those have been ordered according to the phase angle Φ_T , reported as the x coordinate in the plots; (b) is the same as (a) but a phase average has been carried out for each snapshot, considering in the average 25 snapshots before and 25 snapshots after each considered snapshot.

exclude those areas from the scalar product. Typically, this excluded region is the one very near the cylinder rear face, where the available measurements are not trustable. We adopted a discrete scalar product for the projection procedure:

$$\langle \mathbf{u}, \mathbf{v} \rangle_d = \frac{1}{(N_x N_y)} \left(\sum_{l=1}^{N_x} \sum_{m=1}^{N_y} \mathbf{u}(x_l, y_m) \cdot \mathbf{v}(x_l, y_m) \right), \quad (22)$$

where N_x and N_y are the number of grid points in the x and y directions, respectively, available in the PIV measured flow fields. Since those points are equi-spaced, the discrete scalar product in (22) is equivalent to a first-order approximation of the scalar product in Eq. (6). As a result, we have plotted in figure 13 the value of the discrete scalar product between the adjoint unstable mode and the available snapshots, once those have been ordered according to the phase angle Φ_T , reported as the x coordinate in the plots. In figure 13 (b) a phase average has been applied, which has been obtained considering in the average 25 snapshots before and 25 snapshots after each snapshot. From the figure, it is evident that the phase alignment is meaningful, and phase averaging is necessary to balance realignment errors and, mainly, to smooth the results since fluctuations not caused by the shedding process are completely uncorrelated in time, as already discussed. In order to give an idea of the per-

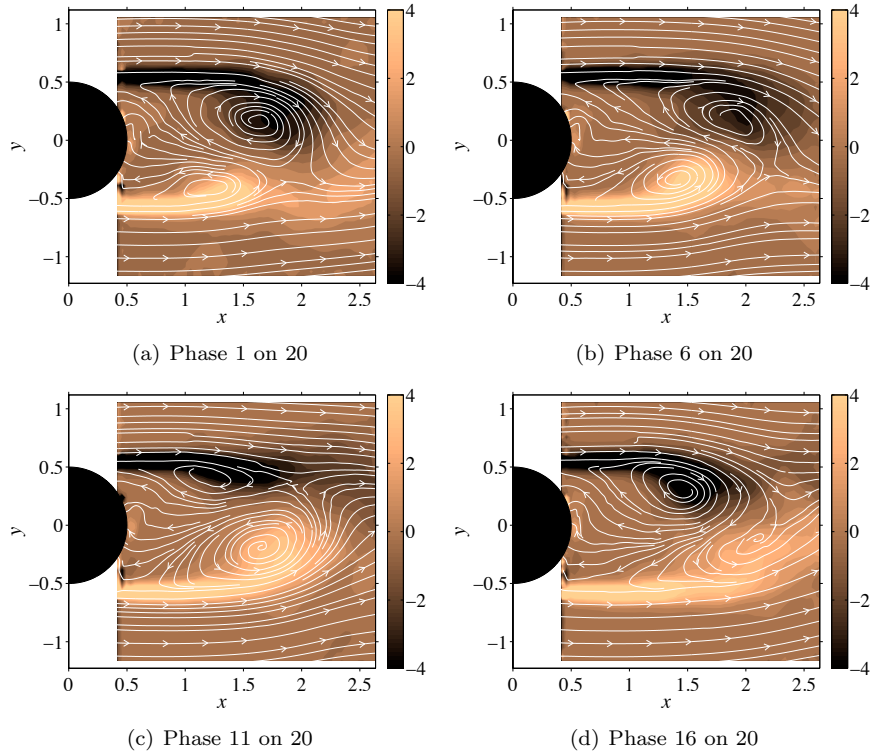


FIGURE 14. EXP: Phase-averaged experimental velocity fields at four uniformly distributed phases with respect to the shedding process for $\Gamma = -2.57$: vorticity field and streamlines of the velocity field.

formance of the reordering procedure, we report in figure 14 a few uniformly distributed phases of the shedding process for $\Gamma = -2.57$ after the phase realignment and phase average. In this case, 20 equal bins have been used for the phase average. For blowing cases, in which two overlapping windows are available, the method in Eq. (21) has been used to estimate the phase of the vortex shedding. The method is applied independently to the snapshots of the two measurement windows, since the two databases are completely independent. As the direct mode used for the procedure is the same for both databases, the estimated phases should match. This has been successfully verified a-posteriori. An example of phase average shedding process in the two windows is given for the case with $\Gamma = 0$ in figure 15, where the same phase is considered for the small measurement window on the left column and for the large one on the

right. Considering that an overlapping exists between the two measurement windows, the matching at the same phase is evident from the figure.

4.4. Phase-averaged flow fields: analysis of the large-scale wake vortices

In the present section phase-averaged flow fields for different values of Γ are post-processed in order to extract information on the kinematics of the large-scale wake vortices. In all cases, the vortex shedding period is divided in 20 uniform bins for phase averaging. It has been verified that the phase distribution of the available snapshots is almost uniform, so each bin collects approximately the same number of instantaneous fields for the average.

4.4a. *Trajectory of the wake vortices.* The extraction of the trajectories of wake vortices is a conceptually difficult task, since the vortices are large and they have a shape which changes as they travel downstream with respect to the cylinder. So it is difficult to univocally define a centre of the vortex to be followed for the identification of a line trajectory. There are different solutions in the literature to this problem. Notice that spatial derivatives of the velocity field can be affected by significant noise here, since the data are experimental measurements of turbulent flows on rather coarse grids, smoothed by phase-averaging. Thus, it is rather difficult to identify local maxima of scalar quantities associated to the gradient of the velocity field, which is the basic ingredient of several methods to define the centre of a vortex.

In this work we propose the following method to localize the trajectory of the wake vortices. At each section in the x direction we consider the phase-averaged vorticity field which passes through that section in time for one vortex shedding cycle, obtaining as a result a 2D vorticity field in the coordinate axes Φ_T - y . At this stage we can consider, instead of the phase-averaged vorticity field, its filtered counterpart, with a filter based on one vortex identification method, so as to keep only vortices in the flow field and filtering out all the vorticity which is not associated to a coherent vortex. In this work we have tested both options (i.e. with and without filter), and the adopted vortex identification method is the "Q criterion" proposed by Hunt and described, for instance, in Wu *et al.* (2005). As an example, we report in figure 16 the vorticity field, unfiltered (*a*) and filtered (*b*), extracted in time at section $x = 3.2$ for case $\Gamma = 0$.

The y position of the positive (negative) vortex trajectory at each considered x section is defined as the y coordinate of the center of gravity of the positive (negative) vorticity passing through the section in one shedding period, i.e. the center of gravity of maps like the ones reported in figure 16. As an example, we report in figure 17 the phase-averaged vorticity field for case $\Gamma = 0$ together with the so-identified trajectories.

The figure shows that the differences between the filtered and unfiltered cases are small, and for this reason we will show in the following only results

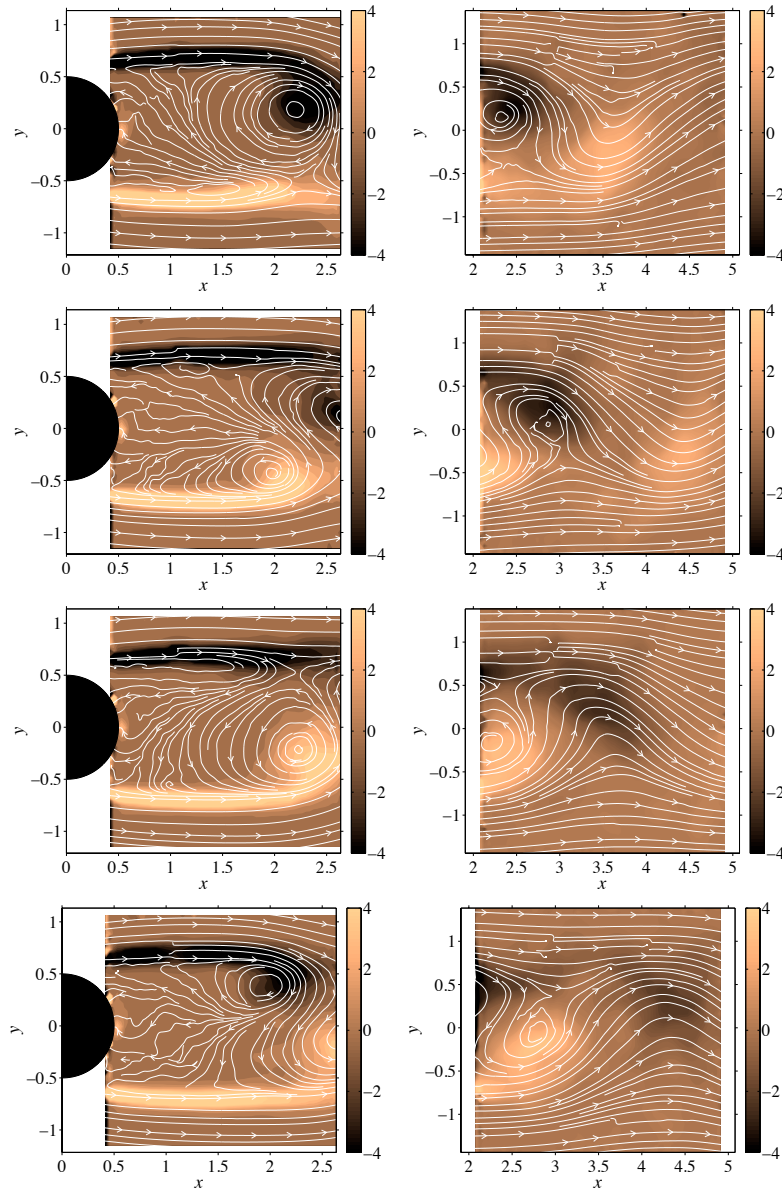


FIGURE 15. EXP: Phase-averaged experimental flow fields at four uniformly distributed phases with respect to the shedding process for $\Gamma = 0$: vorticity field and streamlines of the velocity field in the small (left column) and large (right column) measurement windows. The phases from top to bottom are: (1, 6, 11, 16) out of 20.

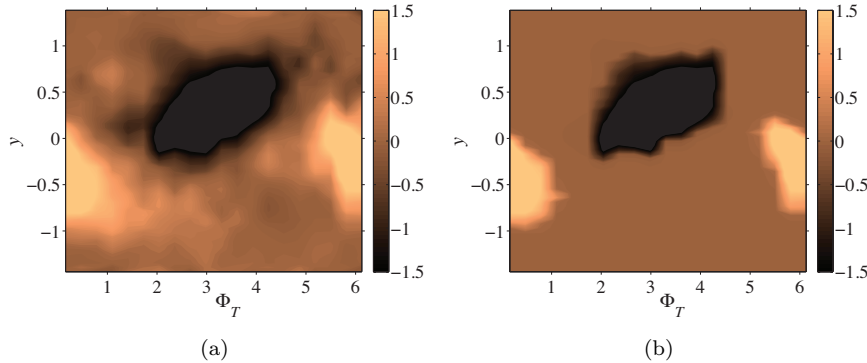


FIGURE 16. Case $\Gamma = 0$: (a) vorticity field and (b) vortices (vorticity field filtered according to the "Q criterion") passing through section $x = 3.2$ in one vortex shedding period.

obtained with the filtered vorticity fields. Only in the region of detaching shear layers, before the vortex formation length, the identifier threshold is reduced so as to take into account the position of the shear-layers in the identified trajectory, too.

The trajectories for all the considered cases are reported together in figure 18. In that figure we have excluded the cases with $\Gamma \leq -3.21$ for the anomalous behavior in the mean velocity field and Strouhal number, since they are also expected to have an anomalous trajectory. Figure 18 shows a rather clear trend of the trajectories, i.e. they monotonically approach the centre line as Γ is decreased. The only exception is the case $\Gamma = 0.68$, in which the estimation of the trajectory in the larger measurement window is affected by oscillations that prevent the determination of a clear trend, even if the trajectory still remains between the cases $\Gamma = 0$ and $\Gamma = 2.57$. The oscillations in this case, as well as in the other cases, are caused by small spurious vorticity spots that seldom appear at the boundaries in the y direction and that are not filtered out by the vortex identifier. For each case, the trajectory of the vortices are converging towards the centre line just behind the cylinder and they seem to follow a path parallel to the x axis further downstream. We know that, further downstream, the trajectories slightly diverge from the centre line, as shown for instance in Zdravkovich (1997). In particular, figure 5.42 (pp. 131) reported in Zdravkovich (1997) shows the trajectory of the wake vortices behind a circular cylinder at $Re = 39\,000$. Comparing those results to the one found here ($\Gamma = 0$) it is possible to notice that, in our case, the wake vortices are located at about $y \simeq 0.36$ at the exit section, while the data reported in Zdravkovich (1997) estimate a distance approximately equal to $y \simeq 0.3$. For the other x sections the trend is the same, i.e. we obtain a larger trajectory

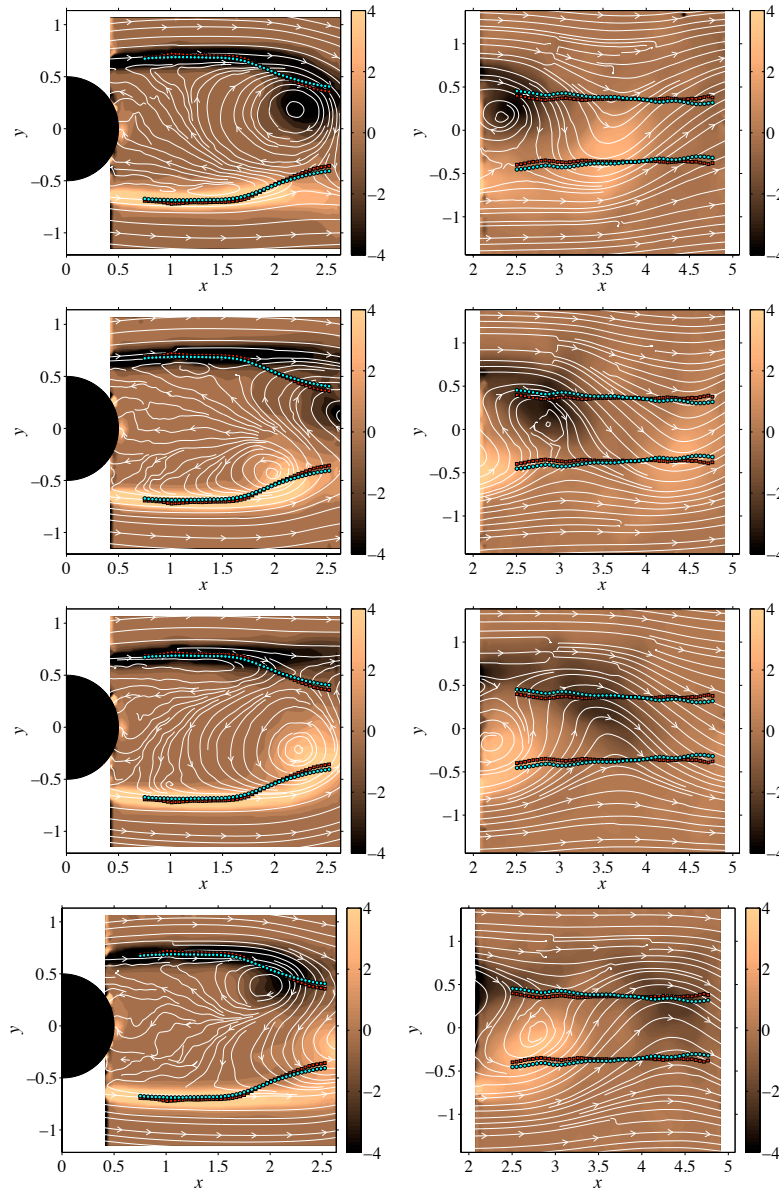


FIGURE 17. EXP: Phase-averaged experimental flow fields at four uniformly distributed phases with respect to the shedding process for $\Gamma = 0$: vorticity field, streamlines of the velocity field and vortex trajectories in the small (left column) and large (right column) measurement windows; squares (circles) indicate the trajectories extracted from the unfiltered (filtered) vorticity field.

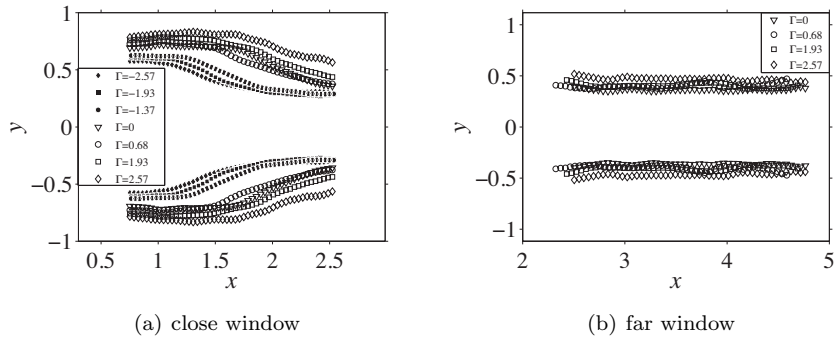


FIGURE 18. Trajectories of the wake vortices extracted from the filtered vorticity field.

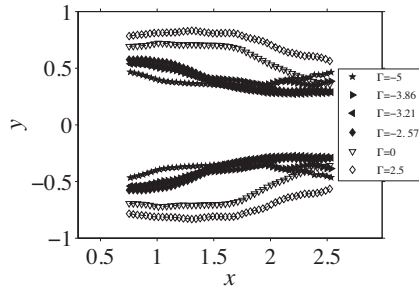


FIGURE 19. Trajectories of the wake vortices extracted from the filtered vorticity field.

with respect to that reported in Zdravkovich (1997) for $\Gamma = 0$. However, the Reynolds numbers of the two cases are quite different. Moreover, as can be noticed in figure 17, there is a tendency of the proposed method to estimate trajectories that are slightly larger at some section of what might be estimated by eye. In any case, the advantage of the proposed procedure is of being a systematic procedure that can be repeated for all the available cases without a subjective influence of the observer. Consequently, it is expected that the relative comparison among cases with different values of Γ is well identified by the proposed procedure, even if it is possible that a slight overestimation of the width of each trajectory might be possible.

The trajectories of the cases with $\Gamma \leq -3.21$ are reported in figure 19, together with some of the other cases, for comparison. As expected, the trajectory has a precise trend with $\Gamma < -2.57$, which is different with respect to the remaining cases. In particular, the distance between the symmetry line

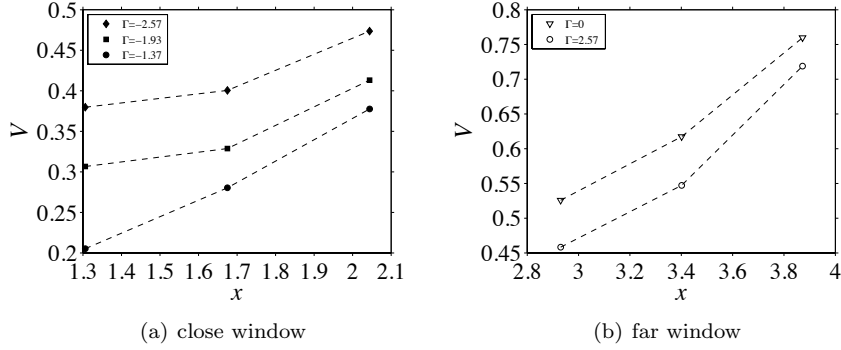


FIGURE 20. Velocity of the wake vortices estimated according to Eq.(23).

and the shear layers monotonically decreases as Γ is decreased for all cases, but, past section $x = 2$, the trajectories diverge again from the symmetry line for $\Gamma \leq -3.86$. Consequently, the trajectories of the cases with $\Gamma \leq -3.86$ intersect some of the other trajectories for $x > 2$. This does not happen for $\Gamma = -3.21$ because it is a border case, after which an inverted behavior starts to take place.

4.4b. *Velocity of the wake vortices.* Once the phase-averaged velocity field is available, the velocity of the wake vortices can be estimated by directly measuring the distance run by the vortices with respect to the phase angle Φ_T and using the experimental value of the vortex shedding period as the time reference scale. Nevertheless, a different procedure is adopted in the present work with the aim to reduce subjectivity of the observer. Starting from the $y - \Phi_T$ maps extracted at each x -section for the computation of vortex trajectories, the following procedure has been followed. Suppose that two different sections, x_1 and $x_2 > x_1$ are considered, at a relative distance equal to $L = x_2 - x_1$. Between the two sections there will be a phase shift $\Delta\Phi = \Phi_{T2} - \Phi_{T1}$ in the position of the vortices, which has been estimated by searching for the relative shift which maximizes the correlation between the vorticity maps extracted at the two considered x sections. In order to reduce noise in this process, we preliminarily filter the vorticity maps in the Φ_T direction using a low-pass Fourier cut-off filter. Once $\Delta\Phi$ is obtained, we estimate the velocity of the vortices between section x_1 and x_2 , normalized by the free-stream velocity, using the experimental value of the Strouhal number:

$$V = 2\pi L \frac{St}{\Delta\Phi} \quad (23)$$

We remind that all quantities in Eq.(23) are normalized using the free-stream velocity and the cylinder diameter. In order to reduce noise in the results,

$L = 10\Delta x$ ($L = 0.36$ and $L = 0.48$ for the small and large measurement window, respectively) has been considered. The results obtained for some of the considered cases are reported in figure 20. Note that, for each case, the estimated points close to the cylinder are meaningful only after the vortex formation length, which is reported for the case at issue (at a different Reynolds number) in Fransson *et al.* (2004) and that can be estimated here by the phase-averaged flow field (see for instance figure 14 and figure 17 for cases with $\Gamma = -2.57$ and $\Gamma = 0$, respectively).

The figure shows that, at least for the cases reported, the velocity of the wake vortices decreases as Γ is increased, and in all cases vortices accelerate with their distance from the cylinder. This is in agreement, at least for case $\Gamma = 0$, with data reported in the literature (see e.g. Zdravkovich 1997). In particular, in figure 5.6 reported in Zdravkovich (1997) an estimation of the velocity of wake vortices is reported at different downstream positions in the range $500 < Re < 1000$ ($\Gamma = 0$). However, a very few points are reported in the near wake and a direct comparison with the present data is difficult. Nevertheless, there is at least a qualitative agreement with the present results. In particular, for $x \simeq 4D$ the estimated velocity reported in Zdravkovich (1997) is approximately equal to $0.8U_\infty$ ($Re = 6450$), which is in reasonable agreement with the value $0.76U_\infty$ estimated here for the case $\Gamma = 0$.

The procedure proposed here can be affected by noise, due to the optimization step involved. However, as already stated, once the phase-averaged flow fields are available it is an easy task to estimate the velocity of the vortices by visual inspection of the fields themselves, using the value of experimental Strouhal number as a time reference.

4.4c. Mean vorticity fluxes at x sections. In the estimation of the vortex trajectories described in subsection 4.4a, the denominator in the expression to derive the y -coordinate of the gravity center of positive (negative) vorticity contains the mean flux of positive (negative) vorticity at the considered section. This quantity is indirectly related to the intensity of the wake vorticity and, in all the considered cases, it has a maximum (minimum) value in the wake which is closely correlated with the vortex formation length. As concerns the intensity of the wake vortices, this can be estimated directly from the phase-averaged fields so that, in this respect, the flux maps are not interesting, but they can be used to estimate the vortex formation length. A typical behavior of the positive vorticity flux is reported in figure 21(a). Comparing figure 21(a) with the phase averaged fields in figure 14 and figure 17 for cases with $\Gamma = -2.57$ and $\Gamma = 0$, respectively, it is possible to notice that there is a close correlation between the vortex formation length and the maximum in the positive vorticity flux (the flux of negative vorticity is a specular curve). We also reported the position of the maxima of the vorticity flux obtained for different values of Γ in figure 21(b). As intuitively expected, the vortex formation length increases

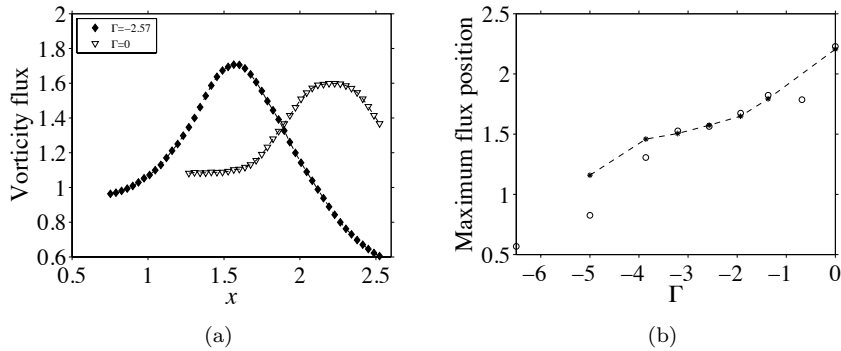


FIGURE 21. Mean flux of positive vorticity in the wake at x sections: (a) typical behavior and (b) position of the maxima of the flux vs Γ , (*)-symbols. In (b) the position of maximum back-flow is also plotted with (o)-symbols for comparison.

with Γ and the same behavior is shown by the maxima of the vorticity flux in the wake. Moreover, there is also a quantitative agreement between the curve of maxima reported in figure 21(b) and the values of vortex formation length vs Γ provided in Fransson *et al.* (2004) for the porous cylinder and in Zdravkovich (1997) for $\Gamma = 0$ (see Fig. 5.12 and related comments in the text). As an example, in Zdravkovich (1997) the vortex formation point is localized near $x \simeq 2 D$ for a Reynolds number similar to the one considered here, and we estimate $x \simeq 2.2 D$ in the present work (see figure 21b). For a direct comparison the position of maximum back-flow for each suction rate is also plotted in figure 21(b). The maximum back-flow is also known to be seen as a vortex formation length and the agreement between the two measures is very good.

5. Conclusions

This work is based on experimental PIV flow fields that have been measured past a porous circular cylinder at $Re = 3.5 \times 10^3$ at different levels of the transpiration parameter Γ . The first part of the work is dedicated to the global stability and sensitivity analysis of the mean flow fields extracted from the available database for each value of Γ . The objective of this first part is to verify whether or not the global stability analysis of the mean flow leads to a reasonable estimation of the vortex shedding frequency and of the global unstable mode at the considered value of Reynolds number. An original aspect of the work is to consider experimentally measured mean flow fields, which poses several technical difficulties for the numerical stability analysis that have been solved and partially documented here. To the authors' knowledge, this verification has been carried out only on the basis of DNS simulations up to $Re = 600$ (Leontini *et al.* 2010), and, moreover, this is the first example in which the

global adjoint unstable mode is derived on the basis of the experimental data and used for a sensitivity analysis of the found instability. Besides the interest in comparing the obtained results with those documented in the literature for the primary instability, the sensitivity analysis provides useful information to verify a-posteriori the adequacy of the size of the measurement window for the stability analysis. This is reported in the paper, which also shows that the predicted values of the Strouhal number of the vortex shedding process are in good agreement with those observed in the experiments, so extending the analysis in Leontini *et al.* (2010) up to $Re = 3.5 \times 10^3$. Surprisingly, the stability analysis is also able to capture an inversion in the behavior of the Strouhal number (St) with respect to Γ , which is observed experimentally for $\Gamma \leq -3.21$. In fact, St increases as Γ is increased, but the opposite happens when $\Gamma \leq -3.21$. This behavior seems to be associated to a similar anomaly in the size of the mean recirculation bubble with respect to Γ , and it needs to be further investigated.

For each value of Γ , the PIV database consists of about 1000 flow snapshots that have been taken without phase triggering at a low frequency with respect to the vortex shedding one. For this reason they can be considered as randomized in phase and only statistical quantities can be directly accessed. In this respect, the availability of the global stability modes allowed the formulation of a procedure to approximately align the available snapshots in phase. Consequently, after applying a phase average on the ordered set of snapshots, the phase-average vortex shedding process vs Γ is available. We underline that the results from the stability analysis are used only to realign the snapshots in phase, and no numerical artifact is added subsequently but only data coming from the experiments are used in the phase average. This allowed an analysis of the kinematics of the wake vortices as a function of Γ (trajectory, velocity and formation length). Results obtained for $\Gamma = 0$ are in reasonable agreement with those reported in the literature, giving confidence that the analysis described here does not only give information on the relative effects of transpiration, but it also provides results that are reasonably accurate from a quantitative viewpoint.

Acknowledgements

The authors are grateful to Dr. F. Giannetti for having provided a part of the computational tools used in the present work. BEGF and JHMF would like to acknowledge the financial support from the Göran Gustafsson Foundation and the Swedish Research Council (VR).

References

- BARKLEY, D. 2006 Linear analysis of the cylinder wake mean flow. *Europhys. Lett.* **75**, 750–756.
- FRANSSON, J. H. M. & ALFREDSSON, P. H. 2003 On the disturbance growth in an asymptotic suction boundary layer. *J. Fluid Mech.* **482**, 51–90.
- FRANSSON, J. H. M., KONIECZNY, P. & ALFREDSSON, P. H. 2004 Flow around a porous cylinder subject to continuous suction or blowing. *J. Fluids Struct.* **19** (8), 1031–1048.
- GIANNETTI, F. & LUCHINI, P. 2007 Structural sensitivity of the first instability of the cylinder wake. *J. Fluid Mech.* **581**, 167–197.
- HERNÁNDEZ, V., ROMÀN, J. E., ROMERO, E. & VIDAL, A. T. V. 2009 SLEPc Users Manual, Scalable Library for Eigenvalue Problem Computations. *Tech. Rep.* Universidad Politecnica de Valencia.
- LEONTINI, J. S., THOMPSON, M. C. & HOURIGAN, K. 2010 A numerical study of global frequency selection in the time-mean wake of a circular cylinder. *J. Fluid Mech.* **645**, 435–446.
- LINDGREN, B. 2002 Flow facility design and experimental studies of wall-bounded turbulent shear-flows. PhD thesis, Royal Institute of Technology.
- MARQUET, O., SIPP, D. & JACQUIN, L. 2008 Sensitivity analysis and passive control of cylinder flows. *J. Fluid Mech.* **615**, 221–252.
- NOACK, B. R., AFANASIEV, K., MORZYNSKI, M., TADMOR, G. & THIELE, F. 2003 A hierarchy of low-dimensional models for the transient and post-transient cylinder wake. *J. Fluid Mech.* **497**, 335–363.
- OBERLEITHNER, K., SIEBER, M., NAYERI, C. N., PASCHEREIT, C. O., PETZ, C., HEGE, H.-C., NOACK, B. R. & WYGNANSKI, I. 2011 Three-dimensional coherent structures in a swirling jet undergoing vortex breakdown: stability analysis and empirical mode construction. *J. Fluid Mech.* **679**, 383–414.
- SIPP, D. & LEBEDEV, A. 2007 Global stability of base and mean flows: a general approach and its applications to cylinder and open cavity flows. *J. Fluid Mech.* **593**, 333–358.
- SIROVICH, L. 1987 Turbulence and the dynamics of coherent structures, parts i, ii and iii. *The Quarterly of Applied Mathematics* **XLV**, 561–590.

- WU, J.-Z., A. K. XIONG & YANG, Y.-T. 2005 Axial stretching and vortex definition.
Phys. Fluids **17**, 038108.
- ZDRAVKOVICH, M. M. 1997 *Flow around circular cylinders - Vol. 1: fundamentals*.
Oxford Science Publications.

Paper 5

On the vortex generation behind a passive V-shaped mixer in a pipe flow

By Bengt E. G. Fallenius and Jens H. M. Fransson

Linné Flow Centre, KTH Mechanics, SE-100 44 Stockholm, Sweden

To decrease the emissions from combustion engines an additive may be injected in the exhaust emissions. In order to optimally compound this additive with the exhaust emissions there is a need to create a stirring process, which in the simplest form amounts to placing a vortex generator in the flow. The drawback, at high velocities, may be its form as a noise generator. It is understandable that different means to alter the generation of noise, in a positive way, are sought after. It has been shown that such a positive effect is obtained if the vortex generator itself is allowed to be dynamic, i.e. if the vortex generator is thin enough so that its stiffness is reduced. In the present investigation the effect of flexible versus stiff vortex generators, in a pipe flow, on the fluid dynamics have been studied. It is shown that there are no major changes in the mean velocity field nor the strength, circulation and size of the generated vortices in the pipe. This result suggests that the mixing process is equally rapid for the flexible vortex generator as the stiff one, but with the advantage of having reduced the noise level.

1. Introduction

In an effort to reduce emissions from internal combustion engines, an additive can be injected in the exhaust emissions. To obtain a fast and homogeneous compound, a vortex generator can be installed near the point where the substance is added. An important issue in this context is the side effect of a generated acoustic field due to the presence of the vortex generator. For practical applications there are limitations on the excessive level of noise being generated, so there is an interest to keep the acoustic field as weak as possible. It has been shown that by allowing the introduced mixer to be flexible one can influence the acoustic source-strength in a positive way (see Karlsson *et al.* 2008). With this result in mind there is obviously an interest to study the effect of flexible vortex generators on the mixing process itself. In the present paper a direct comparison of the generated fluid structures between a stiff and a flexible vortex generator is made. The differences are quantified by means of

small-scale flow structure changes and mean velocity profile changes between a stiff and a flexible vortex generator. Here, we denote this type of vortex generator as a passive mixer since it does not cost any energy to perform the actual mixing, apart from the increased pressure drop in the pipe.

The paper has the following outline. Section 2 describes the experimental setup, the V-shaped vortex generators and the measurement technique. This is followed by a brief summary of the vortex detection program that has been used for the collection of the vortex statistics (section 3). The results are shown in section 4 and the summary and conclusions are found in section 5.

2. Experimental setup and measurement technique

The experiments were performed in the MWL¹ pipe flow facility, which is an open facility mainly used for studies on aeroacoustics. The centre line velocity in the pipe was $U_C = 50 \text{ m s}^{-1}$ in all the measurements performed.

Figure 1 shows two photographs of the experimental setup. The pipe test section is made of plexiglas (*a*) with a length of 1496 mm and is located 3880 mm downstream of the pipe facility contraction. Downstream of the test section the pipe continues with an extension of 3560 mm. The inner diameter of the pipe is $D = 90 \text{ mm}$ and the wall thickness is 5 mm. At approximately 400 mm downstream of the test section entrance, the vortex generator was mounted through a slit through the pipe wall at an angle of 32° and clamped by a holder attached around the pipe (*b*). This is illustrated in figure 2 where a sketch of the geometry is shown with the coordinate system and the placement of the plate in the pipe in (*a*) together with the entire test section and a photograph of the actual vortex generator in (*b*) and (*c*), respectively. Two wedge-shaped vortex generators with varying thicknesses, t , and hence different stiffnesses, were studied. Apart from the thicknesses of $t = 3.0$ and 0.5 mm , from here on denoted the stiff and the flexible vortex generator, respectively, they were identical.

A two-dimensional Particle Image Velocimetry (PIV) system was used for the velocity measurements in the pipe. The laser beam from a Spectra Physics 400 mJ double pulsed Nd:Yag laser (shown in figure 1*c*), operating at 15 Hz, was mirrored to the cylindrical lens (*d*) creating a laser sheet. A screen (*e*) was used to reduce reflections and images were taken using a double-frame Kodak ES1.0 8-bit CCD camera (*f*), with a resolution of 1018×1008 pixels. For the calibration of the PIV-images, a calibration plate (*g*) was placed in front of the pipe and then removed. After calibration the laser sheet and the camera was moved to the centre line of the pipe by means of a manual traversing table (*h*).

The PIV-measurements were performed at four x/D -locations, namely, at -3 , 3 , 6 and 9 in both the xy -plane and the xz -plane (cf. figure 2).

¹Marcus Wallenberg Laboratory

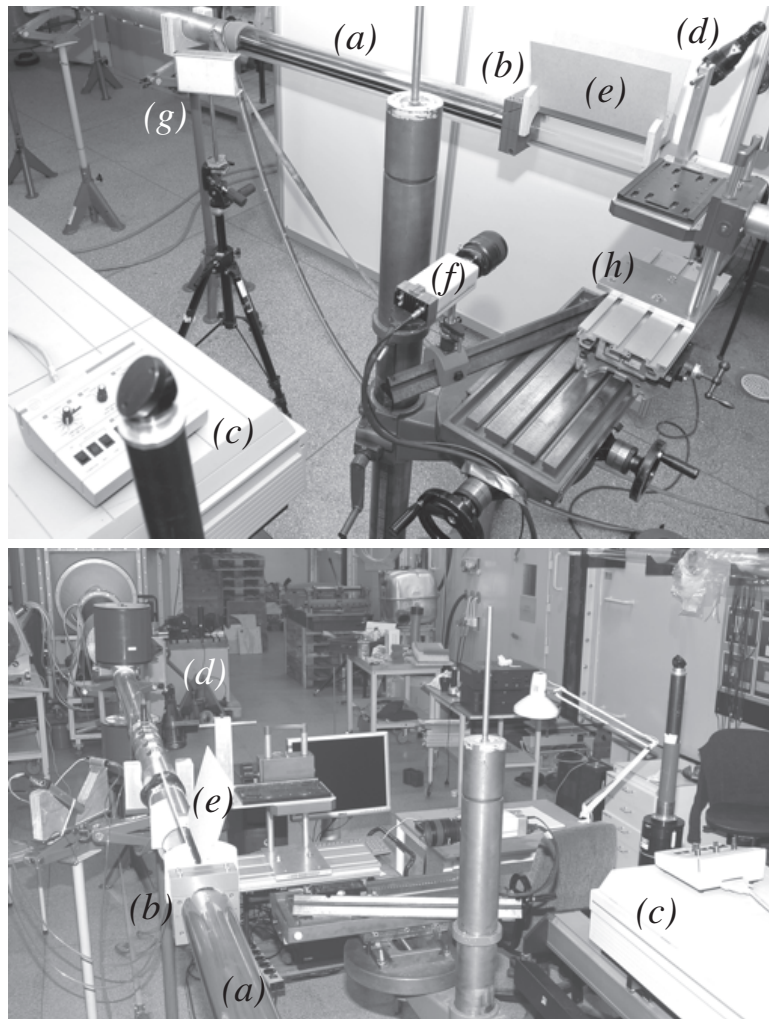


FIGURE 1. Photographs of the experimental setup. The test section (a), the vortex generator (b). The laser beam was mirrored from (c) to the cylindrical lens (d), and a screen (e) was used to reduce the reflections. The camera (f), calibration plate (g) and traversing (h).

Smoke particles, generated by heating a glycol based liquid with a disco smoke generator (JEM ZR20 Mk II), were used to seed the air and the smoke was injected through 5 hoses connected to the contraction (iv) of the pipe apparatus. The injection of smoke into the pipe was achieved by placing the smoke machine inside a pressurised chamber (cf. figure 3). This pressure chamber was regulated via a control valve (i) and the pressure difference between the pipe at the injection location and the chamber was adjusted for suitable smoke density for the captured PIV images using a pressure differential meter (ii). An absolute pressure meter (iii) in the chamber was also used in order to make sure that the pressure did not exceed the chamber specifications.

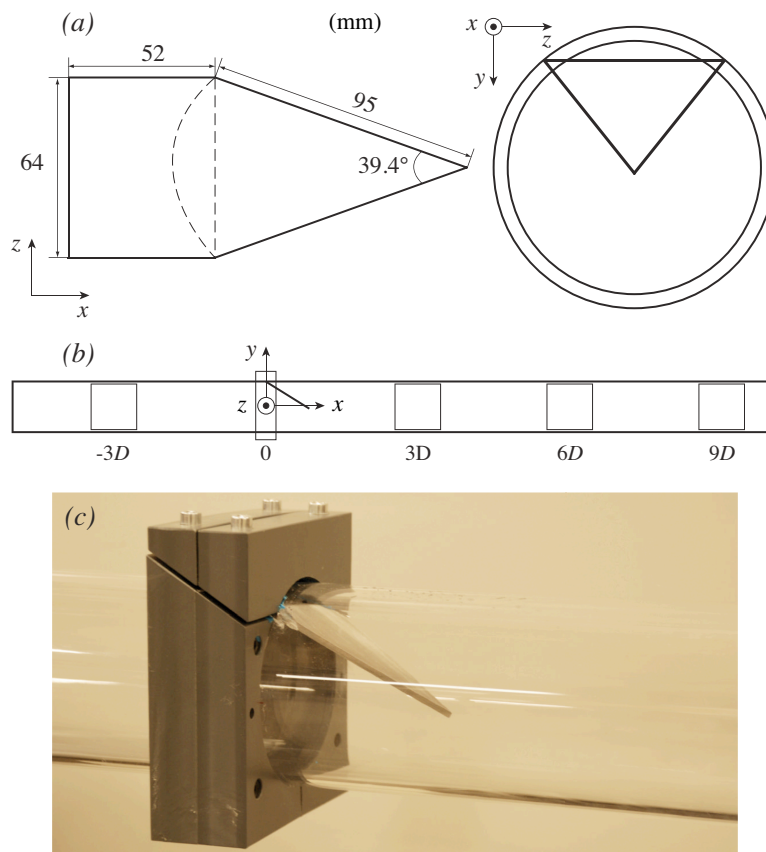


FIGURE 2. (a) The wedge-shaped vortex generator in the xz -plane and the position of the vortex generator in the yz -plane of the pipe. (b) and (c) show the test section in the xy -plane and a real photograph of the vortex generator, respectively.

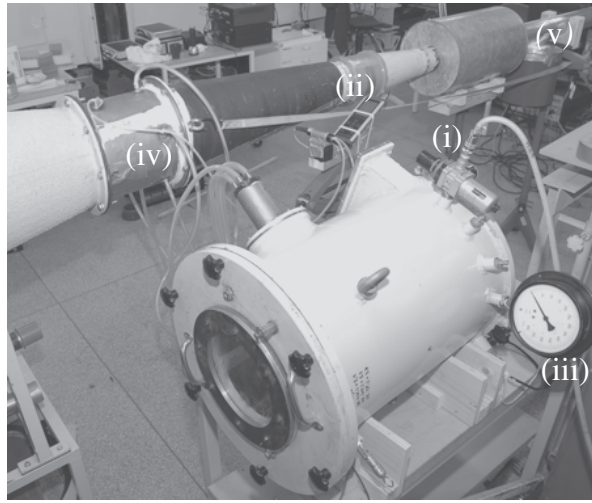


FIGURE 3. The pressurised chamber with (i) a pressure regulator, (ii) a differential pressure meter, (iii) absolute pressure meter. The smoke where injected in the contraction (iv) upstream of the pipe (v).

In order to find out whether the vortex generators were deflected by the flow or not, a Photron APX-RS high-speed camera, with the frame rate set to 3 kHz at a resolution of 1024×128 pixels, was used to capture the movement of the plates.

3. Identification of vortices

The vortex identification algorithm that has been used is similar to the one suggested by Adrian *et al.* (2000), i.e. small scale structures in an instantaneous two-dimensional velocity field is revealed by high-pass filtering. Vortices are identified by finding regions in the high-pass filtered velocity field where the velocity gradient tensor have imaginary eigenvalues, λ_{ci} , implying that the streamlines are closed or spiral, see Chong *et al.* (1990). Each region is then examined and properties of the identified vortices are stored for post-processing and statistical comparisons. A threshold for λ_{ci} has to be implemented to have distinct and reasonable boundaries of the vortices. The threshold in this study was chosen by studying contours for different values of λ_{ci} in the high-pass filtered velocity field. The value was after studying the outcome set to $\lambda_{ci} = 250$.

The high-pass filtering is carried out by convolving a Gaussian filter on the full velocity field \mathbf{u} , which results in a low-pass filtered velocity field $\bar{\mathbf{u}}$. The high-pass filtered velocity field is then obtained by subtracting the low-pass

filtered velocity field from the full velocity field, according to

$$\mathbf{u}'' = \mathbf{u} - \bar{\mathbf{u}} . \quad (1)$$

The low-pass filter is written as,

$$\bar{\mathbf{u}}(m, n) = \frac{\sum_{j=-k}^k \sum_{i=-k}^k g(i, j) \mathbf{u}(m-i, n-j)}{\sum_{j=-k}^k \sum_{i=-k}^k g(i, j)} , \quad (2)$$

where (i, j) is the step in x and y , respectively, and k is the *radius*. Note here that the shape of the filter is square, and hence, the radius is the number of surrounding grid-points in each direction that are averaged with the point (m, n) .

The Gaussian kernel (g) is defined as

$$g(i, j) = \exp \left[-\frac{(i\Delta x)^2 + (j\Delta y)^2}{2\sigma^2} \right] , \quad (3)$$

where Δx and Δy are the grid spacing and σ is the padding of the filter. Here, the parameters k and σ were chosen by counting the number of vortices for varying values of k and σ , as well as different λ_{ci} . For $k = 5$ and $\sigma = 5$, there where no major change in the number of vortices.

The vortex parameters that are stored are the vortex core position, strength, size and circulation. The centre of the vortex is taken to be the highest λ_{ci} in each region. According to Zhou *et al.* (1999), the value of the highest λ_{ci} also corresponds to the vortex strength. The size of the vortex is determined by finding the radius for the maximum circulation γ , which is calculated according to

$$\gamma = \oint_C \mathbf{u}'' \cdot d\mathbf{l} , \quad (4)$$

where \mathbf{l} is the perimeter of the circle C around the vortex centre, which is stepwise increased in size until the maximum value of γ is found.

4. Experimental results

PIV-measurements were performed in both the xy - and the xz -plane (cf. figure 2(a)). A typical image pair of the PIV-measurements is shown in figure 4. As seen in the images, a strong reflection is present in the lower part, which affected the quality of the captured velocity fields. From a mean velocity point of view only some of the points had to be disregarded. However, for the detection and analysis of the small-scale structures, the influence of the reflections on the results was larger, and consequently parts of the velocity field had to

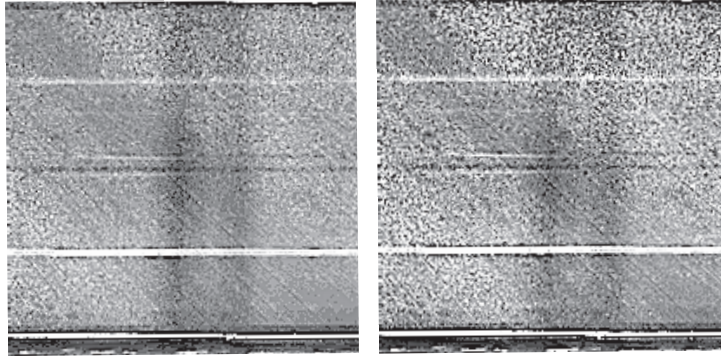


FIGURE 4. *A* (left) and *B* (right) images of a raw data image pair from the PIV-measurements at $x = 6D \pm 0.5D$ with the 3.0 mm vortex generator. The flow is from left to right.

| Plane | | xy | | xz | |
|----------|----------|-----------|-----------------|-----------|-----------------|
| x -pos | t [mm] | no. of IP | no. of vortices | no. of IP | no. of vortices |
| $3D$ | 0.5 | 1024 | 27271 | 1024 | 20840 |
| | 3.0 | 1024 | 30343 | 1024 | 21661 |
| $6D$ | 0.5 | 1056 | 15275 | 992 | 10916 |
| | 3.0 | 1088 | 14703 | 1056 | 10426 |
| $9D$ | 0.5 | 1024 | 8283 | 800 | 6286 |
| | 3.0 | 1024 | 9653 | 1024 | 8413 |

TABLE 1. The number of PIV-image pairs (IP) taken during the experiments and the number of vortices identified in each plane and for the two different vortex generators.

be cut out. Due to the reflections the intervals $-0.12D \leq y \leq 0.42D$ and $-0.42 \leq z \leq 0$ in the xy -plane and the xz -plane, respectively, were used for vortex identification. The latter was decided to be cut at the centreline due to the symmetry of the geometry.

Table 1 shows the number of image pairs (IP) the statistical results have been based on, and the number of vortices that were detected in the reduced velocity fields. In the table one can see that the number of vortices decreases along the pipe in the downstream direction.

The vibrations and maximum deflection of the plates were recorded with the high speed camera. The 3 mm vortex generator showed no noticeable deflection, while the 0.5 mm vortex generator had a static deflection of approximately 4 mm and oscillated with an amplitude in the order of the plate

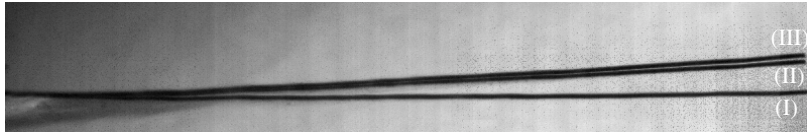


FIGURE 5. The position without any flow (I) of the 0.5 mm plate. (II) and (III) are the maximum negative and the maximum positive deflections of the oscillations, respectively.

thickness. This is shown in figure 5, where position (I) shows the plate without any flow in the pipe. (II) and (III) correspond to the maximum negative and the maximum positive deflection of the oscillations, respectively, which are caused by the flow. Note, that the image has been rotated so that the reference case without any flow is the horizontal one.

4.1. Mean velocity profiles

The upstream flow conditions were characterized at the location $x/D = -3$ from the vortex generator. In figure 6 the mean velocity profile is shown where the no-slip wall condition has been added with bullet symbols. Note that all the velocity profiles shown here are not only time averaged, they are also spatially averaged in the streamwise direction from $-0.5D$ to $0.5D$ from the given x -station. Furthermore, unphysical data points, due to near wall factors and reflections, have been removed in order not to cause confusion. The Reynolds number in the present experiment, based on the pipe diameter and the centre-line velocity, is around 3×10^5 . The dashed line, in figure 6, corresponds to the empirical power law equation,

$$\frac{U}{U_c} = \left(\frac{1}{2}\right)^{-1/n} \left(\frac{1}{2} + \frac{y}{D}\right)^{1/n}, \quad -0.5 \leq y/D \leq 0, \quad (5)$$

with $n = 7$. U/U_c in equation 5 is then mirrored along the centre line to get the profile in the range $0 < y/D \leq 0.5$. The chosen n -value is known to give a good agreement with experimental data in a smooth pipe, at Reynolds numbers on the order of 10^5 , apart from the centre line where the two boundary layer profiles meet and give rise to a rather unphysical discontinuity in the profile derivative. In addition, due to the presence of microphones and loudspeakers (used for acoustical measurements in the same setup) as well as duct joints, there are some surface imperfections, which cause a mismatch across the entire profile as shown in figure 6. It is possible to observe that the empirical velocity profile is fuller close to the surface, till $y/D = \pm 0.4$, and less fully elsewhere, when compared with the experimentally measured velocity profile. However, due to the profile crossing around $y/D = \pm 0.4$ the integrated empirical and experimental mean velocity values agree remarkably well with each other. The

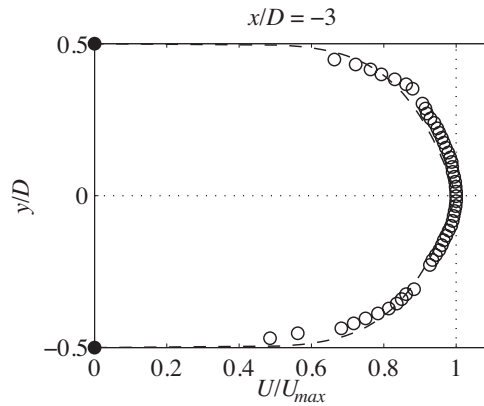


FIGURE 6. Upstream mean velocity profile at $x/D = -3$. Symbols correspond to the measured profile and the dashed line corresponds to the power law, eq. 5, with $n = 7$. Bullets are added data points fulfilling the no-slip condition.

calculated Mach numbers, based on the mean velocity, for both the empirical and the experimental cases become 0.12.

In figure 7 the effect of the 0.5 and the 3 mm thick vortex generators on the velocity field is compared for three different downstream stations. The xy and xz -planes (see figure 2) are shown in the first and in the second column of subfigures, respectively, in figure 7. The velocity profiles have been normalized with the maximum velocity of the two planes across the pipe. In the xy -plane an asymmetric mean velocity distribution is expected due to the accelerated and retarded flow on the bottom and the top side, respectively. The retardation is an effect of the direct blockage of the vortex generator and the acceleration on the bottom is the compensation. The vortex generator can be seen as a wing with a low pressure on the lee- side and a high pressure on the oncoming flow-side. This pressure difference induces strong and steady vortices for small to moderate angles of attack, which become unsteady for higher angles of attack or for flexible and vibrating wings where vortex shedding become the dominating flow phenomenon. These vortices complicate the flow description from a mean velocity point of view. However, the main conclusion drawn from figure 7 is that there is hardly any difference of the mean velocity distribution between the two different plates. Furthermore, a comparison between the xy and the xz -planes at $x/D = 9$ does hardly show any indication of an upstream located vortex generator since the velocity distribution seems to be more or less axisymmetric. The xz -plane, as expected, shows a symmetric velocity distribution across the pipe. Maybe less expected is how remarkably well the two different velocity profiles agree with each other.

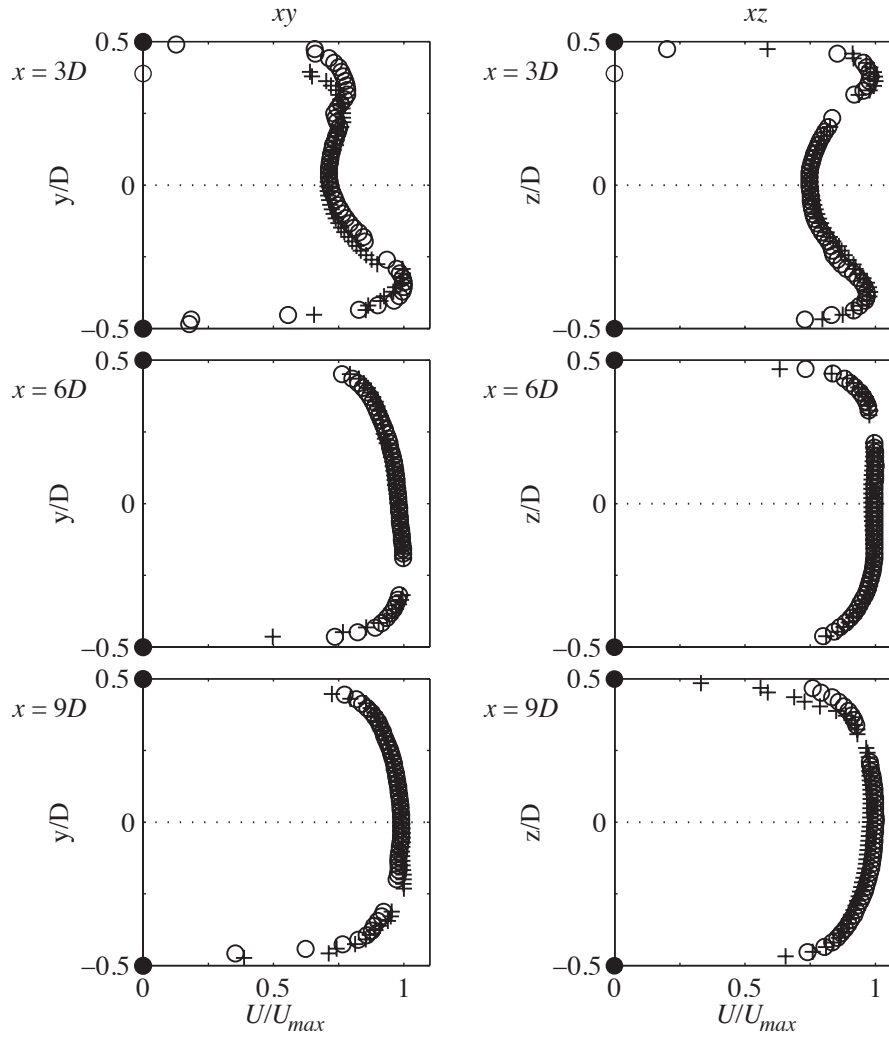


FIGURE 7. Mean velocity profiles of for the two planes at different positions. (+) and (o) is the 0.5 mm and 3 mm plate, respectively. The bullets represents the no-slip condition.

4.2. Vortex properties

In figure 8 typical instantaneous high pass filtered velocity fields from the xy -plane and the xz -plane are shown for both the 0.5 and the 3.0 mm vortex generators. These fields reveal the smaller structures embedded in their corresponding mean velocity fields and are shown here in order to emphasize the fact that no major flow structure changes are detected between the 0.5 and the 3.0 mm plates. This view is strengthened by looking at the statistics of the vortex parameters, namely, the vortex strength, size and circulation. In this subsection the small differences will be highlighted and discussed.

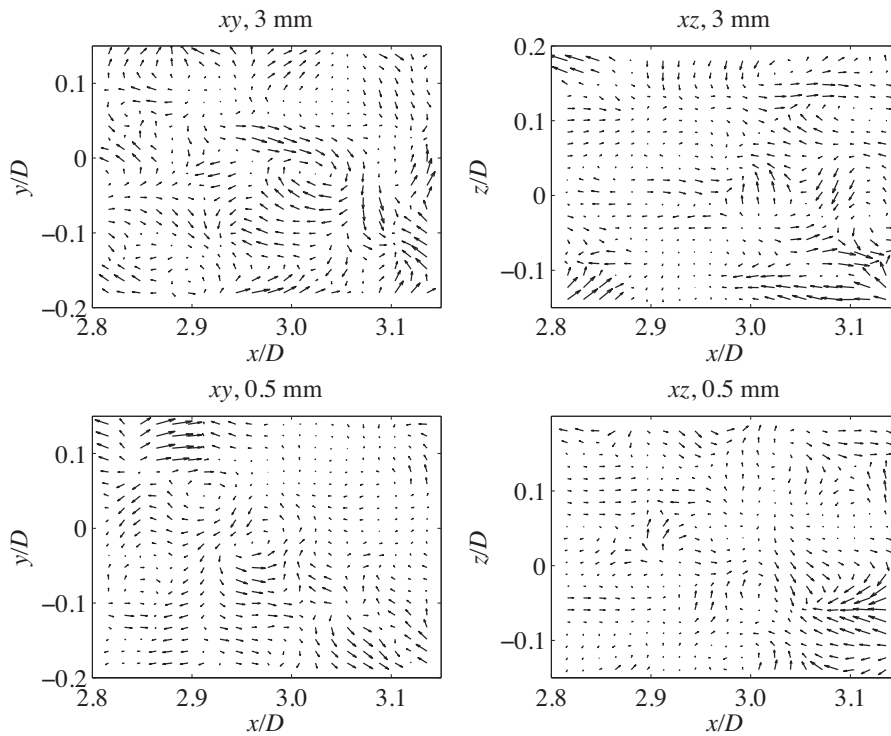


FIGURE 8. Typical instantaneous velocity vector plots for both the xy -plane and the xz -plane. These planes are shown for both the 0.5 and the 3.0 mm vortex generators in the first and second rows of the subfigures, respectively.

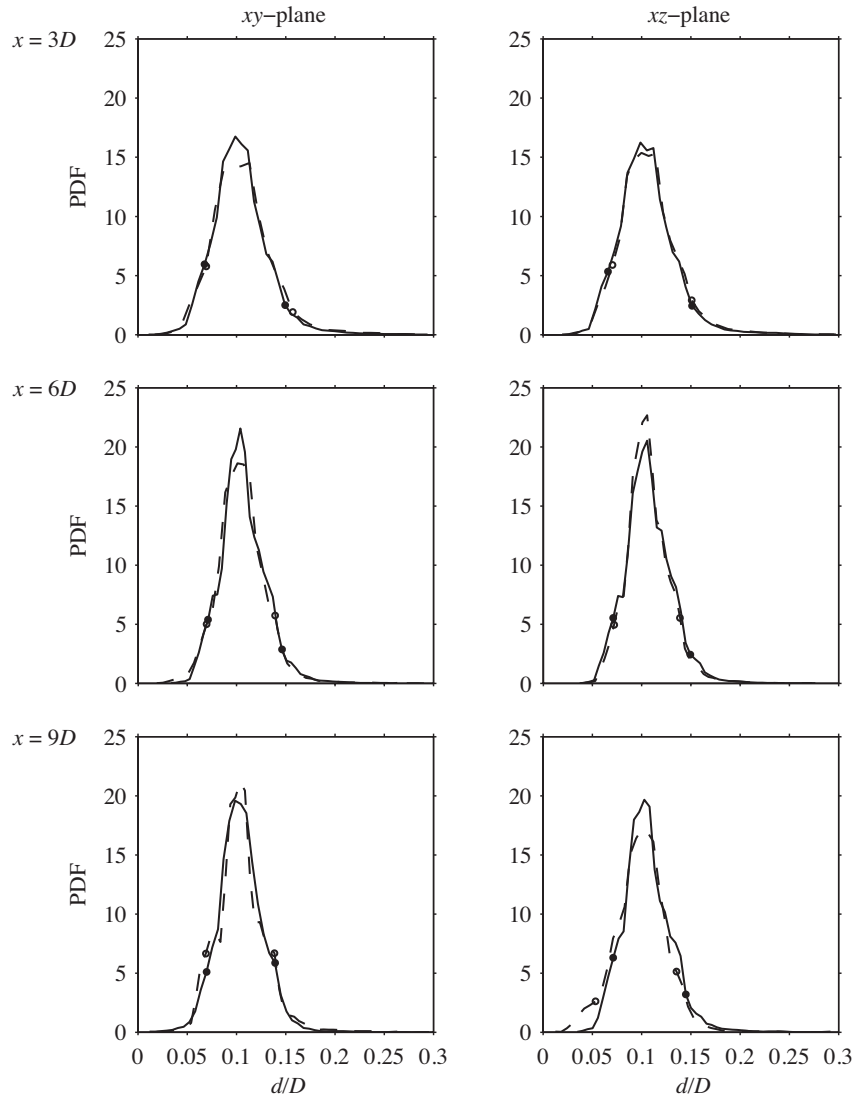


FIGURE 9. The diameter range of the vortices. Dashed and solid lines represent the 0.5 and the 3.0 mm vortex generator, respectively. The lowest and highest 5% of the parameter value for the 0.5 and the 3.0 mm vortex generator are marked by (○)– and (●)–symbols, respectively.

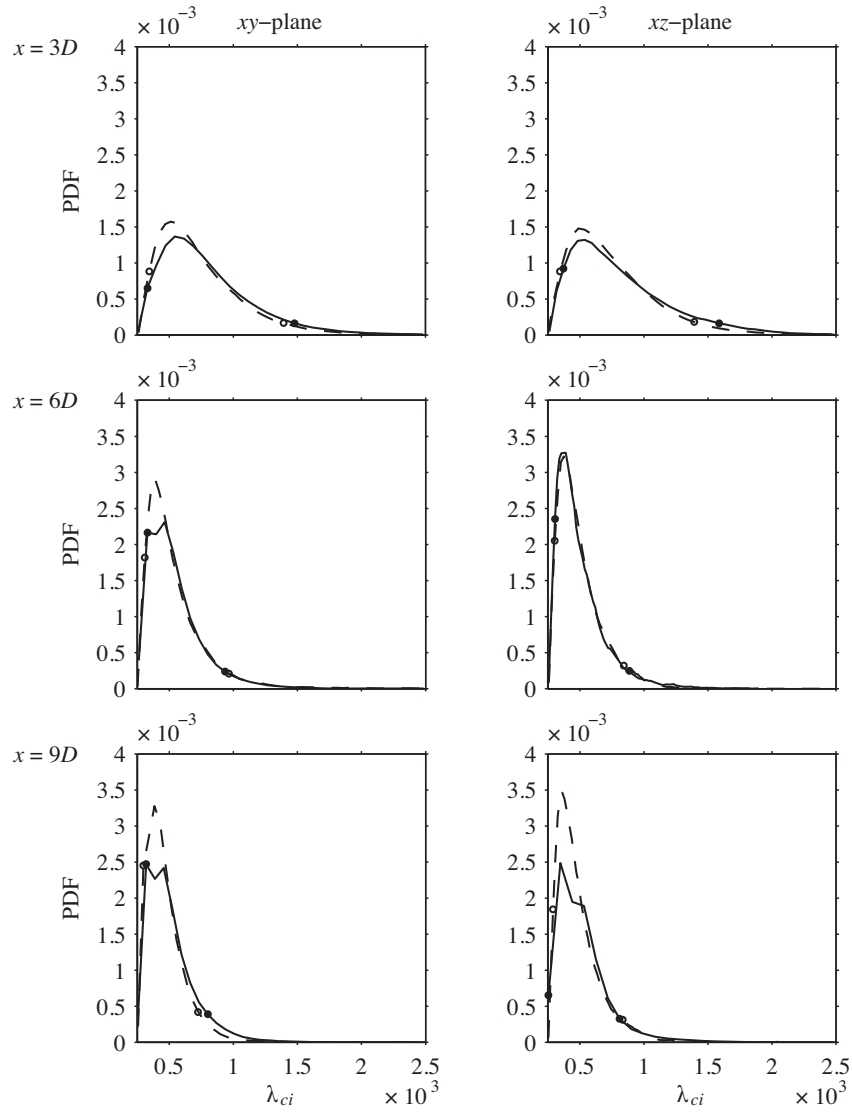


FIGURE 10. The strength range of the vortices. Dashed and solid lines represent the 0.5 and the 3.0 mm vortex generator, respectively. The lowest and highest 5% of the parameter value for the 0.5 and the 3.0 mm vortex generator are marked by (○)– and (●)–symbols, respectively.

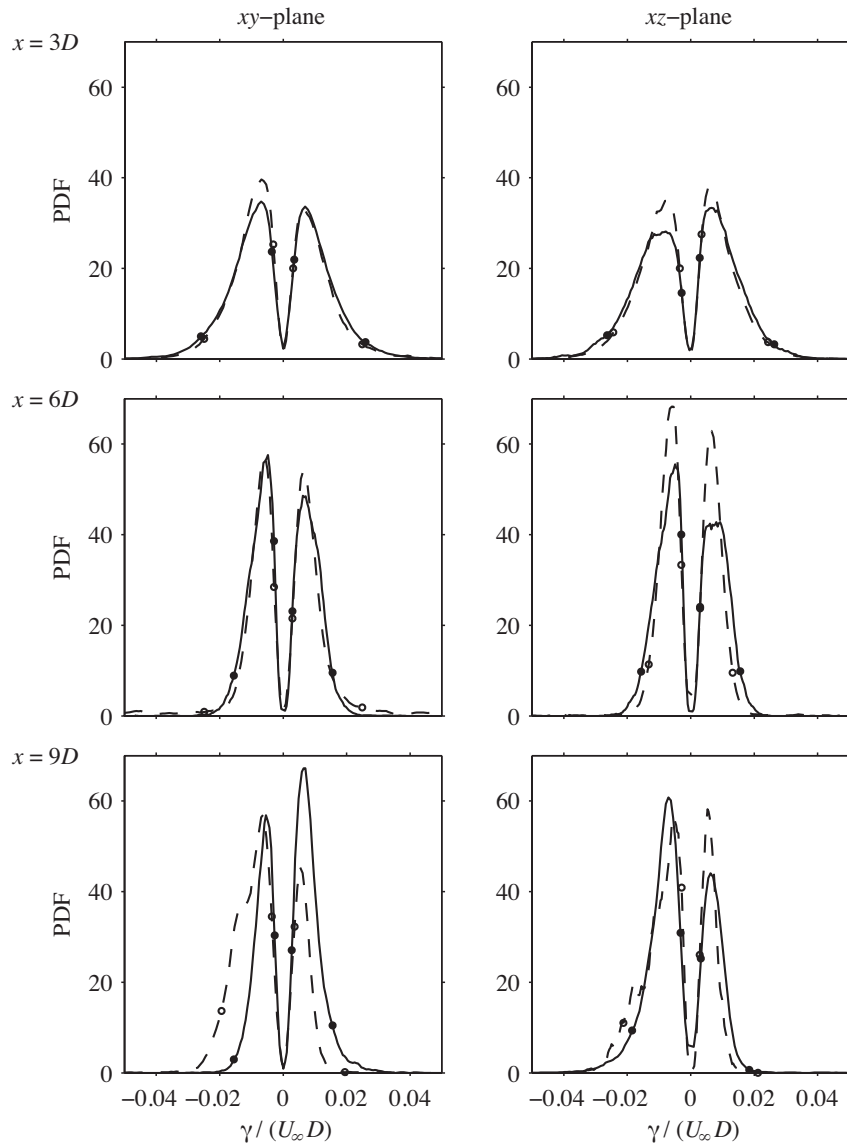


FIGURE 11. The circulation range of the vortices. Dashed and solid lines represent the 0.5 and the 3.0 mm vortex generator, respectively. The lowest and highest 5% of the parameter value for the 0.5 and the 3.0 mm vortex generator are marked by (o)– and (•)–symbols, respectively.

Figure 9 shows the streamwise evolution of the Probability Density Functions (PDFs) of the vortex strength for the two different vortex generator thicknesses as well as for the two different measurement planes. Dashed (with (•)-symbols) and solid (with (◦)-symbols) lines correspond to the 0.5 and the 3.0 mm vortex generator, respectively. The symbols indicate the lowest and highest 5% of the parameter value. Note, that the PDFs have been normalized such that the area under the curves equal unity. This means that PDF height differences are also relevant to be compared. Figure 9 shows that the most common vortex diameter essentially stays constant around $0.1D$, independent of the the vortex generator thickness, the plane considered, or the downstream distance. The latter is a confirmation that the finally analyzed area of the velocity field, after the cut out due to reflections, is large enough since the PDFs in the xy -plane and the xz -plane are similar to each other. The number of detected vortices is however reduced in the downstream distance (cf. table 1), which they should since the vortices lose strength through viscous dissipation. The range of vortex diameters of significant relevance, i.e. within the 5% smallest and 5% largest vortices, is in average $0.07 \lesssim d/D \lesssim 0.14$.

In figure 10 the PDFs of the vortex strength is shown in the same way as in figure 9. For the xy -plane and the most upstream location ($x/D = 3$) one may observe a small shift of the PDF, corresponding to the 0.5 mm thick vortex generator, towards lower vortex strengths when compared with the stiff vortex generator. However, already at the next downstream location the most common vortex strength is the same for the two vortex generator thicknesses. At the most upstream location it is clear that the number of strong vortices is larger compared to the $x/D = 6$ and 9 locations. One may conclude that the fastest decay of vortex intensity take place right after the position of generation, which is in line with general knowledge about streamwise vortex evolution and the exponential decay of the vortex strength (see e.g. Lögdberg *et al.* 2009).

The circulation (γ) is also a measure of the vortex strength, as just discussed in relation to figure 9, but its sign also gives information about the rotational direction of the vortex. Positive and negative circulations correspond to counter clockwise (CCW) and clockwise (CW) rotational directions, respectively. In figure 11 the PDFs of the vortex circulation, normalized by $U_\infty D$, are plotted in the same way as in figures 9 and 10. Here, one may observe that the most common vortex strength is independent of the rotational direction, since the peak locations on the $\gamma/(U_\infty D)$ axis does not change. It should be mentioned that there is an asymmetric distribution of positive and negative vortices, but, which most likely is attributed to small misalignments when setting up the PIV image frames to be captured. This can also explain the most downstream location ($x/D = 9$) of the xy -plane, where the deviation is largest when comparing the flexible and the stiff vortex generators.

5. Summary and conclusions

In an effort to reduce emissions from internal combustion engines, an additive can be injected in the exhaust emissions. To enhance the mixing a vortex generator can be installed, however such a device can also be a source of acoustic noise. Recent results have shown that flexible vortex generators may reduce the level of noise compared to stiff ones. In the present paper a direct comparison of the generated fluid structures between a stiff and a flexible vortex generator in a pipe is made. The differences are quantified by means of small-scale flow structure changes and mean velocity profile changes between a stiff and a flexible vortex generator.

The vortex generator can be seen as a wing with a low pressure on the lee-side and a high pressure on the oncoming flow-side. This pressure difference induces strong and steady vortices for small to moderate angles of attack, which become unsteady for higher angles of attack or for flexible and vibrating wings where vortex shedding become the dominating flow phenomenon. These vortices complicate the flow description from a mean velocity point of view. However, the main conclusion drawn is that there is hardly any difference of the mean velocity distribution between the two different vortex generators.

The vortex size is set by the dimensions of the vortex generator, i.e. a physically small vortex generator will generate small vortices and *vice versa*. Since the size of the vortex generator is the same between the 0.5 and the 3.0 mm thicknesses the generated vortex diameter range was not expected to be significantly changed. However, the vortex strength seems to be somewhat affected by the flexibility of the 0.5 mm vortex generator thickness. This is revealed in a small shift of the PDF, corresponding to the 0.5 mm thick vortex generator, towards lower vortex strengths when compared with the stiff vortex generator.

It is shown that there are no major changes in the mean velocity field nor the strength, circulation and size of the generated vortices in the pipe. This result suggests that the mixing process is equally rapid for the flexible vortex generator as the stiff one, but with the advantage of having reduced the noise level.

Acknowledgements

We would like to thank Prof. Mats Åbom and Mikael Karlsson for hosting us and giving us running time in the MWL pipe flow facility. Andreas Holmberg at the Marcus Wallenberg Laboratory is acknowledged for his assistance during the actual PIV experiments and for running the pipe flow facility. The MWL technicians Kent Lindgren and Danilo Prelevic have been invaluable for the experimental setup. Furthermore, the authors would like to thank the Swedish Research Council, VR, for their financial support under grant number 621-2005-5757. The Göran Gustafsson foundation is also acknowledged.

References

- ADRIAN, R. J., CHRISTENSEN, K. T. & LIU, Z.-C. 2000 Analysis and interpretation of instantaneous turbulent velocity fields. *Exp. Fluids* **19**, 275–290.
- CHONG, M. S., PERRY, A. E. & CANTWELL, B. J. 1990 A general classification of three-dimensional flow fields. *Phys. Fluids* **2**, 765–777.
- KARLSSON, M., HOLMBERG, A., FALLENIOUS, B. E. G., FRANSON, J. H. M. & ÅBOM, M. 2008 Experimental determination of the aero-acoustic properties of an in-duct flexible plate. *AIAA Paper 2008-3057, 14th AIAA/CEAS Aeroacoustic Conference* .
- LÖGDBERG, O., FRANSSON, J. H. M. & ALFREDSSON, P. H. 2009 Streamwise evolution of longitudinal vortices in a turbulent boundary layer. *J. Fluid Mech.* **623**, 27–58.
- ZHOU, J. ADRIAN, R. J., BALACHANDAR, S. & KENDALL, T. M. 1999 Mechanisms for generating coherent packets of hairpin vortices in channel flow. *J. Fluid. Mech.* **387**, 353–396.